# A Search for Slow Magnetic Monopoles Below the Parker Bound

Thesis by

Sophia Kyriazopoulou

In Partial Fulfillment of the Requirements

for the Degree of

Doctor of Philosophy


California Institute of Technology

Pasadena, California

2002

(Defended March 6, 2002)

# Acknowledgements

There is a long list of people that I would like to thank for helping me arrive at the culmination of this long work. So I ask forgiveness if I have left out a lot of kind souls and bright minds I've met during this trip through knowledge and research.

Of course I cannot possibly ever forget my advisor Professor Barry Barish and my co-advisor Professor Charlie Peck, who patiently offered me guidance, support and encouragement. I have always treasured their advice, even when at times I seemed to go against it. I am deeply grateful to them. I only regret that distance and my shyness prevented me from extracting more profit from their wisdom and experience.

I would also like to thank all of the Caltech MACRO group and, in general, all the MACRO collaborators, past and present. Now that MACRO is decommissioned, how many long days – and some adventurous nights – of work do we have to remember! I would especially like to thank Erik and Yianni Katsavounidis for years of useful discussions and generous help, Gary Liu for showing me how electrical circuits can be fun, and Robert (Bob) Nolty for - so spontaneously - undertaking the painful task of editing this thesis. But to him I shall return at the end of these acknowledgments.

I always felt at home in Italy, at the Laboratori Nazionali del Gran Sasso, where this search took place. I have spent seven long years there and I would like to thank the people of the Laboratory for their hospitality and support. I would like to thank Professor Giorgio Giacomelli for financial support during periods of my stay in Italy.

A very special thanks goes to Dr. Michelangelo Ambrosio; for his enormous patience, for his support, for his concern, for his understanding, for his faith in me, for his way of celebrating life.

In this place in Italy, under the tallest peak of the Appenines I've made many friends. I would like to remember them now, at this moment of joy, for, at the moments of sorrow, they stood by me. I owe a lot to Sofia, Giorgia, Artemis, Maria, PierGiorgio and Dimitris for their sweet smiles and their encouraging words during

moments my faith was short. I would especially like to thank Makis for tolerating me, when nobody else would, and for helping me stand on my feet again, when nobody else could.

Of my friends at Caltech, I would like to mention Erik, Yiannis,Chrysa, Nikos and Dimitris, whose company made life at Caltech an easier experience. In particular, many thanks to Dimitris Kallifatides who is still running around so that I may submit this thesis in time. Also, many thanks to the people in the Graduate Office – especially to Natalie Gilmore – the registrar and the secretaries of our group at Caltech who battled bureaucracy for me.

There are no words, however, I can find - in any language - to thank my parents and my grandparents. I only hope they know how much I love them. My grandparents passed away while I was a graduate student and I can't help being sorry that I have been away for so long. To my family I would like to have dedicated my life.

I have been very lucky in my life to have met Gautam Vasisht. He has never refused his help to me. Moreover, he spontaneously offered editorial style in this thesis. But this is not the only reason I want to thank him. With his enlightened spirit and graceful existence he renewed, time and time again, my faith in the world. To Gautam I would like to have dedicated my love.

Finally, I would like to thank again the person who gave me the final push to cross the finish line in this race. This is Bob (Robert Nolty). Sometimes, life walks in circles and one of them is closing with this graduation. Bob was one of the first people I met at Caltech; we were admitted the same year. Don't mistake his amazing kindness for simplicity! In the years that followed Bob proved to be a mature researcher and, recently, the ideal editor to this thesis, giving shape and life to it with his comments and remarks. I am very happy that, after so many years and half the globe away, we graduate together. I hope his trip back to Ithaca is long and adventurous.

Bob, I would like to dedicate this thesis to you.

# Abstract

During the years of high school physics, instructors would tell us how asymmetry in Maxwell's equations express the fact that while there are stable particles carrying electric charge in nature, there are no magnets with a single pole. Yet Dirac had suggested the idea of a magnetic monopole decades before I was born, and around the time I was attending high school, Cabrera was starting his experiments to find one. I first learned about the possibility of the existence of such a particle when in graduate school. The idea of proving wrong something I had learned to take for granted, was exciting. Of course, whether a stable particle which carries magnetic charge does exist or not has profound implications for our understanding of the universe, but still, what makes the very idea of a magnetic monopole so attractive to me is that there are not that many basic, everyday things left – things like the indivisibility of a magnet – to be confirmed yet.

This work describes a search for the magnetic monopole, as it is postulated in many Grand Unified Theories (GUT). Such monopoles are expected to be heavy ($\sim 10^{17}$ GeV), may have a large range of velocities and – from current astrophysical constraints – must be very rare. The most widely accepted upper limit to their flux comes from considerations of the survival of the galactic magnetic field (the Parker Bound [1]), and it is of the order of $\sim 10^{-15}$ cm$^{-2}$sr$^{-1}$s$^{-1}$ [33]. This flux regime was explored by MACRO (Monopole Astrophysics and Cosmic Ray Observatory), a large area detector built in Gran Sasso in Italy.

Specifically, this was a search for slow-moving magnetic monopoles with the MACRO detector. MACRO featured a large acceptance ($\simeq 10,000$ m$^2$ sr), and three separate detector systems for monopoles. This search relies primarily on one of these systems: the scintillation detector. A custom-made trigger was developed to

[1] The limit quoted here is actually the one obtained in [33] by Turner, Parker and Bogdan and it is the limit we are going to refer to as the Parker Limit or the Parker Bound or the TPB limit from now on.

detect the passage of slow-moving magnetic monopoles ($v \sim 10^{-4}\ c$ to $4.3 \times 10^{-3}\ c$) through a scintillator tank. This trigger was employed for the initial selection of events over the data-taking period between June 1995 and May 2000. There were around 28 million relevant triggers during this period. These represent potential monopole events; each must be examined carefully to see if all recorded details are consistent with the signature of monopole passage. Analysis of the events and final selection was performed mainly with the help of a system which digitally sampled and recorded the waveforms of photomultipliers monitoring the scintillation detectors. A specially-designed pattern recognition algorithm, following the philosophy of the slow monopole trigger, was developed, in order to identify the signature of slow monopoles in the waveform system, while suppressing background generated due to cosmic-ray muons or electronic noise.

No events were observed that are consistent with the passage of a slow monopole. Detailed data quality checks were performed for each data run and the resulting actual configuration of the detector was used in a Monte Carlo calculation of the detector's acceptance on a run-by-run basis. Based on the exposure time due to MACRO over these five years of data taking, this search sets an upper limit to the flux of magnetic monopoles of

$$F \lesssim 2.5 \times 10^{-16}\ \mathrm{cm}^{-2}\ \mathrm{sr}^{-1}\ \mathrm{sec}^{-1}$$

for particles in the velocity range $v \sim 10^{-4}\ c$ to $v \sim 4.1 \times 10^{-3}\ c$.

# Contents

# List of Figures

# List of Tables

# Chapter 1

# Theory and Searches for the Magnetic Monopole

## 1.1 Theoretical Motivation

Since Dirac's original paper on magnetic monopoles in 1931 [2], there have been many theoretical attempts to describe how these particles arise at every level of our understanding of physics: from classical electrodynamics to grand unification. An extended review on the theory of magnetic monopoles is by Preskill [3]. I summarize the highlights of monopole theory and some intricacies in the following sections, but for the reader already acquainted with the subject, I will begin with the question: *why do we (still) search for magnetic monopoles?*

Since magnetic monopoles necessarily exist in most Grand Unified Theories (GUTs), a worrisome question arises: GUTs predict the existence of monopoles and also predict monopole abundances far greater than are experimentally seen or inferred from astronomical observations. Therefore, should GUTs containing monopoles be excluded? An interesting way out of this seeming controversy is provided by the inflationary scenario. Suggested initially by Alan Guth [17] in order to address the horizon and flatness problems of the universe, it offers as a side consequence the possibility of suppressing magnetic monopole abundances.

Subsequently, theorists have developed various scenarios which have predictions for monopole abundances that vary from no monopoles to densities high enough to cause cosmological catastrophes. Inflation itself is well supported by recent experimental data, but its particular form is still far from identified. Now, more than ever, additional experimental data is necessary in order to narrow down the possibilities. Now, more than ever, it makes sense to search for magnetic monopoles at densities below limits set by astrophysical considerations. In fact, the goal of this search is to

look below one of the most respected of these limits: the so-called Parker Bound (as modified in TPB [33]).

### 1.1.1 Magnetic Monopoles in Classical Electromagnetism

The concept of magnetic monopoles, which means the presence of individual magnetic poles is in direct contradiction with the second Maxwell equation, $\vec{\nabla} \cdot \vec{B} = 0$, where $\vec{B}$ is the magnetic field, while the presence of discrete electric charges is allowed by the first of Maxwell equations, that is $\vec{\nabla} \cdot \vec{E} = 4\pi\rho_e$, where $\vec{E}$ is the electric field and $\rho_e$ is the electric charge density. But physicists and, it seems, nature like symmetries and love invariance under transformations. So we may symmetrize the equations of Maxwell with respect to electric and magnetic charges and verify that these equations remain invariant under duality transformations. In fact, assume the existence of a magnetic charge density $\rho_m$ and a magnetic current density $\vec{J_m}$. Maxwell's equations in Gaussian units would then take the form [1]:

$$\vec{\nabla} \cdot \vec{E} = 4\pi\rho_e$$
$$\vec{\nabla} \cdot \vec{B} = 4\pi\rho_m$$
$$\vec{\nabla} \times \vec{E} = -\frac{1}{c}\frac{\partial \vec{B}}{\partial t} - \frac{4\pi}{c}\vec{J_m}$$
$$\vec{\nabla} \times \vec{B} = \frac{1}{c}\frac{\partial \vec{E}}{\partial t} + \frac{4\pi}{c}\vec{J_e}$$

The above equations are invariant under the transformation of sources and fields by a real angle $\theta$ :

$$\vec{E} = \vec{E'}cos\theta + \vec{B'}sin\theta$$
$$\vec{B} = -\vec{E'}sin\theta + \vec{B'}cos\theta$$
$$\rho_e = \rho'_e cos\theta + \rho'_m sin\theta$$
$$\rho_m = -\rho'_e sin\theta + \rho'_m cos\theta$$
$$\vec{J_e} = \vec{J'_e}cos\theta + \vec{J'_m}sin\theta$$
$$\vec{J_m} = -\vec{J'_e}sin\theta + \vec{J'_m}cos\theta$$

In addition, the Poynting vector $\frac{c}{4\pi}\vec{E}\times\vec{B}$ and the energy density $\frac{1}{8\pi}(E^2+B^2)$ remain invariant. Then, as long as all particles have the same ratio of magnetic to electric charge, we can perform the above duality transformation setting $\theta$ such that $\rho_m = 0$, $\vec{J_m} = 0$ to arrive to the Maxwell equations in the form that they are usually known. Discrete magnetic charges are, thus, compatible with classical electromagnetism; however, they are not necessary.

### 1.1.2 Dirac Monopoles

Dirac entertained the idea of indefinite phases for wavefunctions in the scheme of quantum mechanics. That is, he assumed that the phase of a particle's wave function does not need to be definite at any point in space, thus the change in phase around a closed curve does not need to vanish. He showed that this may be interpreted physically as the existence of isolated magnetic poles [2].

Here we are going to follow a simplified version of Dirac's original arguments in order to demonstrate that the existence of isolated magnetic poles is compatible with quantum mechanics and to derive Dirac's quantization condition for the magnetic charge of the magnetic monopole. Assume that a magnetic monopole of magnetic charge g resides at the origin of our coordinate system. To entertain the idea of symmetry between electric and magnetic charges, we assume that the magnetic field of the magnetic monopoles in spherical coordinates is given by

$$\vec{B} = \frac{g}{r^3}\,\vec{r}. \tag{1.1}$$

Then the flux of $\vec{B}$ over a closed surface S surrounding the magnetic monopole is

$$\oint_S \vec{B}\cdot d\vec{S} = 4\,\pi\,g. \tag{1.2}$$

This means that the vector potential $\vec{A}$ associated with $\vec{B}$ must be singular at least

at one point on the surface, because otherwise we would have had

$$\oint_S \vec{B} \cdot d\vec{S} = \oint_S (\vec{\nabla} \times \vec{A}) \cdot d\vec{S} = \int_V \vec{\nabla} \cdot (\vec{\nabla} \times \vec{A})\, dV = 0 \tag{1.3}$$

According to these arguments, this is true for any closed surface enclosing the magnetic monopole. Thus, these points where $\vec{A}$ is singular form a semi-infinite line ending on the magnetic monopole. This is what Dirac called a "nodal line." The location of the nodal line may be arbitrarily chosen; thus, the physical observables should not depend on where the line is. An electron described by its wavefunction $\psi = \psi_1 e^{i\gamma}$, where $\psi_1$ and $\gamma$ are real functions of x,y,z and t, moving on a closed curve L around the line should not be able to detect it, i.e., the electron's phase change $\Delta\gamma$ can only be multiples of $2\pi$

$$\psi \rightarrow \psi' = \psi_1\, e^{i(\gamma + 2\pi n)}. \tag{1.4}$$

On the other hand, the presence of electromagnetic field results in a change of phase of the electron's wavefunction by $(-e/\hbar c)\vec{A} \cdot \vec{r}$. Thus, around the closed curve L the phase change $\Delta\gamma$ in the electron's wavefunction due to the electromagnetic field is

$$\Delta\gamma = -\frac{e}{\hbar c} \oint_L \vec{A} \cdot d\vec{l} = -\frac{e}{\hbar c} \int_S (\vec{\nabla} \times \vec{A}) \cdot d\vec{S} = -\frac{e}{\hbar c} \int_S \vec{B} \cdot d\vec{S}, \tag{1.5}$$

where S is a surface which is bounded by the closed line L and which does not intercept the nodal line. Eqn. 1.5 shows that, since $\vec{A}$ is singular on the string, the integral leads to undetermined phases on the nodal line. On the other hand, continuity arguments do not allow undetermined phases unless the wavefunction of the electron vanishes. Thus, Dirac assumed that the wavefunction of the electron vanishes along the nodal line so that undetermined phases are allowed. As the closed curve shrinks and gets infinitesimally close to the nodal line, the surface encloses the total magnetic monopole flux given by Eqn. 1.2. Thus, from Eqns. 1.4, 1.5 and 1.2

we get Dirac's quantization condition:

$$\frac{e}{\hbar c}4\pi g = 2\pi n \Rightarrow g = n\frac{1}{2}\frac{\hbar c}{e^2}e = n\frac{1}{2}\frac{e}{\alpha}, \tag{1.6}$$

where $\alpha$ is the fine structure constant.

At a time when no other explanation of the quantization of the charge was known, the above consequence of the hypothesis of the existence of isolated magnetic poles was spectacular. It was much later (1974) that t'Hooft [9] and Polyakov [8] independently showed that in Grand Unified Theories monopoles are a necessity, i.e., they emerge as stable solutions. Remarkably, in those theories the quantization of the electric charge also emerges as a necessity; this is due to the fact that the charge operator obeys nontrivial commutation relations with the other operators.

### 1.1.3 GUT Monopoles

Grand Unified Theories attempt to unify gravity, strong and electroweak interactions. The starting points are theories that unify strong and electroweak interactions, whose apparently independent coupling constants seem to evolve toward unification at very short distances, i.e., at very large mass scales. To describe this tendency, various Grand Unified Theories (GUTs) have been suggested and have led us toward the understanding of many experimentally observed phenomena.

All GUTs possess a large group of exact gauge symmetries that mix strong and electroweak interactions. The large GUT group is spontaneously broken at very short distances to the standard low energy gauge group: $GUT \rightarrow SU(3)_{color} \otimes [SU(2) \otimes U(1)]_{electroweak}$, where $SU(3)_{color}$ describes the strong (color) interaction and $[SU(2) \otimes U(1)]_{electroweak}$ – known as the Weinberg-Glashow-Salam model – describes the electroweak interaction. It has been shown that such GUTs, where $U(1)_{EM}$ is embedded in a non-Abelian simple or semi-simple group that undergoes spontaneous symmetry breaking (SSB):

a) impose quantization of electric charge [7],[3]

b) contain magnetic monopoles [8], [9].

The exact mechanism of the breaking does not influence the above outcomes.

The simplest unified group that satisfies the above requirements is SU(5). Making the assumption that there are no surprises between current energy scales (100 GeV) and the unification scale (this assumption is widely known as desert hypothesis), we expect unification around[1] $M_x \sim 10^{14} - 10^{15}$ GeV [4],[5]. The monopole mass, which is of the order of $M_m \sim \frac{M_x}{\alpha_x}$ [9], is then expected to take on values around $M_m \sim 10^{16}$ GeV. In the above relation $\alpha$ is the coupling constant at unification scale (for SU(5) it is $\sim 1/40$). The core of a monopole is of order $M_x^{-1} \sim 10^{-28}$ cm, and therefore much larger than its Compton wavelength $M_m^{-1} \sim 10^{-30}$ cm. Thus, GUT monopoles are almost classical objects with a mass comparable to that of a bacterium. Who would not want to discover one?

Unfortunately, SU(5) seems not to be compatible with experimental data. SU(5) predicts the proton lifetime to be between $1.6 \times 10^{30}$ yr to $2.5 \times 10^{28}$ yr. Attempts to observe proton decay at this level have failed. More importantly, in SU(5) the extrapolations of the experimentally measured coupling constants to the unification scale do not meet at a single point. The lack of gauge coupling unification in the SU(5) model is depicted in Fig. 1.1.

However, in the minimal supersymmetric extension of SU(5) (MSSM) the coupling constants converge (as seen in Fig. 1.2). This unification happens at a higher mass scale ($M_x \sim 10^{16}$GeV), where the running coupling constant is of the order of $\sim 1/25$. A higher mass for monopoles ($M_m \sim 10^{17}$ GeV) is therefore predicted [2]. The minimal SUSY SU(5) predicts a higher proton lifetime, which is currently not ruled out by experiment.

Since the mass of the magnetic monopole depends on the unification scale, consideration of different GUT theories [11] can result in lighter monopoles (in the range $10^7 - 10^{13}$ GeV) which carry a multiple Dirac magnetic charge. Monopoles also arise in Kaluza-Klein theories, which unify Einstein's theory of gravitation with strong

[1] For a big part of this chapter we are going to use the so-called natural units. In this system the constants $\hbar = c = 1$ and there is one fundamental dimension, energy.

[2] This search is not directly dependent on the exact value of the monopole mass. We will use $10^{17}$ GeV as the typical mass of a GUT monopole from now on.

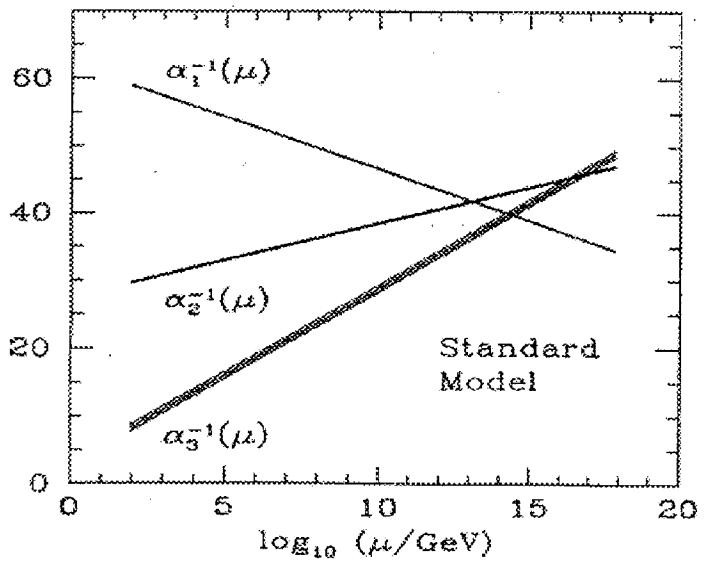


Figure 1.1: Evolution of the coupling constants to high energy scales in the SU(5) model. The inverse of the coupling constants is plotted against the mass scale $\mu$. The values of the coupling constants at the weak scale are the experimentally measured values. The figure is reprinted from ref. [10]. The evolution is calculated using the renormalization group equations.

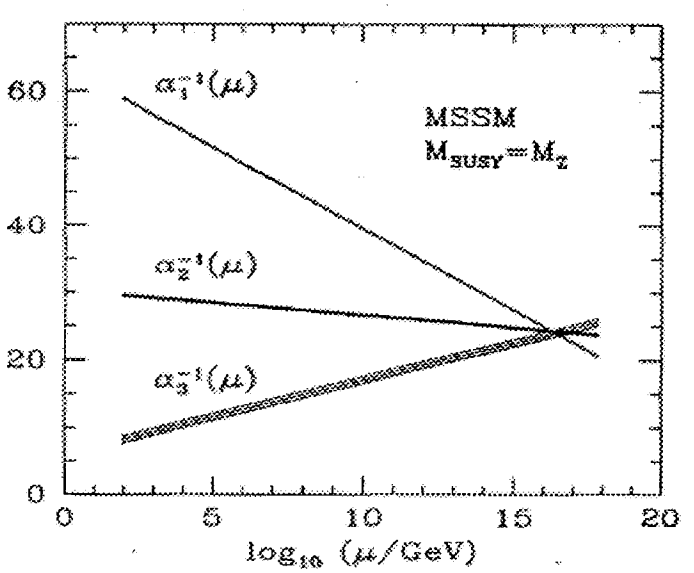


Figure 1.2: Evolution of the coupling constants to high energy scales in the MSSM model. The figure is reprinted from ref. [10].

and electroweak interactions. These have larger masses ($\sim 10^{19}$ GeV)[3].

Once magnetic monopoles are allowed (one could well say "imposed") by the theory, many other variants may descend upon the scene. Magnetic monopoles may carry electric charge, a configuration called a "dyon," or monopole-electric charge bound states may exist [13].

So we see that monopoles haunt GUTs persistently enough to make us eager to observe them. Of course, with masses of order $\sim 10^{17}$ GeV, we do not expect to construct them in present day particle accelerators. Instead, we are forced to consider primordial monopoles, i.e., those that may have been produced at the time of the beginning of the universe. And by searching for these particles we hope to travel back in time and shed light on some of the shadows of the very early universe.

## 1.2 Monopole Production in the Very Early Universe

At this point the trip back in time reveals a big contradiction between cosmology and particle physics: as I explain below, GUTs predict monopole production in the very energetic epoch immediately after the Big Bang in quantities too large to be compatible with the subsequent evolution of the universe.

As the universe began, the grand unified gauge symmetry was unbroken and the scalar field $\phi$, which acts as the order parameter of the breakdown of the gauge symmetry, had zero expectation value. Since the symmetry had not gone through SSB, there were no monopoles at this epoch. As the universe expanded its temperature decreased. When it fell below a critical temperature $T_c$, of order the unification mass scale $M_x$, the symmetry was broken by a phase transition of the Higgs field $\phi$ from the symmetric phase to the broken phase (Higgs mechanism), and the vacuum did not respect the symmetry anymore. That means that the $\phi$ acquired a non zero expectation value and magnetic monopoles arose through the Kibble mechanism [14]. The Kibble mechanism basically expresses the fact that during any cosmological phase

transition, a correlation length, $\xi$, is always limited by the particle horizon length $d_H$. The correlation length sets the maximum distance over which the Higgs field may show correlation. Since during a phase transition the Higgs field cannot be correlated at distances larger than this correlation length, we end up with configurations of $\phi$ that cannot be deformed into a configuration where the expectation value of the field everywhere is the vacuum value. Instead, there are points where the field necessarily vanishes. These points are stable topological defects that are the magnetic monopoles. Topological defects of higher dimensions may also arise, for example cosmic strings (one dimension) or domain walls (two dimensions) [15].

The monopole production mechanism depends on the nature of the phase transition: strongly first order, weakly first order or second order.

In the case of weakly first order or second order transition, we have large random fluctuations of the scalar field $\phi$ when the temperature $T$ goes near the critical temperature $T_c$. The field $\phi$ is uncorrelated over distances larger than a correlation length $\xi$, and seems to develop a domain structure. At the intersection point of several domains, with non-trivial field orientation, monopoles or antimonopoles form. The density of monopoles is comparable to the density of these domains. The correlation length cannot be larger than the horizon length $d_h$ at $T_c$ [16] and we have

$$(n_m)_{init} \sim p d_h^{-3} \sim p(\frac{T_c^2}{CM_{Pl}})^3, \tag{1.7}$$

where p is the probability of monopole formation (perhaps 1/10), $M_{Pl}$ is the Planck mass and $C \sim \frac{1}{20}$ in a minimum GUT [16]. If the subsequent evolution of the universe is adiabatic, then it is convenient to use the ratio $n_m/s$, where s is the entropy density. The ratio $n_m/s$ is the monopole number per comoving volume and is preserved during adiabatic expansion. Also, since $s \sim T^3$ the relic abundance of magnetic monopoles is conveniently given by

$$\frac{n_m}{T^3} \sim p(\frac{T_c}{CM_{Pl}})^3. \tag{1.8}$$

In a typical GUT (SU(5)) we have $T_c \sim 10^{15}$ GeV and thus,

$$\frac{n_m}{T^3} \sim 10^{-10}. \tag{1.9}$$

On the other hand, in the case of a strongly first order transition, supercooling occurs. The temperature $T$ decreases below $T_c$ until bubbles of the new broken-symmetry phase start nucleating, expanding and colliding. Each bubble $\phi$ is quite homogeneous, but the orientation of the field has no correlation with that of another bubble not in contact. When the bubbles collide to fill the space, topological knots are formed which are the monopoles and antimonopoles. We expect the density of monopoles to be comparable to the density of bubbles at the time of coalescence. A calculation of the density has been performed in [18] and results in a monopole abundance of order

$$\frac{n_m}{T^3} \sim [(\frac{T_c}{M_{Pl}}) \ln(\frac{M_{Pl}^4}{T_c^4})]^3, \tag{1.10}$$

where the logarithmic factor accentuates further the production of magnetic monopoles:

$$\frac{n_m}{T^3} \sim 10^{-7} \tag{1.11}$$

This abundance can be subsequently reduced by monopole-antimonopole pair annihilation. The annihilation rate, however, is very low [12], and the abundance is not suppressed considerably. In this manner and if we use Eqn. 1.9, we arrive at a predicted present day monopole density of $\sim 10^{-7}$ cm$^{-3}$. It is easy to see that using Eqn. 1.11 would lead to an even larger present monopole density. It also suffices to recall that $M_m \sim 10^{17}$ GeV to realize, as outlined below, the utter incompatibility of the above scenarios with the observed universe. The mass density due to magnetic monopoles is

$$\rho_m = M_m\, n_m \sim 10^{-4}(\frac{M_m}{10^{17}\, GeV})(\frac{n_m}{s})\, g\, cm^{-3} \tag{1.12}$$

and if we keep in mind the above predicted monopole density form Eqn. 1.9, we

obtain

$$\rho_m \sim 10^{-14}(\frac{M_m}{10^{17}GeV})\, g\, cm^{-3}. \tag{1.13}$$

On the other hand, the total average mass density $\rho_{TOT}$ in the universe may be written as $\Omega_{TOT}\rho_c$ where $\Omega$ is the density parameter defined as

$$\Omega_{TOT} = \frac{\rho_{TOT}}{\rho_c}, \tag{1.14}$$

and $\rho_c$ is the critical density

$$\rho_c \simeq 1.9 \times 10^{-29} h^2\, g\, cm^{-3}. \tag{1.15}$$

In Eqn. 1.15, $h$ is defined as $h = H_0/100$, where $H_0$ is the Hubble constant in units of km $s^{-1}$ $Mpc^{-1}$. Astronomical constraints place $h$ in the range $0.4 < h < 1$ [15], while $\Omega_{TOT}$ has recently been determined to be $\Omega_{TOT} \sim 1.1$ with microwave background anisotropy observations [27]. Therefore, Eqn. 1.13 results in a mass density and an expansion rate completely incompatible with current observations. The above conflict between particle physics and observational cosmology is known as the monopole problem, and efforts to resolve it have led to the conception of revolutionary theoretical scenarios that we summarily review in the next section.

## 1.3 Inflation and the Return of Magnetic Monopoles

By the early 1980s, standard Big Bang cosmology suffered from several important problems in addition to the monopole puzzle. Basic questions like *"Why is the universe so old and flat?", or " Why is it so homogeneous and isotropic on large scales?"* would not find satisfying answers. The attempt to give an answer to the above questions and to solve the monopole problem led to the development of inflation.

The paper that brought the attention of the world to this idea was written by Guth [17] in 1981, and it is now referred to as "old inflation." It was based on

the occurrence of supercooling during cosmological phase transitions. The scenario suggested that the universe started in a phase where symmetry was unbroken; thus, the expectation value of the Higgs field $\phi_0$ was zero. As it cooled down to the critical temperature, $T_c$, a second minimum for the potential $V(\phi)$ developed at $\phi_B$. During such a phase transition, bubbles of the low temperature phase $\phi_B$ would nucleate and grow. If the nucleation rate was low, then the universe would continue to expand and cool in its high temperature phase $\phi_0$, down to some temperature $T_s$, many orders of magnitude below $T_c$. The energy density $\rho_0$ in the high temperature phase $\phi_0$ is necessarily higher than that in the low temperature phase $\phi_B$. As $T \to 0$ in the high temperature phase, the energy density would be dominated by $\rho_0$ and would, thus, remain constant. Constant energy density then leads to a constant expansion rate $H \equiv \dot{R(t)}/R(t)$, where R is the cosmic scale factor and, thereby to an exponentially expanding universe : $R(t) \propto e^{Ht}$. This stage of exponential increase in the scale factor is called inflation. During the expansion, a small, smooth and causally coherent part of the universe with initial size of the order of the horizon length $d_h$ may grow to a size that today may engulf the entire observable universe. All inhomogeneities and other troublesome topological defects are, thus, conveniently diluted away. When eventually the phase transition did take place, latent heat that is characteristic of the energy scale $T_c$, would be released and the universe would reheat to a temperature $T_r$ comparable to $T_c$. As a result, the entropy density would increase by a factor of roughly $(\frac{T_r}{T_s})^3$.

Unfortunately the scenario had many problems, but the core idea was so attractive that physicists have entertained many other variants such as the "new inflationary" or "slow-rollover" scenarios proposed by Linde [19] and Albrecht and Steinhardt [20]. The evolution of the field $\phi$ in this model is represented graphically in Fig. 1.3. The universe started again in the phase where the expectation value of the Higgs field $\phi$ was zero and the symmetry was unbroken. As it cooled down to the critical temperature, $T_c$, a second minimum for the potential $V(\phi)$ developed at $\phi_B$, which for $T < T_c$ became the global minimum (see Fig. 1.3). The field $\phi$ initially had to overcome any potential barriers (region A in Fig.1.3). It then started rolling toward

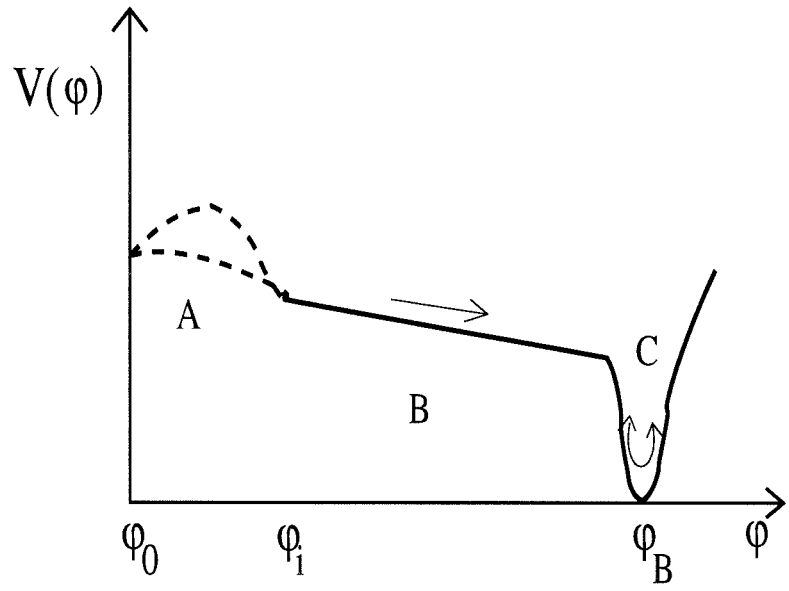


Figure 1.3: Motion of the scalar field $\phi$ in the case of a slow-rollover inflationary potential $V(\phi)$. In region A, there is barrier penetration. In region B, the scalar field rolls slowly toward its new vacuum expectation value and the universe expands exponentially. In region C, we have rapid oscillations of the field, creation of elementary particles and reheating.

$\phi_B$ (region B). The motion of $\phi$ in region B was similar to that of a ball rolling down the hill with friction:

$$\ddot{\phi} + 3H\dot{\phi} + \frac{dV(\phi)}{d\phi} = 0. \tag{1.16}$$

If the potential was flat enough, $\phi$ would take a long time to reach $\phi_B$, when compared with the expansion time scale. During this time, the temperature dropped and the energy density was dominated by the vacuum energy density $V(\phi_0) \sim M_X^4$. The universe then expanded rapidly with [19]:

$$H^2 = \frac{8\pi}{3\,M_{Pl}^2} V(\phi_0). \tag{1.17}$$

Eventually, $\phi$ reached region C, where rapid oscillations of the field take place and are eventually damped due to rapid particle creation. As the decay products reached thermal equilibrium, the universe reheated. The non-adiabatic reheating process accompanied a large increase in entropy.

The initial model of the "new inflationary" scenario had several shortcomings

[26][15], but pointed the way towards construction of more successful models. Today, most models of inflation are based on this principle of "slow" evolution of the scalar field and inflation has become a mainstay of cosmology. Recent experimental results from Maxima-1, Cobe-DMR and Boomerang cosmic microwave background observations [27] are consistent with inflation, even though the specific model is not yet identified.

In 1983, Linde suggested a very elegant model [21] called "chaotic inflation" where the potential is very simply $V(\phi) \propto \phi^n$. The potential minimum is at $\phi = 0$ while initially $\phi$ is away from zero. The initial value of the field, $\phi_{init}$ is chaotically distributed in different parts of the universe. In Fig. 1.4 we outline the inflationary evolution in the case of a field with mass $m$ and potential energy density $V(\phi) = (m^2/2)\phi^2$.

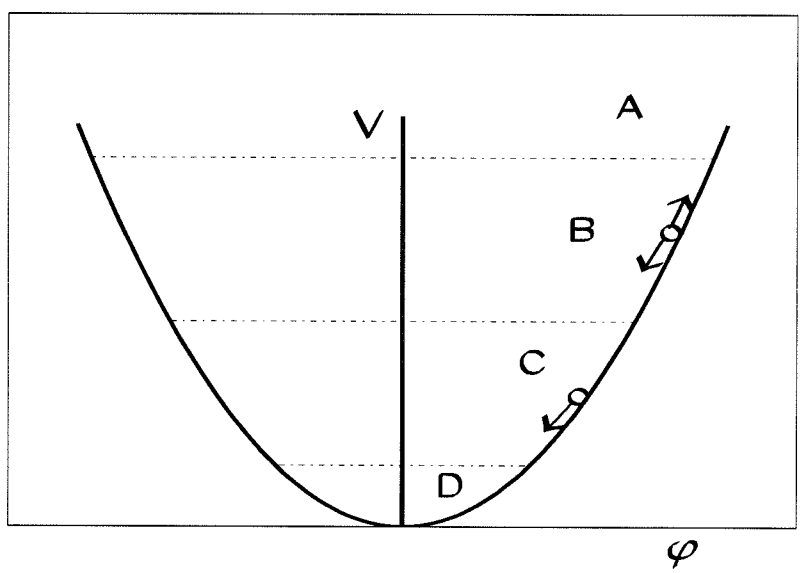


Figure 1.4: Motion of the scalar field $\phi$ in the case of a chaotic inflationary scenario $V(\phi)$. In region A, we have the space-time foam. In regions B and C, the universe expands exponentially. In region B, quantum fluctuations of the field are so large that the field can increase and this leads to eternal reproduction of the inflationary universe. In region D, there is rapid oscillation of the field, creation of elementary particles and reheating.

Several different regimes are possible depending on the value of $\phi$. If the potential energy density of the scalar field is greater than the Planck energy density $M_{Pl}^4$, quantum fluctuations of space-time are very strong and this state is referred to as space-time foam. At smaller energy density, $m^2 M_{Pl}^2 < V(\phi) < M_{Pl}^4$, the scalar field moves down very slowly in analogy with a ball in a viscous liquid, where the viscosity is proportional to the expansion rate of the universe given by the Hubble's constant $H$. During this stage (region B and C in Fig. 1.4) the universe grows approximately as $e^{Ht}$ (inflation). When $\phi$ becomes sufficiently small, the inflationary phase ends. The scalar field $\phi$ begins to oscillate near the minimum of $V(\phi)$ (region D). Like any rapidly oscillating field, it loses its energy by creating elementary particles which through subsequent interactions with each other come to a state of thermal equilibrium. This stage is called "reheating." Region B ($mM_{Pl}^3 < V(\phi) < M_{Pl}^4$) in Fig. 1.4 is somewhat peculiar, because large quantum fluctuations of $\phi$ here have a dramatic consequence: the eternal self-reproduction of inflationary universe. A small causally connected initial domain with radius $H^{-1}$, with large $\phi$, expands in time $\Delta t \simeq H^{-1}$ by $e^3$. Quantum fluctuations of $\phi$, with typical wavelength scales of $H^{-1}$, may be larger than the decrease of $\phi$ during $\Delta t$. Therefore, at the end of $\Delta t$ we end up with a domain $\sim 20$ times larger than the initial one, in half of which the field increases more than decreases. Hence, the total volume of the universe with growing $\phi$ increases ten times. Due to a large $\phi$, the process repeats and the universe enters the eternal process of self-reproduction.

Eternal inflation may have even more dramatic effects when considering multiple scalar fields as realistic models of elementary particles require. In this case the potential energy of the scalar fields may have several minima corresponding to different types of symmetry breaking, i.e., to different laws of low energy physics. Quantum jumps of the scalar fields during inflation may lead to the formation of infinitely many, exponentially large domains with different laws of low energy physics. If this is the case, the initial conditions do not matter anymore. The Big Bang loses in a way some of its importance for the further evolution of the universe; the laws of physics that govern the observable part of the universe are just one of the many

possibilities. This possibility is expressed with an accented philosophical tone in the "Anthropic Principle." It states that we experience these particular laws of physics because our kind of life could not be in any of the other (possibly existing) parts of the universe where physical laws are maybe different.

It is obvious by now that the magnetic monopole puzzle instigated the conception of revolutionary cosmological scenarios, the purpose of which was (amongst other things) to suppress the monopole abundance. However, it soon became clear that in many branches of the inflation monopoles arise again. In fact, many of the scenarios predict the further creation of magnetic monopoles as well as other topological defects soon after inflation ends (region D), during reheating when the field oscillates near the minimum of its effective potential.

The slow-rollover scenario predicts thermalized production of superheavy monopoles in rare, energetic particle collisions during the reheating process. The effective monopole mass oscillates about a value $m$ as the vacuum expectation value of the scalar field oscillates about the symmetry-breaking minimum of the scalar potential. Owing to this effect, monopole production is greatly intensified, with dependence on the exact form of the scalar potential and details of the reheating process [22].

Recently, it has been suggested that in many inflationary models the first stages of reheating occur in a regime of broad parametric resonance called preheating [23]. The main idea is that during the oscillations of the field around its broken symmetry vacuum value, each time the field approaches the broken symmetry vacuum value new particles are produced in proportion to the number of particles produced in previous oscillations. Hence, we have an explosive particle production. This explosive particle production leads to large fluctuations $< (\delta\phi)^2 >$ which may be large enough to restore symmetries with SSB at $\sim 10^{16}$ GeV. Topological defects can then be produced in the standard way when the symmetry breaking occurs again. The production of topological defects is easily compatible with inflation [25] and their absence is not an automatic consequence of inflation anymore.

Another popular form of inflation, the hybrid inflation, is also susceptible to overproduction of topological defects [24] (Hybrid inflation are scenarios with two

involved fields: one drives the inflation until the other undergoes SSB [26].) There is currently a lot of work being done on inflationary scenarios trying to cope with this problem. We mention here the work of Lazarides and Shafi [28], which – in the framework of hybrid inflation – dilute the flux of magnetic monopoles by invoking subsequent thermal inflation on an intermediate mass scale. They end up with a possible magnetic monopole flux below but near the Parker Limit (see section 1.4.1 for a definition of this limit), thus giving, more contemporary relevance to the search described in this thesis. Other possible solutions are suggested [29] within the framework of SUSY GUTs and hybrid inflationary scenarios where the GUT is already broken during inflation and therefore no topological defects may form at the end of the inflationary period.

At this point we may also resurrect older suggestions to suppress monopole abundance by considering a possible superconducting phase of the evolution of the universe at temperatures $T \geq 10^3$ GeV [31]. During this phase monopole-antimonopole pairs become connected through flux tubes and annihilate rapidly [32] decreasing monopole abundance.

The monopole puzzle remains unsolved. The plethora of available theories, which predict a wide range of monopole abundances, make the need for experimental evidence all the more important. New evidence – positive or negative – will help provide new constraints and provide direction towards a correct choice of theory, or perhaps once more lead to the evolution of new ones.

## 1.4 Astrophysical Limits on the Monopole Flux

The fate of magnetic monopoles after their first seconds of their possible birth is much less dramatic. With a very small annihilation rate (unless a superconducting phase of the universe enhanced this rate significantly) they should remain in kinetic equilibrium until the epoch of $e^{\pm}$ annihilations. Subsequently their velocities would decrease, as the universe expanded, and their present day velocities would be quite small. Astrophysical mechanisms, however, such as the presence of large scale

gravitational and magnetic fields should increase these velocities.

Hence, magnetic monopoles should be roaming the present day universe and, if in reasonable abundance, should be detectable through various effects by an interested observer. In fact, the absence of the effects sets limits on the current flux of monopoles. In order to define the effects of the existence of magnetic monopoles on astrophysical quantities, many assumptions have been made that allow room for doubt regarding the resulting limits. One of the most robust upper limits to the monopole flux is the Parker Limit as modified by Turner, Parker and Bogdan [33] (TPB limit). It is based on the survival of the galactic magnetic field, and sets the goals for the experiment that we describe in this manuscript. In the following sections we also discuss limits based on the mass density in the universe, and on monopole-induced nucleon catalysis.

### 1.4.1 The Parker Bound

A magnetic monopole crossing the universe would be subject to forces when crossing B-fields, for instance large scale fields such as the intergalactic or galactic magnetic fields. Through this interaction it would gain or lose energy at the expense of the field. Since our understanding of the galactic field is better, TPB have used it in deriving their upper limit on the background monopole flux [33].

According to the best current estimates the galactic magnetic field has an average strength of $< B_P > \simeq 3 \times 10^{-6}$ G. To derive their limit TPB have also used the following set of parameters for the field: a coherence length of about $l_P \simeq 10^{21}$ cm, a spatial extent of $L_P \simeq 10^{23}$ cm and a regeneration time of $t_{reg} \simeq 10^{15}$ s due to dynamo action. In order to keep the derived limit independent of these parameters the following scaling factors are used: $B_3 = B/(3 \times 10^{-6} G)$, $l_{21} = l/(10^{21} cm)$, $L_{23} = L/(10^{23} cm)$ and $t_{15} = t_{reg}/(10^{15} s)$, where $B$, $l$, $L$, $t_{reg}$ are the values for the strength, the coherence length, the spatial extent and the regeneration time of the galactic field, respectively. We expect that the scaling factors $B_3$, $l_{21}$, $L_{23}$ and $t_{15}$ are of order one. In addition, the scaling $M_{17} = M_m/(10^{17} GeV)$ is used, where $M_m$ is

the monopole mass. A magnetic monopole of mass $M_m = M_{17}\,10^{17}$ GeV, and Dirac charge $g$, entering a coherent region $l$ of field $B$ with negligible velocity will acquire a velocity:

$$v_{magn} \sim (\frac{2gBl}{M_m})^{1/2} \sim 10^{-3}c(l_{21}B_3/M_{17})^{1/2}. \tag{1.18}$$

We see from Eqn. 1.18 that monopoles with $M_m \lesssim 10^{17}$ GeV can easily be accelerated to velocities larger than the galactic escape velocity, $v_{esc} \sim 10^{-3}c$, and therefore will not be bound by the galaxy. Thus, if $v$ is the velocity of the monopoles, the following cases remain: i) monopoles cluster in the galaxy and $v \sim 10^{-3}c > v_{magn}$, ii) monopoles do not cluster in the galaxy and $v > 10^{-3}c > v_{magn}$ and finally, iii) monopoles do not cluster in the galaxy and $v_{magn} > v > 10^{-3}c$.

For cases (i) and (ii), where $v > v_{magn}$ the effect of the B-field is of second order and monopoles will experience only minor deflections. The change in energy is

$$\frac{1}{2}M_m\vec{v}\cdot\vec{\Delta v} + \frac{1}{2}M_m(\Delta v)^2. \tag{1.19}$$

The first term averages to zero for an isotropic monopole flux and/or for equal fluxes for monopoles and antimonopoles. When averaged the second term yields

$$\Delta E = \frac{1}{2}M_m(\Delta v)^2 \sim \frac{1}{2}M_m(\alpha_{magn}l/v)^2 = \frac{1}{2}M_m(\frac{gB}{M_m}\frac{l}{v})^2 \tag{1.20}$$

for the average energy gain per monopole. If $F$ is the flux of magnetic monopoles, then $(4\pi) \times (\pi l^2) \times F$ monopoles interact with the field per unit time, and in time $t = t_{reg}$ they should drain from the field an energy $4\pi^2 l^2 F \Delta E t$, which should be less than the total magnetic energy of this region $\frac{B^2}{8\pi}\frac{4\pi l^3}{3}$. This gives the following flux upper limit of

$$F \lesssim 10^{-15}\frac{M_{17}}{l_{21}t_{15}}(\frac{v}{10^{-3}c})^2\, cm^{-2}\, sr^{-1}\, s^{-1}. \tag{1.21}$$

Eqn. 1.21 is the TPB flux limit for $M_m \gtrsim 10^{17}$ GeV.

In the third case, where $v_{magn} > v > 10^{-3}c$, the monopole will be accelerated quickly to $v_{magn}$ and will continue its trip through the galaxy gaining or loosing energy

$\Delta E \sim gBl$ in each coherent region. By the time it leaves it has crossed around $L/l \sim 100L_{23}/l_{21}$ such regions draining an average energy of $\Delta E_{mon} \sim \sqrt{100L_{23}/l_{21}}\Delta E$. Again the survival of the galactic field imposes the condition

$$(4\pi) \times (\pi L^2) \times F \times \Delta E_{mon} \times t < \frac{B^2}{8\pi}\frac{4\pi L}{3} \Rightarrow F \lesssim 10^{-15}\frac{B_3}{t_{15}}(\frac{L_{23}}{l_{21}})^{1/2}\, cm^{-2}\, sr^{-1}\, s^{-1}. \tag{1.22}$$

Eqn. 1.22 is valid for $M_m \lesssim 10^{17}$ GeV and along with Eqn. 1.21 constitutes the TPB flux limit. It is a limit based on well-understood theory and is derived by making minimal assumptions. The design goal of the MACRO detector was to better this limit.

A more stringent limit is obtained when considering the survival of intergalactic fields, but until we have better knowledge of the structure and strength of these fields, these are subject to doubt. The survival of magnetic fields of stars also pose limits to the monopole flux. Harvey et al., assuming the existence of a superconducting core in neutron stars, derive an extremely stringent limit of $F \lesssim 5 \times 10^{-22}$ cm$^{-2}$sr$^{-1}$s$^{-1}$ [34] considering a $10^9$ yr old pulsar. The obtained flux limit is several orders of magnitude below the TPB limit, but uncertainties are involved in its derivation. The limit depends strongly on the age of the pulsar, which is uncertain. In addition, this model assumes a charged pion condensate in the core of the neutron star. The existence of such condensate depends upon the stellar mass and the stellar equation-of-state of matter with supranuclear densities, both of which are highly controversial as the authors themselves admit [34]. In addition, other scenarios may invalidate the above model. In fact, monopoles and antimonopoles inside the superconducting core may become connected with flux tubes and annihilate quickly, that is monopoles may not be captured as effectively as is assumed in the scenario [35].

While this search was in progress, the issue of the survival of the galactic field was revisited. In 1993, Adams et al. [36] obtained an "extended Parker Bound" by requiring survival and growth of a small galactic seed field after collapse of the protogalaxy. Assuming, in this case, a field coherence length of 1 kpc ($3 \times 10^{21}$ cm), a turbulent dissipation of the field and a seed field of $10^{-20}$G $< B_0 < 10^{-11}$ G, they

obtain

$$F \lesssim 1.2 \times 10^{-16} M_{17}\, cm^{-2}\, sr^{-1}\, s^{-1} \tag{1.23}$$

for $M \gtrsim 3 \times 10^{11}(B_0/10^{-11}G)$ GeV and

$$F \lesssim 3 \times 10^{-22}(B_0/10^{-11}G)\, cm^{-2}\, sr^{-1}\, s^{-1} \tag{1.24}$$

for $M \lesssim 3 \times 10^{11}(B_0/10^{-11}G)$ GeV. Recently (2001), the "protogalactic extension" of the Parker Bound (already advertised in the previous paper) has lowered further the allowed monopole flux limit. This limit is derived by assuming the survival and growth of a small seed field during the collapse of the protogalaxy. During that epoch, a probable absence of a regenerating dynamo perhaps rendered the field more vulnerable to magnetic monopoles [37]. The corresponding limit takes on the values:

$$F \lesssim 5 \times 10^{-21}(M_{17})\, cm^{-2}\, sr^{-1}\, s^{-1} \tag{1.25}$$

for $M \gtrsim 2 \times 10^{15}$ GeV and

$$F \lesssim 9 \times 10^{-23}(B_0/10^{-9}G)\, cm^{-2}\, sr^{-1}\, s^{-1} \tag{1.26}$$

for $M \lesssim 2 \times 10^{15}$ GeV.

The above limits are illustrated in Fig. 1.5 as "galactic seed" and the "protogalactic extension of TPB" respectively. For the galactic seed limit, we use $B_0 \simeq 10^{-9}$ G in order to make a direct comparison with the protogalactic extension of the Parker Bound, even though in the original paper $B_0$ was adopted to be $10^{-12}$ G. There are various uncertainties existing in the derivation of the above two limits, especially in the protogalactic extension of the Parker Bound; these are in the estimates of coherence scales for the protogalactic era, the strength of the seed field, etc. Most importantly, the basic assumption on which the protogalactic limit is based (the absence of any amplifying mechanism other than flux freezing during the collapse of the protogalaxy) has been questioned. Also, recent work [38] on other forms of field am-

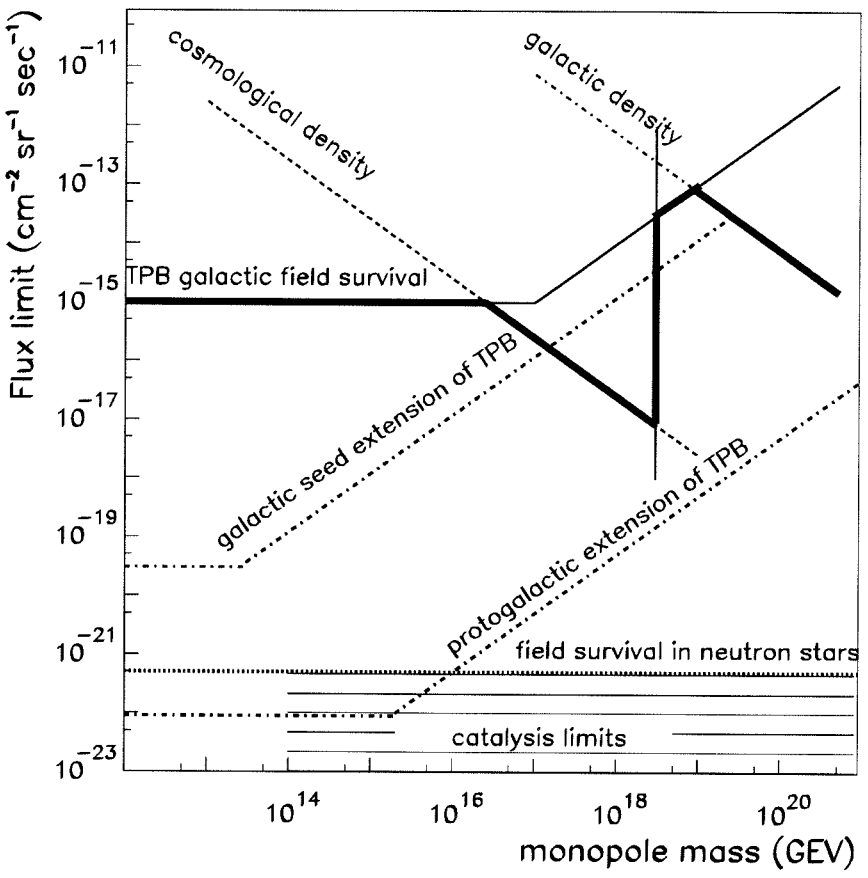


Figure 1.5: Monopole flux upper limits on astrophysical grounds. The monopole velocity is assumed to be $10^{-3}c$. The monopole mass above which it is bound to the galaxy is $3 \times 10^{18}$ GeV. The heavy line illustrates the combined galactic field survival and cosmological-galactic density limits. The limits, based upon catalysis and field survival in neutron stars, are stringent limits, but are plagued by many uncertainties.

plification mechanisms (such as homogeneous Kolmogorov turbulence) may render the above limits many orders of magnitude larger, and not as impressive anymore.

### 1.4.2 Limits Based on Mass Density

Monopoles are heavy particles and thus a high number density would lead to an excessive averaged mass-energy density in the universe, as mentioned in section 1.2. If $\rho_{TOT}$ is the average mass-energy density in the universe, then we recall from sec-

tion 1.2 that $\Omega_{TOT}$ is defined as

$$\Omega_{TOT} = \frac{\rho_{TOT}}{\rho_c}, \tag{1.27}$$

where $\rho_c$ is the critical density:

$$\rho_c \simeq 1.9 \times 10^{-29}\, h^2\, g\, cm^{-3}. \tag{1.28}$$

The factor $h$ is defined as $h = H_0/100$ with the Hubble constant $H_0$ expressed in units of km $s^{-1}$ $Mpc^{-1}$. We also recall that the currently favored value for $\Omega_{TOT}$ is close to 1 and $0.4 < h < 1$ as explained in section 1.2. Then, an upper limit of the monopole flux can be obtained if we dictate that the mass-energy density due to magnetic monopoles $\rho_m$ is less than the mass-energy density in the universe $\rho_{TOT}$. If the monopole number density is $N_m$, then $\rho_m = N_m\, M_m$ and, if $v$ is the monopole velocity, the monopole isotropic flux is $F = N_m v/4\pi$. Hence, requiring that $\rho_m < \Omega_{TOT}\, \rho_c$ results in

$$F < 2.5 \times 10^{-16}\, M_{17}^{-1}\, (\frac{v}{10^{-3}c})\, cm^{-2}\, sr^{-1}\, s^{-1}. \tag{1.29}$$

The limit gets less severe if we consider monopoles bound to the galaxy. Observational data imply a local density in the galaxy about $3 \times 10^4$ times the cosmological density and thus, the flux upper limit scales accordingly, and

$$F < 7.5 \times 10^{-12}\, M_{17}^{-1}\, (\frac{v}{10^{-3}c})\ cm^{-2}\, sr^{-1}\, s^{-1}. \tag{1.30}$$

In order to have long-term clustering of magnetic monopoles with the galaxy, we should have $M_m \gtrsim 3 \times 10^{18}$ GeV [33]. Therefore, the flux limit of Eqn. 1.30 is valid for $M_m \gtrsim 3 \times 10^{18}$ GeV. If we combine the TPB and mass density flux limits in their corresponding regimes of validity in terms of mass, we get the heavy line in

Fig. 1.5. The less stringent flux limit is $F \lesssim 10^{-13}$ cm$^{-2}$sr$^{-1}$s$^{-1}$ for monopoles of $M_m \sim 10^{19}$ GeV.

### 1.4.3 Catalysis in Neutron Stars

One of the most controversial topics in monopole physics is the rate at which they catalyze nucleon decay. Since GUT is restored in the monopole core, geometrical considerations would imply a tiny cross section ($10^{-56}$ cm$^2$) for non-conservation of baryon number. Yet Rubakov [39] and Callan [40] have argued that the cross section $\sigma$ of nucleon catalysis in the presence of a monopole is comparable to that due to strong interactions. If we denote $\sigma = (c/v)\,\sigma_0\,10^{-28}$ cm$^2$ (where $\sigma_0$ is a dimensionless factor), then they argue that $\sigma_0$ is of $O(1)$ or higher. There has been considerable debate on the factor $\sigma_0$ and many authors argue that its value is too small for the effect to be interesting. Bais et al. argue that $\sigma_0$ takes on values in the range $10^{-5} < \sigma_0 < 10^{-3}$ [41]. Walsh et al. argue that when the conditions assumed for the Rubakov-Callan effect (which are: massless fermions and SU(2) monopoles instead of GUT monopoles) are not met, the process stops in at least the SU(5) case [42]. Even if the Rubakov-Callan process does not work, Schellekens [43] and Sen [44] argue that monopole catalysis of proton decay still proceeds, but with cross sections presumably many orders of magnitude smaller.

If the Rubakov-Callan effect indeed applies, it would impart excessive luminosity to many types of astrophysical objects. The accumulation of magnetic monopoles inside a star depends on the monopole flux and on the duration for which the star has been exposed to monopoles, i.e., its age. Neutron stars can easily accumulate heavy monopoles which, by inducing nucleon catalysis, would contribute significantly to the star's luminosity. Flux limits of the order of $F \lesssim 10^{-21}$ cm$^{-2}$ sr$^{-1}$s$^{-1}$ [45] have been derived using old pulsars. Somewhat less stringent limits may be obtained using white dwarfs [46] and other astrophysical objects. The total photon luminosity of old neutron stars in the galaxy has also been used in the derivation of similar limits [35]. The above mentioned limit derived from pulsars is one of the most stringent ones,

and can become more stringent by around six orders of magnitude if effects on the progenitor star are considered. We have to keep in mind, though, that there are many uncertainties involved in the derivation of such limits. There are assumptions made that depend strongly on the equations-of-state of the neutron stars that affect the total luminosity of the neutron stars. There are additional uncertainties introduced when estimating the number density of the old neutron stars in a galaxy. Moreover, monopole capture may not be as efficient in a neutron star as is assumed in the above models, or the abundance within the star may be reduced due to monopole-antimonopole annihilation, as also mentioned in section 1.4.1. In general, there are many suggested mechanisms that can drastically alter the aforementioned models and thus invalidate the associated flux limits. However, the most important drawback is that the above limits depend directly on the catalysis cross section $\sigma$, which varies by many orders of magnitude in different theoretical models.

Thus, in conclusion, we understand that our lack of precise knowledge of the behavior of monopoles should lead us to focus only on astrophysical limits that are derived from few assumptions. As we have seen above, many upper limits suffer from important uncertainties. The most robust and straightforward one is the TPB limit, combined with limits from mass density considerations. Improving upon this upper limit has been the goal of this search.

## 1.5 Magnetic Monopole Searches

After this brief glance at the theory of magnetic monopoles, it should be evident to the reader that there are very few attributes of GUT magnetic monopoles that are not in dispute; other than that they should carry magnetic charge and that they are very rare. The first attribute has led to induction experiments. The second attribute, verified also by the induction experiments, has led to the use of large scale detection techniques based on ionization or nucleon catalysis.

### 1.5.1 Induction Searches

The most straightforward approach to a search for monopoles is to use their property of magnetic charge. Induction techniques make use of the long range electromagnetic interaction between the monopole and the macroscopic quantum state in a superconducting ring. Integrating Maxwell's equation $\vec{\nabla} \times \vec{E} = -\frac{1}{c}\frac{\partial \vec{B}}{\partial t} - \frac{4\pi}{c}\vec{J_m}$ on the surface $S$ of a superconducting ring, we get

$$\int_S \vec{\nabla} \times \vec{E} \cdot d\vec{S} = -\frac{1}{c}\int_S \frac{\partial \vec{B}}{\partial t} \cdot d\vec{S} - \frac{4\pi}{c}\int_S \vec{J_m} \cdot d\vec{S}, \tag{1.31}$$

which simplifies to

$$\oint \vec{E} \cdot d\vec{l} = -\frac{\partial \phi}{\partial t} - 4\pi g \delta(t), \tag{1.32}$$

where $d\vec{l}$ is integrated along the ring and $\phi$ is the magnetic flux through the ring. Since $\vec{E}$ vanishes along the circumference, we have

$$\phi(t) = \phi_{sup} + \phi_{mon} = -4\pi\, g\, \theta(t). \tag{1.33}$$

When a monopole with Dirac magnetic charge $g$ passes through the ring there is a change in flux of $4\pi g = \frac{hc}{e}$, which is double the flux quantum, $\phi_0 = \frac{hc}{2e}$, in a superconductor. The induced supercurrent is $-IL = 2\phi_0$, where $L$ is the ring inductance, and its detection is possible with the use of SQUIDs (Superconducting Quantum Interference Devices). However, the induction method has a very serious

limitation: the expected change in flux is very small compared to possible accidental ambient flux changes, and very careful shielding is required. Superconducting shields and other methods such as the use of macrames have been employed in order to guarantee low noise operation for induction experiments. In 1982 a single candidate event was detected by Blas Cabrera [48] using a four-turn, 5-cm diameter superconducting loop after 151 days of operating time. This is the only monopole candidate ever reported. Since present limits on the monopole flux are of the order of $2 - 3 \times 10^{-16}$ $cm^{-2}sr^{-1}s^{-1}$, it is improbable that the candidate event was actually a monopole event. The announcement of the monopole candidate, however, generated a wind of enthusiasm which resulted in the relative ease of realization of more ambitious projects for monopole detection.

The fact that the induction method is independent of monopole mass or velocity makes it an attractive technique, yet the need for appropriate shielding makes it unsuitable for largescale searches. As a consequence, when it became clear that the monopole flux must indeed be very small and large scale experiments were necessary, induction techniques fell out of favor. The present combined induction limit is $3.8 \times 10^{-13}$ $cm^{-2}sr^{-1}s^{-1}$ [49],[50] and has been surpassed by other techniques by several orders of magnitude.

### 1.5.2 Ionization Searches

Ionization detectors have been used for a long time in high energy physics. They are relatively easy and inexpensive to construct and operate, and can be used in large area detectors without insurmountable technical problems. The MACRO detector, on which this search has been performed, is a system of ionization detectors and has dominated the search for heavy magnetic monopoles over the past decade. The design of such a project relies on reasonable confidence in the capacity of ionization detectors to detect monopoles.

Since monopoles remain undetected to date, we are forced to extrapolate available experimental information and theoretical models for ionization signatures due to

electrically charged particles, to ionization signatures of magnetic monopoles.

The detection of the electrically charged particles depends on their E-field interactions with the atomic electrons of the parent medium that they are traversing. Transfer of energy to the medium takes place via atomic ionization or bound excitation. This may subsequently be observed as charged ions, scintillation light, Cherenkov radiation, etc. Moving magnetic monopoles, on the other hand, will interact with atomic electrons via the Lorenz force $\vec{F} \equiv e(\vec{E} + \frac{\vec{v}}{c} \times \vec{B})$, where $\vec{v} = \vec{\beta}\, c$ is the monopole velocity. The bound electrons in the medium are subject to a force due to an equivalent electric charge of $g\frac{v}{c}$, $g$ being the monopole strength. We use this effect, and the observed signature of charged particle traversal, to deduce the behaviour of monopole passage through matter.

For fast moving particles the ionization losses are well described by the Bethe-Bloch formula. The energy loss goes approximately as $dE/dx \propto (Ze)^2/\beta^2$. This, when extrapolated to magnetic monopoles, implies $dE/dx \propto g^2$. Therefore, the energy loss is approximately constant and $\sim 4.7 \times 10^3$ times that of a particle of elementary electrical charge $e$. This general formula is valid for velocities larger than atomic electron velocities. Ahlen [51] has introduced corrections to the Bethe-Bloch formula giving a more accurate theoretical description of the energy losses of monopoles with $\beta > 0.1$ (see Fig. 1.6).

For slower particles, $\beta < 0.1$, the Bethe-Bloch formula becomes inaccurate and other models are required. Lindhard [52] [53] has constructed a model for $\beta < 0.01$ by approximating the electronic structure of atoms in the medium by a Fermi distribution. Ahlen and Kinoshita [54] applied the above model to magnetic monopoles to obtain a linear dependence of energy loss on the monopole velocity. Their result is shown in Fig. 1.6 as the low velocity curve for $\beta < 0.01$ and for $g = 137e/2$. The extension of their formula to $\beta < 10^{-3}$ is seen in the same figure, but the subject needs more attention: kinematics limit the maximum energy that can be transfered to an electron. This energy should be larger than the ionization energy of the medium in order for electronic energy loss to occur.

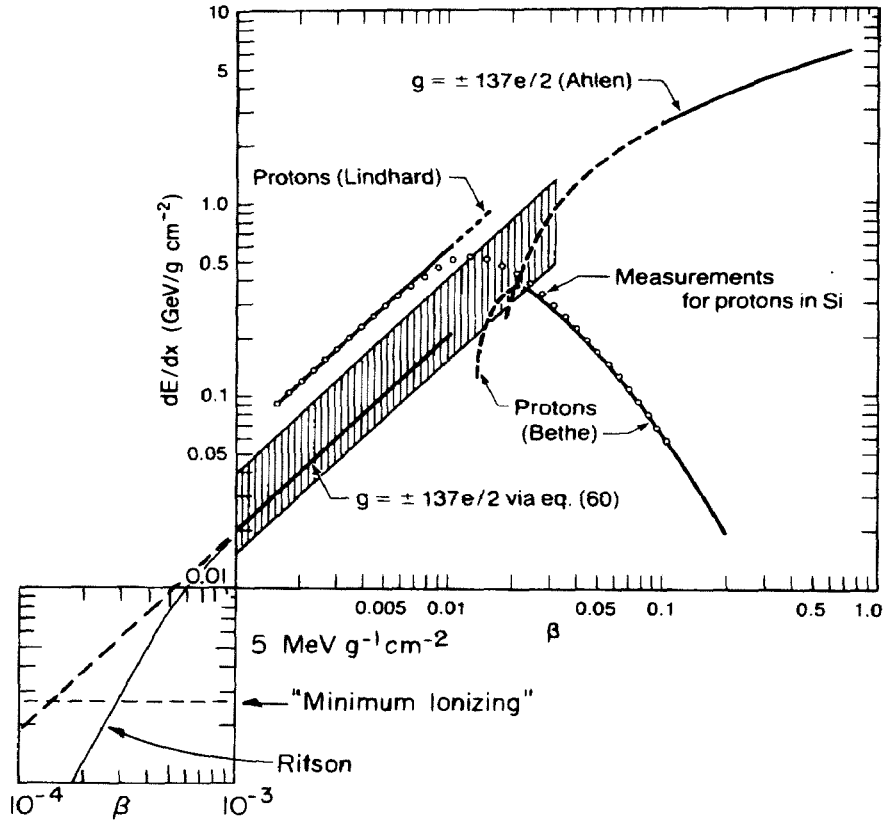


Figure 1.6: Theoretical predictions for the energy loss of monopoles as calculated by Ahlen and Kinoshita [54]. The figure is reprinted from ref. [47]. Solid lines are theoretical calculations and described in the text. Dashed lines are extrapolations. The open circles are averaged values from high quality measurements of proton stopping power in silicon.

### Scintillation Detectors

Ahlen and Tarlé used the above models to derive the response of plastic scintillator NE110 to magnetic monopoles [55]. They concluded that the scintillator cut-off is at $\beta \sim 6 \times 10^{-4}$. Experimental data, however, has indicated that this result is probably too conservative.

Ficenec et al. [56] have observed scintillation light in a NE110 scintillator from recoil protons with $\beta$ as low as $2.5 \times 10^{-4}$. They have found that their experimental results are better described by Lindhard's formula multiplied by an adiabatic correction factor $F_{ac}$. To get the scintillation yield for a bare monopole, they use the primary yield from electronic stopping, as calculated by Ahlen and Kinoshita, and

modified by the factor $F_{ac}$. The resulting monopole light yield curve is shown in Fig. 1.7.

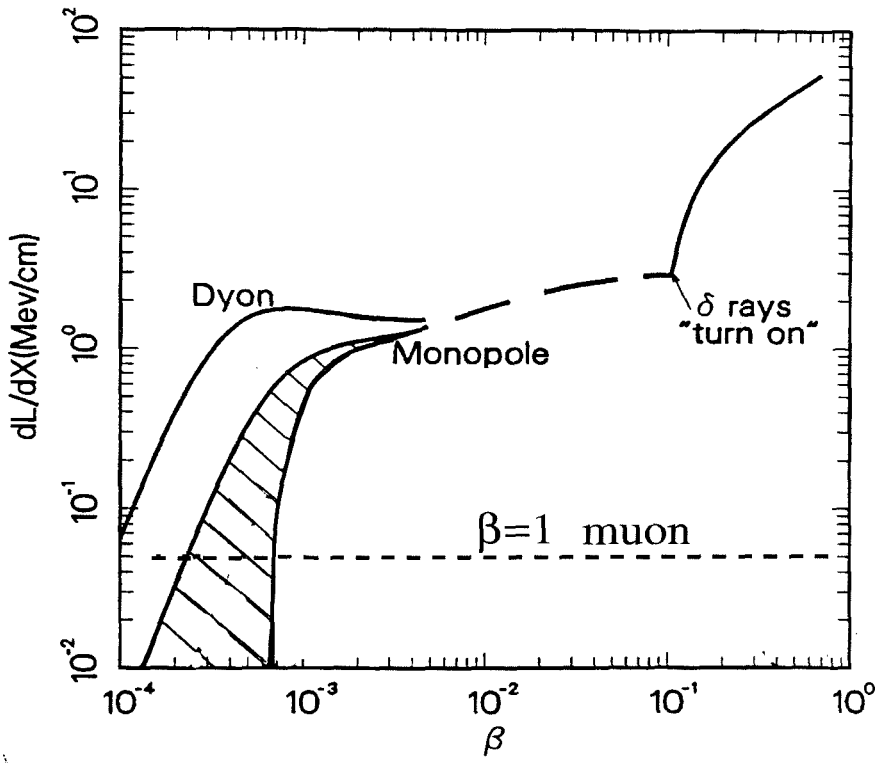


Figure 1.7: Scintillation light yield of monopoles and dyons in plastic NE110. The lower bound of the shaded region is the overconservative curve by Ahlen-Tarlé. The upper bound is the extrapolation to monopoles of the Ficenec slow proton data. The figure is reprinted from reference [56].

In the low velocity region, no clear cut-off for the detection of protons was identified and thus, no statements can be made about the corresponding behavior of monopoles. Dyons, or in general monopole composites, have greater light yields since they also lose energy due to their electric charge. For high energy depositions the scintillator exhibits saturation. For $\beta > 0.1$, delta rays are produced that result in an abrupt increase of the scintillation yield. This result on the light yield of magnetic monopoles will be used extensively later on, as a guideline for the MACRO scintillators. Calculations for the MACRO liquid scintillator [57] gave similar results to NE110. For a description of the MACRO liquid scintillator see section 2.3.

Fig. 1.8 is taken from reference [57] and shows the light yield for bare magnetic monopoles of various magnetic charges in the MACRO scintillator. Fig. 1.9 illustrates the light yield of dyons (or of the M+p composite) and of the M+Al composite in the MACRO liquid scintillator as a function of $\beta$.

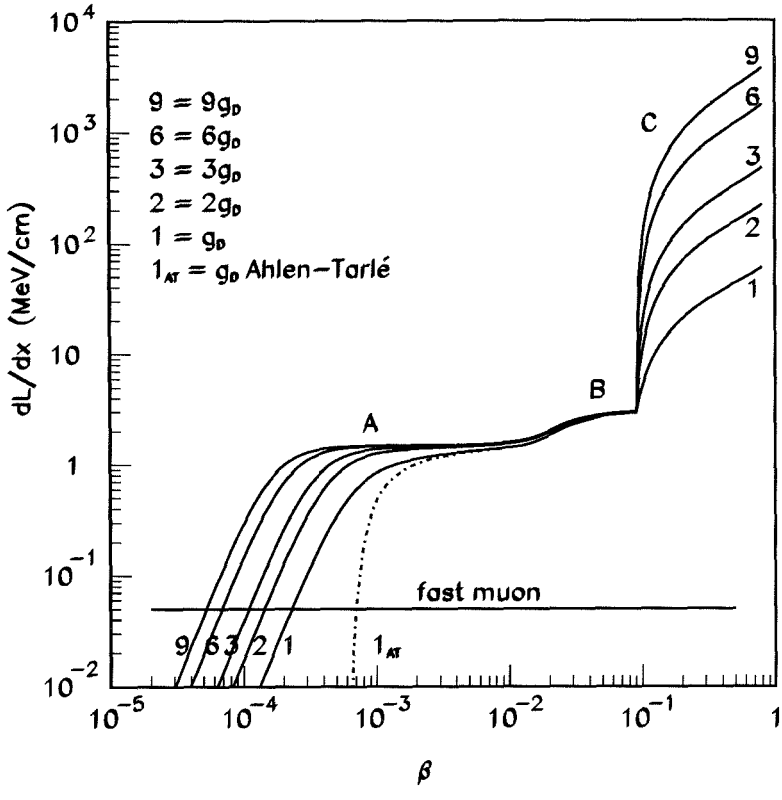


Figure 1.8: Scintillation light yield of monopoles of various magnetic charges in the MACRO liquid scintillator. $g_D$ is the Dirac magnetic charge. The figure is reprinted from reference [57].

Most scintillation experiments, before this search, had sensitivity for bare monopoles of $\beta > 10^{-3}$. The best scintillator limit of $F \lesssim 6.8 \times 10^{-16}$ cm$^{-2}$sr$^{-1}$s$^{-1}$ for $\beta > 10^{-3}$ was held by the 1850 m$^2$ sr$^{-1}$ Baksan detector [58]. This limit has already been surpassed by scintillator searches on MACRO, as illustrated in Figs. 1.11 and 1.12.

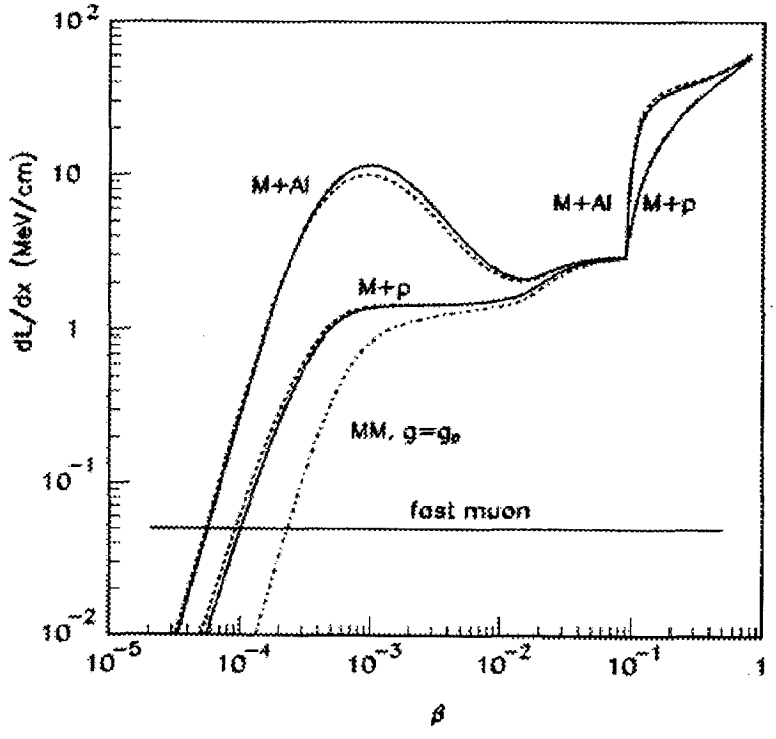


Figure 1.9: Scintillation light yield of dyons. The M+p line is for dyons with Dirac magnetic charge and +e electric charge (or equivalently M+p composite). The M+Al line is for dyons with Dirac magnetic charge and +13e electric charge (or equivalently a monopole+Al composite). The dashed lines are for plastic scintillator NE110 medium, and the solid lines are for the MACRO liquid scintillator. The figure is reprinted from reference [57].

### Gaseous Detectors

In gaseous tube detectors, the typical excitation potentials (slightly higher in noble gases than in scintillators) impose a higher theoretical velocity cut-off according to kinematic limits. But exploitation of the Drell effect, in combination with the Penning effect, makes the use of gaseous tubes suitable for monopole detection down to $\beta \sim 10^{-4}$. The Drell effect, first suggested in 1982 [59], considers the interaction of the electron spin with the monopolar magnetic field. This interaction occurs in the adiabatic approximation due to the very low velocity of the monopole. As the monopole approaches an atom, say located at a coordinate origin, the energy

levels undergo Zeeman splitting. As the monopole passes the origin, energy levels corresponding to different principal quantum numbers can cross. Atomic electrons may then occupy energy levels corresponding to different principal quantum numbers and may be left in an excited state by the time interaction with the monopole is over. The excited atom will subsequently transfer its energy to other species, for instance a quenching gas, with an ionization potential lower than the excitation energy of the atom (Penning effect), thus ionizing the second species. The ionization is then detected as usual. Wire chambers often use Helium and argon. The total cross section for the excitation of Helium [60] and the corresponding energy loss of a slow monopole are given by

$$\sigma = (3.96 \pm 0.03) \times 10^{-18} (\beta/10^{-4})(1 - \frac{\beta_c^2}{\beta^2})^{3/2}\, cm^2, \tag{1.34}$$

$$\frac{dE}{dx} = 11(\beta/10^{-4})(1 - \frac{\beta_c^2}{\beta^2})^{3/2}\, MeV\, cm^2\, g^{-1}, \tag{1.35}$$

where $\beta_c = 9.242 \times 10^{-5}$ is the critical velocity, a factor that corrects for nuclear recoil effects and limits the Drell effect.

Before MACRO, most experiments did not make use of the Drell effect, either because they were not using a suitable gas mixture that would allow for the Penning effect to take place, or because their triggering system was not sensitive to lower monopole velocities. Fig. 1.12 shows the two best limits before MACRO. They are by i) the Soudan-2 collaboration [62] which reports an upper flux limit of $8.7 \times 10^{-15}$ cm$^{-2}$sr$^{-1}$s$^{-1}$ for $\beta > 2 \times 10^{-3}$ and ii) the Kolar Gold Field experiment [63], which using the ionization method has reached $3 \times 10^{-15}$ cm$^{-2}$sr$^{-1}$s$^{-1}$ for $\beta \gtrsim 10^{-3}$. The MACRO streamer tube detector, on the other hand, makes use of the Drell effect. The expected energy loss of magnetic monopoles of various magnetic charges in the MACRO streamer tube gas is shown in Fig. 1.10, as calculated in [57]. A description of the MACRO streamer tube detector is given in section 2.4.

Searches for magnetic monopoles with the MACRO streamer tube system have set flux limits surpassing previous ones set by other experiments.

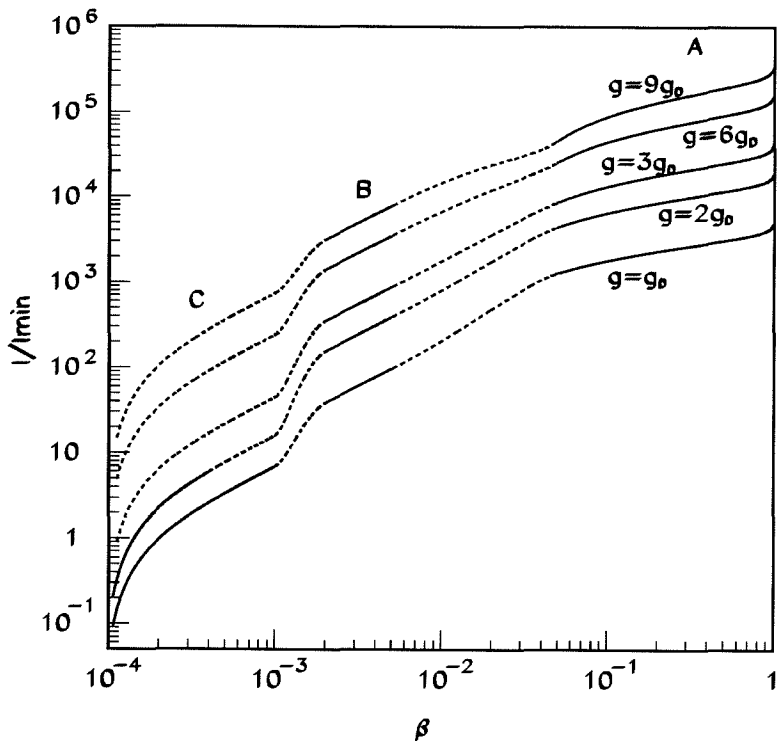


Figure 1.10: Energy losses of monopoles of various magnetic charges in the MACRO streamer tube gas normalized to the energy loss of minimum ionizing particle (MIP). Dashed lines are interpolations between the regions where calculations are more reliable. The figure is reprinted from reference [57].

This is shown in Fig. 1.11 and in Fig. 1.12.

### Nuclear Track Detectors

Nuclear track detectors are solid-state detectors that exploit the fact that when electrically charged particles go through matter, they leave behind a trail of local radiation damage. In certain materials the damaged regions are more susceptible to chemical etching and, when treated, the damaged area becomes visible. Track-etch detectors may be plastic polymers such as CR39 and LEXAN or crystalline materials such as mica. Either electronic energy losses (in CR39 & LEXAN) or damage due to nuclear recoil (in mica) may be responsible for the damage. In particular, CR39

is sensitive to $\beta \gtrsim 2 \times 10^{-2}$ due to electronic losses, and to $\beta$ around $10^{-4}$ due to diamagnetic repulsion of atoms. Orito et al. [64] report the limit seen in Fig. 1.12 in Ohya. The CR39 detector in MACRO has surpassed this limit [65] as seen in Fig. 1.11 and Fig. 1.12.

The strongest experimental limit ever set on monopoles is derived with mica by Price [66],[67]. Mica is not sensitive itself to bare magnetic monopoles, but only to magnetic monopoles of $\beta \sim 10^{-3}$ that carry a nucleus with Z> 10. This can happen when magnetic monopoles traverse rock, where they may capture $^{27}Al$. Price has used very old mica to obtain his flux limit. Since monopoles that have captured protons do not capture $^{27}Al$ nuclei, his limit depends on the percentage of monopoles initially bound to protons. His lowest limit is of the order of $\sim 10^{-18}$ $cm^{-2}sr^{-1}s^{-1}$ for $\beta \sim 10^{-3}$ assuming that 90% of monopoles arriving are not bound to protons. The limit should be considered with caution, however, since it depends strongly on the estimated cross section for the radiative capture of a nucleus by a monopole. Various approximations were used to derive the above cross section which could prove inaccurate. Moreover, there are many conceivable scenarios where monopoles may emerge from the early universe either as dyons or bound to protons [13]. In that case the limit does not hold. Another caveat of the above limit is that it is not valid if monopoles catalyze proton decay with a high cross section. To all of the above, we should also add uncertainties about the mica's age and history (if the mica is reheated, the damaged area anneals and is not distinguishable anymore.) As in most indirect monopole searches, there is a large amount of uncertainty involved, which weakens the strength of the derived conclusions and points us towards direct searches for more definite answers on monopolar abundances.

### 1.5.3 Catalysis Detectors

A different technique for the search of magnetic monopoles is through the detection of proton decay catalysis. Large proton decay detectors can provide limits on the flux of monopoles based on the absence of catalysis events. If a monopole catalyzes

proton decay with large enough cross sections, then it is expected to leave a trail of proton decay events along its passage through a proton decay detector.

There are many problems involved with this technique. First of all, it is technically challenging to create a trigger that will not reject monopole induced events; the simultaneous presence of fast (decay products) and slow (magnetic monopole) particles in the detector might confuse the triggering systems and complicate the data analysis procedures. In addition, there are problems related to clear interpretation of the data due to the strong dependence of the analysis on the catalysis cross section. The most important monopole flux limits, based on proton decay experiments, are by the Baikal and the IMB experiments. The Baikal experiment [68] has set a flux limit of $\sim 10^{-16}$ cm$^{-2}$sr$^{-1}$s$^{-1}$ for $10^{-5} < \beta < 10^{-4}$ based on the assumption of a very large catalysis cross section ($\sigma > 10^{-22}$ cm$^2$). The IMB experiment [69] gives a limiting flux of $F \lesssim 10^{-15}$ cm$^{-2}$sr$^{-1}$s$^{-1}$ for $\sigma \sim 10^{-25}$ cm$^{-2}$. Comparing the various limits is not a trivial matter due to differing assumptions about the catalysis cross section. The detection of monopoles through induced proton decay is reliable only in the case of a positive outcome. In the case of negative outcome, we cannot make a strong statement on the maximum flux of magnetic monopoles because the detection is so strongly dependent on the catalysis cross section. As elaborated in section 1.4.3, the catalysis cross section is uncertain to many orders of magnitude and we cannot rely on catalysis limits with a great degree of confidence.

### 1.5.4 Monopole Search from Cherenkov Detectors

Relativistic monopoles should produce high intensity Cherenkov radiation. Exploiting this property, recent searches have been performed by the Baikal [70] and AMANDA [71] collaborations. The AMANDA collaboration has produced the best existing limit thus far: $F \lesssim 1.55 \times 10^{-16}$ cm$^{-2}$sr$^{-1}$s$^{-1}$ for $\beta \simeq 1$. Their limit is plotted in Fig. 1.12. As mentioned earlier, the search is valid only for relativistic monopoles. We do not currently know of any mechanism that could accelerate heavy monopoles, $M_m \sim 10^{17}$ GeV, to relativistic speeds. Thus, Cherenkov radiation searches are more

relevant to populations of lighter monopoles.

### 1.5.5 The MACRO Detector

Since MACRO is the detector on which this search was performed, it will be described extensively in the next chapter. The detector was built with the express purpose of searching for magnetic monopoles. Its large collecting area meant that sensitivity to monopole fluxes of around $\sim 10^{-16}$ $cm^{-2}sr^{-1}s^{-1}$ could be reached in about five years of operation in its final configuration. Its uniqueness lies in the fact that it is not a simple monopole detector, but a system consisting of three different monopole detectors subsystems employing different detection techniques: scintillation counters, streamer tubes and track-etch detectors. Each detector-type is equipped with various triggers, with sometimes overlapping monopole velocity ranges so as to guarantee a high degree of redundancy. MACRO's design, as discussed in [72], is based on the philosophy that since there is lack of indisputable understanding of monopole physics, various possibilities should be considered when building a monopole detector. Monopoles may come as dyons or may strongly catalyze nucleon decay, thereby invalidating the mica limit. They may have velocities that track-etch detectors are not sensitive to, or they may be accompanied by large positive charges and the Drell effect may be greatly suppressed due to electron screening. MACRO's conception emphasized complementarity. On the other hand it also aimed on redundancy. As was well understood, monopole events, if any, should be very rare, and their indisputable identification was of crucial importance. By employing three separate techniques, MACRO offered the possibility of detection in more than one detector. After almost five years of running, MACRO has not seen any monopole candidate and has set limits on the monopole flux from its various detectors, as seen in Fig. 1.11, taken from among the 34 monopole-related articles published by MACRO collaboration to-date.

The best MACRO scintillator limit (scint. D in Fig. 1.11) is at $2.6 \times 10^{-16}$ $cm^{-2}sr^{-1}s^{-1}$ for $1.2 \times 10^{-3} < \beta < 10^{-1}$ obtained by the PHRASE trigger (see next

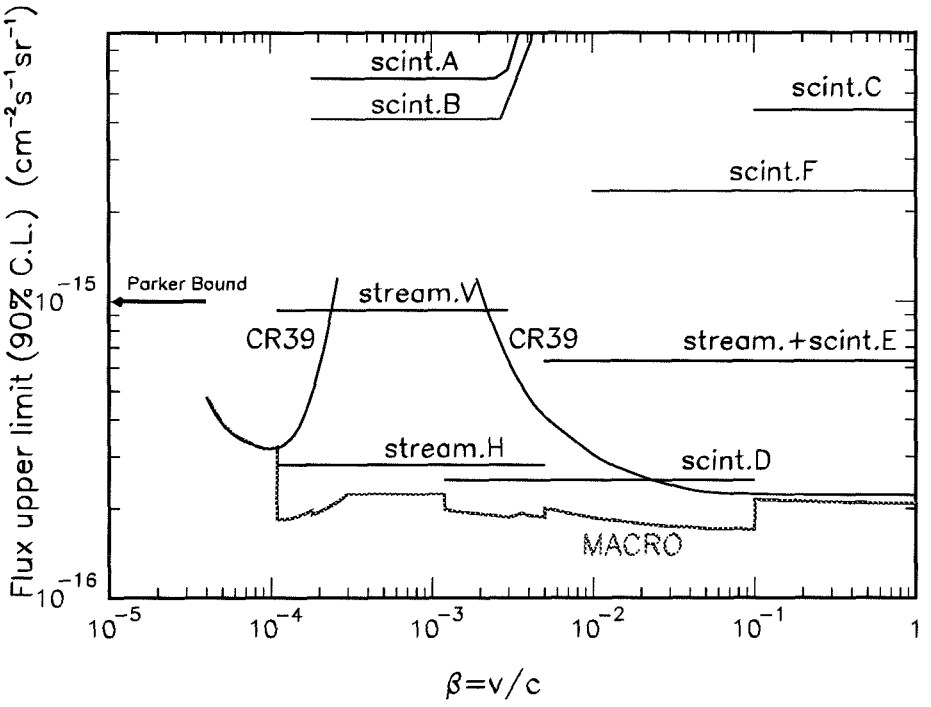


Figure 1.11: Magnetic monopole limits set by various searches performed on the three MACRO sub-detectors. The bottom line is the up-to-date (2001) combined MACRO limit. This search described in this manuscript is not included in this plot. The figure is reprinted from [65].

chapter and [65]). The same figure shows the streamer tube and the CR39 detector limits. Fig. 1.12 shows the current MACRO sensitivity with respect to other scintillator, CR39 and gaseous-tube experiments.

This search employed use of the scintillators to achieve a flux limit of $\simeq 2.5 \times 10^{-16}$ cm$^{-2}$sr$^{-1}$s$^{-1}$ for $10^{-4} \lesssim \beta \lesssim 4.1 \times 10^{-3}$. Moreover, it is based on a custom-made monopole trigger and utilizes high accuracy fast waveform digitizers in order to unambiguously sample the characteristics of slow magnetic monopole passage.

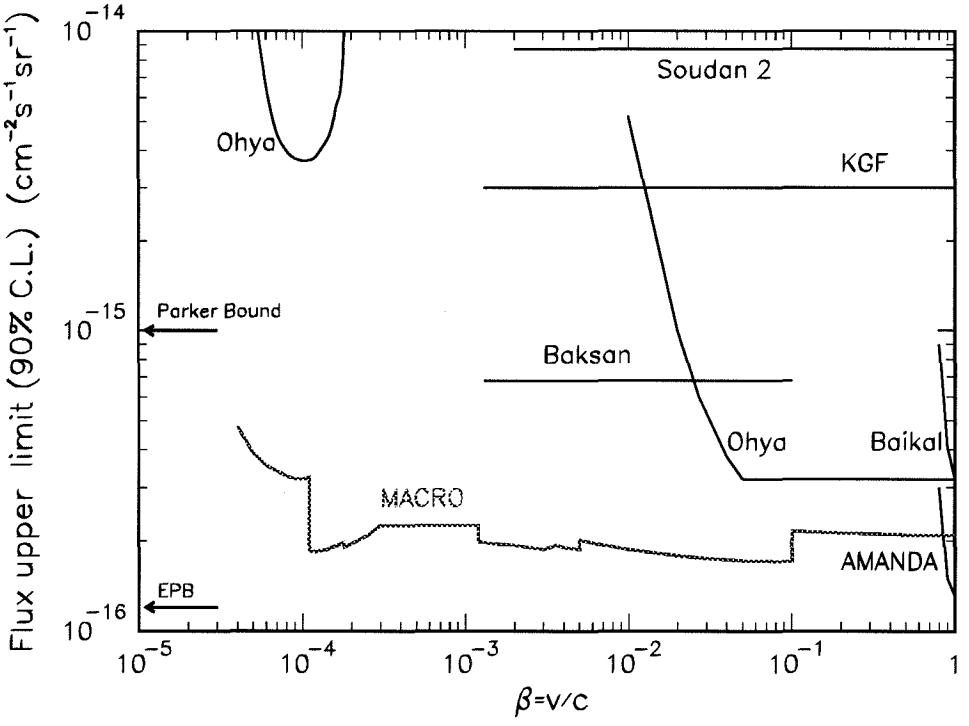


Figure 1.12: Magnetic monopole limits set by various experiments. The MACRO limit is the up-to-date 2001 limit set by combining searches performed on all three MACRO subdetectors. (This search is not included in this combined MACRO limit.) The figure is reprinted from [65].

# Chapter 2

# The MACRO Detector

The Monopole Astrophysics and Cosmic-Ray Observatory (MACRO), was – as its acronym implies – a large area detector, designed to carry out sensitive searches for rare particles. MACRO was built at the Gran Sasso Laboratory, where, shielded by a great rock burden in its natural habitat, it offered the ability to carry out searches for GUT monopoles in a low-background environment.

## 2.1 The Big Rock

In the heart of a sun-bathed country, the Gran Sasso (or Big Rock) Laboratory (LNGS) lies under the tallest peak of the Appenines, which provides shielding to the underground experiments it hosts. The opacity of the rock reduces the muon flux

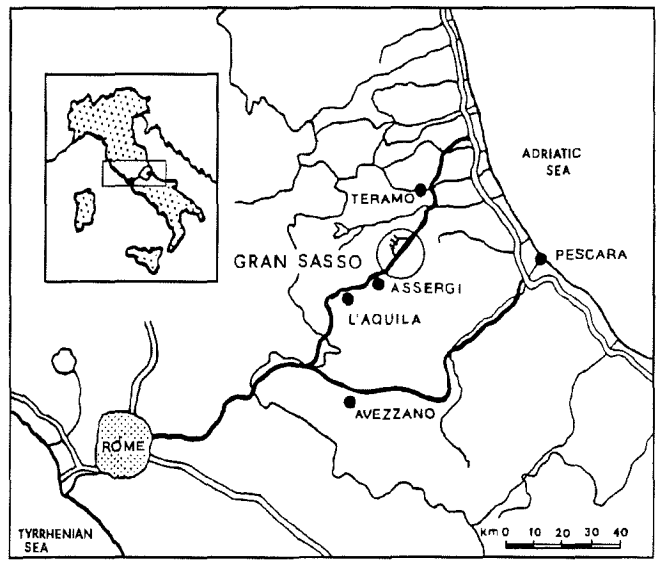


Figure 2.1: Map of Italy. The Abruzzo Area where the Gran Sasso Laboratories are located.

to less than $10^{-6}$ of its value at the earth's surface. The underground laboratory, consisting of three large halls, was constructed in the ten kilometer long A24 highway-tunnel that cuts through the Appenines (see Fig. 2.2). The eternal city is only 110 km away; yet, in a lab of cutting-edge technology and electronics we are looking further back in time for relics from the beginning of the universe. Some relevant parameters of the underground laboratory are given in Table 2.1.

| LOCATION | |
|---|---|
| Latitude | $42^o\ 27'\ 09''N$ |
| Longitude | $13^o\ 34'\ 28''E$ |
| Altitude | 963 m.a.s.l. |
| ROCK | |
| Composition | |
| in rel. weight | Ca(27%), O(51%), C(12%), Mg(8%), Si(1%) |
| Minimum thickness | 1160m |
| Average thickness | 1400m |
| Mean density $\rho$ | $2.71 \pm 0.05$ g cm$^{-3}$ |
| Mean atomic number (by weight) | $11.4 \pm 0.2$ |
| Mean atomic weight (by weight) | $22.9 \pm 0.4$ |
| MUONS | |
| flux | $\sim 1$ muon m$^{-2}$ h$^{-1}$ |
| minimum energy at surface | $\sim 1.4$ TeV |

Table 2.1: Some relevant parameters of the LNGS underground laboratories

The MACRO detector occupied 127m×17m×17m of space in Hall B of the laboratory. From the main highway tunnel, supplemental tunnels provide easy access by car to the experimental halls. The external laboratory is located on the surface on the western side of the mountain. Inside a pastoral Italian setting, modern computer facilities provide support to various underground physics experiments. Some of the

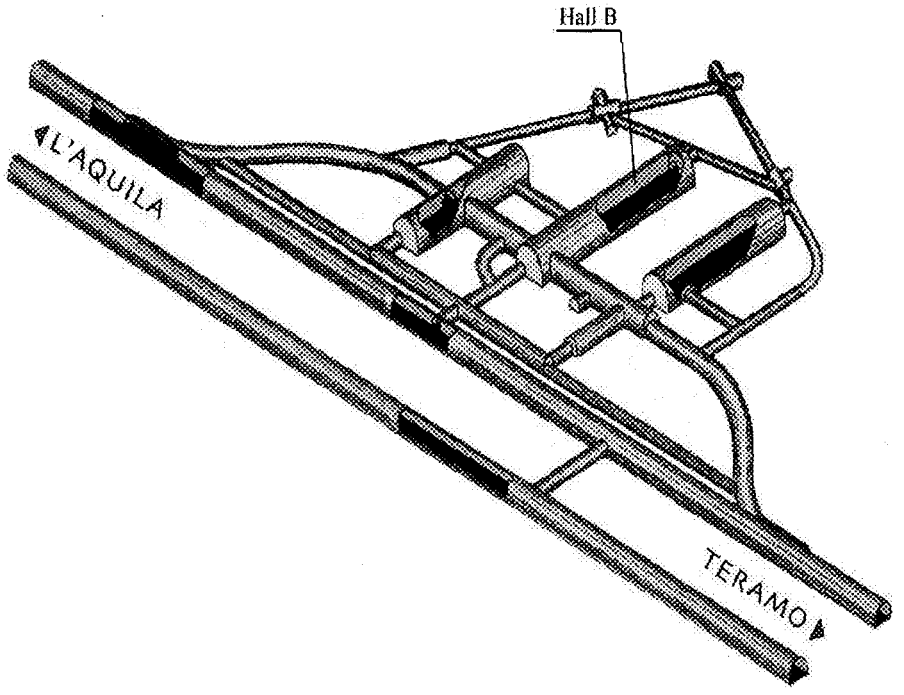


Figure 2.2: The Gran Sasso underground laboratories. MACRO is located in Hall B.

searches taking place in the experimental facilities of the Gran Sasso Laboratories include the following:

- the search for magnetic monopoles,
- the detection of neutrinos resulting from stellar collapse,
- the detection of solar neutrinos,
- the search for neutrino oscillations,
- the detection of high energy muons to study the composition and spectrum of very high energy primaries,
- the detection of lightly ionizing particles,
- the search for dark matter,
- the search for double $\beta$ decay, etc.

## 2.2 A General Description of the Detector

Since its inception, several doctorate theses have been written on experiments done at MACRO, a testament to the fact that current issues in physics could be explored with this detector. It was designed primarily to detect GUT monopoles. Since, from astrophysical limits, GUT monopole passages are expected to be rare, the detector was designed with large overall dimensions, 77m×12m×9.9m, and subtended an acceptance of $\simeq 10,000$ m$^2$ sr to an isotropic particle flux. This allowed MACRO to reach down to flux limits of the order of $10^{-16}$ cm$^{-2}$sr$^{-1}$s$^{-1}$ over a five year running period. A view of the detector as it was in its final configuration is shown in Fig. 2.3. The apparatus was built in six identical modules, the so-called "supermodules," for

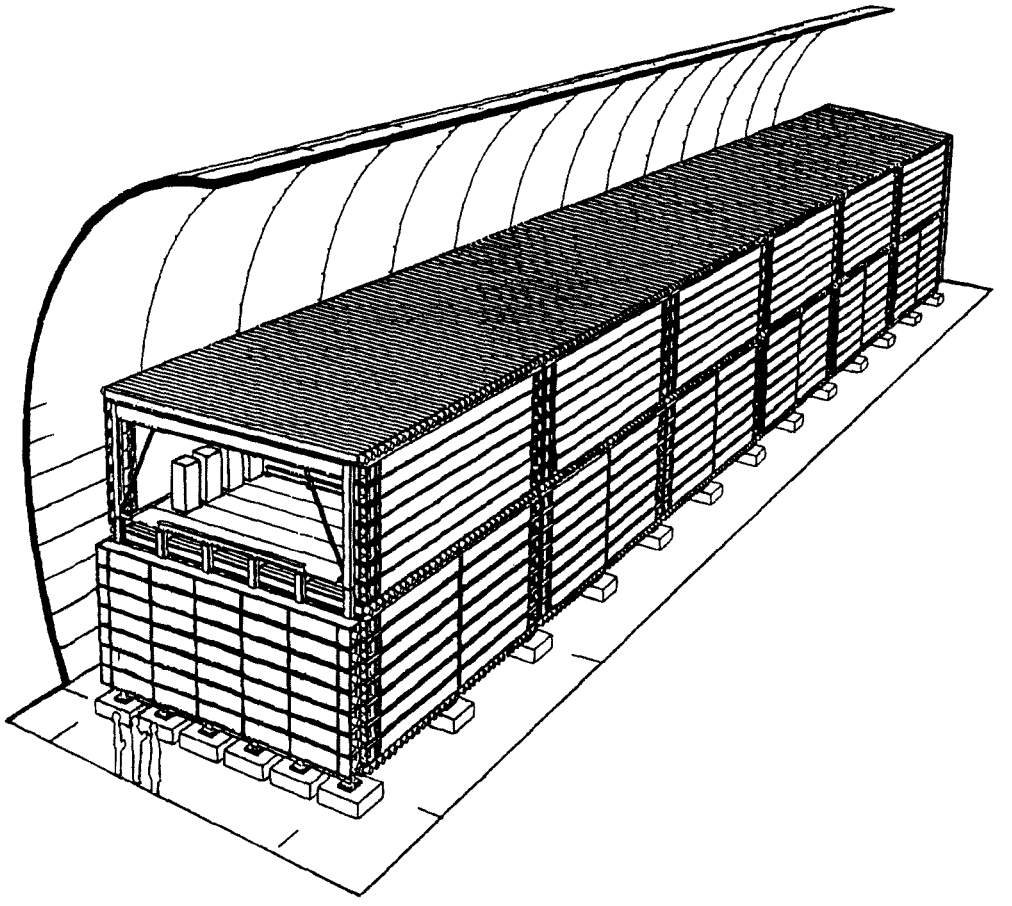

Figure 2.3: The MACRO detector. Graphical representation.

better detector management (monitoring, calibrations, data taking, maintenance, etc.). The cross section of a supermodule is shown in Fig. 2.4.

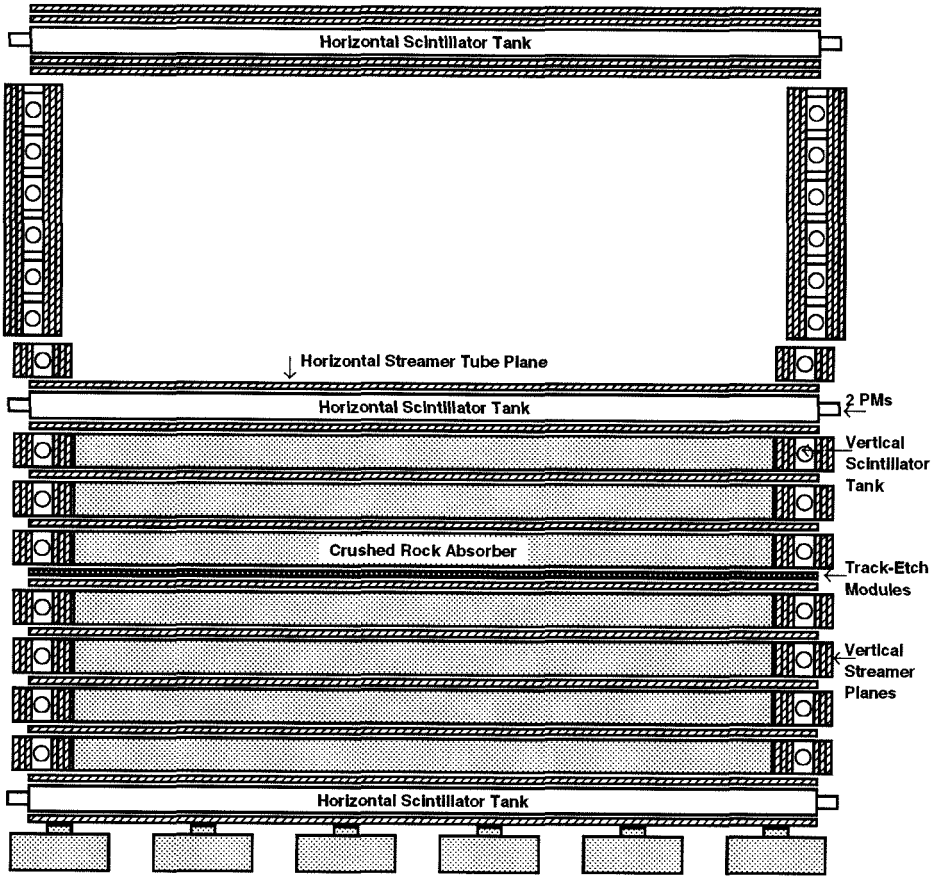


Figure 2.4: Cross section of a supermodule.

Given the expected rarity of monopole events, three independent detector systems were employed for increased redundancy; these are scintillator counters, limited streamer tubes and track-etch detectors. Each supermodule had three layers of 16 horizontal 12-m long scintillator counters, the *bottom*, the *center* and the *top* '*face*' (to be more accurate, there were 17 horizontal counters in the top layer as there were no structural gaps). On the sides of each supermodule there were two layers of 14 vertical 12-m long counters named *west* and *east* layers due to their location with respect to the detector. The *north* and the *south* walls of the first and sixth supermodule, respectively, were only partially covered with seven vertical scintillator

counters. This allowed access to the free space and the electronics, which were placed between the center and top layers of the detector.

The section between the center and bottom layers is referred to as the *lower* part of the detector, while the section above the center face is called the *attico*. The scintillation detector is used mainly for fast and slow timing, energy reconstruction and identification of slow monopoles (the latter due to the expected signature of a slow monopole when passing through a scintillator tank). The bottom and center face of scintillators had a horizontal layer of streamer tubes above and below each face while the top face had two layers of horizontal streamer tubes, also both above and below. There were six more layers of horizontal streamer tubes equidistant between the center and bottom faces, separated by crushed rock absorber as shown in Fig. 2.4. The absorber sets the minimum energy threshold of $\sim$ 1 GeV for a muon crossing the apparatus in a vertical fashion.

The vertical scintillator counters had three layers of vertical streamer tubes on either side. The limited streamer tubes offered slow timing information and provided the ability to track particles crossing the detector.

The track-etch detector was used primarily as a measure of redundancy in the monopole search. Each track-etch module consisted of three layers of LEXAN, three layers of CR39 and a layer of aluminum absorber between them. The layers of track-etch detector were located in the lower middle part and on the east and north faces of the detector.

## 2.3 The Scintillator System

The scintillator counters were rectangular parallelopiped tanks made with 0.63 cm thick PVC. There were 49 horizontal and 28 vertical tanks in each supermodule except for the two end supermodules, which also included seven vertical tanks of the north and south faces. The horizontal tanks had dimensions of 11.9m$\times$0.75m$\times$0.25m and were aligned with their long axis in the East-West direction. The vertical tanks had dimensions of 12m$\times$0.25m$\times$0.5m and were aligned with their long axis in the

North-South direction. There were a total of 476 tanks in the detector, each associated with several electronic subsystems, thus uniquely naming the tanks was necessary.

As a rule each counter name was composed of four characters according to its location. For example, consider tank 4W14. The first character denotes the supermodule (SM) number (in this case SM4). The second, the face: this tank was in the west face. The last two characters denote the tank number: this tank was the $14^{th}$ tank counting from bottom to top. Along the horizontal faces numbering increased when counting from North to South. The two ends of each tank were named end 0 and end 1. In the horizontals and north and south verticals, 0 is the West facing end side and 1 is the end on the East side. In the east and west face verticals 0 is the North end, and 1 is the South end.

The tanks were divided into three chambers separated by 0.32 cm thick transparent PVC windows. The middle chamber ($\sim$ 11 m long) was filled with scintillator mix to a nominal height of 19 cm for the horizontal and 41 cm for the vertical tanks. The end chambers hosted the light collecting photo-multiplier tubes (PMTs); separating them from the scintillator to allow easy access for maintenance purposes. There were two PMTs in either end chamber in the horizontal tanks, and one PMT in either end chamber in the vertical tanks as illustrated in Fig. 2.5.

The length of the tanks required the use of clear mineral oil, with attenuation length more than 20 m, as a solvent. The scintillator was pseudocumene which emits at $\simeq$ 290 nm; PPO and bis-MSB were the wavelength shifters from 290 nm to $\simeq$ 420 nm, which is in the sensitivity range of the PMTs. The composition of the scintillator mix is shown in Table 2.2.

The light production mechanism of monopoles in the MACRO scintillator was described in chapter 1. The composition of the mix was optimized for the scintillator to have an attenuation length greater than 12 m. The inside of the tanks was covered with white Teflon-FEP material with a refractive index of 1.33. The refractive index of the liquid scintillator was 1.48. Thus, total internal reflection was achieved for light rays making an angle $\theta$ with the liner surface less than $25.6^{o}$. The maximum

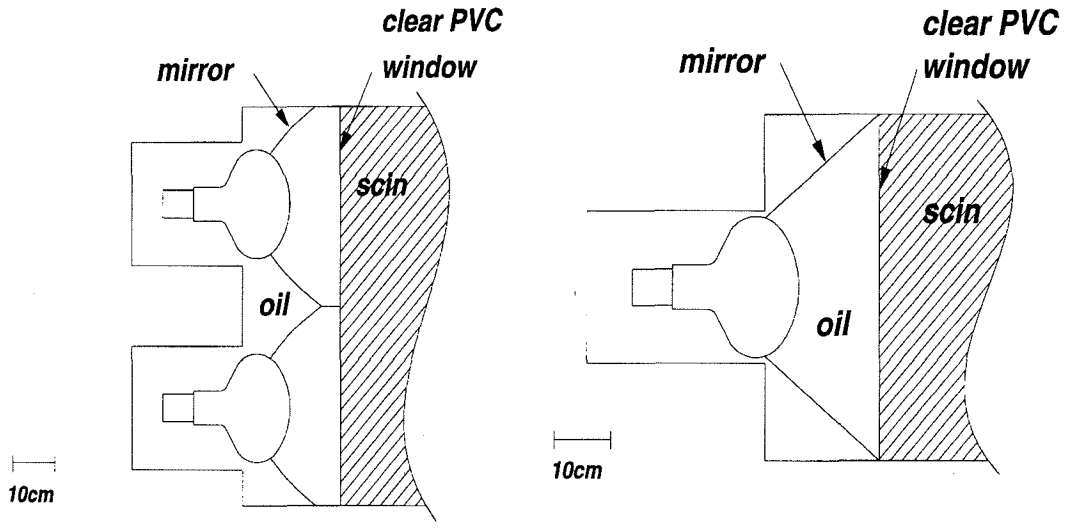


Figure 2.5: PMTs in the end chambers of horizontal (two PMTs) and vertical (one PMT) tanks.

| | |
|---|---|
| mineral oil | 96.4% |
| pseudocumene | 3.6% |
| PPO | 1.44 g/l |
| bis-MSB | 1.44 mg/l |

Table 2.2: The MACRO liquid scintillator.

angle for total internal reflection on the scintillator-air surface was $47.3^o$.

The end chambers were filled with clear mineral oil (no scintillator) and contained specially designed mirrors to help increase the light collection efficiency of the PMTs. The PMTs were of two separate types. The lower part and the top horizontal layer of the detector were equipped with EMI D642 20-cm hemispherical tubes. The vertical counters of the attico were equipped with 20-cm hemispherical Hamamatsu R1408 PMTs. Both types operated at negative voltage biases, typically $-1600$ V. The gain could be varied by adjusting the high voltage, and for the duration of the experiment it was set to $-4$ mV per SPE (Single Photo-Electron). A typical muon passing through 19 cm of scintillator would produce a pulse-height of $\simeq$ 2 V (see

appendix A) with a risetime of about 15 ns.

Higher PMT gains would have allowed for increased sensitivity to low velocity monopoles, which have low light yield. However, saturation effects would have impeded searches for fast monopoles and muons. The gain of each PMT was set with the help of a LeCroy 3001 multichannel analyzer (QVT) and an LED calibration system of the scintillator tanks, which is described further in section 2.3.2. The EMI PMTs were characterized by their well-defined SPE peak. A typical SPE charge spectrum is shown in Fig. 2.6.

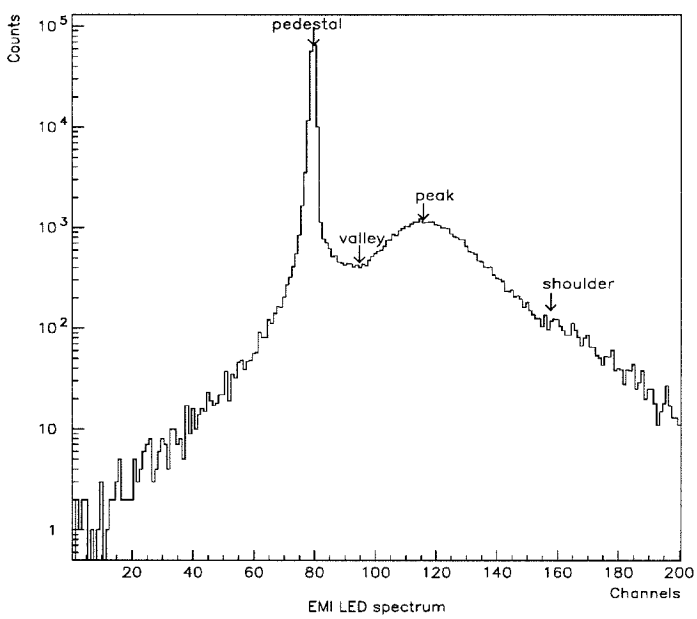


Figure 2.6: Typical EMI spectrum as measured with the LECROY 3001 multichannel analyzer. The spectrum is taken with LED pulses with a mean number of electrons less than one.

The Hamamatsu PMTs had an exponential SPE charge spectrum, as shown in Fig. 2.7. Even though the more predictable SPE pulse characteristics of the EMI PMTs were preferable for a monopole search, the Hamamatsu tubes had certain advantages as well. They proved to be insignificantly affected by earth's magnetic field and, unlike the EMI tubes, were not subject to degradation. The latter needed periodic high voltage adjustment to keep their $-4$ mV per SPE response.

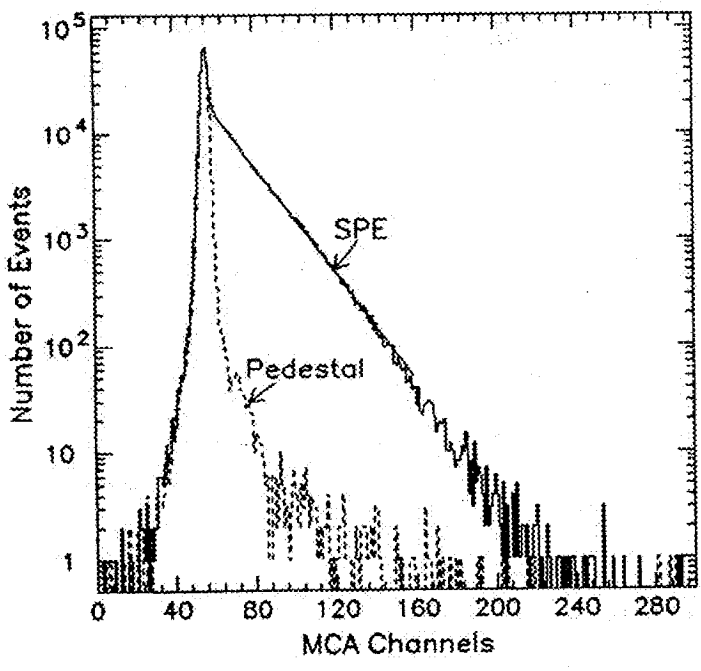


Figure 2.7: Typical HAMAMATSU spectrum as measured with the LECROY 3001 multichannel analyzer. The SPE spectrum is taken with LED pulses.

### 2.3.1 Scintillator Electronics

Many different electronic subsystems were employed to take full advantage of the various capabilities of the MACRO scintillator detector. As mentioned above, monopoles, neutrinos from stellar collapse and muons were the main physical targets of MACRO. There were two muon triggering systems called ERP and SPAM_MUON, one fast monopole trigger called SPAM_FMT, and one slow monopole trigger called SMT. There were two triggers for gravitational collapse called ERP GC and PHRASE, one trigger for lightly ionizing particles called LIP, and one trigger for highly ionizing particles, HIPT. In addition to these triggering systems, there was a Waveform Digitizer (WFD) recording system and a special trigger to prevent it from saturating on large pulse height events (LAMOSSKA). A linear fan-in fan-out system distributed the PMT pulses from each tank-end to the various triggering and waveform recording systems. The Slow Monopole Trigger (SMT) plays the most important role in

making this search possible and a whole section is dedicated to it. In this section we continue with a short overview of the other triggers.

The Energy Reconstruction Processor (ERP) was designed for muon and gravitational collapse detection. The ERP trigger was a single counter trigger. The pulses at the two ends of a counter were integrated and digitized by two flash analog-to-digital converters (FADCs). The integration gate of 240 ns allowed integration of typical 50 ns wide muon pulses, and accounted for the light travel time from one end of the counter to the other. The integrated and digitized pulses were then translated to total energy deposition in the counter with the help of an 8 k $\times$ 8 k software programmable RAM look-up table (LUT). The LUT decided if the energy deposition justified a "muon" trigger (threshold of $\sim$ 16 MeV), or a low level GC trigger with a threshold of $\sim$ 8 MeV. In case of more than one tank firing the ERP, timing information was available within $\sim$400 ns of the first ERP trigger.

The SPAM_MUON trigger was a coincidence trigger for fast particles. For the purposes of this trigger, the pulses of eight (seven for verticals) continuous tanks were fanned in. From now on we will call this set a *supercounter*. If the fanned-in signal exceeded an amplitude threshold of 100 mV at both ends of a supercounter within a duration of 100 ns, a 1 $\mu$s gate was opened. If, within this microsecond, another supercounter from another face of the same or adjacent supermodule fired, a SPAM_MUON trigger occurred. Each SPAM_MUON trigger module served two supermodules and in order to cover the entire detector a tile-like scheme was used. In order to traverse the 4.5-m distance between two horizontal scintillator planes within the 1-$\mu$s SPAM_MUON gate, a particle needed to have velocity greater than $1.5 \times 10^{-2}c$. The large majority of particles detected by MACRO at these velocities were muons.

The Fast Monopole Trigger (called SPAM_FMT) used electronics similar to the SPAM_MUON but allowed for a $\sim$ 10 $\mu$s time gate during which the face coincidence was allowed to happen. The trigger was vetoed by SPAM_MUON. In this way, the trigger was sensitive to particles with velocities in the range $\sim$ $1.5 \times 10^{-2}c$ to $\sim$ $1.5 \times 10^{-3}c$ that created pulses which exceeded the amplitude threshold of

SPAM_MUON. GUT monopoles at these velocities have calculated light yields at least an order of magnitude higher than Minimum Ionizing Particles (MIPs) and were expected to fire the trigger with ease.

The Highly Ionizing Particle Trigger (HIPT) used the same electronic system as SPAM_MUON, but had a higher amplitude triggering threshold of 2 V.

The Pulse Height Recorder And Synchronous Encoder (PHRASE) and the ERP Gravitational Collapse (ERP GC) triggers were to search for neutrino bursts from supernovae by detecting energy depositions of order few MeV in a single tank. In the case of either trigger an alarm system would warn researchers of a potential supernova explosion.

The LIP trigger used triple plane coincidences of energy deposition of a few MeV, in coincidence with the streamer tubes, to search for fractionally charged particles.

Finally, the LAMOSSKA trigger was not dedicated for the search of any particle per se, but was formed to warn the acquisition of high light yield in any one of the counters. It was basically a leaky integrator of the PMT pulse which fired for high light yields and forced the waveform system to halt about 125 $\mu$s after the pulse. This way the presence of the pulse was guaranteed in the effective memory width of the WFDs.

### 2.3.2 The Scintillator Calibration System

MACRO was a large multi-purpose detector with a complex electronics system that required tuning at the time of installation, and was required to run around the clock for more than five years in its final form. Monitoring of the detector was essential in order to guarantee that all systems worked at desirable levels of efficiency. To cope with the task of continuous monitoring of a detector of this size, the scintillator system of MACRO was equipped with two calibration systems: the Light Emitting Diode (LED) calibration system and the LASER calibration system.

The calibration system used red HLMP-3001 Hewlett-Packard LEDs mounted on the mirror of each PMT in the scintillator counters. The connections were different

for vertical and horizontal tanks. These are shown in Fig.2.8. These were driven by

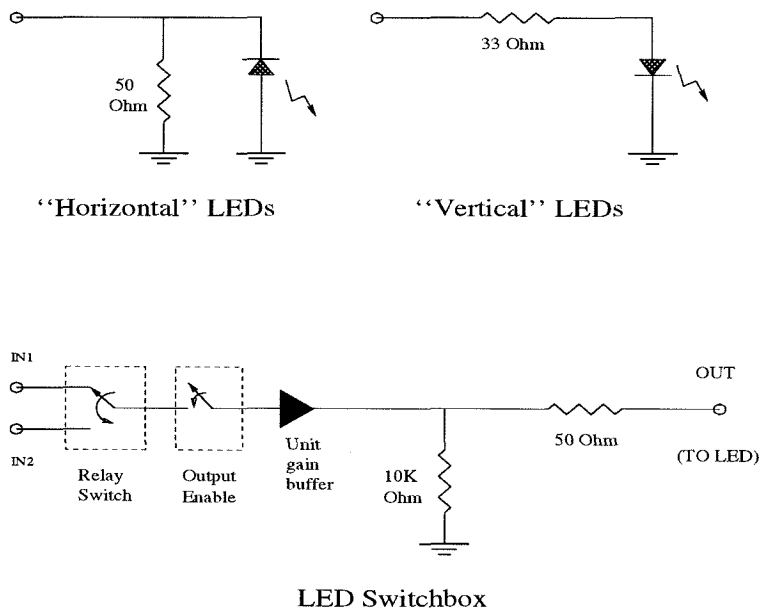


Figure 2.8: LED connections in the LED calibration system.

two Hewlett-Packard programmable pulsers. The pulsers were accessed via CAMAC and each had two independent outputs. The pulse characteristics (such as height, duration, rise and fall times, delay and period) of the pulser outputs were fully programmable. The four outputs were distributed via a custom made distribution system shown schematically in Fig. 2.9. This way four independent signals could be produced and directed to the desired scintillator tank-ends. The LED system was used to calibrate timing for the muon and monopole electronics, but for the purposes of this search, it was used to simulate very low light-yield slow-monopole pulses in order to calibrate the efficiency of the slow-monopole electronics. These calibrations are described extensively in chapter 3.

The LASER calibration system used nine VSL337 nitrogen lasers (one for each supermodule in the lower detector plus one for every two supermodules in the attico) that were operated at maximum power. The output was controlled by means of a programmable attenuator and directed through optical fibers to the center of

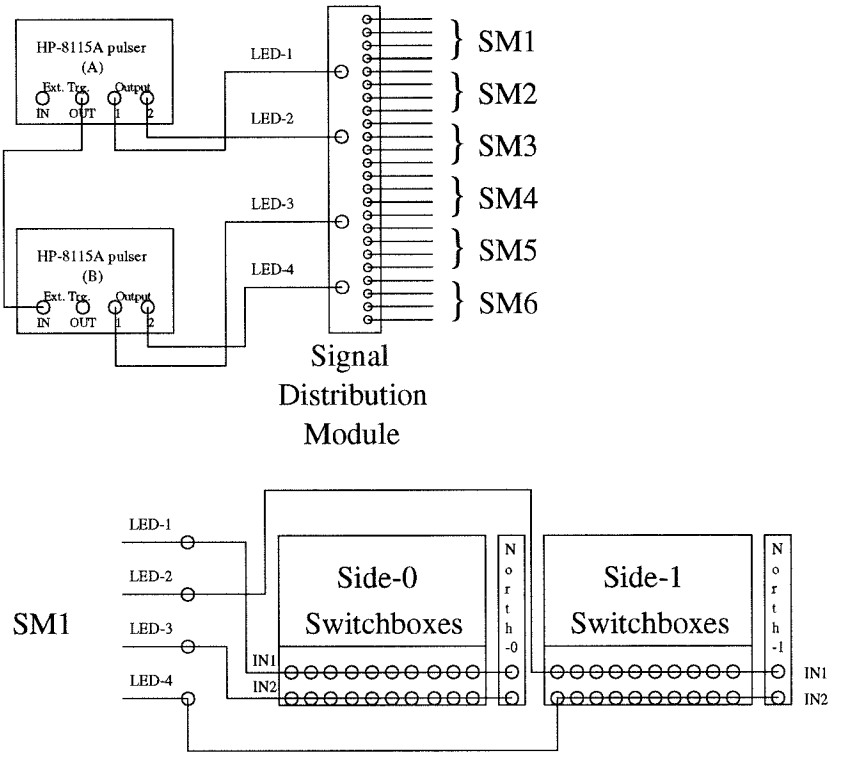


Figure 2.9: LED distribution system.

each scintillator tank. The pre- and post-attenuation laser power was measured by two reference PMTs. The LASER calibrations were fully automated and were used primarily to calibrate the ADC and TDC response of the muon electronics.

Calibrations could run independently in one-third of the detector while the remainder of the detector could be in acquisition mode. Normally, calibrations were performed on a weekly basis for a third of the detector at a time.

## 2.4 The Streamer Tube System

The MACRO streamer tubes were gaseous tubes working in the limited streamer mode. We are going to outline below this way of operation and we are going to give a brief description of the MACRO streamer tube detector. For a more detailed description the reader is directed to [73], [74] and references therein. The energy

losses of monopoles in streamer tube gas were discussed at some length in chapter 1.

The streamer tubes in MACRO were 3.2cm×25cm×12m units of eight PVC streamer tube cells each. A typical eight-cell is depicted in Fig. 2.10. In the lower

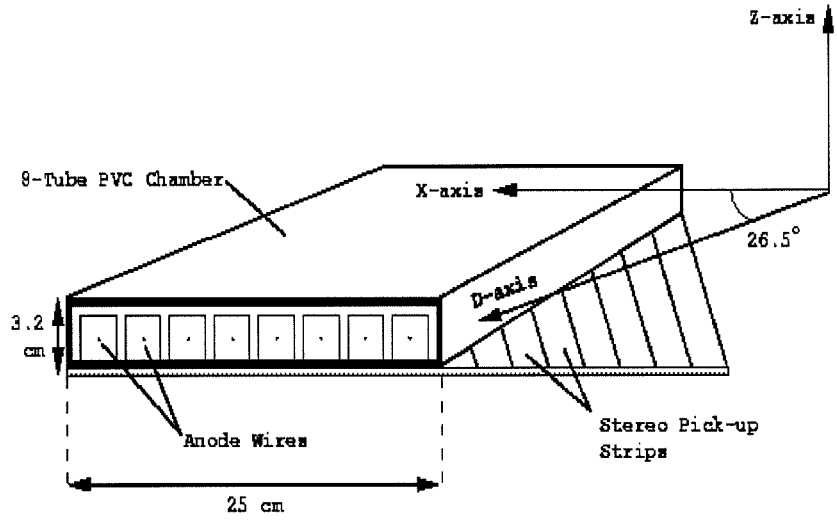


Figure 2.10: A MACRO eight cell streamer tube.

part of each supermodule there were ten horizontal layers of streamer tubes consisting of 48 eight-cell units. In the attico part of each supermodule there were four horizontal streamer tube layers (two above and two below the top horizontal scintillator face) containing 51 eight-cell units each. Finally, each supermodule had 12 layers of vertical streamer tubes (three layers on each side of the west and east vertical scintillator faces) of 28 eight-cells each, while on each side of the north and south faces there were three layers of 14 eight-cells. Full-up MACRO had 49,536 wires in operation.

The streamer tubes were placed with their longest dimension along that of the scintillator counters. A silvered Be-Cu anode wire of 100 micron diameter was run along the long axis of each cell. Three of four long walls of each cell were covered with low resistivity graphite acting as the cathode. The tubes were filled with a mixture of 73% He and 27% n-pentane gas, which was controlled and refreshed by a central gas supply system. Helium was chosen to take advantage of the Drell-Penning

effect in the detection of slow magnetic monopoles (see section 1.5.2). The passage of a monopole with $\beta \geq 1.1 \times 10^{-4}$ near a He atom would leave the atom in an excited metastable state [59]. N-Pentane could then be ionized through collisions with excited He atoms (Penning effect). The high cross section for these processes ensured almost 100% efficiency in the detection of bare monopoles with this gas mixture. The measured single ion-pair efficiency for MACRO streamer tubes was over 20% [75], allowing monopole detection even when the Drell cross section is reduced for monopoles that may have captured atomic nuclei. In the higher velocity region ($\beta > 10^{-3}$), where the assumptions used in the Drell calculation do not apply, the standard ionization mechanism for charged particles ensured an energy release several orders of magnitude higher than that due to minimum ionizing particles. These features allowed the detection of magnetic monopoles with any $\beta > 10^{-4}$.

The tubes worked in the limited streamer mode. In this mode, a narrow column of avalanches is produced which is the so-called "streamer." The streamer initiates with ion-electron pairs that are formed along the path of an ionizing particle. The electrons, under the influence of the strong electric field in the tube, drift towards the anode creating an avalanche while the heavy ions move at slower rate toward the cathode. Secondary avalanches are created because of ultraviolet radiation produced as a result of recombination of gas ions with electrons. These avalanches form the column of ionized plasma that we called streamer. The typical voltage bias required to operate the streamer tubes in this mode was +4.25 kV. As shown in Fig. 2.11, the streamer tube response was fully efficient over about a 0.7 kV plateau. In that region, streamer tube operation is practically noiseless and the background was mainly due to radioactivity at the rate of $\sim$ 50 Hz m$^{-2}$. The cell dimensions and the drift inside the tube produced a timing jitter with triangular shape and a base width of 600 ns, corresponding to a time resolution of 140 ns. The dead region on a streamer wire, due to formation of a streamer, was of the order of a few millimeters, with a dead time of 300 $\mu$s.

Facing the side of a streamer tube without the electrodes were pick-up strips which provided a second read out dimension. For the horizontal streamer tube layers

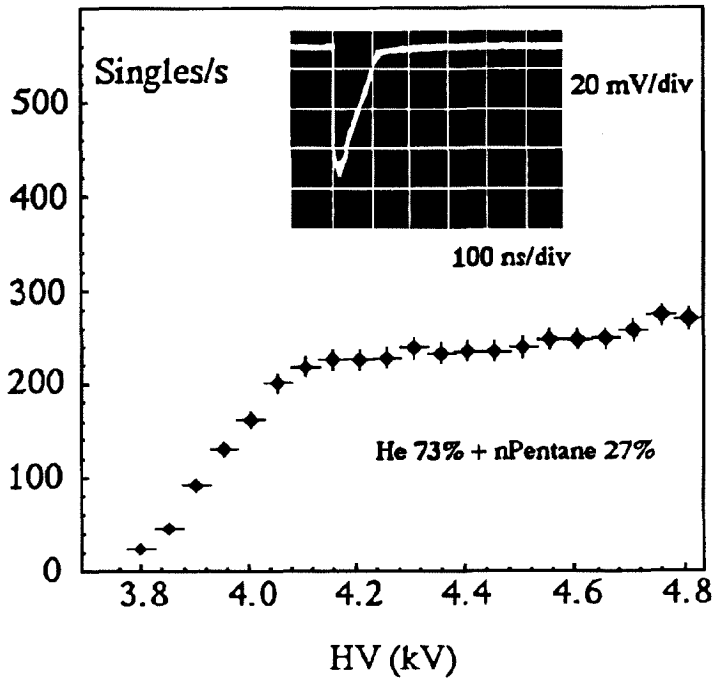


Figure 2.11: Singles rate for MACRO streamer tubes.

(in the lower part), strips were made of aluminum ribbon 3 cm wide, 40 $\mu$m thick, and laid out on a 1 mm PVC foil. Strips made an angle of 26.5$^o$ with the wires. The vertical layers of the lower part were not equipped with pick up strips. For the attico, vertical strips were made of copper 5.5 cm wide, 18 $\mu$m thick and laid on 5 mm thick propylene. They had a 6 cm pitch and formed a right angle with the wires. The strips of the horizontal planes were 3.1 cm wide and had a 3.25 cm pitch.

The two-dimensional read-out provided by the streamer wires and strips may be used to reconstruct particle tracks with good accuracy. Tracking was performed separately for both the wires and the strips. The track may be reconstructed in three dimensions by keeping in mind the angle between wires and strips. MACRO had excellent tracking capabilities. The typical uncertainties in the slopes for muon tracks that crossed four or more planes were 0.14$^o$ in the wire view and 0.29$^o$ in the strip view. Streamer tube timing, though, was not adequate for fast particles due to high jitter (600ns).

### 2.4.1 Streamer Tube Electronics

For the purposes of this study, information from streamer tube system is used only as back-up support for any conclusions reached from data acquired by the scintillator system. The streamer tube system is described in great detail in many theses and papers that have used it extensively and its description here will be brief.

Streamer tube electronics is made up of two systems: the STAS and the QTPs, and is triggered mainly by two triggers – the Bari Trigger and the Streamer Tube Monopole Trigger. For the Streamer Tube Acquisition System (STAS), wire hits were discriminated at 40 mV and created two gates that were 10 $\mu$s and 500 $\mu$s long. These digital pulses were sent to shift registers referred to as the "fast" and "slow" chain, respectively. Digital readout was also performed for the strips. The length of the fast chain memory for the strips was 14 $\mu$s and the strips were fanned in four-to-one, while the length of the slow chain memory was 550 $\mu$s. As mentioned earlier, MACRO streamer tubes operated in the limited streamer mode. This meant that the charge of the streamer was very loosely dependent on the ionization inside the tube. The charge collected on the wires had a logarithmic dependence on the energy released inside the active cell. Because fast GUT magnetic monopoles are so highly ionizing, a charge measurement allows one to distinguish between fast monopoles and muons (see Fig. 2.12.)

To exploit this possibility, analog readout was also performed by QTPs (Charge(Q) and Time Processors) for the wires. QTPs had a 640 $\mu$s memory, and were also used for measurements of the pulse time and duration with a time resolution of 150 ns. This allowed identification of slow particles by measurement of their time-of-flight across the apparatus.

The two triggering systems were the Bari Trigger and the Streamer Tube Monopole Trigger. Both made decisions using the OR of all tubes in a streamer tube layer of a supermodule (*plane hit*). The Bari Trigger identified the passage of fast particles using the streamer tube fast chain (10 $\mu$s-long memory). The trigger searched for multiple coincidences within the 10 $\mu$s duration among the streamer planes. Its

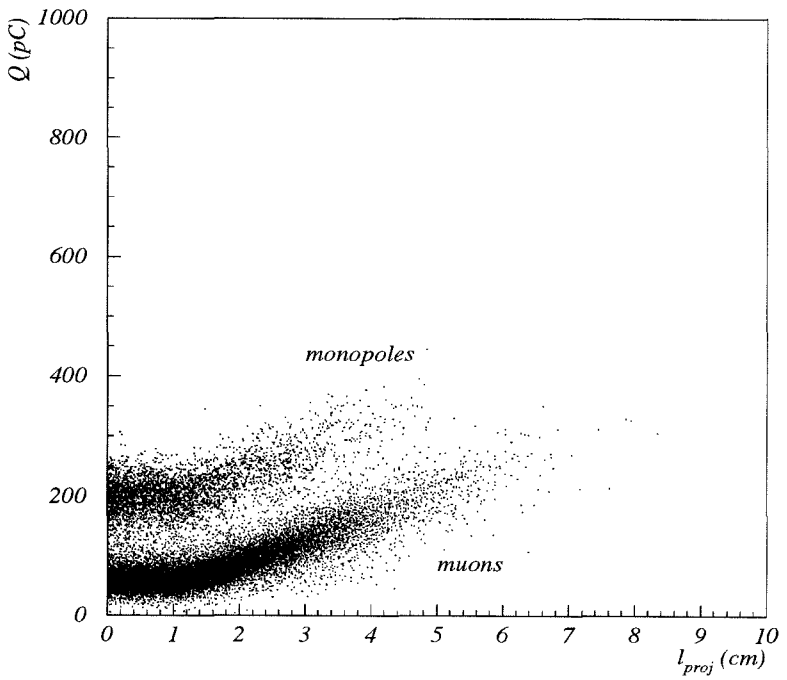


Figure 2.12: Mean charge for a sample of muons and for simulated relatively fast monopoles ($v \simeq 5 \times 10^{-3}c$) as a function of projected track length.

sampling frequency was 3.3 MHz.

The Streamer Tube Monopole Trigger, on the other hand, was used to identify the passage of slow particles. This trigger used the slow chain memory and distinguished between horizontal and vertical layers of the streamer tubes. The Horizontal Streamer Tube Monopole Trigger was based on the recognition that a monopole passing through the horizontal planes of streamer tubes would retain a constant velocity, even though the velocity magnitude would be unknown. The vertical position of the streamer tube layers hit would be a linear function of time, where the constant slope provides the vertical component of the particle velocity. Serial-in parallel-out shift registers were employed in the hardware to construct this z-coordinate vs. time diagram. A diagram constructed in this manner was divided into 320 slices (160 slices for downward-moving particles and 160 slices for upward-moving ones), each corresponding to a small range of velocities. Alignment of plane hits within one of these slices produced a hardware trigger. The trigger logic is graphically represented

in Fig. 2.13. The register depth used in the trigger was 480 $\mu$s (which corresponds to

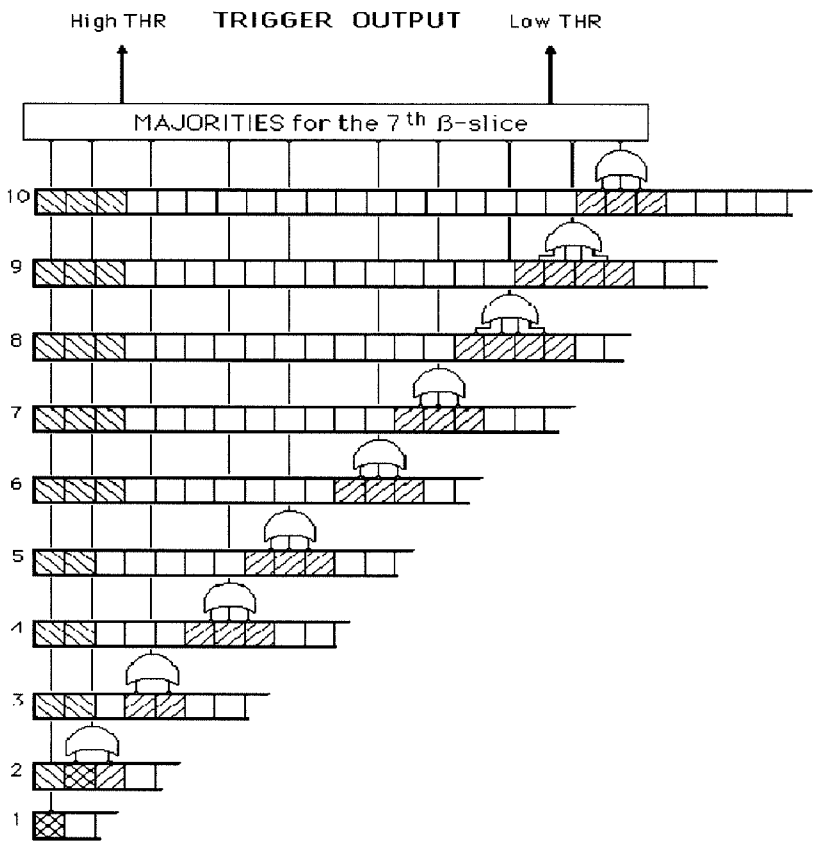


Figure 2.13: Graphic representation of a slice in the horizontal streamer monopole trigger.

minimum velocity of a vertically incident particle of $\simeq 3.3 \times 10^{-5}c$, with resolution of $\simeq 2$ $\mu$s). Time alignment of seven horizontal plane hits was required to form a trigger and the formation of an alignment was tested at a frequency of 1 MHz. In the event of an alignment of eight horizontal planes, a "high threshold" monopole trigger caused the Waveform Digitizers of the scintillator system to be stopped and read out.

The monopole trigger for vertical layers of streamer tubes was less sophisticated and was based on coincidence of planes hit within certain time limits. Out of six vertical streamer tube planes, four were required to have a hit in a time window of 45 $\mu$s. In addition, the three outer (or the three inner) layers were required to be in

coincidence with each other within a 9.5 $\mu$s window. The trigger logic is graphically represented in Fig. 2.14. If the crossing time between the inner and outer planes

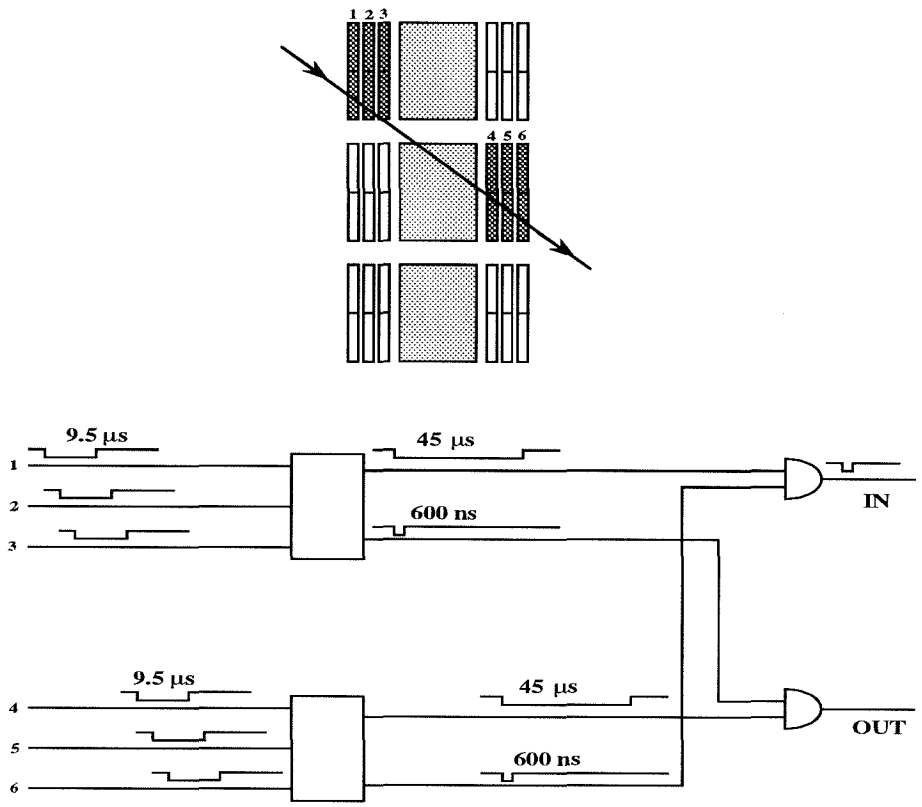


Figure 2.14: An incoming particle entering MACRO (from left to right in the figure) is detected by the vertical trigger. Six roughly aligned pairs of streamer chambers are interested. The timing of the signals is schematically reported: if the crossing time between the inner and outer planes is greater than 600 ns, the circuit recognizes the particle direction.

was greater than 600 ns, the circuit recognized the particle's direction; otherwise the trigger was named Fast Monopole Streamer Tube Trigger ($\beta > 3 \times 10^{-3}$). In the event of a slow trigger with coincidence of five out of six vertical planes, the WFDs were stopped and read.

The efficiency of the wires and the strips was checked for every run, based on the percentage of missing hits from muon tracks. In general, it remained at the level of 95% for wires and 80% for the strips. The overall angular resolution of the streamer

tube system was calculated by the space angle between double muons and was also verified by the shadowing of primary cosmic rays by the Moon. About 68.3% of events have the space angle accurate to within $1.0^o$.

The efficiency of the streamer monopole trigger was evaluated by monitoring the ratio of the measured trigger rate to that expected from accidental coincidence of background streamer hits. The measured trigger efficiency was typically over 99%. After 71,193 hours of running time, the horizontal trigger found no monopoles and sets a monopole upper flux limit of $2.8 \times 10^{-16}$ $cm^{-2}sr^{-1}s^{-1}$ for the velocity range $10^{-4} < \beta < 10^{-3}$ [65]. The vertical monopole trigger, after 31,521 hours of live time, has set an upper limit of $9.3 \times 10^{-16}$ $cm^{-2}sr^{-1}s^{-1}$ for $1.1 \times 10^{-4} < \beta < 3 \times 10^{-3}$ [65].

## 2.5 The Track-Etch Detector

The track-etch technique is based on the fact that local damage occurs along the trajectory of an ionizing particle through a track-etch material. The damage is initially invisible but can be enhanced by chemical etching, which renders the damage visible with an optical microscope. The MACRO track-etch detector consisted of 25cm×25cm tiles called wagons. Each wagon was made of two types of track-etch material, CR39 and Lexan, in six alternating layers; requiring spatial coincidence reduced the background. The CR39 layers were 1.4 mm thick and were mainly used for the detection of slow monopoles with $\beta > 10^{-5}$. The Lexan layers were 0.25 mm thick and were sensitive to high velocity particles $\beta > 0.1$. An aluminum foil of thickness 1 mm was placed between the layers to absorb low energy ions produced by spallation.

The wagons were grouped in "trains," each train having 47 wagons, and a horizontal layer of track-etch detector in each supermodule consisted of 48 trains. Each wagon could be extracted by sliding the train in which it was located on mounting rails. In addition, the East and North walls were covered by the same wagons, thereby raising the total area covered by track-etch to $\simeq 1300$ $m^2$.

The track-etch search was performed both in triggered and stand-alone mode.

The former means that the track-etch detector is used to verify candidates discovered in the analysis of the data from the other two detector systems (scintillators and streamers), and involved the extraction and processing of the tiles in the area pointed to by streamer and/or scintillator analysis. In the stand-alone mode, tiles were scheduled to be extracted from the detector and processed periodically at the external Gran Sasso Laboratories. A total of 545 $m^2$ of CR39 has been analyzed with an average exposure of 9.1 years, giving no monopole candidates. The limit at the 90% confidence level on the monopole flux from the track-etch search is $2.4 \times 10^{-16}$ $cm^{-2}sr^{-1}s^{-1}$ at $\beta \sim 1$ and $3.4 \times 10^{-16}$ $cm^{-2}sr^{-1}s^{-1}$ at $\beta \sim 10^{-4}$ [65].

## 2.6 Data Acquisition Organization

Data acquisition for the MACRO scintillator and streamer tube detectors was performed by three realtime microVAX computers running VAXELN. Another three microVAX computers were used to manage PHRASE (the gravitational collapse trigger) data. Each of the microVAXes served two supermodules in the detector. The microVAXes used for streamer and scintillator (non-PHRASE) data management were named microVAX 1, microVAX 2 and microVAX 3 and served supermodules 1-2, 3-4 and 5-6, respectively. Scintillator and streamer data from each supermodule were collected by the respective microVAXes through three parallel CAMAC branches. The data logging was performed by a central VAX station running on the VAX/VMS platform. All of the data logged for a continuous period of time comprised a data *run*.

Most of the data-taking period used for this search utilized a run duration of the order of six hours. The output file for each run consisted primarily of Waveform data. The output file was analyzed automatically after each run, and general statistics files as well as Data Summary files (DSTs) were created. All data files were subsequently saved on DLT tapes. In general, the change from one run to the next was automatic. Physicists and technicians supervised smooth data-taking almost continuously.

## 2.7 The Decomissioning of MACRO

Even though a big part of this work was written while MACRO was operational, MACRO has stopped taking data in December, 2000. The slow monopole search described here stopped taking data when the WFDs were removed in May, 2000.

# Chapter 3

# The Slow Monopole Electronics

Slow magnetic monopoles are rare and difficult to trigger on. A Slow Monopole Trigger (SMT) for the scintillator system was developed expressly for this purpose. This trigger was used to select monopole candidates for the search described in this thesis. We examine the functionality and the sensitivity of this trigger to monopoles in the remainder of this chapter.

## 3.1 The Slow Monopole Trigger

Magnetic monopoles may have a range of velocities; they might be relativistic, or have galactic-level velocities $\sim 10^{-3}\,c$, or velocities as low as the escape velocity of the Earth $\sim 3.7 \times 10^{-5}\,c$. Their light yield, when crossing a scintillator counter, depends on their velocity. As we have seen in section 1.5.2, a slow GUT monopole of $v \simeq 10^{-4}\,c$ is expected to produce a factor ten less light than a Minimum Ionizing Particle (MIP) when crossing a MACRO scintillator tank, while a monopole of $v \simeq 10^{-3}\,c$ is expected to produce, on an average, more than ten times the light of a MIP.

It is not straightforward to construct a trigger that could detect monopoles over a wide velocity range. In the previous chapter, we discussed the Fast Monopole Trigger, which was sensitive to monopoles with velocities larger than $1.5 \times 10^{-3}\,c$. That trigger was a coincidence trigger, discriminating hits above 100 mV. This is fine for fast monopoles which are expected to have large light yields and short times of passage through the detector. In contrast, slow monopoles are characterized by long times of passage and accompanying low light yields. As a consequence, a very small discrimination level – of the size of a Single Photo-Electron (SPE) – and a large coincidence window are required (a vertical monopole of $\sim 10^{-4}\,c$ requires

about 330 $\mu$s to traverse MACRO). A simple coincidence trigger would result in an enormous trigger rate due to the 30 kHz radioactivity background present in MACRO scintillator tanks. Therefore, an additional level of intelligence had to be built into a trigger for slow monopoles.

The Slow Monopole Trigger was based on the time of passage of a slow monopole through a scintillator tank, and that the monopole would have constant velocity, and would induce scintillation at a constant rate. A relatively fast monopole with velocity $\simeq 3 \times 10^{-3}\, c$ would typically pass through 19 cm of scintillator in $\simeq$ 210 ns. Its light yield is expected to be more than an order of magnitude greater than that of a MIP (see Fig. 3.1), and would create a continuous pulse of width of $\simeq$210 ns (see Fig. 3.2). As the velocity of the monopole falls, the duration of the pulse grows

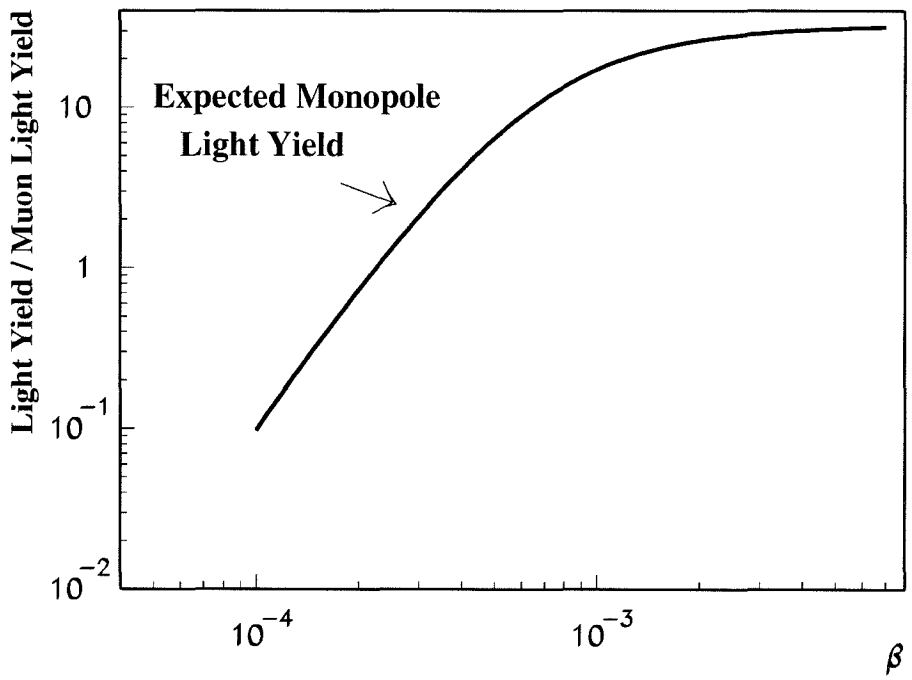


Figure 3.1: Monopole Light Yield in the scintillators.

longer; the light yield falls gradually until there is no more a continuous pulse. At this stage the signal degenerates into flickering SPEs that obey Poisson fluctuations, with time invariant statistics. We refer to this as an *SPE train* (see Fig. 3.2).

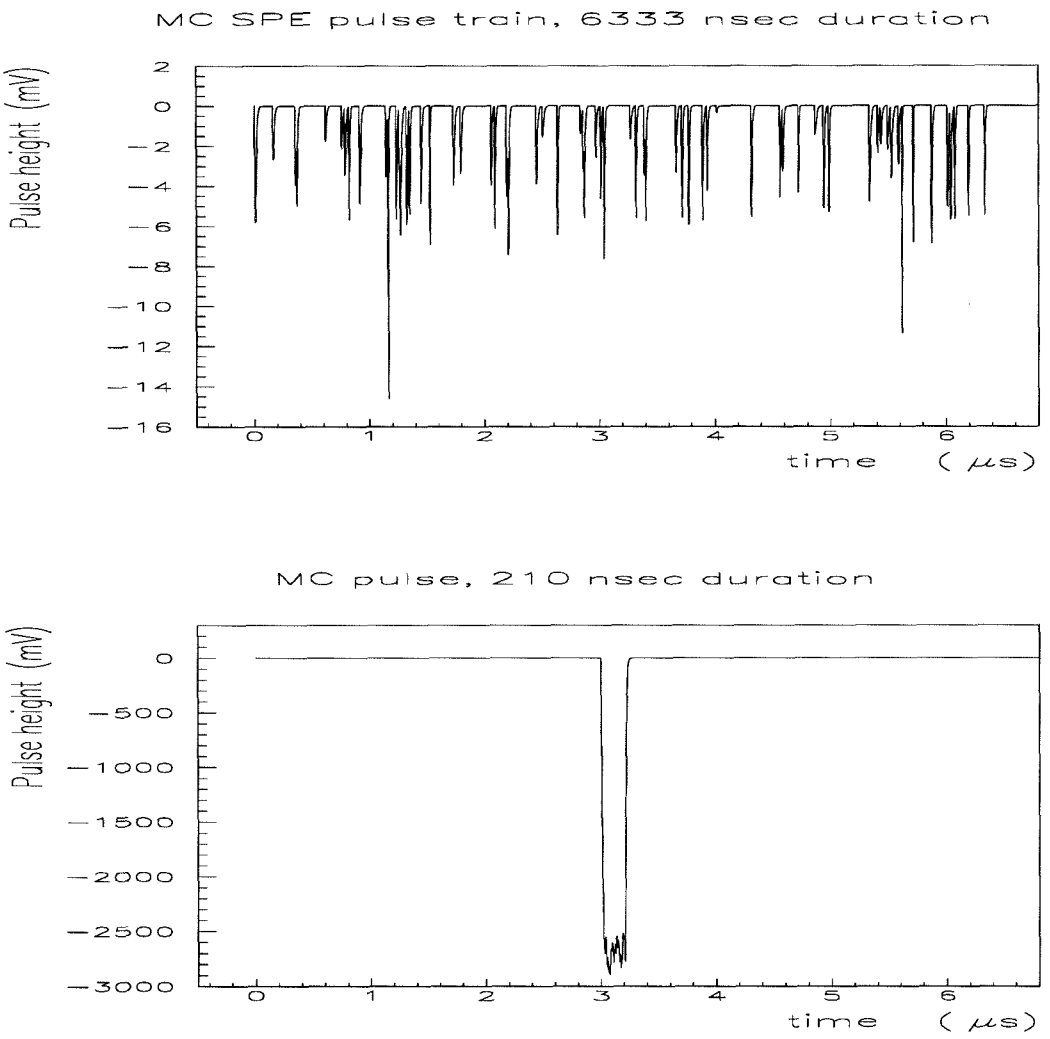


Figure 3.2: A Monte Carlo generated pulse of 6.3 $\mu$s duration of around 63 SPEs (top), corresponding to $\beta \simeq 10^{-4}$ assuming the monopole crosses typically 19 cm of scintillator. A Monte Carlo generated pulse of 210 ns duration and with 11200 SPEs corresponding to $\beta \simeq 3 \times 10^{-3}$ (bottom).

A well designed trigger had to fire on a wide gamut of pulses between these two extreme pulse types. Moreover, it had to reject radioactivity and muons which produce 30-40 ns wide pulses at FWHM, but may be up to ~200 ns wide at their base. The trigger designed to accomplish all of the above was the SMT, was built at the California Institute of Technology (Caltech) and was made up of two parts: the *Time Over Half Maximum (TOHM)* analog part and the *Leaky Integrator (LI)* digital part.

The TOHM uses the negative pulses of the PMTs as inputs. For every input pulse, the TOHM circuit ideally outputs a TTL pulse of width the full width at half maximum of the input analog pulse. It achieves this by means of an analog circuit represented graphically in Fig. 3.3. The input pulse follows two routes. Along

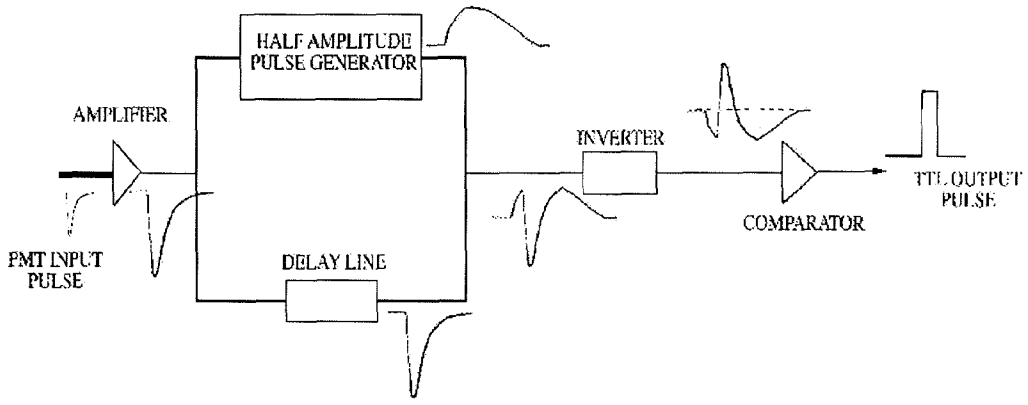


Figure 3.3: TOHM schematic diagram.

the first route, it is inverted, divided in half and stretched. Along the second, it is delayed just enough in time to be added to the inverted and divided pulse from route one. The sum of the two pulses when inverted and discriminated near zero results in a TTL digital output which is approximately as wide as the original input pulse at half maximum, hence the name "Time Over Half Maximum." The comparator of the TOHM was adjusted so that 50% of all 2 mV pulses generated an output pulse. In reality, the TOHM output for pulses of the order of 1 V or higher did not accurately reflect the true FWHM of the pulse, but tends to be wider (pulse stretching).

The TOHM output was fed to the digital LI. The LI is simply a counter that counts up at a constant rate ($T_{up}^{-1}$) when the input is high and counts down at all times at a considerably lower rate ($T_d^{-1}$). The design is such that the counter is restrained from going negative. The contents of the counter will be called *LIcounts*. The count-up rate was 66.6 MHz (or $(15\text{ ns})^{-1}$). In comparison, the mean value of the time over half maximum of SPEs produced by the PMTs is about 12.5 ns. To account for variations in the SPE width, pulses of full width at half maximum in the range 5 to 30 ns generate a single count up. The period of the down counter

was chosen to be as slow as possible, so that the trigger be able to fire on a very low light yield, while keeping a manageable trigger rate for acquisition. The period of the down counter was set to 660 ns for the horizontal counters and to 1500 ns for the vertical ones. The difference in the LI parameters reflects upon the different radioactivity rates for the two types of counters. When the counter reached a preset CAMAC programmable threshold, the *trigger threshold*, the pulse was identified as a monopole-like pulse and a trigger from that specific tank-end was generated. The value of this threshold was also chosen as a compromise between the need to trigger on very slow monopoles and the desire to keep the trigger rate manageable. This threshold was 11 LIcounts for the horizontal counters and 10 LIcounts for the vertical counters.

To better understand the function of the SMT let us examine its behavior towards three separate classes of input pulses: a continuous wide pulse from a fast monopole, an SPE train pulse expected from a slow monopole, and a muon-like pulse.

In the case of a broad monopole pulse, shown in Fig. 3.4, the pulse duration $T_p$ of 250 ns is equal to the time of passage across the scintillator tank. Ideally, the TOHM output is a TTL pulse as wide as the FWHM of the initiating pulse. The LI counts up while the pulse is high for about $(\frac{T_p}{T_{up}} - 1)$ LIcounts. The $-1$ is due to the fact that the first two up-counter periods generate only one count. The down counter is asynchronous with the input pulse with a period much longer than the pulse duration; it might generate at most one down count for the duration of the pulse. With a trigger threshold set at 11 LIcounts, the pulse will generate a trigger as long as

$$LI counts = \frac{T_p}{T_{up}} - 1 - Down\,Counts \geq trigger\,threshold \tag{3.1}$$

From the above argument, we see that for pulses wider than 195 ns, the LI should trigger. By its very design the trigger threshold limits how narrow a pulse may be detected with the SMT. As a direct consequence, this sets a strong condition for the upper velocity of slow monopoles detectable with the SMT. The trigger threshold

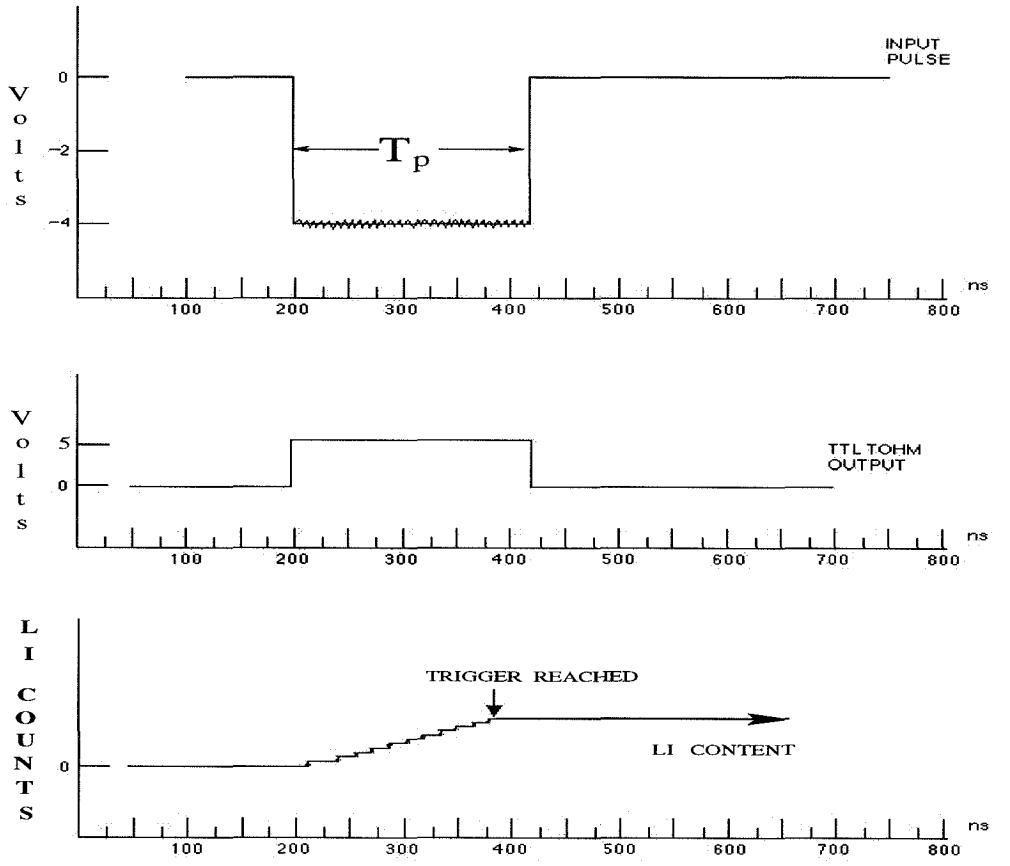


Figure 3.4: Schematic diagram of the behavior of SMT for big and broad pulses.

sets a maximum detectable velocity to $v \sim 3.2 \times 10^{-3}\, c$, assuming that, on average, the monopole crosses 19 cm of scintillator. In actuality, the SMT fires on narrower PMT pulses due to pulse stretching of high amplitude pulses in the TOHM, as mentioned earlier. The effect is accentuated by afterpulsing of the PMTs (more details on the subject of PMT afterpulsing are in chapter 5 and in appendix A). We describe a measurement of the actual minimum pulse width (thus the maximum monopole velocity) that the SMT fires on in section 3.4.2. For faster monopoles the SPAM_FMT trigger was more efficient; however, such fast monopoles will not be considered in this work.

In the case of Fig. 3.5, a slow moving magnetic monopole of $v \simeq 10^{-4}\, c$, with accompanying low light yield, passes through the 19 cm of scintillator in about 6.3 $\mu$s,

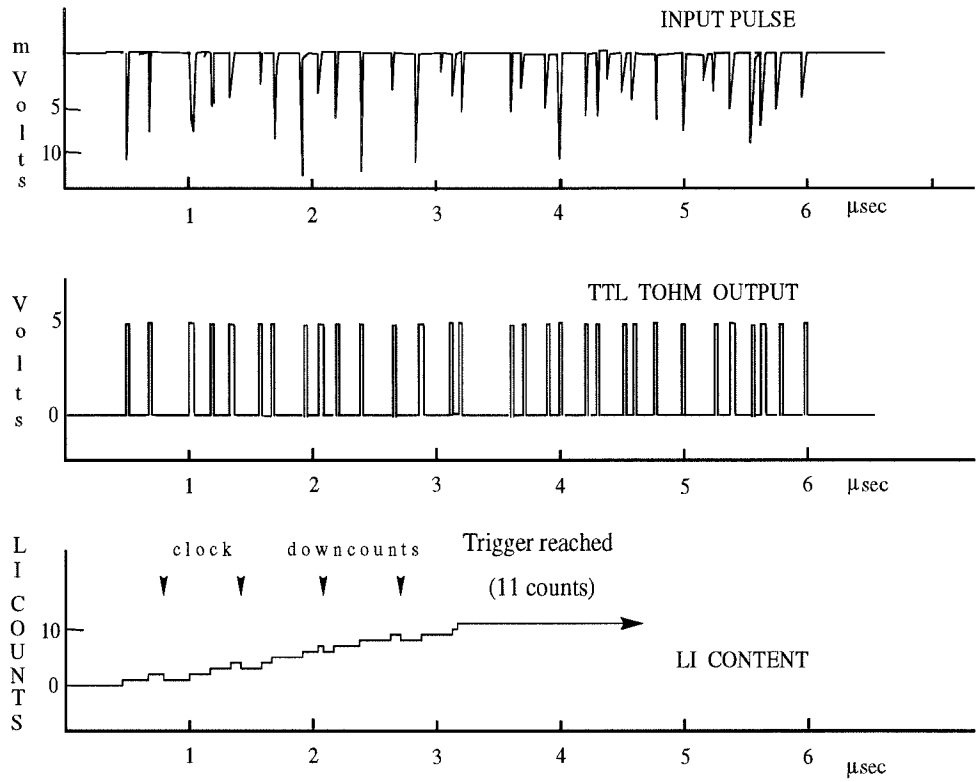


Figure 3.5: Schematic diagram of the behavior of SMT for SPE train pulses.

generating a few SPEs. The resulting TOHM output is a train of $N_{spe}$ TTL pulses as wide as the SPE pulses at half maximum (typically 12.5 ns). The counter counts up for these TTL pulses, but during the 6.3 $\mu$s it also counts down about 10 counts, thus the final count will be

$$LIcounts = N_{spe} - \frac{T_p}{T_d}. \tag{3.2}$$

Obviously in this case, both the down counter rate and the light yield of the monopole play an important role in the decision making process of the SMT. In a horizontal counter (with trigger threshold 11 LIcounts) a 6.3 $\mu$s SPE train pulse will fire the SMT as long as it contains more than 21 SPEs. Equivalently, in a vertical tank (trigger threshold 10 LIcounts) more than 14 SPEs are needed to fire the trigger.

Finally, in the case of a muon pulse (Fig. 3.6), the base of the pulse might be as

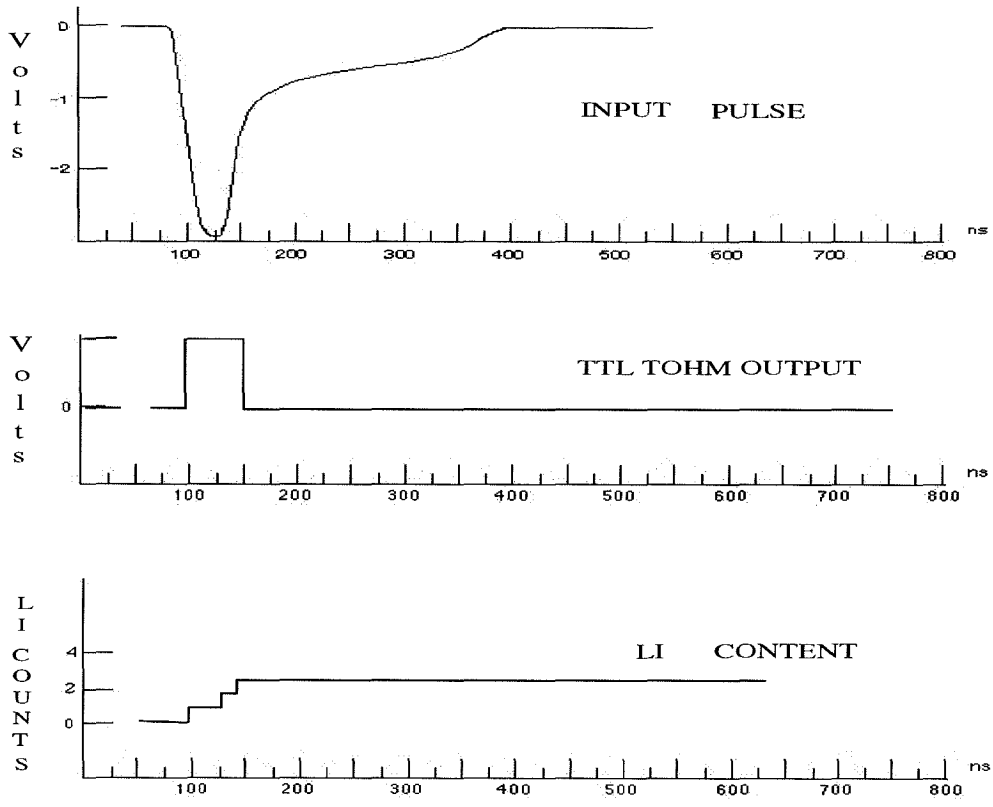


Figure 3.6: Schematic diagram of the behavior of SMT for big muon-like pulses

wide as a few hundred ns, but the pulse typically has a FWHM of about 30-50 ns. The TOHM output, ideally, will be a TTL pulse of this width and the LI counter will count up one to three counts, which clearly does not fire the SMT. However, during the actual experiment a big percentage of muons did fire the SMT. The reason was the pulse stretching of high amplitude pulses in the TOHM, along with PMT afterpulsing. The SMT trigger rate due to muons did not create any major technical hurdles. During the data analysis, various other filters were used to reject relativistic particles that fired the SMT.

The SMT trigger was a single-tank end-to-end coincidence trigger. When a pulse issued from one tank-end was identified as monopole-like, a CAMAC-programmable gate was opened in wait for coincidence from the opposite end of the same tank. A slow monopole in the vicinity of one tank-end may immediately generate a trigger

at that end because of good light collection. On the far end, however, fewer photons are likely to arrive and a delay may be associated with the time of formation of the trigger (if it is formed at all). This time of formation is roughly the time of passage of the monopole through the tank. Taking this into account, the trigger coincidence gate was chosen to be $\simeq 20\,\mu$s. This allows end-to-end coincidence for monopoles with velocities down to $\simeq 3 \times 10^{-5}\,c$.

In addition to the trigger threshold, there was a lower programmable threshold called the *activity threshold.* This was set to four LIcounts for the horizontal counters and to three LIcounts for the vertical counters. The end-to-end coincidence of the activity within $\simeq 4.5\,\mu$s started the *Beginning Of Event (BOE)* gate. The BOE gate decided the processing time of the SMT trigger. The digital output trigger pulse of the SMT was formed about $6\,\mu$s after the BOE for the lower part of the detector and about $20\,\mu$s for the attico.

Finally, the LI circuitry would record the SMT channels that showed activity or trigger coincidence. In the event of an SMT trigger the information with the SMT channels that went over the trigger or the activity threshold was read by the computer. This was used to locate for which tanks the waveforms were to be read out. In addition, the logical-OR of the SMT triggers of a detector face was formed and delivered to the waveform Stop Master (described in section 3.3), where the face and the time of the trigger were recorded. The SMT, unlike other MACRO equipment, ignored the computer BUSY signal that was active during the acquisition of an event.

Throughout the detector, tank-end signals had dedicated SMT channels (TOHM and LI). That amounted to 952 SMT channels in all. More specifically, the SMT trigger was designed and constructed in two versions. The first version used traditional Si components and gate arrays. The lower part of MACRO was outfitted with these. The newer version served the attico part of MACRO (and the north and south faces). It featured surface-mount components and field programmable gate arrays (FPGAs). This new version was far more compact and reduced the total electronics space by a factor of five. Every one of the six CAMAC slot modules consisted of nine TOHM analog daughter cards mounted on a fully digital LI board. There were 21

FPGA chips of five separate functional designs performing the LI functions described above. A picture of such a module is shown in Fig. 3.1. A total of 14 modules served

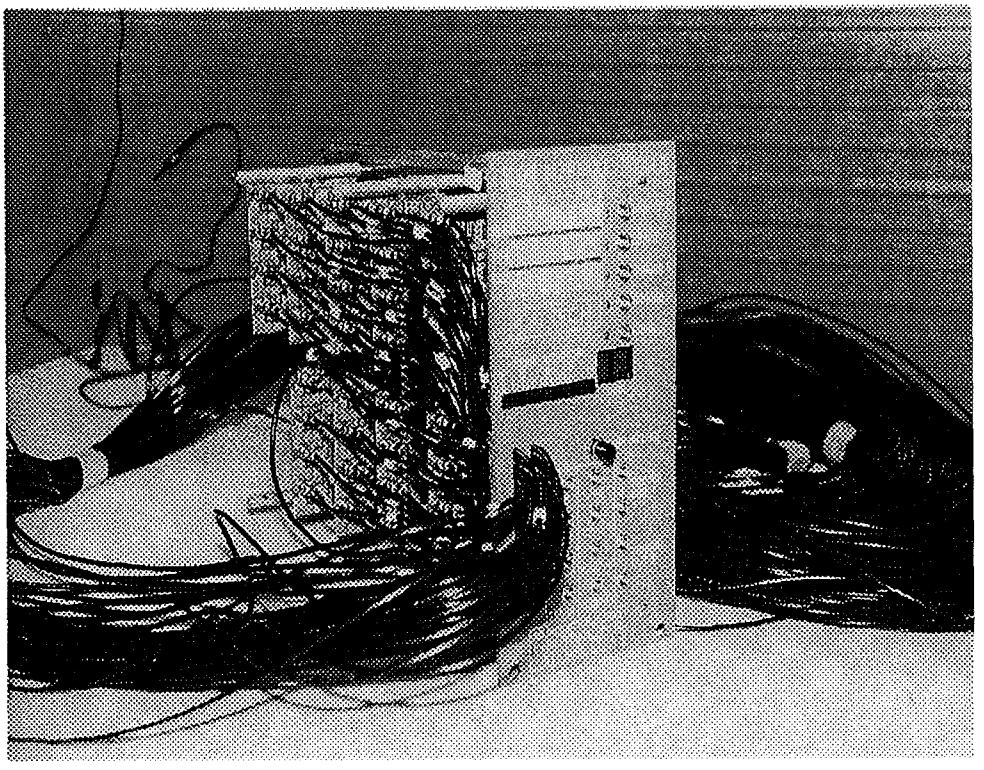

Figure 3.7: An SMT board. This board has 36 channels and may serve up to 18 scintillator tanks.

the 400 channels of the attico. Due to the complexity of the SMT modules, each one had undergone extensive manual and computer interfaced testing before installation on the detector. In addition, calibrations showing healthy performance of the system were performed for the whole detector and are described in section 3.4. The second version of the SMT was completely implemented at MACRO by December 1995.

## 3.2 The Waveform Digitizers

The PMT pulse shape information for each SMT trigger was recorded by a custom-made 200 MHz Waveform Digitizer (WFD). Waveform recording was necessary for the unambiguous identification of a monopole, or rejection of muon or electronic interference pulses that might trigger the SMT. The WFD system utilized was a

custom made VMEbus-based system. Each supermodule was served by ten 9U VME boards (11 for SM1 and SM6 to accommodate North and South faces) with four channels each. A schematic of such a board is shown in Fig. 3.8. Each channel had

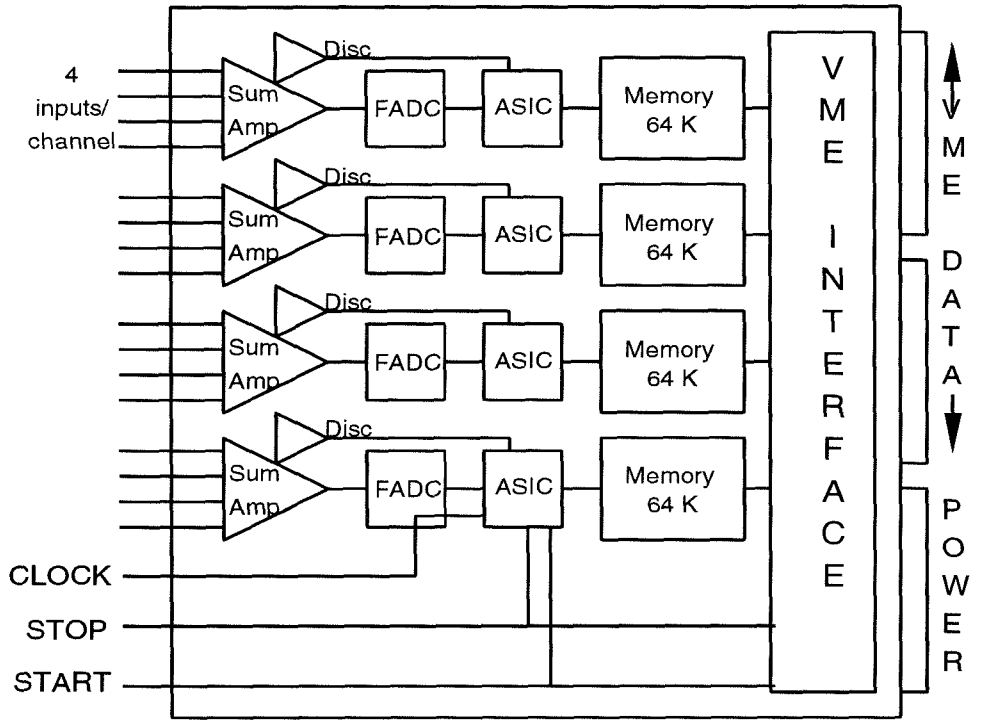


Figure 3.8: Schematic diagram of a WFD board.

four inputs and there were START, STOP and CLOCK controls on each board which were driven simultaneously for all the cards in a supermodule. The four inputs of each channel were fanned-in to one 8-bit flash ADC, that digitized the added signals. A discrete discriminator for each input, set at 2.5 mV, indicated which inputs were active. The discriminator ignored signals with heights in the range +2.5 mV to −2.5 mV, but positive pulses greater than +2.5 mV were recorded. Thus SPE train pulses could be distinguished from bipolar noise, which had appreciable positive content. When one of the four inputs crossed the discriminator threshold, its signal was digitized with a sampling rate of 5 ns. The rate was necessary in order to record

the details of the single photoelectron pulse (of mean width of 12.5 ns) trains. The FADC digitization was nonlinear so that it could cover ranges up to 10 V while retaining a reasonable resolution (0.8 mV) for SPE levels (typically 4 mV).

While a channel was active, a group of data was recorded every 20 ns; this data-group included the four pulse samples, a time stamp, and a 16-bit word indicating which discriminators were over threshold at each of the four digitization instances. When no discriminator was active, no data was recorded. The WFD had no trigger of its own, but after other relevant triggers occurred (e.g., SMT), a STOP signal forced the digitizing to stop; the information recorded by the WFDs was subsequently read by the acquisition system. Only the channels with trigger conditions were read. In the case of an SMT, the channels that had an SMT trigger or activity latched were read out.

The WFD system had a 1 ms deep memory, and was stopped and read 1 ms after a relevant trigger. A monopole of $\beta \simeq 3 \times 10^{-5}$ crosses $\simeq$ 10 m (typically two or three faces) of the MACRO detector in $\simeq$ 1 ms. Therefore, the 1 ms history was sufficient to capture two or three waveforms for a monopole of $\beta$ as low as $\simeq 3 \times 10^{-5}$. In the case of monopoles catalyzing nucleon decay, the fast products of the catalysis (in the absorber or on the rock surface of the hall walls) might have been able to fire a fast trigger well before the monopole produced an SMT trigger. In such a case, the 1 ms window was long enough for the monopole to cross at least two faces before the WFDs were stopped. The maximum buffer size of the WFD channels was software controlled and could be set up to 64 kB. For the largest fraction of the five-year data-taking period, the maximum buffer size of the WFD channels was set to 50 kB; that was the maximum size the acquisition system could handle without problems. If the channel had undergone continuous digitization, 50 kB would only hold about 125 $\mu$s worth of data. In reality, with the datarate suppression technique (i.e., no digitization when the discriminator was below threshold), this memory was adequate enough for holding more than one millisecond of history in most cases.

There was one major retrofit to the WFD system since the beginning of the relevant data collecting period, casually referred to as the WFD-fix. Before the

WFD-fix, capacitive coupling between the WFD system and the PMT fan-out system caused large pulses to be followed by positive overshoot that crossed threshold for more than 125 $\mu$s, thereby filling the WFD 50 kB memory. As a direct result, the original pulse was lost and only the afterpulse remained in memory. The channels where the initiating pulse was lost were easily distinguishable as their memory buffers were full. Since June 1997, this problem was fixed and an additional provision was made with the introduction of the LAMOSSKA trigger, whose function was described earlier in chapter 2. After events with large pulses, the WFDs were halted in less than 125 $\mu$s, ensuring the event was recorded within the memory's capacity. There were still events, after June 1997, without a LAMOSSKA trigger, with runout on the 50 kB WFD buffers. This occurred when the zero suppression circuitry was temporarily switched off for unknown reasons. The effect was rare enough to have negligible impact (less than once in a run), and it usually happened for the first event read by any $\mu$Vax during a run. The effect of WFD buffer overruns before June 1997, however, is significant as it is correlated with the light yield of the particle(s). In this case, since no valid WFD data is available, other filters have to be used for the slow monopole search. We will revisit this issue in the data analysis chapter (chapter 4) and again in the hardware monitoring chapter (chapter 7).

## 3.3 The WFD Stop Master

The Stop Master was a custom-made CAMAC board, one for every supermodule, which managed the stopping of the WFD system after relevant triggers like SMT, SPAM_FMT, high threshold Streamer Slow Monopole Trigger, etc. Generally, it stopped the WFDs around 1 ms after the occurrence of a trigger. The only exception was the LAMOSSKA trigger. In that case, the Stop Master was bypassed and the stop was generated 115 $\mu$s after the initiating trigger. This way the actual pulse was included in the 125 $\mu$s of continuous datastream that the WFD system provided.

The WFD Stop Master would set a bit for all triggers that occurred during the milli-second before the stop. This is seen in Table 3.1, where we see a decoding of the

Stop Master data. The first word recorded by the Stop Master was the word denoted as TRGPT. In this case, bits 1,2 and 8 were asserted – indicating that triggers SMT, ERP(muon), and HIPT fired in the event. The arrival of the first trigger would start

| | | | | |
|---|---|---|---|---|
| TRGPT | 1:SMT | 2:ERPM | 8:HIPT | |
| TRGTM | 1(SMT):49 | 2(ERPM):9 | 3(STmn):10016 | 4(FMTm):10016 |
| TRGTM | 5(SPAM):10016 | 6(LIPT):10016 | 7(xSTP):10016 | 8(HIPT):0 |
| SMTPT | 1:x2Fc | 2:CENT | 7:TOP | 12:i2Fc |
| SMTTM | 1(CENT):0 | 2(BOTT):10002 | 3(WEST):10002 | 4(EAST):10002 |
| SMTTM | 5(NorS):10002 | 6(TOP):159 | 7(SM-1):10002 | 8(SM+1):10002 |

Table 3.1: Stop Master decoding. Detailed explanations are given in the text.

a counter clocked by a 100 ns clock; this counter recorded the arrival times of any subsequent triggers in units of 100 ns. For example, in Table 3.1 the words recording the arrival times of the triggers can be seen in the rows called TRGTM. There were a total of eight such words per Stop Master module. In the case of Table 3.1, word 1 corresponds to the arrival time of the SMT and indicates that the SMT arrived 4.9 $\mu$s after the trigger that started this counter. (The trigger that started the counter had the time word equal to zero and, in this case, it was the HIPT.) If a trigger had not fired within 1 ms after the initial trigger, the time word corresponding to it was the maximum value of the counter, which was slightly different for each Stop Master module. In the case of the Stop Master of Table 3.1, it was 1.0016 ms.

The Stop Master was also used to record which faces of the detector had had an SMT trigger. The logical-OR of the SMT triggers from each face of a supermodule was directed to the Stop Master. There, it would assert a bit indicating which face had fired. This is illustrated, in Table 3.1, in the row called SMTPT. The decoding of this word shows that bits 1, 2, 7 and 12 were set, meaning that the center (bit 2) and the top (bit 7) faces had had an SMT trigger. We explain the purpose of bits 1 and

12 a little later). The logical-OR of the SMT from each face would also start another counter, clocked by a 100 ns clock. This counter would record the arrival times of the SMT triggers from the faces that fired subsequently (within 1 ms). This way the relative timing of the SMT triggers in the various faces of the detector is determined to the 100 ns resolution of the counter clock (The lower part of MACRO and the attico have different SMT processing times, which must be taken into account.) For example, in Table 3.1, the words recording the arrival times of the SMT from each face can be seen in the rows called SMTTM. There were a total of eight such words per Stop Master module and the face that corresponds to each word is shown in the same table. The seventh and the eighth word correspond to SMT triggers arriving from the previous and subsequent supermodules respectively. In the case of Table 3.1, the SMT from the center face arrived first, and was followed by the SMT from the top face (15.9 $\mu$s later). The remaining faces did not have an SMT, thus the time word corresponding to those faces recorded the maximum value of this counter.

The WFD Stop Master was used to select valid two-face monopole triggers within 1 ms. The SMT latched a bit for each tank that fired. However, as mentioned in section 3.1, the SMT ignored the computer BUSY signal and kept recording hits even when the acquisition system was "busy" reading an event. Therefore, the trigger that was latched in the SMT may have occurred towards the end of the previous event's readout (up to several seconds before the trigger causing the current readout), or it may have occurred during the current readout (up to many tens of ms after the initiating trigger). Therefore, we rely on the Stop Master to identify which faces had had SMT triggers within the event window. SMT triggers outside of this window were not considered in this analysis, which is based on the identification of a monopole pulse in the waveforms.

The late or early SMT triggers that occurred during the computer BUSY (more than 1 ms after the current trigger) would not be recorded in the 1 ms-deep WFDs and would not result in data that can be analyzed correctly. These late or early SMT triggers should be unrelated to the current event, but, even if they were due to a putative monopole, we may still calculate the flux correctly after applying a

dead time correction. On the other hand, if these late hits were indeed related to the recorded event, then the monopole was either too slow for our sensitivity range and/or its pathlength in the detector was very long. In both cases, the acceptance calculation correctly predicts that we cannot recognize such a monopole.

In the case of a two or more face SMT triggers within a millisecond, a coincidence bit in the Stop Master was set to inform us of the occurrence of a two face SMT. This bit is seen in Table 3.1 in the SMTPT word as bit 12 (coincidence within 1 ms within the supermodule). An additional bit (bit 1 in word SMTPT in Table 3.1) was set when there were two or more faces with SMT triggers within 1 ms in adjacent supermodules. The performance of the Stop Master is examined in chapter 7.

In summary, the triggering scheme in the scintillator detector for slow magnetic monopoles was a one-tank end-to-end trigger and was as follows: The signals from the PMTs from the two ends of a single tank were distributed through the linear fan-in-fan-out to TOHM. The output of the TOHM circuitry went to the LI which decided whether both tank-ends satisfied the conditions of a slow monopole trigger within a certain timeframe. The logical-OR of the SMT triggers from a single supermodule

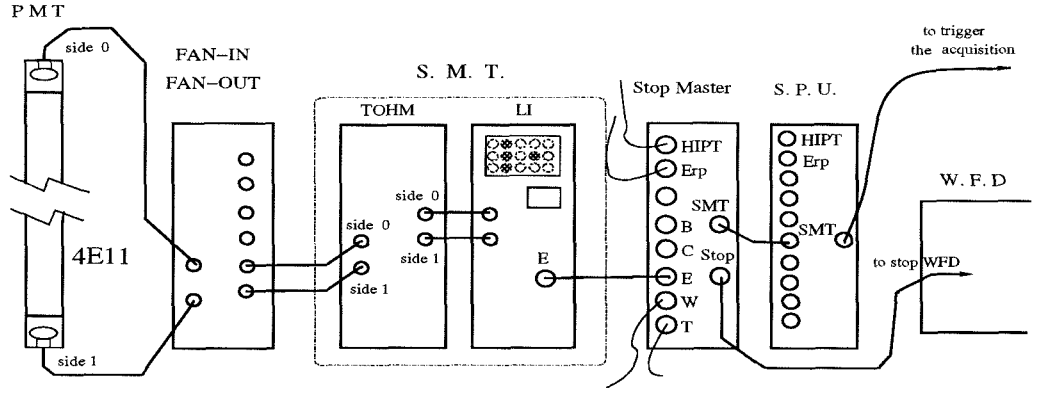


Figure 3.9: Scheme of slow monopole trigger procedure.

face was sent to the Stop Master. The Stop Master stopped the WFDs and forwarded the trigger to the Scintillator Pattern Unit (SPU). The SPU (one per microVax) was a module that latched the various triggers (SMT, LIP, SPAM_MUON and SPAM_FMT, Streamer Slow Monopole Trigger, etc.) that arrived from the two supermodules served by that microVax and sent a trigger to the computer to stop the acquisition.

A functional block diagram of the SMT procedure is shown in Fig. 3.9.

## 3.4 Calibrations: Measuring the SMT Sensitivity

The sensitivity of the SMT for slow monopoles is of major importance for this study. The philosophy of the trigger design has been previously described in this chapter. Extensive testing of the hardware was done at Caltech during intial assembly and testing. These tests were performed by means of a pulse generator and demonstrated that the hardware behaved according to design specifications.

In addition to those tests, the MACRO LED calibration system was used for in situ hardware tests with light pulses simulating the passage of a slow moving particle. Very slow magnetic monopoles are expected to generate very little light in the scintillator. This would be translated by the MACRO PMTs into a pulse consisting of a few photoelectrons, distributed in a Poissonian fashion, during the passage time of the slow particle through the tank. Thus, measuring the photoelectron threshold required to fire the SMT (within a certain pulse duration) measures effectively the least-ionizing monopole (or another particle) that the SMT hardware is sensitive to, as a function of velocity.

A procedure was developed simulating monopoles with velocity and light-yield distributions which was run weekly on a pair of supermodules throughout the data-taking period. All six supermodules were checked by rotation within a three week period. In addition to these routine calibrations, extensive calibrations were performed at four points in time: in 1996 after the installation of the SMT hardware for the attico, in 1998 after several modifications to the LED hardware, in May 2000 just before the removal of a big part of the WFDs, and in December 2000 just before the decomissioning of MACRO. These calibrations investigated the sensitivity limits of the SMT and demonstrated proper functioning and stability over the period of operation. In addition, the calibrations that were performed in December 2000 in SM3 and SM4 tried to investigate, with LED pulses, the fastest monopoles that the SMT was sensitive to.

### 3.4.1 Calibration Technique

The SMT is a one-tank, end-to-end coincidence trigger, meaning that both ends of one tank must pass the SMT threshold in order to trigger. To test each tank-end independently, we fire the LED of the end opposite to the one being calibrated. This way a small amount of light – simulating the light yield of a slow moving monopole – reaches the end being calibrated so that it fires sometimes, while much more light reaches the tank-end close to the LED ensuring that it always fires. The width with which we fire the LEDs simulates the time the monopole spends in the tank. A characteristic LED induced pulse is shown in the waveforms of Fig. 3.10.

Since there were two programmable pulse generators with two independent analog outputs, we were able to individually drive four LEDs and thus to calibrate four tank-ends simultaneously. The information on the output pulse parameters (amplitude and pulse width), as well as the location of the tank-ends that were calibrated, was written into two output registers. An additional pulse was sent to an ERP channel which would fire and trigger the acquisition even if no SMT was formed. The waveforms of both ends of the tanks being calibrated were stopped and read out. The Slow Monopole Trigger and the output registers were also read out. When the acquisition was done reading an event, the pulser was triggered for a subsequent event.

### 3.4.2 Calibration Analysis and Results

The waveforms read out for each calibration event were analyzed by an algorithm identical to the one used in the main analysis. The performance of the algorithm is discussed in chapter 5. In summary, this algorithm is a software simulation of the Slow Monopole Trigger. The automated procedure scans the waveforms produced, simulates in software the TOHM and LI function of the SMT, counting up and down with the same parameters as the actual counter in the LI digital motherboard, and reports the LIcounts the hardware should have measured. We chose to use this quantity because it is a direct measure of the way the hardware works. It also

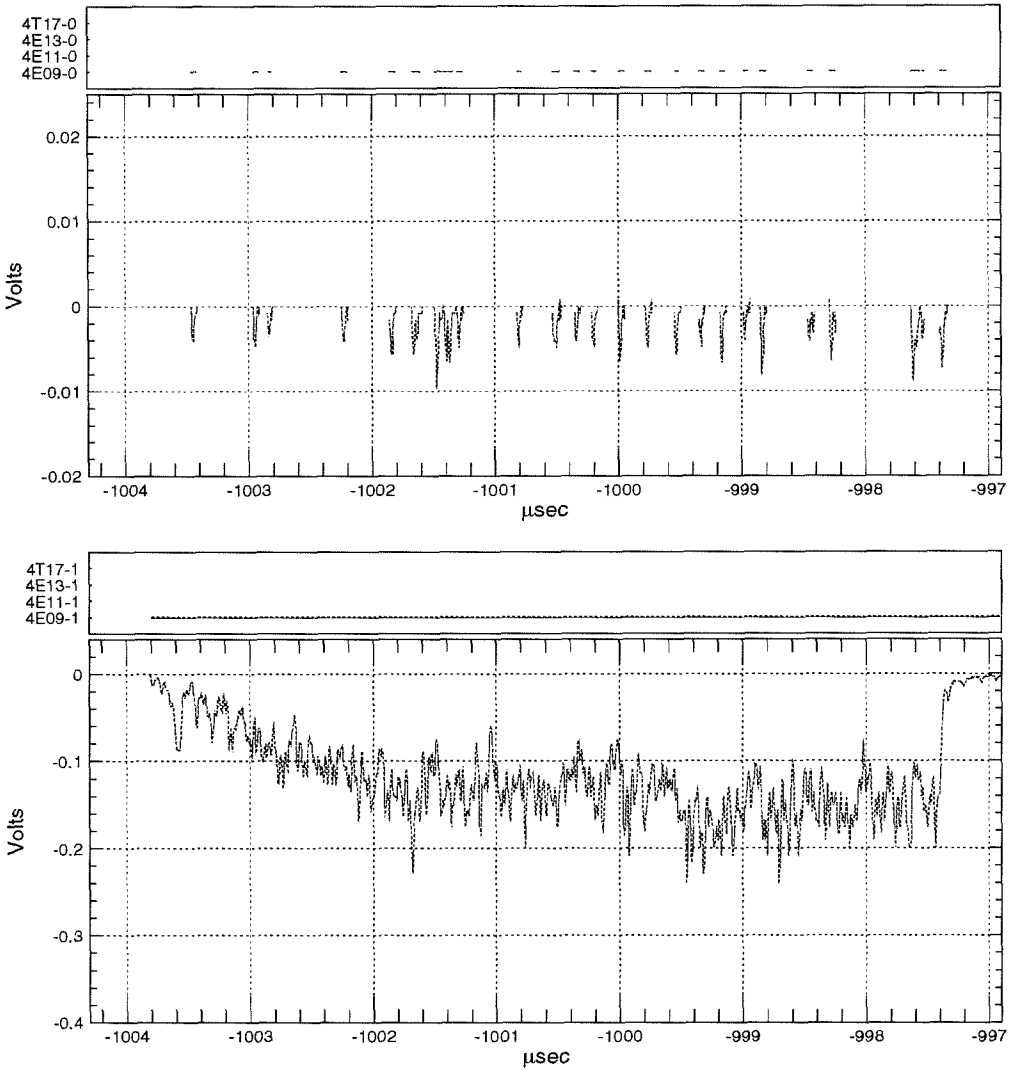


Figure 3.10: LED induced pulse. The plots shown above correspond to four tank-ends: 4E09, 4E11, 4E13 and 4T17. The upper plot corresponds to tank-end 0 (north end), while the bottom, to tank-end 1 (south side). The waveform plots show voltage versus time, where time is measured in $\mu$s before the waveform stop. The dots (forming a line in the lower plot) next to the tank names indicate that the discriminator for that particular tank was over threshold. In this plot we see that only tank 4E09 contributes to the resulting pulse. In this event the LED of tank-end 4E09-1 is fired producing a big pulse in this tank-end; the characteristic rise time of the LED is visible. There are around 30 SPEs produced in the far end as seen in the upper plot. The SMT fired for this event, indicating a trigger at both ends.

combines information for both light yield and pulse duration. Thus, *it is intrinsically independent of the exact pulse duration* (i.e., on the time of passage of the monopole through the tank). Many events were generated in order to calibrate one tank-end. Pulses of various amplitudes and widths were used to fire the LED of each tank-end, creating sets of waveforms of different light yields and durations. Analysis of waveforms was used to construct, for each tank-end, the efficiency curve of the SMT hardware vs. the LIcounts measured in the waveform by the software. The plot in Fig. 3.11 is a characteristic efficiency curve taken when firing the LED at various amplitudes with constant 6.333 $\mu$s width. The curve is fit by a sigmoid. We define the efficiency-turn-on point as the number of LIcounts corresponding to the 90% efficiency point on the curve. This was approximately equal to the triggering parameters imposed on the hardware (11 LIcounts).

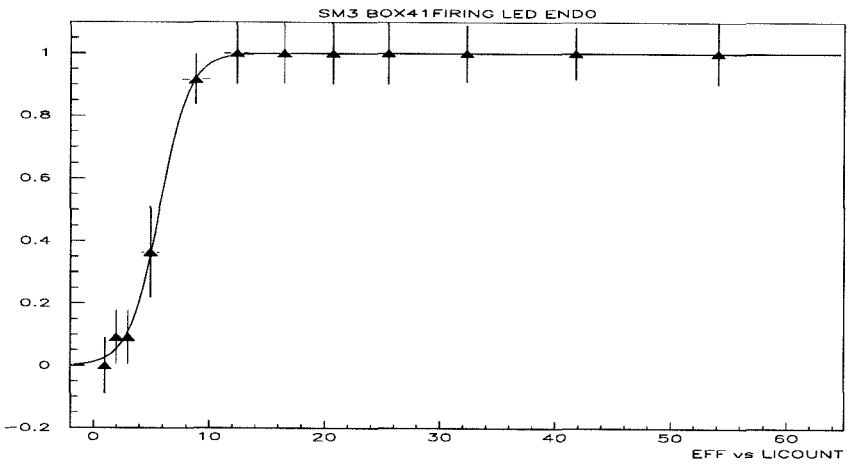


Figure 3.11: Efficiency sigmoid for 3E01-1 constructed from LED events of 6.3 $\mu$s duration. Each triangle on the sigmoid summarizes at least ten data points. The efficiency-turn-on point is where the fit curve reaches 90%, which for this channel is at 9.7 LIcounts.

The distribution of the efficiency-turn-on point for the entire detector, for pulses of 6.3 $\mu$s duration and corresponding to a monopole of $\beta \simeq 10^{-4}$ passing through 19 cm of scintillator, is shown in Fig. 3.12a. This distribution is for the May 2000 calibrations. The false bin at zero LIcounts is assigned to 20 tank-ends, 2 of which were not properly calibrated due to LED hardware problems. The remaining 18 belonged to 10 tanks with one or more tank-ends disconnected from the SMT. At

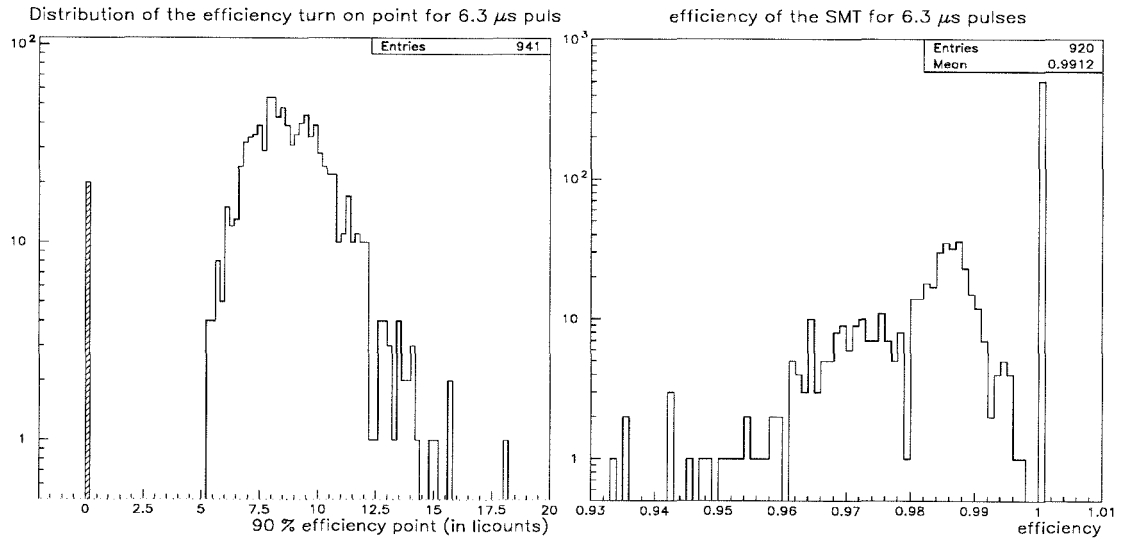


Figure 3.12: (a) Distribution of the efficiency-turn-on point for 941 out of 952 SMT channels in the detector for pulses of 6.3 $\mu$s duration. 11 channels with thresholds >20 LIcounts are not seen. (b)Distribution of the average efficiency above the efficiency-turn-on point for channels with measured thresholds <20 LIcounts. Only the SMT channels with at least 30 points above the efficiency-turn-on point are plotted.

any given time, some malfunctioning channels had an LI threshold greater than 20 LIcounts; such channels represent only 1.3% of the detector. About 95.6% of the detector has an efficiency-turn-on point below 14 LIcounts. For each SMT channel that had efficiency-turn-on point less than 20 LIcounts, we calculate its average efficiency for pulses with LIcounts (i.e., for light yields) greater than its efficiency-turn-on point. For example, for tank-end 3E01-1 of Fig. 3.11, this average effiency is the ratio of pulses that fired the SMT versus the total number of pulses with LIcounts greater than 9.7 (which is the efficiency-turn-on point for this tank-end). The distribution of the average efficiency of the SMT channels is shown in Fig. 3.12. For good statistics, only channels with more than 30 data points above the efficiency-turn-on point have entries in the plot. The mean efficiency of 95.6% of the detector was 99%.

Similar results were obtained with pulses of 1 $\mu$s width (corresponding to $\beta \simeq 6.3 \times 10^{-4}$) and of 0.35 $\mu$s width (corresponding to $\beta \simeq 1.8 \times 10^{-3}$). The

efficiency-turn-on point distribution for pulses of 1 $\mu$s width is in Fig. 3.13. A fraction 95.4% of the SMT channels in the detector had their efficiency-turn-on point below 18 LIcounts. The distribution of the average efficiency of each of the SMT channels above the efficiency-turn-on point is also shown in Fig. 3.13. The mean efficiency of 96.2% of the detector was 99%.

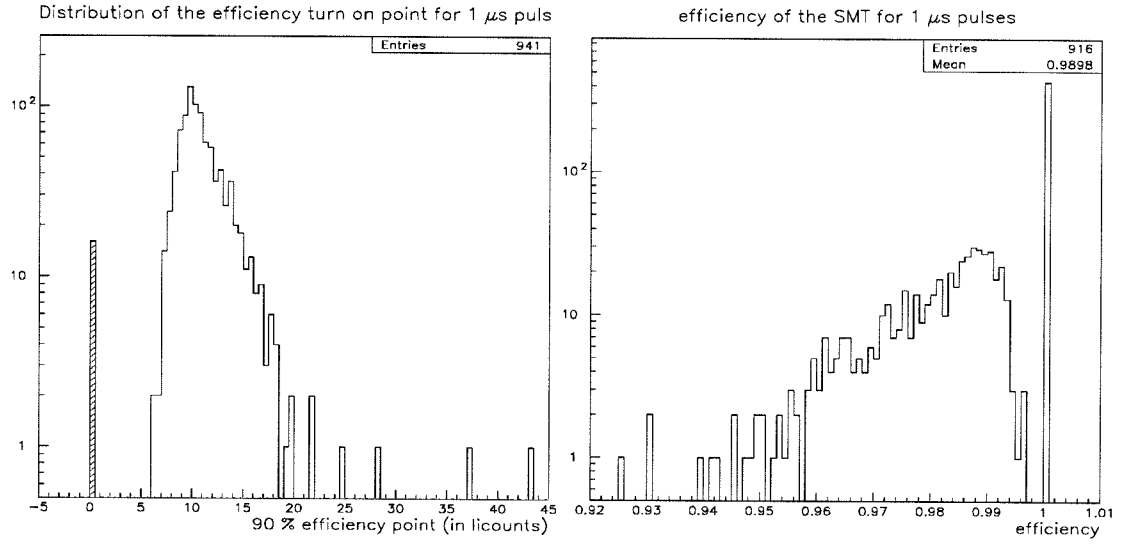


Figure 3.13: (a) Distribution of the efficiency-turn-on point for 941 out of 952 SMT channels in the detector for pulses of 1 $\mu$s duration. 11 channels which had higher thresholds are not plotted here. (b) Efficiency above the efficiency-turn-on point.

The efficiency-turn-on point distribution for pulses of 0.35 $\mu$s width is shown in Fig. 3.14. 95.4% of the SMT channels had their efficiency turn-on point at less than 19 LIcounts. The distribution of the efficiency above the efficiency-turn-on point is shown in Fig. 3.14. The mean efficiency of 95.5% of the detector was at the 99% level.

In addition to the calibrations performed with pulses of 6.333 $\mu$s, 1 $\mu$s, and 0.35 $\mu$s, we performed special calibrations of different pulse width settings with the aim of identifying the narrowest pulses that the SMT fires on (and as consequence, the highest monopole velocity it could detect). The nominal limit of the SMT, according to its design and to the parameters used, was set to 195 ns (corresponding

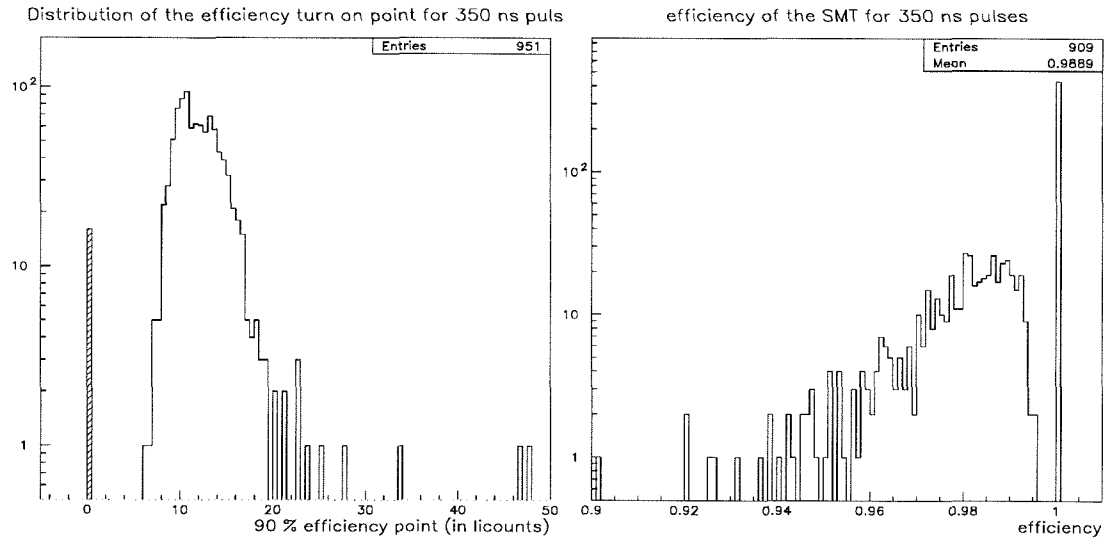


Figure 3.14: (a) Distribution of the efficiency turn on point for 951 out of 952 SMT channels in the detector for pulses of 0.35 $\mu$s duration. (b) Efficiency above the efficiency-turn-on point.

to $\beta \simeq 3.2 \times 10^{-3}$). In reality, as we have mentioned in 3.1, the SMT quite often fired for shorter pulses of high amplitudes, mainly due to the pulse stretching of high amplitude pulses in the TOHM part of the SMT. The output of TOHM for pulses with amplitudes of the order of 1 V and higher did not accurately reflect the Time Over Half Maximum of the pulse, but tended to be wider. PMTs afterpulsing between 5-8 $\mu$s following the pulse could also mimic an SPE pulse train and make the SMT fire. (More details on the subject of PMT afterpulsing are in chapter 5 and in appendix A.) The triggering efficiency of the SMT at pulse widths of 190 ns was tested during laboratory testing with fake pulses. Calibrating, however, the SMT with LED pulses of the same width is hard due to the LED rise time, which resulted in a PMT pulse shape different from that expected for a fast monopole. Nevertheless, in December 2000 we performed a series of calibrations of different LED width settings. In this case, the calibrations were performed in a third of the detector (SM3 and SM4) because the WFDs had already been removed from the other supermodules. In addition, some of the SMT channels had been disconnected (most of them in SM4) during the six intervening months. Thus, width calibrations were performed

on 256 channels. These calibrations were considered representative of the entire detector, as no systematic differences were found between supermodules in previous calibrations. These calibrations involved firing the LED of the opposite tank-end with short pulses of various amplitudes. The waveforms were analyzed in order to measure the time over half maximum of the pulse. In particular, we measured the pulse width between the first and the last occurrence of its half maximum. This way we sometimes overestimated the Time Over Half Maximum of multi-peaked pulses (and thus underestimated the SMT sensitivity). Only pulses corresponding to less than ten times the light yield of a MIP were considered. We constructed, for every tank-end, the efficiency versus pulse width curve, which is again a sigmoid. (An example is shown in Fig. 3.15.)

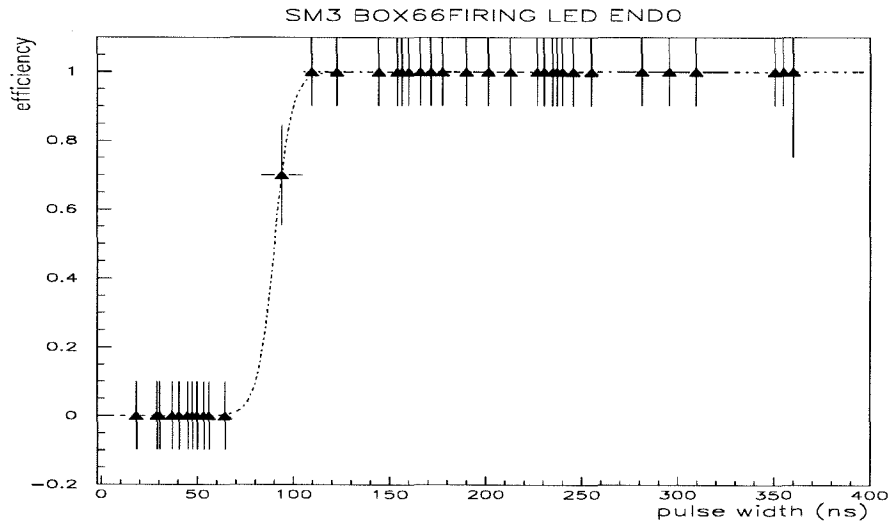


Figure 3.15: Efficiency sigmoid for 3T02-1 constructed from LED events of various duration. Each triangle summarizes at least ten data points. The efficiency-turn-on point for this channel is at 100 ns.

On the curve we define the efficiency-turn-on point as the width corresponding to 90% efficiency. In Fig. 3.16a we plot the distribution of the efficiency-turn-on points for the SMT channels that were calibrated. And in Fig. 3.16b we plot the average efficiency of the SMT channels for pulses with widths above the efficiency-turn-on width. We see that more than 95% of the calibrated channels are 99%

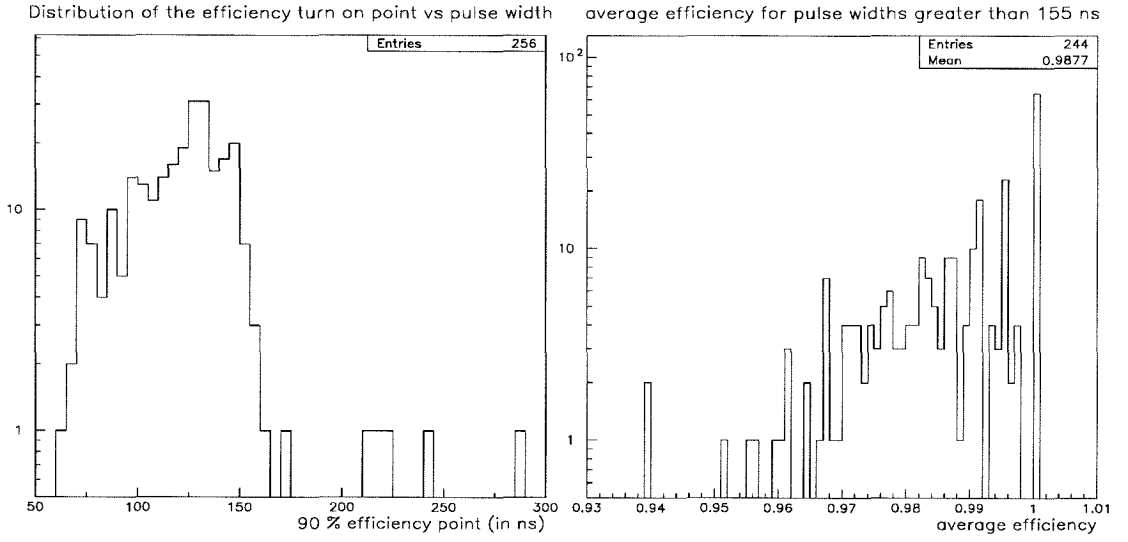


Figure 3.16: (a) Distribution of the efficiency turn on point for 256 SMT calibrated channels in the SM3 and SM4 detector for various widths of LED pulses. (b) Efficiency above the efficiency-turn-on point. All SMT channels had at least 30 points above the efficiency-turn-on point.

efficient for pulses wider than 155 ns. This sets the maximum detectable velocity of $v \simeq 4.1 \times 10^{-3}\, c$ for a monopole crossing a typical 19 cm of scintillator. We have used pulses corresponding to less than ten times the light yield of a MIP; therefore, we can conservatively deduce that this limit is valid for monopole light yields ten times or more the light yield of a MIP. This limit is plotted, on a light yield versus velocity plot, in Fig. 3.17.

In the same Fig. we have also plotted the results of the 6.333 $\mu$s, 1 $\mu$s and 0.35 $\mu$s calibrations, where we have translated the rather technical term LIcounts into the total quantity of light. In chapter 5, we describe how light yield (i.e., SPEs) and number of counted (by the analysis code) SPEs are connected. The result obtained there has been used in order to translate the LIcount measured by the analysis code in the waveforms into the number of SPEs needed to fire the SMT. In Fig. 3.17 the sensitivity curves of the SMT circuit are shown in a plot of light yield vs. $\beta$, where we have normalized to the light yield of a MIP. In order to be conservative, we used the light yield from a MIP hitting the far end of a counter, which is $7.3 \times 10^2$ SPEs

for a horizontal tank and $3.8 \times 10^2$ SPEs for a vertical tank [76]. The circles and the squares are the experimental points derived from the calibrations for the vertical and horizontal counters, respectively. The line connecting the experimental points is a guide to the eye. For comparison, the light yield for bare monopoles with single Dirac charge is also shown [56]. About 95% of the SMT channels in the detector are at the 99% sensitivity level to monopoles with velocities down to $10^{-4}\,c$. The sensitivity curves derived from the LED calibrations will be used in calculating the upper limit to the monopole flux from this analysis.

As mentioned before, these calibrations were taken at the end of the data taking period and demonstrate that the triggering system performed well, right up to the end of the five-year run.

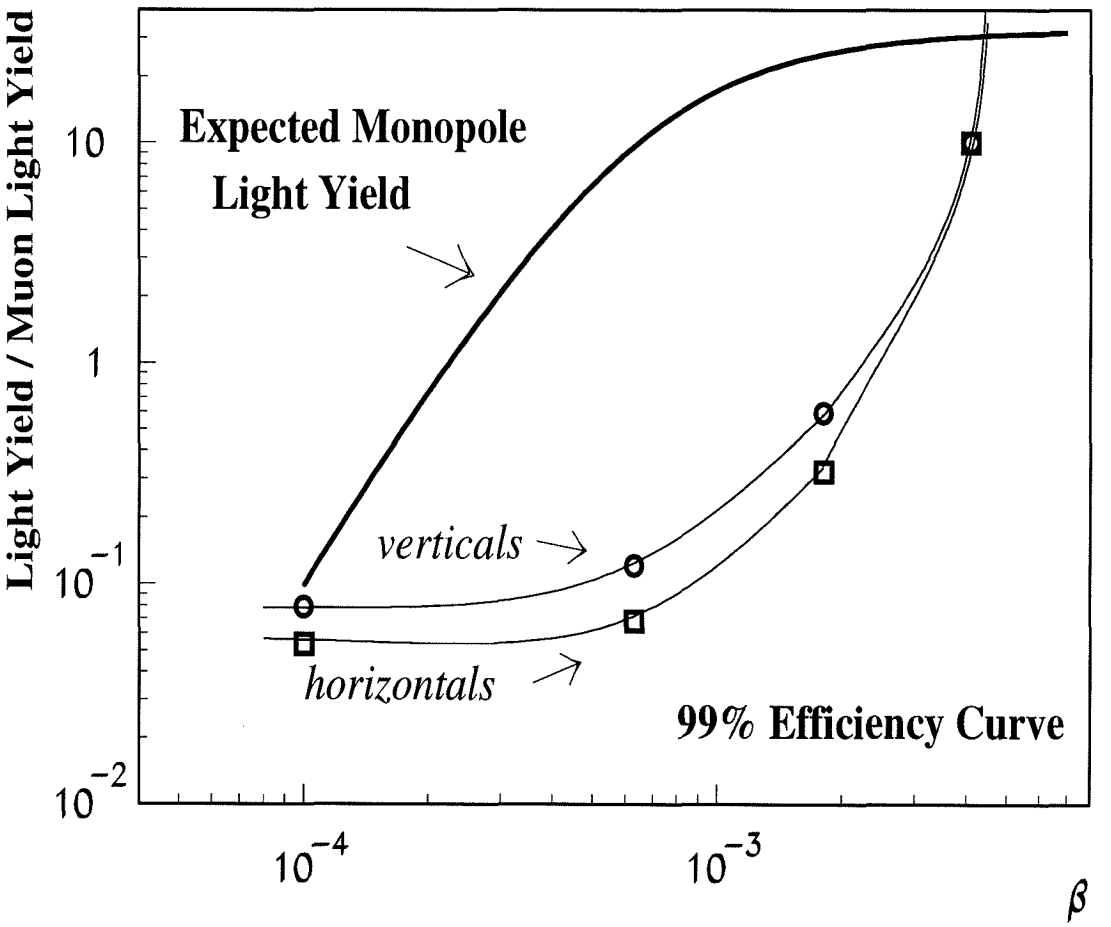


Figure 3.17: Sensitivity curves of the SMT circuit. The plots show the required light yield for the SMT circuit to fire as a function of velocity (normalized to the light yield of a Minimum Ionizing Particle). The probability of a particle with light yield above the sensitivity curves to fire the SMT is 99%. For comparison, the expected light yield of a monopole [56] is also plotted. The circles and the squares are the experimental points; the line is a guide to the eye.

# Chapter 4

# Slow Monopole Analysis

## 4.1 Data Set: Monopole Data Summary Tapes

In the previous chapter we described the Slow Monopole Trigger (again SMT) and the calibrations done to assess its sensitivity to slow monopoles. This search for slow ($10^{-4} \lesssim \beta \lesssim 4.1 \times 10^{-3}$) monopoles uses the SMT system for initial event selection. Final verification of whether a trigger was indeed due to the passage of a slow monopole through the scintillator relies primarily on the WFD system.

The data-taking period for this search began in July 1995, when both the SMT and the WFD systems were implemented, but ran only in the lower part of the detector. The SMT hardware for the Attico was completed later by December 1995. The WFD system itself underwent a major retrofit in June 1997. To make better use of MACRO's redundancy and complementarity, not only the WFDs, but also the streamer tube system, was stopped and recorded for every scintillator SMT event. The end of the data-taking period was in May 2000 and was due to the decommissioning of the WFDs.

During the 4.75 yr of data-taking, more than 2 terabytes of data were accumulated, comprising mostly of digitized waveforms. To overcome this huge data volume, Data Summary Tapes (DSTs) were produced, which selected all the events that had SMT triggers present in more than one face of the detector. Only these events were analyzed for this study.

In order to clarify the use of the term "face," we mention that the detector was considered to be a closed rectangular box with six faces and an additional horizontal "face" in the center (or the central scintillator layer). An event is referred to as a two-face monopole event if the SMT fired in two or more faces. For such an event the

entire event record was saved on the DST. The two face requirement was a compromise between, on the one hand, the need to manage the overwhelming data volume and to be able to identify with greater certainty the passage of a slow monopole, and, on the other hand, the desire to maximize the detector acceptance. As was shown in the previous chapter, no major loss in detection efficiency is introduced by this requirement. The only actual loss is in geometric acceptance. For monitoring and acceptance studies, the full data set is used.

## 4.2 Initial RUN Selection

This analysis starts with RUN 10557 taken on the $24^{th}$ of July, 1995, and ends with RUN 19499 on the $4^{th}$ of May, 2000. During this period there were a total of 8782 runs, out of which 7712 had the following characteristics: (i.) they had at least one supermodule of SMTs and WFDs in acquisition, (ii.) had durations of more than five minutes and, (iii.) were non calibration runs. From these, 7161 had all three microVAXes in acquisition, 481 had two out of three microVAXes in acquisition, and 71 had just one microVAX in acquisition. The total livetime for this selection is about 1582 d.

In Fig. 4.1 we plot the duration of the runs. In the plot we did not include four runs with duration longer than 800 min. The runs usually lasted until the output data file reached a certain size. The data file was mostly comprised of WFD data. Its size was chosen such that the run duration was around six hours. Fig. 4.1 shows that the duration distribution peaks around 300 to 350 minutes. This is because the typical run duration diminished over the years from around 380 minutes to 290 minutes due to increasing SMT rate (which resulted from aging of the photomultiplier tubes, their contamination with He, and slight aging of the SMT). Runs with longer durations happened when the detector ran with a subset of the equipment normally in acquisition. Short runs were either due to some problem which forced a crash or were manually halted before normal completion; these were runs with some fraction of the equipment firing often enough to produce a very high data rate, or runs

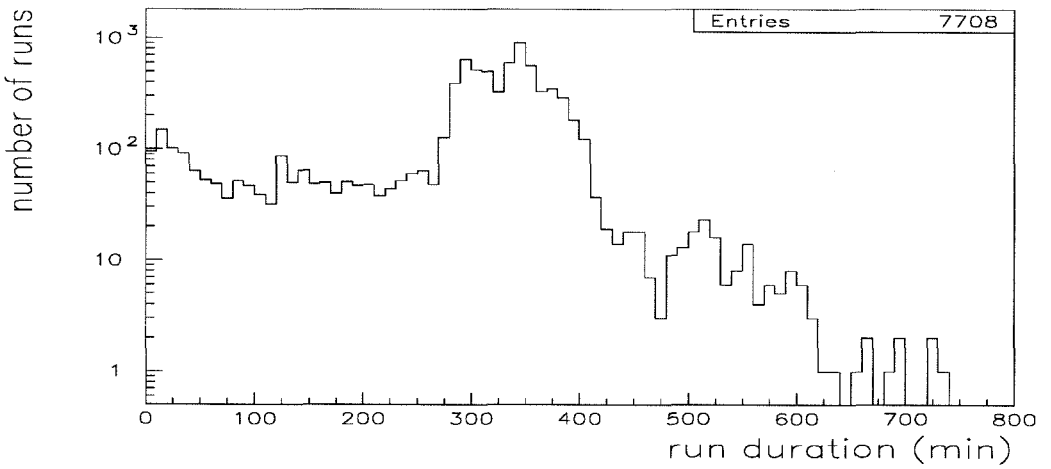


Figure 4.1: Actual durations of runs in the data set.

during maintenance days. It was difficult to monitor the reasonable performance of the detector for very short runs due to inadequate statistics. We rejected runs that lasted less than 20 minutes. This cut rejects 244 runs with 2 days worth of data (or 0.13% of the data set).

In order to study the behavior of the SMT over the years, we plot the SMT rate in Fig. 4.2 (number of SMT triggers divided by the normalized run duration in minutes). By "normalized" run duration we mean the average livetime of the six supermodules of the detector. For better illustration, we excluded roughly 50 runs with abnormally high SMT rates from the plot. In the figure, the increase of the SMT rate with time is obvious. However, we do not make any data selection cuts based on the SMT trigger rates, because the acquisition performed well at all trigger rates.

## 4.3 Analysis Path

During the entire data-taking period there were around 28 million Slow Monopole Triggers. Of course, there were not this many monopoles. Electronic noise, radioactivity pile-ups and some percentage of muons account for the largest fraction of

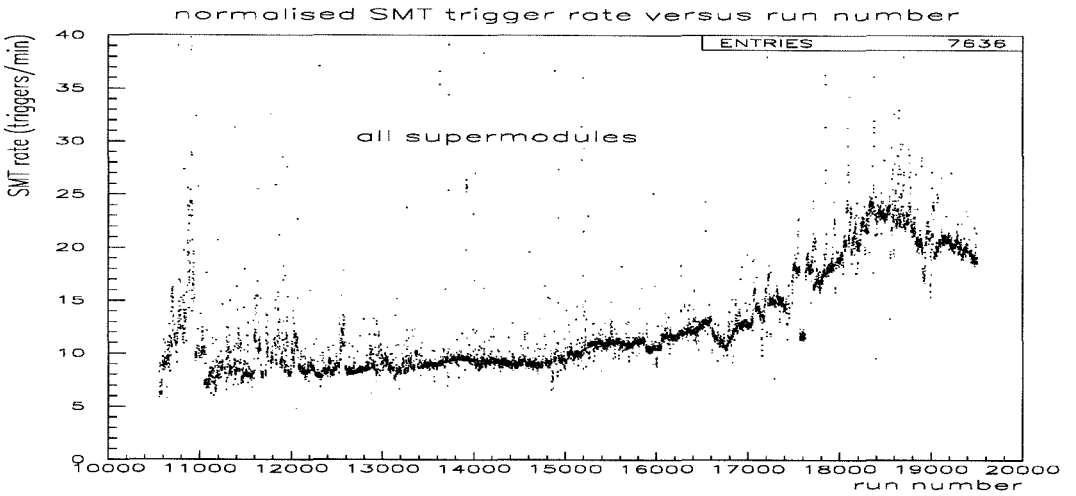


Figure 4.2: SMT normalized trigger rate plotted versus run number.

triggers. Radioactivity pile-ups usually cause an SMT trigger in a single scintillator box, muons might fire two or more boxes along their path, and noise, depending on its character, may fire entire faces. In order to filter the large dataset, such physical considerations were used to reject most of the background. Five primary filters were developed, which reduced the eventual number of candidates to 40. The first four filters of the analysis arise naturally and are explained below. The fifth filter – the monopole pulse pattern recognition technique – is explained below but will be extensively described and tested in chapter 5. The secondary set of filters will be elaborated upon in subsequent chapters.

In order for an event to be considered as a monopole candidate, the following five criteria were required:

1. **The event should have had a Slow Monopole Trigger in at least two faces of the detector.**

   The two-face requirement reduces the dataset to around 4 million triggers. The kinetic energy of GUT monopoles is orders of magnitude larger than its anticipated ionization losses in MACRO; the monopole is expected to cross the detector without stopping. If MACRO were a closed box, monopoles would be

expected to cross at least two scintillator faces. However, the faces were not fully populated with instrumentation, and there were trajectories that could strike just one face and exit through a dead zone. Thus, events with a single-face SMT could be due to monopoles. However, such a monopole crossing would be unconvincing, because consistency of metrics like the time-of-flight between faces, and the time spent within the scintillator counters are key pieces of evidence that the waveforms were not spurious noise. Filtering out single face SMT events in the analysis is in accordance with the strict requirement of redundancy in order to unmistakably identify a rare event. On two-face monopoles one obtains three estimates of the velocity, which should all be consistent: time spent within the first scintillator counter, time of flight (TOF) between the two scintillator counters and time spent within the second scintillator counter.

The two-face requirement results in approximately a 17% loss in acceptance to an isotropic flux (as determined with Monte Carlos). On the other hand, this requirement dramatically eliminates radioactivity pile-up events, some noise events and some muons that fire the SMT, which is a small price to pay.

2. **The event should have SMT triggers in two faces within 1 ms.**

   A monopole of $\beta \simeq 10^{-4}$ requires 1 ms to cross $\simeq$ 30 m. This requirement guarantees that the monopole signature is present in the waveform digitizers in two faces of the detector. The hardware component used to enforce this requirement was the WFD Stop Master (see section 3.3). As mentioned earlier, the WFD Stop Master recorded the time of arrival of the SMT triggers from separate faces of the supermodule relative to the earliest such trigger. For an event to be a valid two-face trigger, the time of arrival of the SMT has to have a valid (not overflow) value for at least two faces. We recall that this overflow value corresponds to 1 ms from the arrival of the first SMT trigger. The events rejected by this requirement are accidental coincidences of radioactivity pile-ups or noise that falls within the time window of the acquisition's computer BUSY signal. This happened because the SMTs were alive and collecting triggers

even during the computer BUSY, which was when the acquisition system was reading out events. The same is not true for the Stop Master, as we have explained in section 3.3. The readout time was typically 100 ms per event. With approximately $3 \times 10^3$ SMT triggers during a typical five-hour run dead time, we expect around 50 such events. These events will correctly be rejected by this cut. These events constitute about 10% of the 500 two-face monopole triggers we have typically in any run. This cut introduces a decrease of $\sim 4\%$ in the actual exposure due to occasional malfunction of channels of the Stop Master and due to the rejection of very slanted tracks (tracks that crossed two faces of non-adjacent supermodules). It is, however, a necessary requirement in order to have valid waveforms in at least two faces.

3. **The event should not have a scintillator fast trigger.**

   After we apply the above two filters, the remaining 98% of events appear to be induced by fast muons due to pulse stretching in the TOHM circuitry or afterpulsing in the PMTs. Fast muons fired the SPAM_MUON trigger, which is a two-face coincidence trigger within 1 $\mu$s (see section 2.3.1). Most slow monopoles were not expected to fire this trigger, so events with SPAM_MUON trigger are rejected. A monopole of $\beta \simeq 3.4 \times 10^{-3}$, during the 1 $\mu$s time window, will barely traverse one meter. The SPAM_MUON veto reduces the acceptance by $\sim$5% for this monopole velocity (according to Monte Carlo simulations), but the loss rapidly decreases with a decrease in the monopole velocity. For $\beta \simeq 10^{-3}$ the loss is only 0.01%. On the other hand, this cut efficiently cleans the data of fast particles which fired the SMT. However, SPAM_MUON inefficiencies allowed for some fast events to leak into the final data set. Moreover, the 17th tank in MACRO's Attico (TOP) horizontal tanks in each supermodule was not connected to the SPAM_MUON trigger. Thus, fast events which involved that tank may have not been rejected.

   The SPAM_MUON's sister circuit, the SPAM_FMT, did not veto any events, because it should fire on some monopoles in the velocity range that the SMT

overlaps with. The SPAM_FMT was a two-face, 10 $\mu$s coincidence trigger and was sensitive to monopoles down to $\beta = 10^{-3}$. However, even a monopole as slow as $7 \times 10^{-4}c$ may have fired that trigger if its total pathlength between two faces of the detector was less than 2 m. Since the velocity region that SPAM_FMT was sensitive to partially overlaps with that of the SMT, events detected with SPAM_FMT were not rejected. In principle, the SPAM_FMT was vetoed in the hardware by the SPAM_MUON trigger. However, sometimes both occurred during the same event suggesting possible malfunction. In order to be sure that no potential monopole candidates were rejected, the SPAM_MUON software filter was not applied when a SPAM_FMT trigger was present.

The application of the SPAM_MUON filter, as described above, reduces the dataset to 42055 events. Among these, 41644 events do not have an accompanying SPAM_FMT trigger and their distribution in the runs is shown in Fig. 4.3. There are various peaks in the distribution that attract attention:

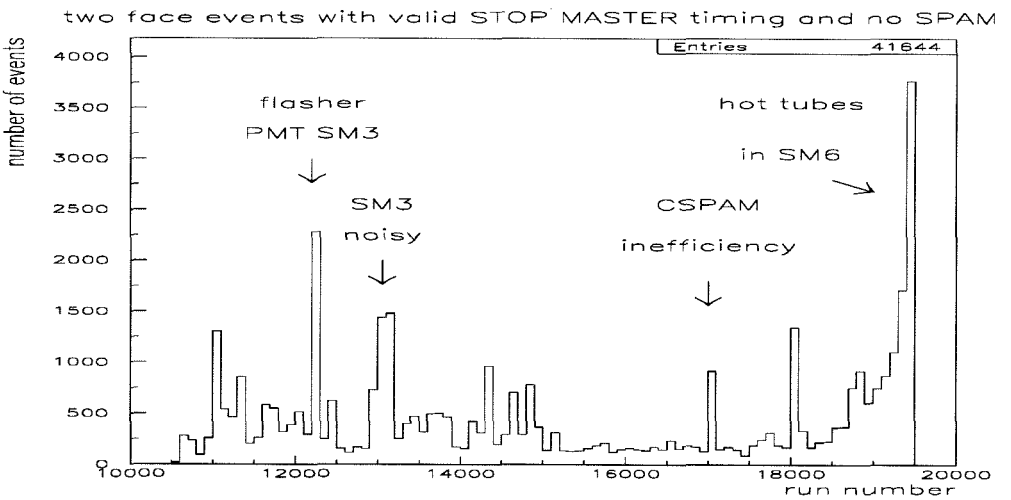


Figure 4.3: Distribution of the two face events with valid Stop Master timing and no SPAM_MUON or SPAM_FMT. We mark the sources of some prominent peaks.

- RUNS 12205 to 12264 contribute 2179 events due to a spuriously firing PMT (3E14) and two SMT channels with an abnormally high triggering

rate that corresponded to counters 3W08 and 3W09.

- RUNS 13020 to 13180 contribute 2734 events due to hardware problems in SM3.
- RUNS 14606 to 14617 contain 520 events from which more than 400 have all the 31 tanks in the Attico in SM6 firing. This problem was associated with two new SMT modules in the Attico.
- RUNS 14873 to 14875 contribute more than 600 events, mainly muons, due to SPAM_MUON problems in SM5 and SM6.
- RUNS 17007 to 17015 contribute 799 events due to SPAM_MUON inefficiency.
- RUNS 18087 to 18097 contribute 1032 events due to frequent firing SMT channels in SM3 (mainly 3T17 and 3E13).
- RUN 19399 contributing 774 events due to hardware problems in SM6.
- RUNS 19410 to 19414 which contribute 3031 events due to the SMT channels corresponding to tanks 6B03, 6B12 and 6C11.

These abnormal peaks were listed for reasons of understanding only. No quality cuts on these runs were performed and every trigger was analyzed.

The remaining 411 events have a SPAM_FMT trigger, and their distribution in the runs is plotted in Fig. 4.4. The peak during runs 11642-11693 was due to hardware problems in the SPAM_FMT module servicing supermodules 5 and 6 and does not affect our analysis. From the analysis, we excluded three runs (12015, 12016, 12017) where the SPAM_MUON trigger did not veto the SPAM_FMT, which resulted in all muons having SPAM_FMT triggers. We have also excluded the short run 16971, which was infected by many LED hits from calibrations that were being performed in the rest of the detector. The resulting effect on the acceptance, by the exclusion of these four runs, is negligible.

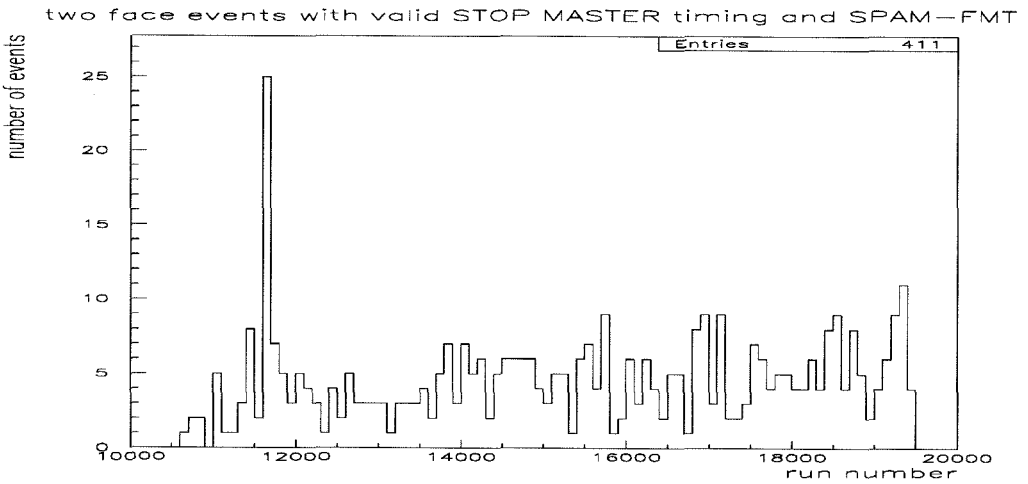


Figure 4.4: Distribution of the two face events with valid Stop Master timing and SPAM_FMT.

4. **The event should have an SMT trigger in at most four detector faces and in at most three tanks in each face.**

   Monopoles, in the examined velocity range, are not expected to shower; therefore, they are expected to hit at most two external faces plus the central face. In this analysis we allow four faces to have an SMT trigger, in case of an accidental coincidence with a noisy tank, or radioactivity. Most tracks that cross at least two faces in the detector pass through one or two tanks in each face. We allow three tanks per face to fire the SMT. The loss in acceptance due to this cut is $\simeq$1% (very slanted tracks). This primarily eliminates electronic noise events, which tend to fire the SMT in many detector faces and in many tanks in each face. Many of these events involve bipolar noise like the one seen in Fig. 4.5, which is obviously unphysical because properly operated PMTs cannot produce positive voltages.

   When applied to the sample of events that have SPAM_FMT triggers, this cut primarily eliminates muon events that induced electromagnetic showers in the detector.

   We have to be careful, while making this cut, so as not to reject monopoles that might cause crosstalk in the SMT electronics. LED calibrations in SM3 and

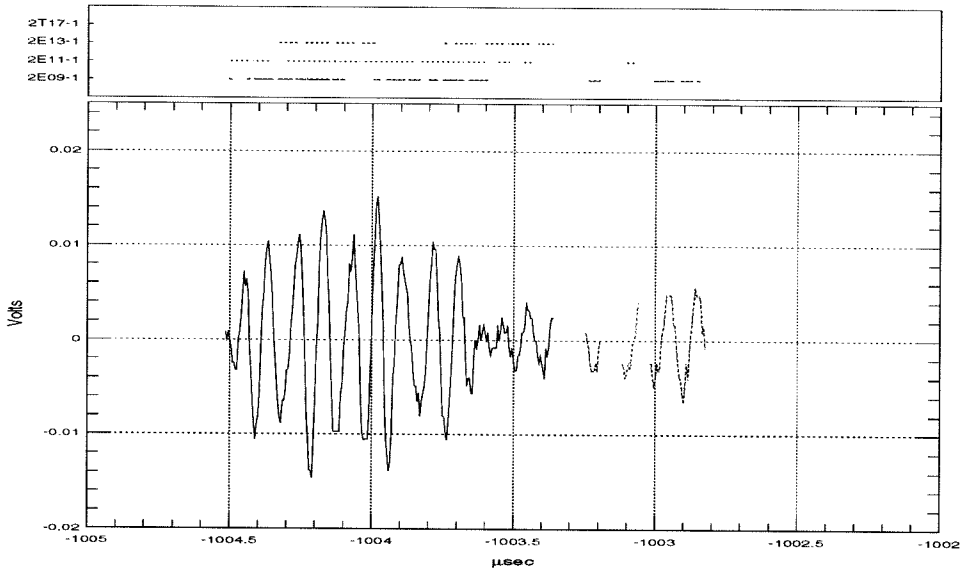


Figure 4.5: Bipolar noise in the scintillator electronics as seen by the WFDs.

SM4 investigating the presence of crosstalk in the hardware found no evidence of crosstalk. Nonetheless, in order to be conservative we designed the cut so that it is not susceptible to crosstalk. We count SMT channels that share TOHM hardware as just a single tank, even if two or more triggered. That means that the four SMT channels in each TOHM module for the lower part of MACRO count as one, as do the two SMT channels in the same TOHM daughter-card for the Attico part of MACRO. This way some bipolar noise might leak though the cut, but we are sure not to reject monopoles. The above requirement rejects 6154 events. The 35901 surviving events are divided into 35658 events without a fast monopole trigger and 243 events with a SPAM_FMT. We see their distribution in Figs. 4.6 and 4.7.

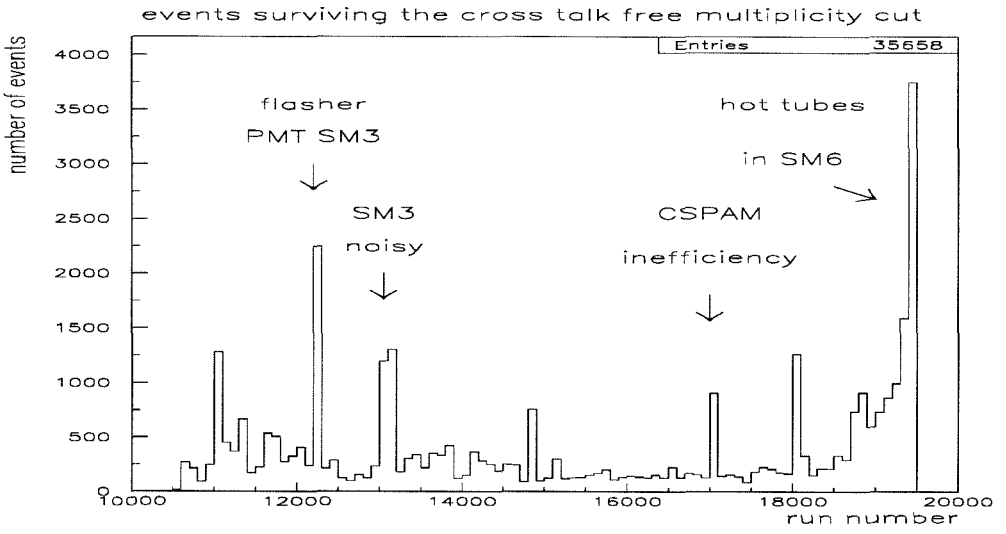


Figure 4.6: Two-face events with valid Stop Master timing, no SPAM_MUON or SPAM_FMT, which pass the Slow Monopole Trigger multiplicity criterion.

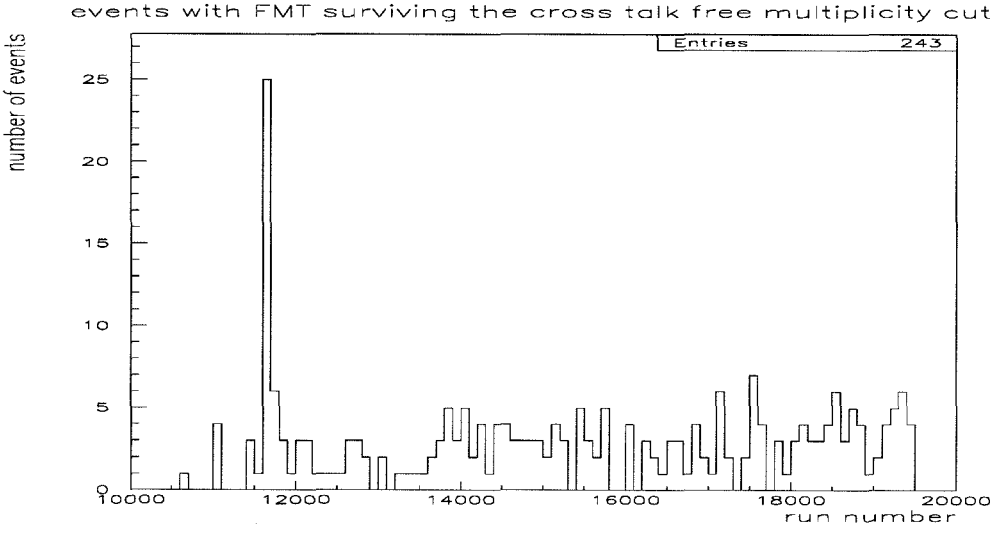


Figure 4.7: Two-face events with valid Stop Master timing and with SPAM_FMT which pass the Slow Monopole Trigger multiplicity criterion.

5. **The characteristic pulse of a monopole crossing should be present in at least two faces in the detector and should be recognized by a specifically developed automated pattern recognition (PR) algorithm.**

Since only monopoles that traversed two or more faces of the scintillator detector were considered, we have at least four waveforms (one for each tank-end) containing the monopole signature. An automated procedure was implemented in order to analyze these waveforms and to decide if they contained anything of interest. The development of the PR algorithm followed the philosophy of the hardware design. Since waveform analysis is at the heart of this search, this algorithm and the way we measure its sensitivity to monopole-like pulses is described in considerable detail in chapter 5. The sensitivity measurements, as we will see in that chapter, showed that the efficiency of the PR algorithm was better than the currently measured efficiency of the SMT hardware. Therefore, the sensitivity of the analysis to monopoles is dominated by the efficiency of the hardware. And since in the hardware we required two faces of the detector to identify a monopole, without additional penalties to our efficiency we require that there are tanks in at least two faces in the detector that pass this WFD analysis. There were only 40 events that have tanks that satisfy the algorithm requirements for both tank-ends, in at least two faces, demonstrating the large power of rejection of the algorithm. In Fig. 4.8 we see the distribution of theses events in the runs.

This step of the analysis was affected by a hardware problem in the WFDs, that lasted from the beginning of the data-taking period in July 1995 to June 1997. This was the problem of the positive overshoot in the WFDs that dominated the WFD system and would render the WFD information useless for this analysis. The positive overshoot following large-amplitude wide pulses would pass the WFD discriminator inducing continuous digitizing of the data, filling the WFD memory buffer beyond its depth, and resulting in the loss of the

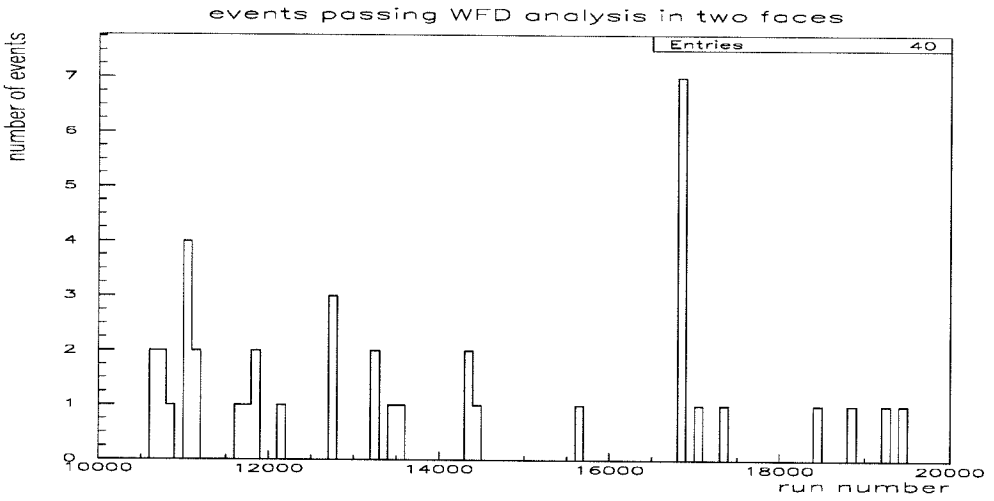


Figure 4.8: Events that pass the WFD analysis requirements in tanks in at least two faces in the detector.

initiating pulse. The problem was fixed in June 1997. This problem was affecting our sensitivity to monopoles in the fastest subset of the velocity regime considered here; fast monopoles are expected to have higher light yields which result in stronger overshoots. This was all mentioned earlier in section 3.2 and it will be extensively discussed with other characteristics of the WFD system in chapter 7. It is noteworthy that studies showed that the overshoot problem obscured detection capability for monopoles with $\beta \gtrsim 4-7\times10^{-4}$; therefore, in order to avoid losses in that range, all waveforms which suffer from data-filled WFD buffers before June 1997 are categorized as valid monopole waveforms.

After June 1997, the WFD system sporadically had memory-filling events, but these were due to the zero suppression circuitry being switched-off for unknown reasons, acquisition glitches or persistent bipolar noise, but not the positive overshoot problem. For data after June 1997, we identified the troublesome WFD channels with hardware problems, and excluded them from the acceptance.

There were 40 events that passed all of the above requirements, seven of which

are accompanied by a SPAM_FMT trigger. These 40 surviving candidates will be analyzed further in chapter 6.

Considerations about the good operation of the hardware used to perform the steps of this analysis will be presented in chapter 7. In the next chapter we describe, in some detail, the pattern recognition algorithm that performs the waveform analysis and its sensitivity to slow monopoles. We have already demonstrated the sensitivity of the SMT hardware to these slow magnetic monopoles in chapter 3.

# Chapter 5

# The WFD Analysis Algorithm

On the basis of hardware triggers only, the first four analysis cuts reduced the number of candidates to ~36000. That, however, is still too much data to scan by eye. An automated way was developed in order to assist identification of monopole waveforms in a fast and efficient way, while effectively suppressing the background coming from isolated radioactivity, incident muons and electronic noise. This pattern recognition (PR) algorithm has the additional attractive feature that – in contrast with the decision making process of a "trained physicist" – its efficiency can be measured.

## 5.1 A Description of the Algorithm

### 5.1.1 General Description

The expected characteristics of a slow monopole, when passing through a scintillator tank, have been described in previous chapters of this manuscript. The hardware trigger was designed to efficiently identify this signature, and the software followed the same philosophy. We recall that a monopole of $\beta \sim 10^{-4}$ has small light yield and produces a train of single photoelectron (SPE) pulses. A faster monopole has higher light yield and creates enough photoelectrons to form a continuous pulse with a width approximately equal to the time of passage of the monopole through the tank. A monopole of $\beta \simeq 3 \times 10^{-3}$ is expected to pass through the 19-cm short axis of a horizontal tank in ≃210 ns, creating a continuous PMT pulse roughly 210 ns wide. The production of light in the scintillator is expected to be of constant rate (subject to photon statistics) and the pulse is expected to be rectangular in shape, with a time over half maximum approximately equal to the time of passage through the tank (see Fig. 5.1).

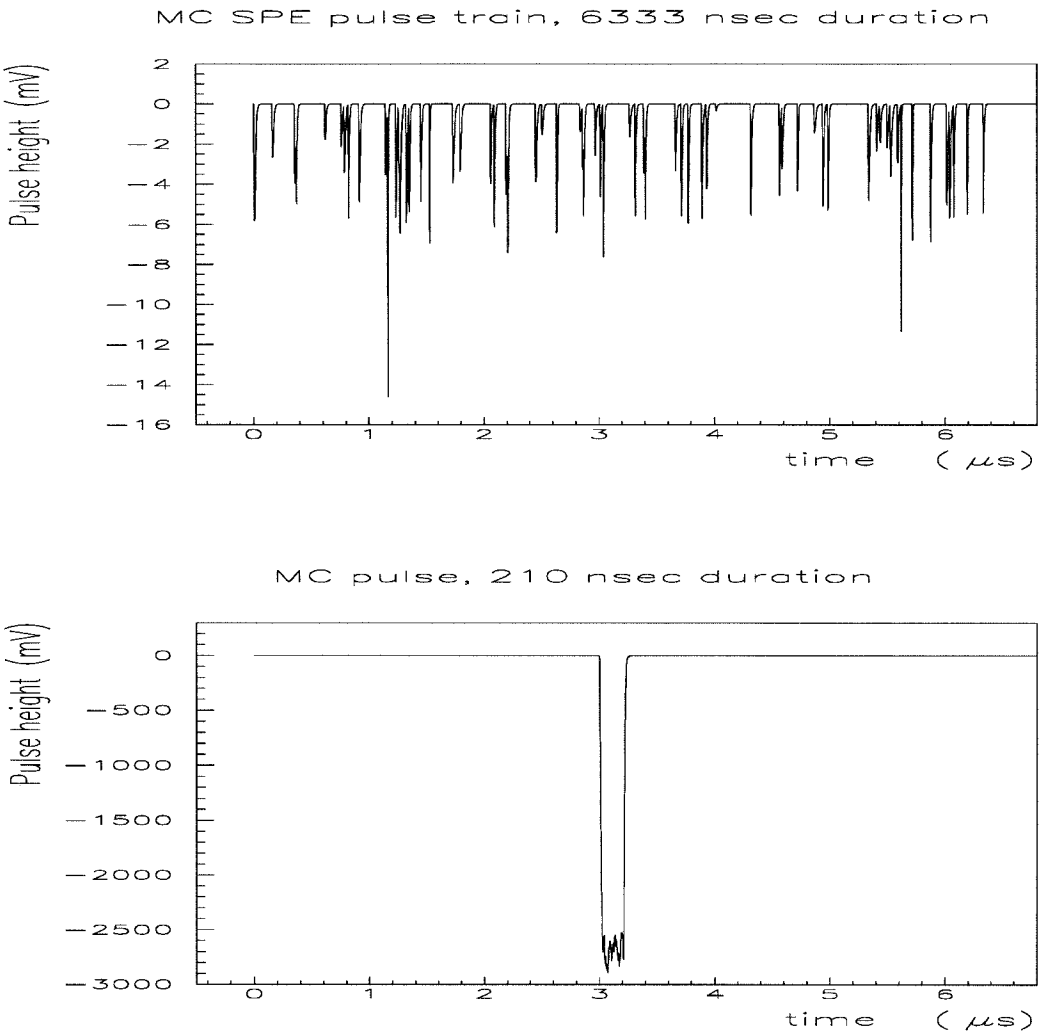


Figure 5.1: A Monte Carlo generated pulse of 6.3 $\mu$s duration of around 63 SPEs (top), corresponding to $\beta \simeq 10^{-4}$ assuming the monopole crosses typically 19 cm of scintillator. A Monte Carlo generated pulse of 210 ns duration and with 11200 SPEs corresponding to $\beta \simeq 3 \times 10^{-3}$ (bottom).

The analysis algorithm simulates the hardware and, in particular, the functionality of the SMT's analog front-end (TOHM) and digital up-down counter (LI). In addition, it specifically looks for pulses larger than 100 mV and wider than 150 ns. The input to the PR algorithm is the waveform as recorded by the 200 MHz WFD system.

The waveform is decompressed and translated from ADC counts to volts in accordance with an empirical fit determined by the specifications of the WFDs. The ADC

pedestal for this conversion is nominally 26.5 counts. Fluctuations from the nominal value would reduce our ability to identify SPEs. For that reason, in the actual analysis we perform an event-by-event pedestal calculation. The effect of possible inaccuracies in the pedestal will be examined in some detail below. The stability of the pedestal is examined in section 7.3.1. The decompressed pulse in the form of a *Voltage Array* $V(t)$, where $t$ is time, is fed (in software) to the monopole pulse pattern recognition algorithm. In Fig. 5.2a we show a segment of an example Voltage Array input to the PR algorithm. The algorithm searches for local maxima. For

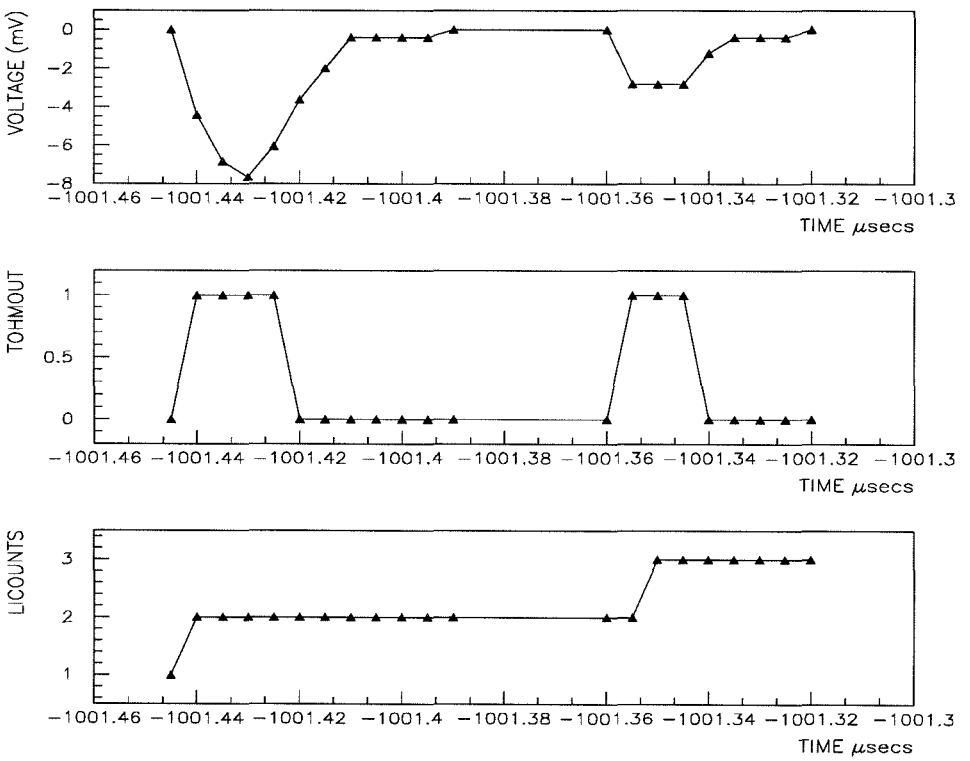


Figure 5.2: a) Part of LED generated pulse, as recorded by the WFD and decompressed into voltage versus time. Time is in $\mu$s before the WFD Stop. This is the input to the SMT simulator. b) Output of the TOHM simulator for the above input. c) Output of the LI simulator for the above input.

every local maximum found, it computes the value of the half-maximum. It sets a flag for every bin for which the voltage is above the current half-maximum. In this manner it creates an output array, which contains logical-ones for all points above

half maximum and zero elsewhere, analogous to the output of the hardware TOHM. As in the hardware, in order to limit the background, we discriminate against pulses less than 2 mV high. A segment of the output array, called TOHMOUT(t), can be seen in Fig. 5.2b. This pulse is then fed to the LI simulator. The LI simulator counts up when the input is high and counts down at a lower frequency at all times. It is clocked with the same period as the LI in the hardware: 15 ns for the up-counter, 660 and 1500 ns for the down-counter for horizontal and vertical tanks respectively. As in the hardware, we call the contents of the counter *LIcounts*. If the counter reaches a threshold – 11 LIcounts for horizontal tanks, 10 for verticals, as in the hardware – a *trigger flag* is set that alerts us to the fact that the waveform contains a pulse resembling a monopole pulse. The output of the LI simulator can be seen in Fig. 5.2c. For every waveform analyzed, the value of the trigger flag is saved, along with the time at which the LI simulator reached trigger threshold, the maximum LIcount reached, and the time at which the maximum was reached.

A slow monopole pulse would be identified by the algorithm for the same reason that it would be identified by the hardware: a train of SPEs would produce, in the TOHMOUT array, a train of software logical-one pulses as wide as the input pulses at their half maximum. The LI will count this pulse train and it will count up (if enough SPEs were produced) to trigger level. In case of higher light output and a continuous PMT pulse, the TOHMOUT will be a software logical-one pulse approximately as wide as the original pulse. If the pulse is wide enough, the LI simulator will count up to its trigger level. To avoid double counting SPEs that might have TOHMOUT greater than 15 ns, every TOHMOUT pulse between 15 to 30 ns wide is counted by the LI as a single count only. Pulses between 30 and 45 ns may give one or two counts (depending on where the clock falls), while pulses above 45 ns will give at least 2 counts, and so on. If $T_p$ is the pulse width, $T_{up}$ the up counter period and $T_d$ the down counter period, then the narrowest square pulse that should trigger this software counter is given by

$$\frac{T_p}{T_{up}} - Down\,counts - 1 \geq Trigger\,Threshold, \tag{5.1}$$

where the $-1$ is due to the fact that the first two up-counter periods generate only one count. For the parameters of the horizontal counters, the narrowest pulse that necessarily triggers this part of the algorithm is 195 ns. This corresponds to a monopole of $\beta \simeq 3.2 \times 10^{-3}$ passing through 19 cm of scintillator. In addition to the counter, the algorithm specifically checks the width over half maximum of the three largest pulses in the waveform. If any of these pulses is larger than 100 mV and wider than 150 ns, the algorithm triggers. This sets the velocity of the "fastest" monopole we might detect, passing through 19 cm of scintillator, to $4.2 \times 10^{-3}$ c. Obviously, there is no limit to the "longest" pulse the algorithm could identify as a monopole pulse, as long as there are enough SPEs in the pulse to overcome the LI down counting.

### 5.1.2 Pulse Tail Fitting

Pulses produced by radioactivity or fast particles crossing the detector tend to have a tail which, combined with ADC fluctuations, may result in lower-amplitude local maxima on the pulse tail, thereby fooling the algorithm (see Fig. 5.3). The presence of the lower maxima on the tail would lead to a "false" overestimate of the time of half maximum of the pulse, compromising the PR algorithm's ability to filter out radioactivity and muon hits. In order to avoid this, we fit the tail of every pulse of 100 mV amplitude or higher to a triangle-like shape whose dimensions were determined by precise amplitude of the pulse. The formula was extracted empirically from studying and fitting of many muon and radioactivity pulses. For purposes of the TOHMOUT, we ignore any trailing local maxima with amplitude below the fit shape. An example of this procedure is shown in Fig. 5.3.

Instead, if a pulse is not contained within this shape, it is an indication that the trailing local maxima following the initial maximum are not part of the pulse tail, but probably additional pulses following the initial pulse. In this case we do not ignore the consequent local maxima, but we perform normal TOHM/LI simulation analysis exactly as described in section 5.1.1.

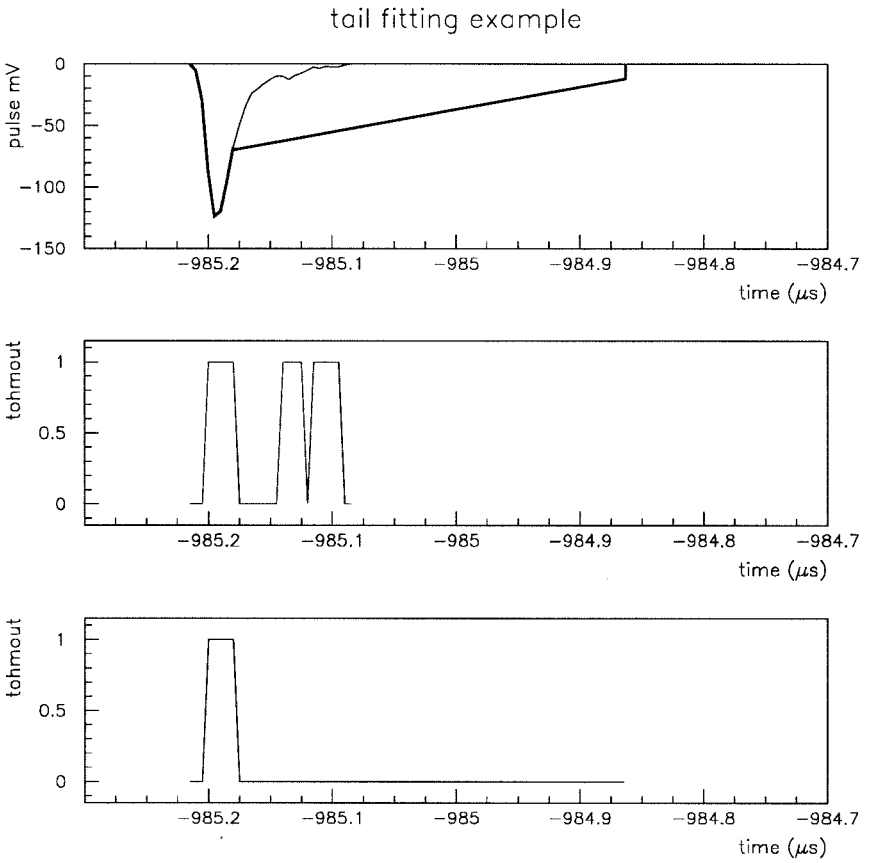


Figure 5.3: a) A WFD pulse. Shown is the triangle-like shape within which the pulse is fitted. b) The TOHMOUT array as it would be without the tail cut. The local maxima at around -985.160 and -985.1 $\mu$s are on the pulse tail and lead to an incorrect evaluation of the time over half maximum of the pulse. c) The TOHMOUT array after the pulse tail cut. Here the time over half maximum of the pulse is evaluated correctly.

### 5.1.3 Muon-like Pulse Rejection

Fast muons passing through the scintillator typically produce pulses that are wide in the base but narrow (around 50 ns) at half maximum. The height distribution of muon pulses in the waveforms show a strong peak around 2 V (see Fig. 5.5). Muons should not trigger the SMT hardware, yet quite a large percentage do. This happens for two reasons: A) The analog part in the TOHM hardware overestimates the time over half-maximum of large pulses. Of course, the software simulation does

not suffer from the same problem. B) Large primary signals in the PMTs tend to produce afterpulses due to the presence of Helium (He) or other elements inside the phototube (see Fig. 5.4). These afterpulses arrive too late in time to be suppressed by the tail-cutting procedure and can easily look like monopoles. Thus, they could easily trigger both the SMT hardware and the monopole pulse recognition algorithm.

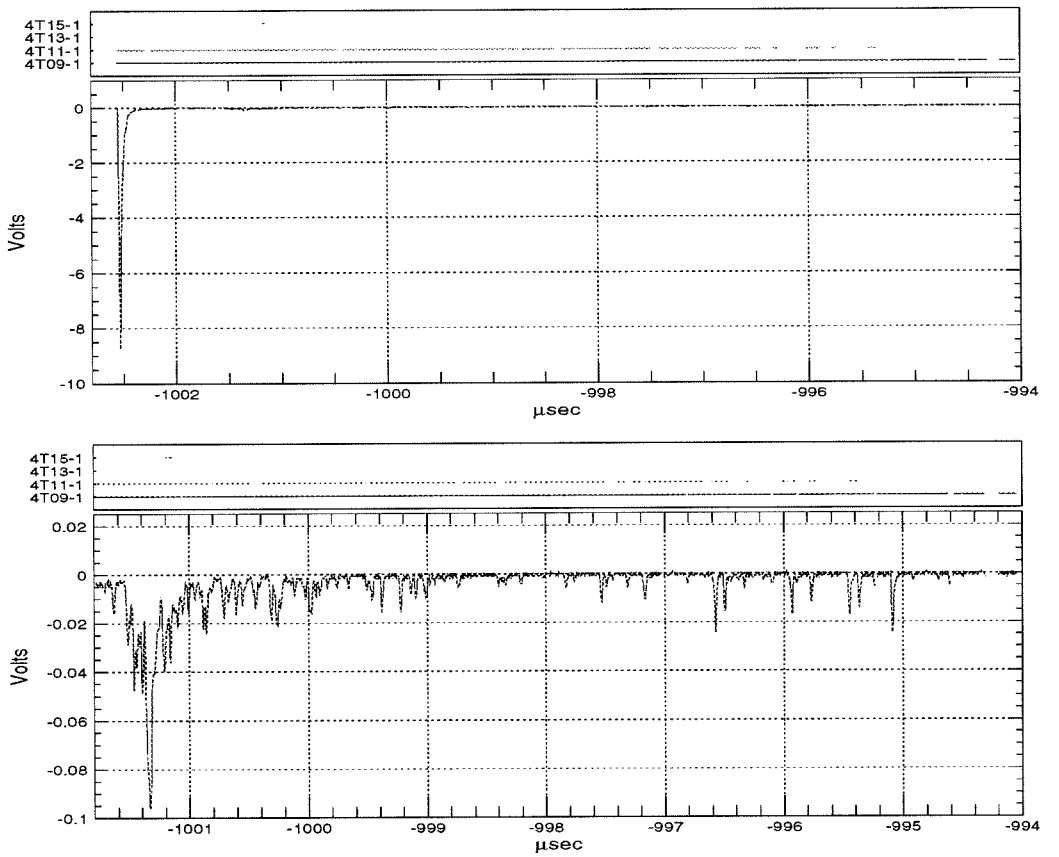


Figure 5.4: a) A muon pulse at $\sim -1002.5\ \mu$s before the stop. b) Zoom-in on the tail of the pulse. Notice the strong afterpulsing at $\sim -1001.3\ \mu$s and the SPE train-like afterpulsing at $\sim -996\ \mu$s before the Stop.

This effect varies in intensity from tube to tube, but as shown in appendix A, on average it depends on the charge of the initial pulse. It is also noticeable that there are three clear "danger" time zones, at $1.2\ \mu$s, $2.4\ \mu$s and $\sim 7\ \mu$s after the initial

pulse, where these afterpulses are prominent. In the third time zone, afterpulsing often resembles the SPE train pulses. The SMT emulation in software is certainly subject to the effects of these monopole-like afterpulses.

In order to negate the effects of PMT afterpulsing, we assert a dead time interval both preceding (2 $\mu$s) and following (25 $\mu$s) a muon-like pulse that has an amplitude greater than 800 mV. The effect of introducing this dead time over the total live time is insignificant. Considering that we have around five thousand muons in a regular six hour run, the probability that an accidental muon passes through the same tank in less than 25 $\mu$s before a monopole is less than $10^{-7}$ per monopole.

The value of 800 mV was chosen as a threshold over which we impose the 25 $\mu$s dead time, because that is the level at which the muon contribution to the general distribution of pulse heights starts to become significant. In Fig. 5.5 we show the

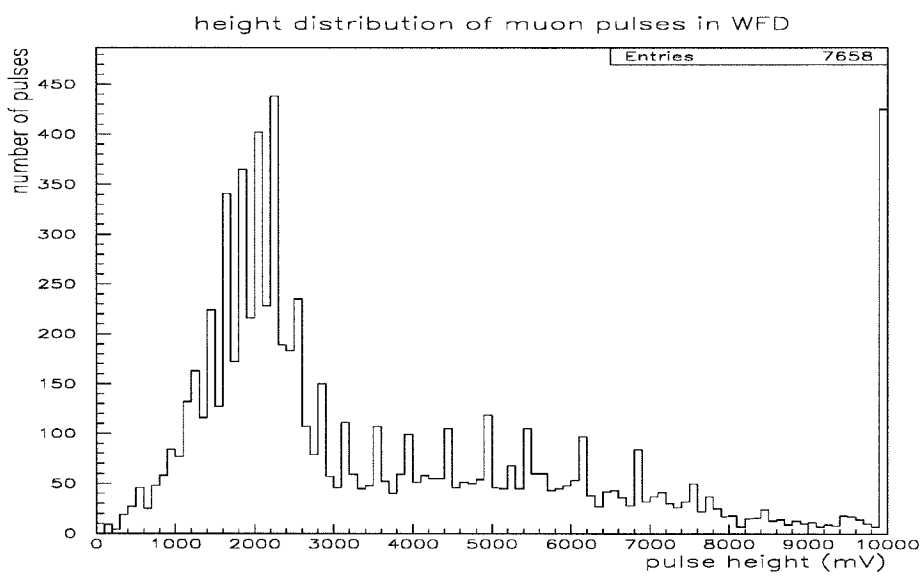


Figure 5.5: Distribution of pulse heights for muon pulses. The peak is clearly at 2 V. The binning artifacts are because of the nature of WFD ADC. The last bin collects all pulses greater than 10 V due to ADC saturation.

distribution of muon pulse heights during a typical run. These pulses were selected from 2-face SPAM_MUON events, with 2-face ERP trigger, in the boxes that fired the ERP. The pulses are located around 1 ms before the WFD stop, i.e., at the time the Stop Master was triggered. The peak is clearly at 2 V. In Fig. 5.6 we see for

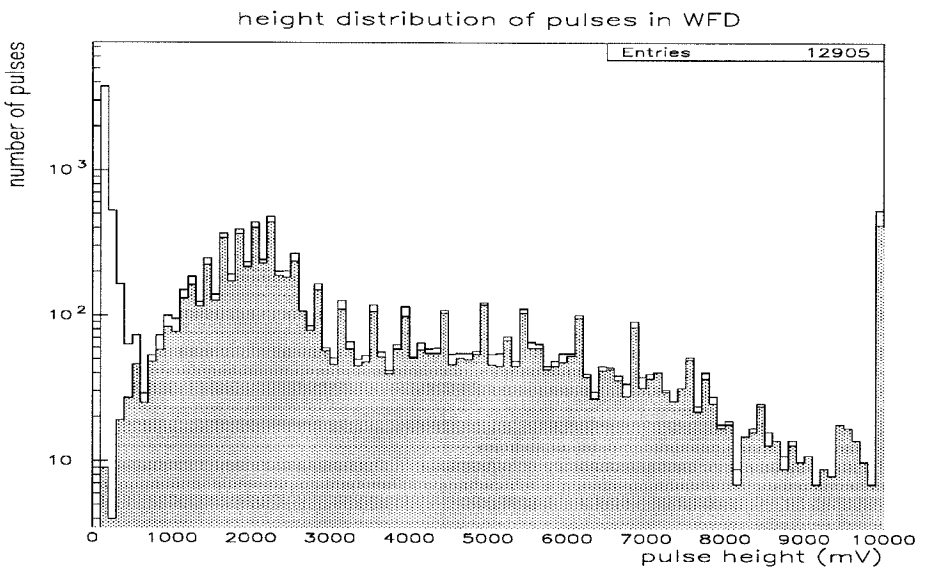


Figure 5.6: Distribution of pulse heights for pulses present in the waveforms. The peak for small pulse heights is due to radioactivity pulses. The peak around 2 V is due to muons. In grey are the pulses that were selected in the previous figure (muon pulses).

a typical run the distribution of heights of all the pulses present in the waveforms, superimposed over the selected muon pulses. The large peak for small pulse heights is due to radioactivity pulses.

Of course every pulse larger than 800 mV is not automatically flagged as a muon-like pulse and rejected. Instead, its time over half-maximum is checked. A pulse greater in amplitude than 800 mV with time over half maximum greater than 150 ns could indeed be a monopole. For this reason, for pulses greater than the 800 mV threshold, the time over half maximum needs to be scrutinized. In fact, as mentioned earlier in 5.1.1, pulses larger than 100 mV and wider than 150 ns are flagged as valid monopole candidates and retained for further analysis.

## 5.2 Algorithmic Testing

In order to test the efficiency of the algorithm in the identification of monopoles, a number of fake monopole waveforms were generated digitally. In simulation of the

passage of a monopole through scintillator, an SPE train, obeying photon statistics, was generated. The velocity of the simulated monopole determines the duration of the pulse. The monopole's light yield determines the mean number of SPEs that are generated. In Monte Carlo fashion, we simulated monopole pulses corresponding to velocities ranging from $4.4 \times 10^{-3}c$ (pulse width 0.145 $\mu$s) down to $10^{-4}c$ (pulse width 6.333 $\mu$s) and with light yields as low as less than 0.1 MIP. The ratio of the events selected by the algorithm over the total number of events generated defines the algorithm's efficiency at a given pulse width and light yield.

### 5.2.1 Monopole Pulse Simulation

When a monopole crosses a scintillator tank, the velocity of the particle and, as a result, the density $\lambda$ of photoelectron generation is constant for the duration $T$ of the passage. The density of the photoelectrons is given by

$$\lambda = \frac{N_{pe}}{T}, \tag{5.2}$$

where $N_{pe}$ is the total number of photoelectrons. To simulate monopole pulses of duration $T$, we generate pulses according to Poisson statistics. If the $n^{th}$ SPE was produced at time $t_n$, then the $(n+1)^{th}$ SPE is produced at time $t_{n+1}$ given by

$$t_{n+1} = t_n - \frac{1}{\lambda}\ln(R), \tag{5.3}$$

where $R$ is a random number distributed uniformly between zero and one. The photoelectron pulse $P_{spe}(t)$ is modeled according to

$$P_{spe}(t) = -\frac{Qte^2}{W^2}e^{-\frac{et}{W}}h(t), \tag{5.4}$$

where $h(t)$ is the step function with transition at t=0, $Q$ is the charge of an SPE and $W$ its width. The charge of the single photoelectron pulse is sampled from a Gaussian of average charge 50 mV×ns and a $\sigma$ of 17 mV×ns according to the characteristics

measured for the EMI PMTs, while the width is obtained from a Gaussian of average width of 12.5 ns and of $\sigma$ of 3.0 ns. Summing over all the single photoelectron pulses that were generated, we obtain the waveform

$$Pulse(t) = \sum_{n=1}^{n} SPE(t - t_n) \tag{5.5}$$

Emphasis was given to digitizing the signal in a manner as close as possible to the way it is done in the WFD system. Therefore, all pulses with heights less than 2.5 mV were not digitized. Pulses that exceed 2.5 mV were digitized by taking the average of the pulse in a 5 ns long window (the WFDs are run at 200 MHz) and converting into ADC counts. Once again, the volts-to-ADC counts conversion was performed in accordance with the empirical formula determined by the specifications of the WFDs. In the top panel of Fig. 5.7 we show a MC generated pulse of 6.6 $\mu$s duration. In the bottom panel, we show the same pulse after digitization and volts-to-ADC counts conversion and decompression (translation back from ADC counts-to-volts).

### 5.2.2 Algorithmic Efficiency

To measure the algorithmic detection efficiency for monopole-like pulses, Monte Carlos (MC) with the following monopole pulse durations were run:

- 6333 ns corresponding to velocity of $10^{-4}c$
- 3333 ns corresponding to velocity of $1.9 \times 10^{-4}c$
- 1000 ns corresponding to velocity of $6.3 \times 10^{-4}c$
- 666 ns corresponding to velocity of $9.5 \times 10^{-4}c$
- 333 ns corresponding to velocity of $1.9 \times 10^{-4}c$
- 195 ns corresponding to velocity of $3.2 \times 10^{-4}c$
- 160 ns corresponding to velocity of $4.0 \times 10^{-4}c$

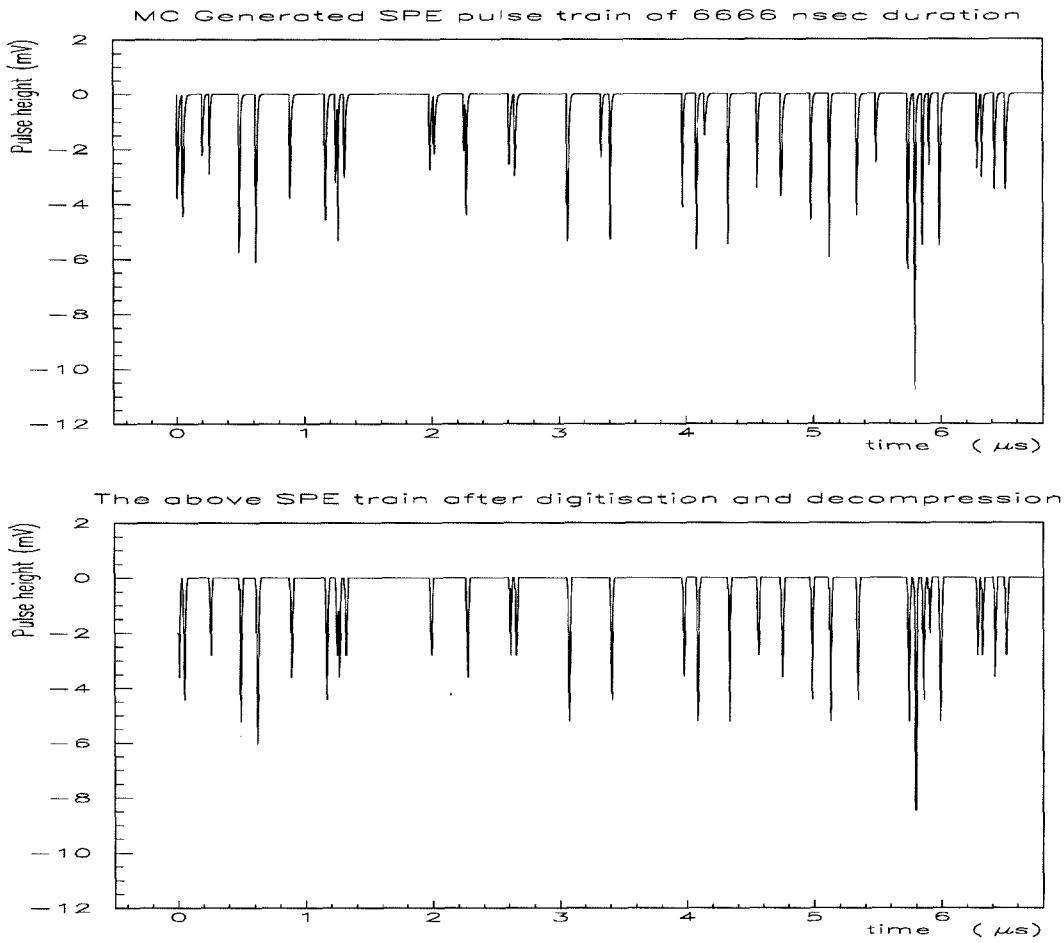


Figure 5.7: MC generated pulse of 6.6 $\mu$s duration. On the bottom we see the same pulse after digitization (volts-to-ADC conversion) and decompression (translation from ADC-to-volts). SPE pulses with amplitude less than 2.5 mV are not digitized.

- 150 ns corresponding to velocity of $4.2 \times 10^{-4}c$
- 145 ns corresponding to velocity of $4.3 \times 10^{-4}c$

The algorithm uses separate triggering conditions for the horizontals and for the vertical counters, in accordance with the hardware. Thus, MCs were performed for both cases.

In order to account for pedestal variations and to measure the effect of a wrong pedestal evaluation on the analysis efficiency, the pedestal values used for the volt-to-ADC and for the ADC-to-volt conversions were treated as independent input parameters. An overestimate of the pedestal value when converting ADC counts

to volts results in underestimation of the PMT signal and consequently in a lower efficiency for the identification of a monopole pulse. A study of pedestal distribution in real WFD data has yielded a Gaussian distribution with a mean of 26.7 counts and an RMS of 0.61 counts (see section 7.3.1). In the Monte Carlo, in order to examine the effect of a pedestal error of one count on our monopole identification efficiency, we ran MCs for each of the pulse durations given above for the three following pedestal conditions:

- digitizing pedestal=26.5, decompressing pedestal=26.5
- digitizing pedestal=25.5, decompressing pedestal=26.5
- digitizing pedestal=26.5, decompressing pedestal=25.5

In order to understand the features of the SMT simulation algorithm, we plot in Fig. 5.8 the mean number of SPEs that the algorithm counted versus the number of SPEs that were generated in the pulse for the various velocities and for the case of equal digitization and decompressing pedestals. We note that as the number of the generated photoelectrons grows, they start falling on top of each other and the algorithm underestimates their number as it counts only widths. As is to be expected, this effect is far more prominent in shorter pulse durations, where single photoelectrons accumulate quickly one on top of the other, to form a continuous pulse. In this case, the algorithm ends up measuring the width of the generated pulse. We have used these results in section 3.4.2 in order to convert the number of SPEs that the analysis code measures to the number of SPEs in the waveforms (light yield).

We map the efficiency of the SMT simulation algorithm by varying the number of SPEs generated for the given monopole velocities and pedestal values. In this calculation over the light yield vs. velocity space we ignore model expectations of light yield of monopoles and sample several light yields at each velocity. In Fig. 5.9 we plot the efficiency curves obtained when the digitization pedestal equals the decompressing pedestal. The resulting efficiency curves are sigmoids. On these curves, we calculate

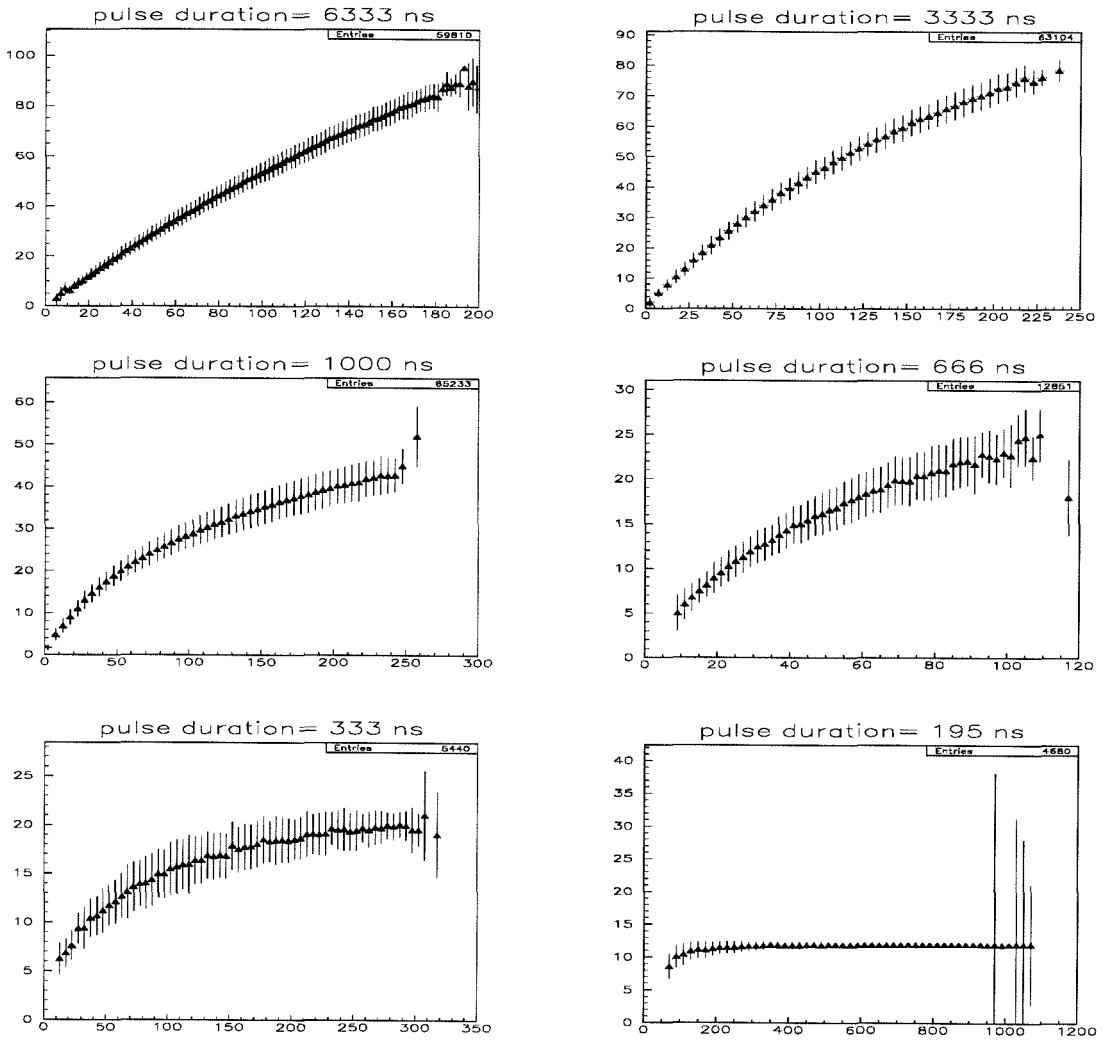


Figure 5.8: Mean number of SPEs measured by the algorithm versus the number of generated SPEs for digitization pedestal 26.5, decompressing pedestal 26.5 and for various pulse durations. Note how the relation flattens as the SPEs start piling on top of each other for a higher number of SPEs.

the required light yield for the SMT simulation algorithm to be efficient at the 99 % level. As mentioned above, MC simulation was also performed for pulses of 145 ns width (corresponding to monopole $\beta \simeq 4.4 \times 10^{-3}$ c), but the pattern recognition algorithm had zero efficiency for pulses of that width. This is to be expected given the design of the software and the triggering parameters selected for the analysis. Thus we conclude that the sigmoid for pulses of 150 ns width defines the velocity

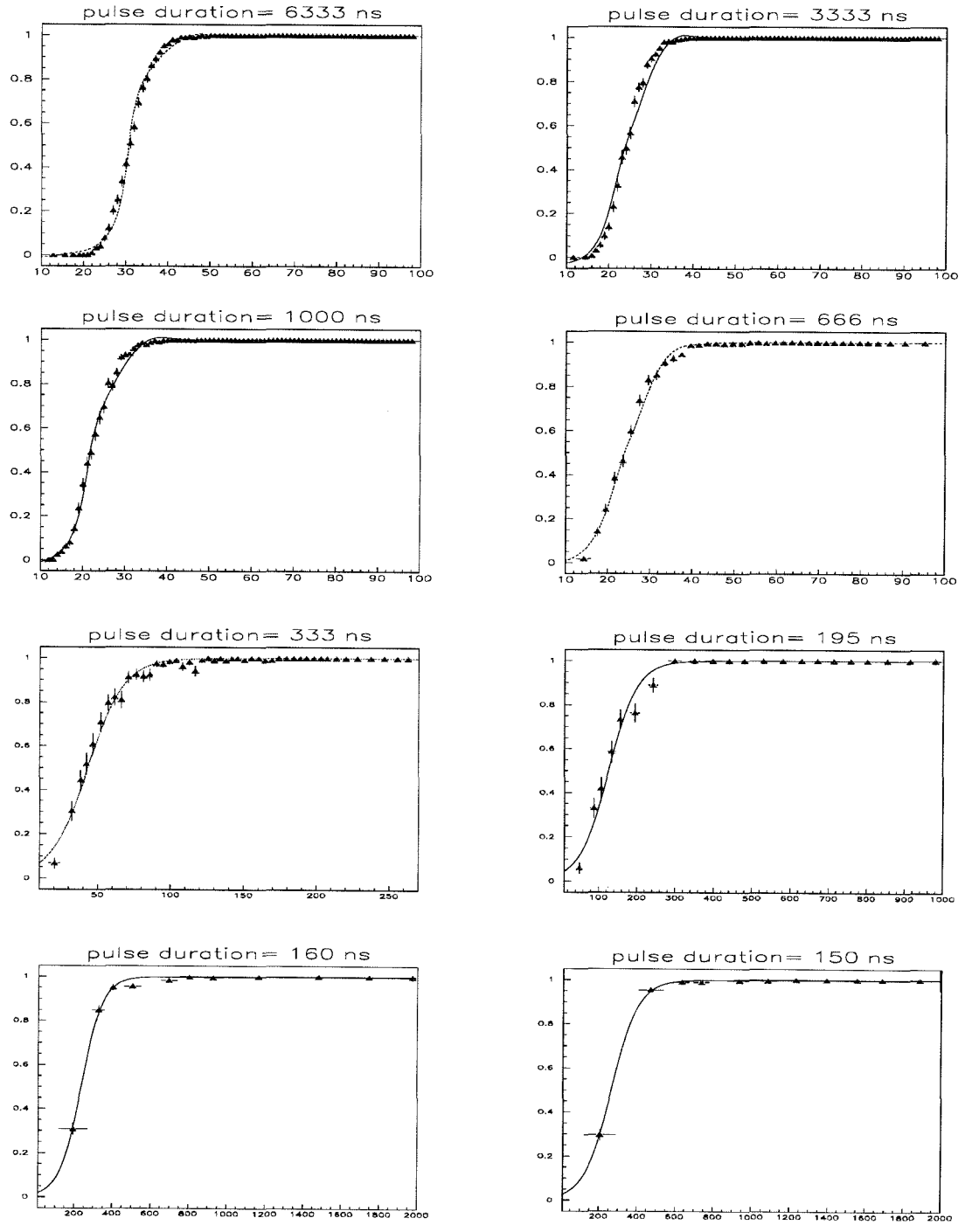


Figure 5.9: Efficiency of the algorithm versus number of generated SPEs for digitization pedestal 26.5, decompressing pedestal 26.5 and for various pulse durations.

upper limit ($\beta \simeq 4.2 \times 10^{-3}$) of the sensitivity. The results deduced from the above simulations are summarized in Figs. 5.12 and 5.13, where we also elaborate on the form of the sensitivity curve. For the moment, in order to illustrate the effects of the digitization and decompression pedestal parameters, we present in Figs. 5.10 and 5.11 the efficiency curves obtained for a digitization pedestal both smaller or larger than the decompressing pedestal, respectively. The effect of these parameters is negligible for narrow pulses (195 ns or less); thus, we present below the sigmoids for pulses of 6.333 $\mu$s to 195 ns width.

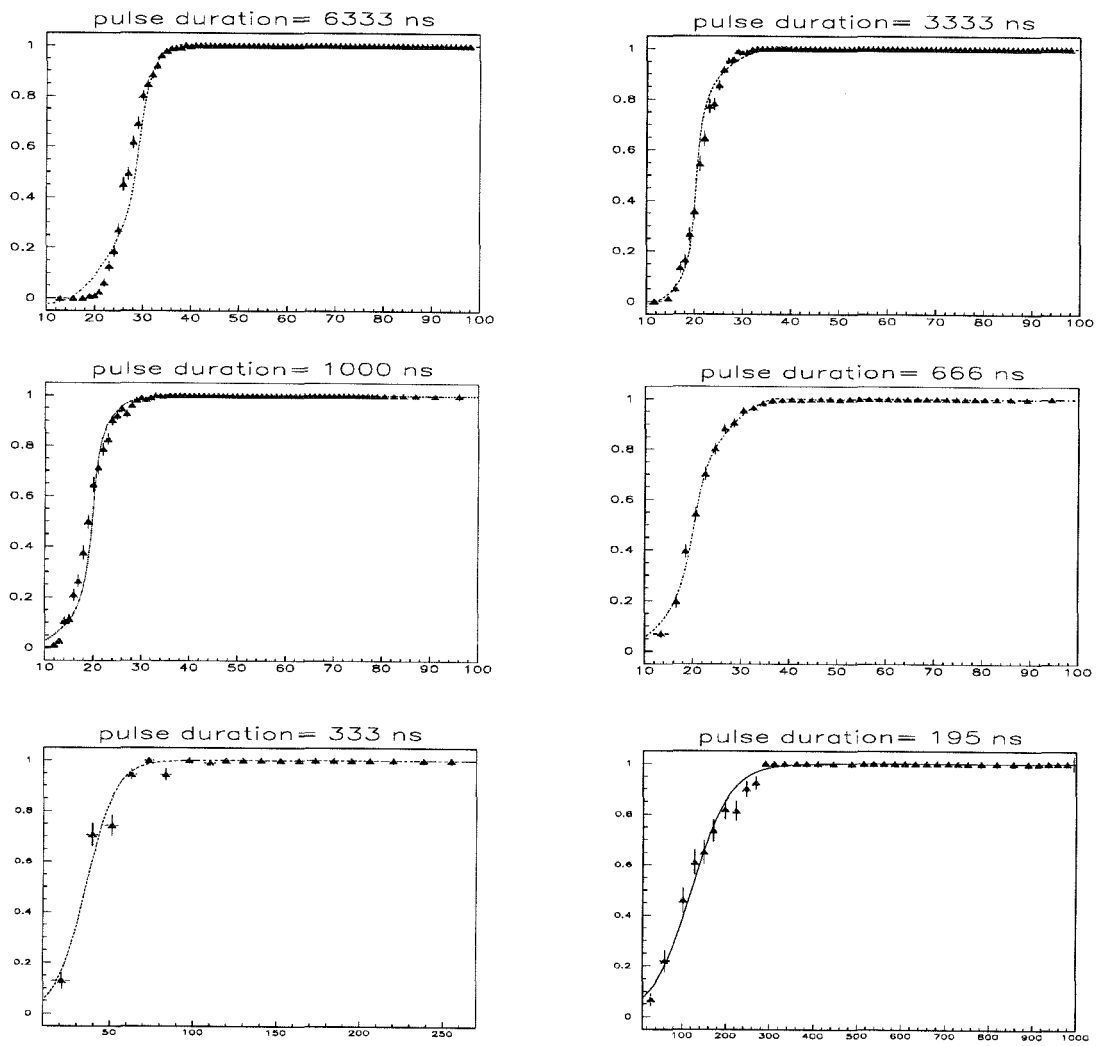


Figure 5.10: Efficiency of the algorithm versus number of generated SPEs for digitization pedestal 26.5, decompressing pedestal 25.5 and for various pulse durations.

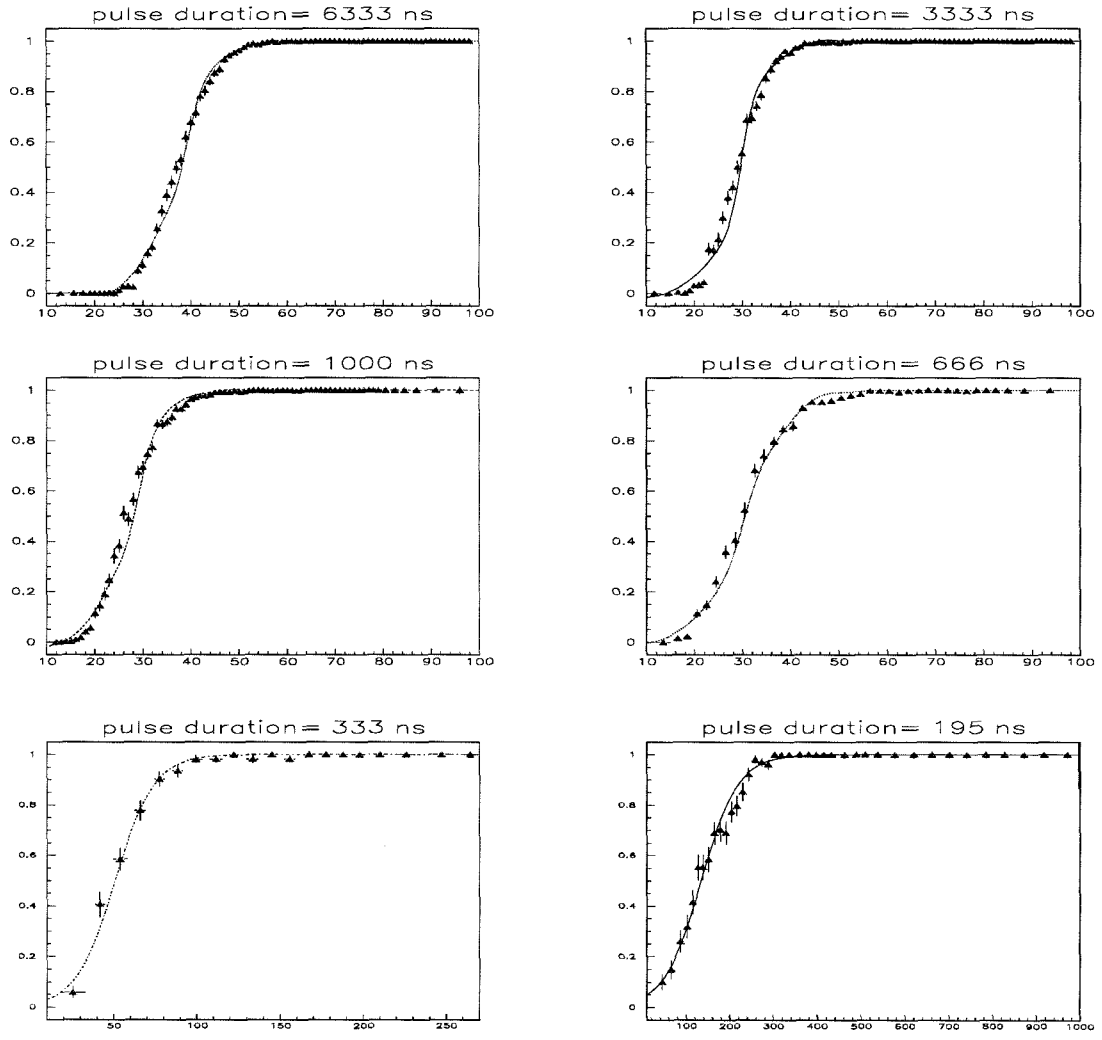


Figure 5.11: Efficiency of the algorithm versus number of generated SPEs for digitization pedestal 25.5, decompressing pedestal 26.5 and for various pulse durations.

The 99% efficiency points obtained by this procedure are exhibited in Table 5.1. The 99% efficiency curves of the algorithm for the three cases of pedestal heights are plotted in a light yield versus velocity plot along with a plot of the expected monopole light yield. In the same figure, we appreciate the effects on efficiency due to possible pedestal errors; an overestimate of the pedestal by one count results in the worsening of the light yield threshold by 10-20%.

The slight rise in the sensitivity curve in the very low velocity ($v \sim 10^{-4}$ c) regime is due to the down-counting of the LI simulation part of the algorithm. The algorithm

| pulse width (ns) | 6333 | 3333 | 1000 | 666 | 333 | 195 | 160 | 150 |
|---|---|---|---|---|---|---|---|---|
| digitization ped=26.5 decompressing ped=25.5 | 36 | 30 | 29 | 35 | 66 | 323 | 494 | 590 |
| digitization ped=26.5 decompressing ped=26.5 | 42 | 35 | 34 | 41 | 101 | 297 | 494 | 590 |
| digitization ped=25.5 decompressing ped=26.5 | 53 | 43 | 42 | 50 | 105 | 328 | 494 | 590 |

Table 5.1: Number of PEs required for 99% algorithm efficiency using the horizontal counter triggering parameters. The three rows correspond to the three different pedestal conditions discussed in the text.

needs more SPEs (light yield) to overcome the larger number of down counts in wider pulses. On the other end of the velocity range, the rise in the efficiency curves is due to the superposition of the SPEs as the pulse width gets shorter. The efficiency of the algorithm in the region around $v \sim 4 \times 10^{-3}$c is due to direct software checks of the width over half maximum of large pulses in the waveform. The pedestal variation has a greater effect for the efficiency-turn-on point for longer duration pulses. This is easily understood by the fact that for shorter pulse durations, the pulses that trigger the algorithm are larger in amplitude and thus not affected seriously by pedestal variations of one count. In contrast, at lower velocities the algorithm will trigger for trains of isolated SPEs, for which pedestal variations of one count (i.e., voltage

variations of around 0.8 mV) become important.

The same MCs were performed for the case of triggering parameters for the vertical counters. We recall that the SMT uses modestly different triggering parameters for the vertical counters (trigger threshold = 10, down counter period = 1500 ns). The resultant 99% efficiency points are shown in Table 5.2. The 99% efficiency curves of the algorithm for the horizontal and vertical triggering cases are plotted in a light yield versus velocity plot (Fig. 5.13), where the expected monopole light yield is plotted alongside (normalized to the light yield of a MIP). Proceeding conservatively, we used the light yield of a MIP hitting the far end of a counter, which is about $7.3 \times 10^2$ SPEs for a horizontal tank and $3.8 \times 10^2$ SPEs for a vertical tank [76].

| pulse width (ns) | 6333 | 3333 | 1000 | 666 | 333 | 195 | 160 | 150 |
|---|---|---|---|---|---|---|---|---|
| horizontal | 42 | 35 | 34 | 41 | 101 | 297 | 494 | 590 |
| vertical | 30 | 26 | 28 | 33 | 82 | 244 | 447 | 545 |

Table 5.2: Number of PEs required for 99% algorithmic efficiency. The upper row corresponds to triggering parameters for horizontal counters, and the lower one, to vertical counters.

In summary, Monte Carlo studies show that the PR algorithm retains satisfactory high efficiency over the entire range of expected monopole velocities and light yields.

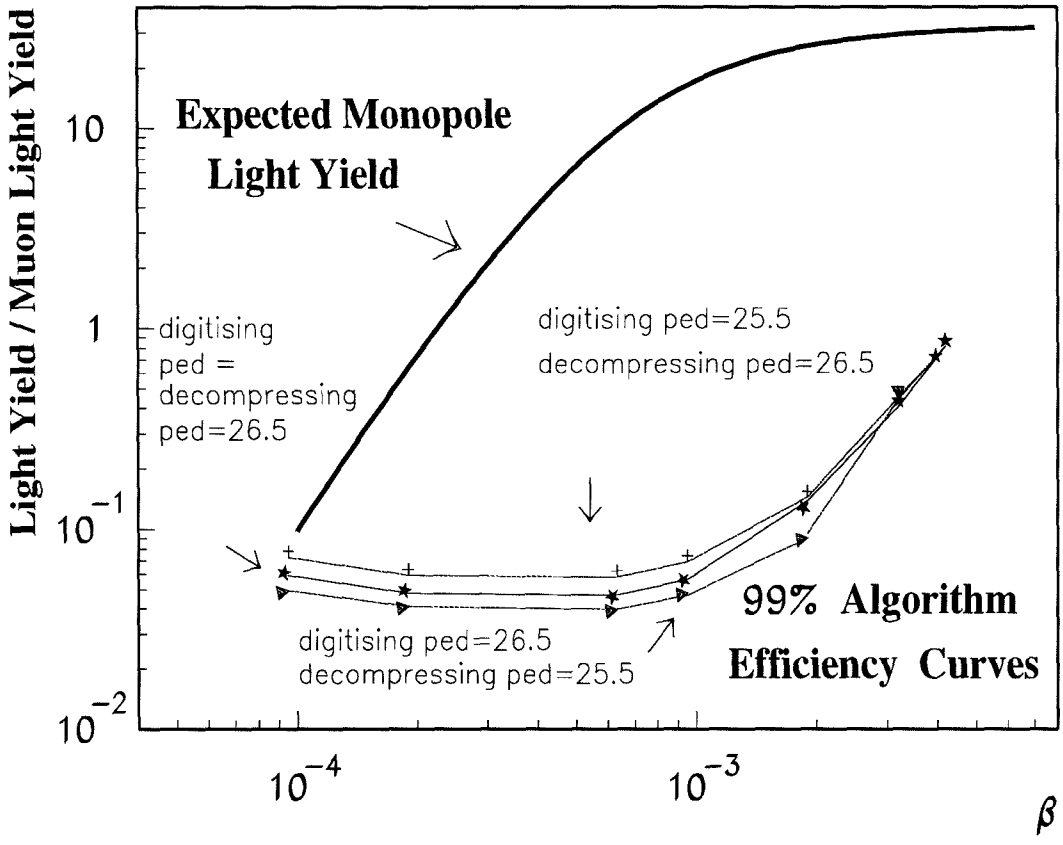


Figure 5.12: 99% triggering efficiency curves of the SMT simulation algorithm. The crosses indicate a digitization pedestal = 25.5, decompressing pedestal =26.5. The asterisks indicate a digitization pedestal = 26.5, decompressing pedestal = 26.5. The triangles are for digitization pedestal = 26.5, and decompressing pedestal = 25.5. The lines are a guide to the eye. The rise on the right (higher velocities) is because of SPE superposition for shorter pulse durations. The rise to the left is due to additional down counting for long pulse duration.

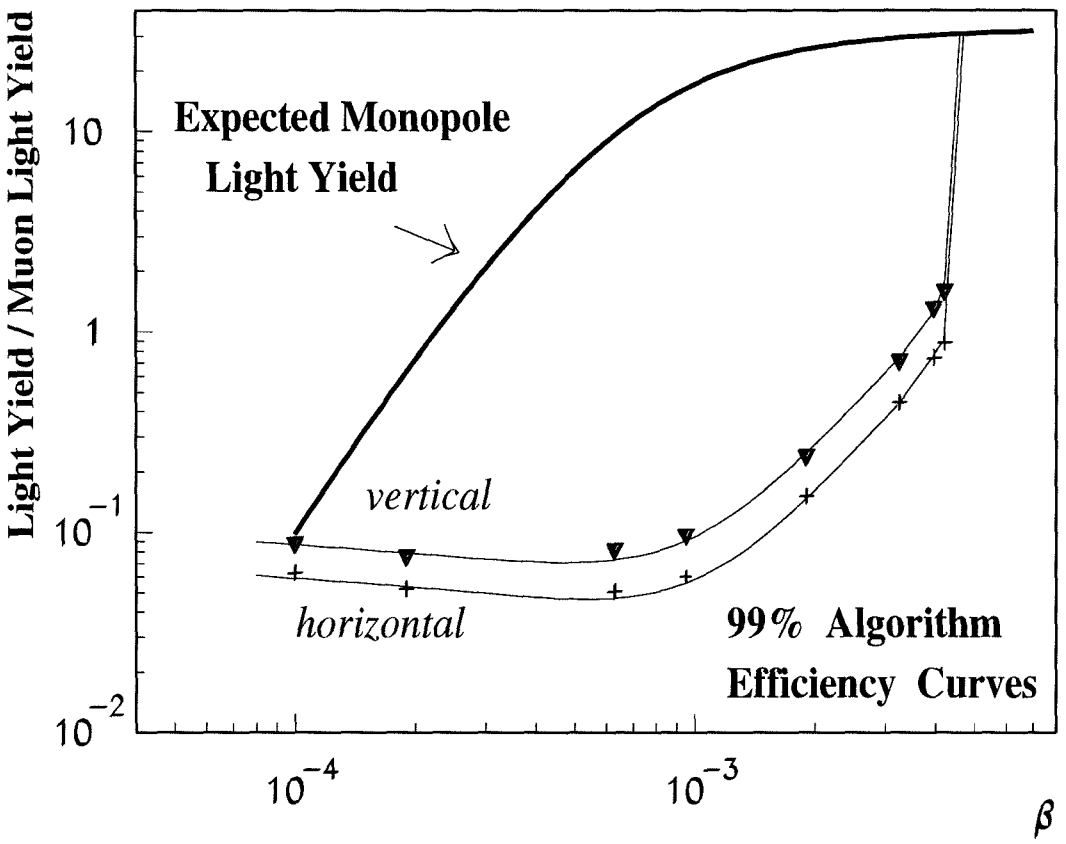


Figure 5.13: 99% triggering efficiency curves of the SMT simulation algorithm for vertical triggering parameters (triangles) and for horizontal triggering parameters (crosses). The lines are a guide to the eye. The rise on the right (higher velocities) is due to SPE superposition for shorter pulse durations. The rise to the left is due to additional down counting for long pulse duration.

# Chapter 6

# Analysis of Monopole Candidates

## 6.1 Events Filtered from the WFD Analysis

In the description of the analysis path (see chapter 4), it was stated that the starting point of the analysis was the selection of two-face monopole triggers. We recall here the requirement that two faces of the detector should have had an SMT within 1 ms. This guaranteed that an event characteristic waveform (e.g., for a monopole) was present in at least two tanks in different faces. A muon trigger (SPAM_MUON) was then used to reject fast events ($\beta > 10^{-2}$), unless a fast monopole trigger (SPAM_FMT) was also present. A loose tank multiplicity cut was then applied. This cut was designed not to be susceptible to the possible electronic crosstalk in the SMT hardware. As discussed in chapter 4, a total of 35,901 events survived the first set of cuts. A third of these survivors were fast particles which leaked through due to inefficiencies inherent in the SPAM_MUON trigger or due to the difference in acceptance between this trigger and the SMT. Such fast events are typically accompanied by fast streamer tube and scintillator triggers. The remaining two-thirds are predominantly electronic noise or radioactivity coincidence events; due to its low trigger threshold, the SMT was susceptible to ground loops and low amplitude electronic interference.

All events surviving these filters subsequently underwent waveform analysis. Waveforms of all tanks that fired the SMT were analyzed. A tank passed the analysis test when the waveforms recorded at both of its ends triggered the pattern recognition (PR) algorithm (described extensively in chapter 5). For the period before the WFD-fix, every waveform that suffered buffer overflow in the WFD was allowed to pass this stage of the analysis. Finally, an event passed the waveform analysis when

at least two faces of the detector contained tanks that had each passed the waveform analysis. There were 40 events at the end of this. The distribution of these events in runs, over time, is shown in Fig. 6.1. From the 40 events that survive the WFD

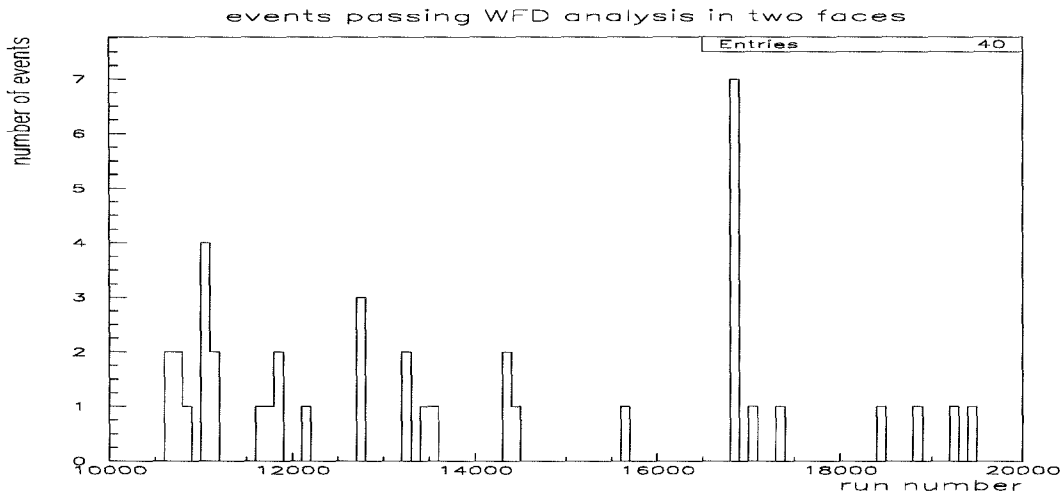


Figure 6.1: Events that pass the WFD analysis requirements in tanks in at least two faces of the detector.

analysis, a subset of seven are accompanied by a SPAM_FMT trigger.

Background that occasionally leaks through all filters up to this stage comes in the following leading categories:

- Electronic noise – Bipolar electronic noise may mimic SPE trains and thus fire the SMT and pass through the PR algorithm, but can be distinguished from genuine SPE trains due to an appreciable amount of positive content in the waveforms. In addition, electronic noise events, typically, involve many tanks firing the SMT. In fact, most of the 40 surviving events have a large number of tanks firing the SMT. This may be seen easily, if we plot the distribution of the number of tanks triggering the SMT for events before and after the waveform analysis (Fig. 6.2). In these two panels, it is evident that a majority of events before the WFD analysis involve just two to three scintillator tanks. In contrast, events surviving the WFD analysis tend to involve many tanks.

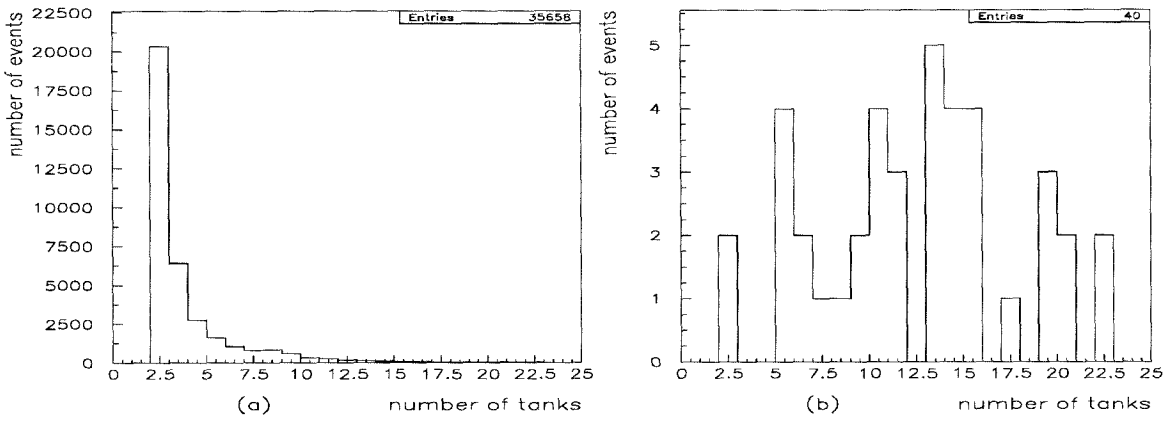


Figure 6.2: a) Distribution of number of tanks firing the SMT for events that will undergo waveform analysis. We note that a large fraction of events involve two or three tanks only. b) The same distribution for events that pass WFD analysis. The surviving events are mainly electronic noise and electromagnetic showering events.

Clearly events with small numbers of tanks involved in triggering are rejected well by the WFD analysis.

- Muon-induced electromagnetic showers – For such events the SMT fires due to the large, wide pulses produced by electromagnetic showers. The events survive the analysis either due to the width of the pulses or because the events had waveforms with overflow buffers (pre WFD-fix data-taking period). These events, which would normally fire the SPAM_MUON trigger and thus be excluded, fail the relevant filter due to inefficiencies in that trigger or due to the simultaneous firing of a SPAM_FMT. These events also tend to involve many tanks in the detector, and the pulses in the waveforms of tanks of separate faces lie within 100 ns. Another characteristic is the presence of several streamer tube hits in the fast chain. As explained earlier in section 2.4.1, the fast chain records streamer tube hits to a memory depth of 10 $\mu$s. With a radioactivity background rate of $\sim$50 Hz in the streamer tubes, we expect 1-2 hits due to background in the fast chain of the 14 horizontal streamer tube layers of one SM. A relatively fast monopole of $\beta \simeq 10^{-3}$ is expected to deposit of order 10-20 horizontal hits in the fast chain. A MC calculation demonstrated

that even in the worst case scenario of monopoles catalyzing nucleon decay at a high cross section ($\sigma = 10^{-25}$ cm$^2$) – and thus producing many streamer tube hits – 98.5% of the time there are no more than 80 hits in the fast chain of horizontal streamer tubes and no more than 50 hits in the fast chain of lateral streamer tubes. However, among the 40 surviving events, 19 had more than 80 hits in the fast horizontal chain and 14 had more than 50 hits in the lateral fast chain. We label as STRH the number of horizontal streamer tube hits in the fast chain (in the supermodule with the largest number of streamer tube hits). Similarly, we label as STRL the number of lateral streamer tube hits in the fast chain in the supermodule with the largest number of streamer tube hits. In Fig. 6.3 we plot the distribution of these two parameters for the events surviving the WFD analysis.

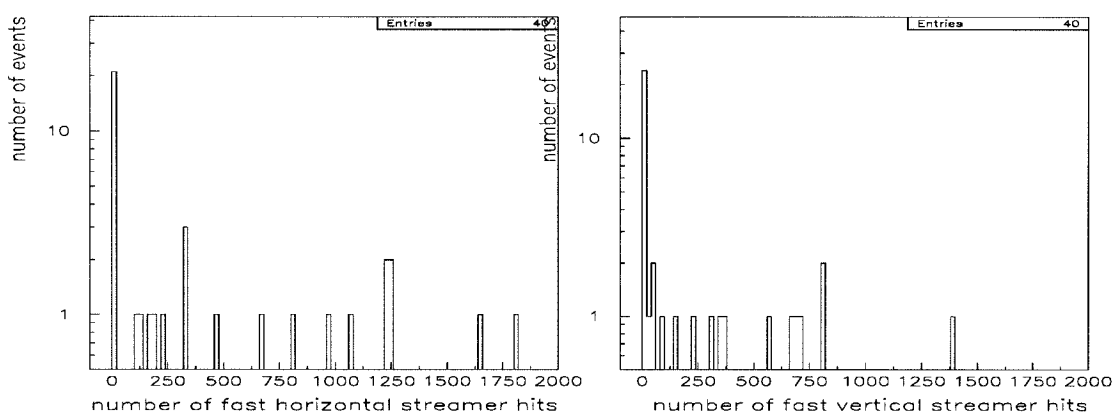


Figure 6.3: a) Distribution of STRH and STRL for events passing the WFD analysis.

- LED events – These events prove to be the most difficult to identify. Even though many measures were taken to prevent accidental contamination of real data with LED firing, some such events managed to leak into the data stream; this was either due to hardware spontaneously firing, or due to human error during calibrations in a different part of the detector. Most LED events have set bits in pieces of the hardware, such as the SPU, and were thus recognized and excluded from the analysis. Occasionally, this did not happen. LED events

before the WFD-fix might result in WFD buffer overflow and a loss of the initial pulse. There are four events in the surviving 40 that are possibly LED-induced. Even though there is uncertainty about the character of these events, geometrical and timing considerations make them incompatible with the passage of a slow monopole (see next section). However, there is one troublesome event for which the above criteria are consistent with that of a monopole. In that case we resorted to identification from its characteristic pulse shape; large LED-induced pulses are recognizable from their long risetimes when compared with pulses due to radioactivity or the passage of a particle through the scintillator. This event will be treated in some detail at the end of the next section.

## 6.2 Rejection Criteria - Individual Scanning of the Events

The 40 survivor events are small enough in number that analysis on an individual basis is a straightforward way to proceed. All 40 were considered individually. When doing so, the shape of the waveforms (when available), timing characteristics from the ERP system (when available) and the WFD system, and geometrical considerations were used to select putative monopole candidates. No such candidates resulted from this search. In the following sections, we describe in detail the rejection criteria for each one of these. We will offer an example event where the corresponding criterion applies. Of course, an event may be rejected due to one or more of these criteria. For most – but not all – of the events, an alternative explanation (either electronic noise, electromagnetic showers or LED-induced pulses) is available. We will summarize the events and the criteria used to reject them at the end of this chapter in Tables 6.2 to 6.5.

### 6.2.1 Waveform Shapes

#### Electronic Noise Waveforms

The waveform shape is an excellent aid in understanding the nature of an event, in particular of events involving bipolar electronic noise. Waveform analysis were at the heart of the slow monopole search with scintillators. The design of the experiment relied heavily on the magnetic monopole signature in the waveforms. The PR algorithm also followed this concept, but some of the background events passed the algorithm. A more sophisticated algorithm that could distinguish bipolar noise could have been designed, but the small number of surviving events did not justify the time and effort required for design and implementation. Moreover, events involving electronic noise had a characteristic shape and were easily distinguishable by eye as they typically had appreciable positive content; this is not expected from properly-functioning PMTs. As mentioned in section 3.2, the WFD discriminator ignored signals with heights in the range +2.5 mV to −2.5 mV, but positive pulses greater than +2.5 mV were recorded. Thus, electronic noise events exceeding the positive threshold of the WFD discriminator were indeed recorded, and this allowed distinguishing between genuine SPE trains and mimicking electronic noise. A bipolar noise waveform (chosen from one of the survivor events) is displayed in Fig. 6.4. The segment of the waveform where the PR algorithm counted the maximum LIcounts is also shown. Events such as this one pass through the WFD analysis, just as they trigger the hardware, which ignores the positive content while perceiving the negative content as a regular train of SPEs. Of the 40 surviving events, 25 have electronic-noise-characteristic waveforms; seven of these events are from one particularly noisy run.

While the visual identification of bipolar noise is straightforward, one might worry that it introduces a measure of subjectivity into the analysis. Fortunately, no bipolar noise event was rejected based solely on the shape of the waveform; in every case, the event also fails one or more other, more objective, criteria.

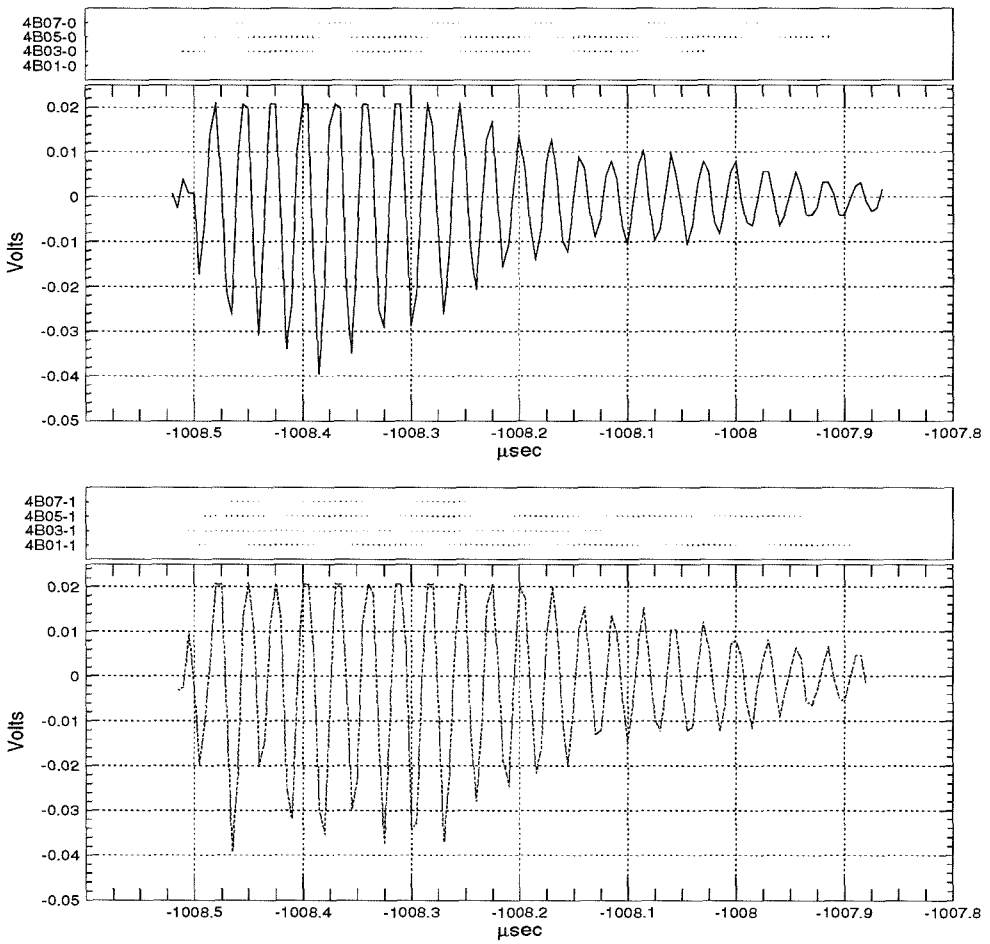


Figure 6.4: Run 13499, Event 615. Bipolar noise event. Time is in $\mu$s before the WFD STOP. The segment of the waveform containing the pulses that triggered the SMT, and as a result passed the PR algorithm, is shown.

### Waveforms Induced by LED Pulses

Among the survivor events, there is one event whose waveforms are characteristic of LED pulses. This is Run 19441, Event 2560. No rejection criteria from the ones used in this search apply for this particular event other than the information we have on its pulse shape. Therefore, the treatment of the pulse shape for this event will be detailed. As this is the most interesting surviving event, we reserve a section for its discussion near the end of this chapter (section 6.2.6).

### 6.2.2 Timing due to the Waveforms

Due to the common STOP of the WFDs, relative timing of the pulses recorded in the WFDs is straightforward. We used this timing, when available, to exclude events that did not exhibit timing consistent with the passage of a slow monopole. In the case of a legitimate monopole event (a monopole is expected to travel with constant velocity), the time spent within each tank must be compatible with the time of flight (TOF) between the detector faces. Electronic noise, on the other hand, tends to be simultaneous in all scintillator tanks. The same applies for muon-induced electromagnetic showers, where the waveforms may show wide pulses, but the time difference between pulses in different detector faces is not compatible with the passage of a single slow monopole (of $\beta < 4.1 \times 10^{-3}$).

In the case of electronic noise, characteristic pulses such as in Fig. 6.4 (or longer in duration) were, in all cases, present in more than one face of the detector simultaneously. This is clearly not expected of a slow monopole passage. A relatively fast monopole of $\beta \simeq 4.1 \times 10^{-3}$, the fastest monopole we are sensitive to, will require 3.25 $\mu$s to travel 4 m in the detector, so we expect TOF between faces of order several microseconds. The shortest TOF this search was sensitive to is 1 $\mu$s; for a TOF$<$ 1 $\mu$s, SPAM_MUON should have triggered and the event would have been rejected. The relatively fast $\beta \simeq 4.1 \times 10^{-3}$ monopole crosses only 1.23 m in 1 $\mu$s; as a result, the SPAM_MUON filter rejects only those monopoles that clip the detector's corners. This is properly accounted for in the acceptance. Therefore, for the purposes of this analysis, a TOF between faces of less than 1 $\mu$s was considered incompatible with the passage of a slow monopole and events with such a TOF were safely rejected.

In reality, for all events for which this criterion was satisfied, pulses occurred simultaneously in more than one face of the detector. The criterion rejects two large categories of events: electronic noise and electromagnetic showers. In all of 25 events that are categorized as electronic noise events, pulses of 300 ns duration or longer were present in the waveforms in many faces of the detector simultaneously. To illustrate this we show a set of waveforms from Run 13281, Event 10500 in Fig. 6.5.

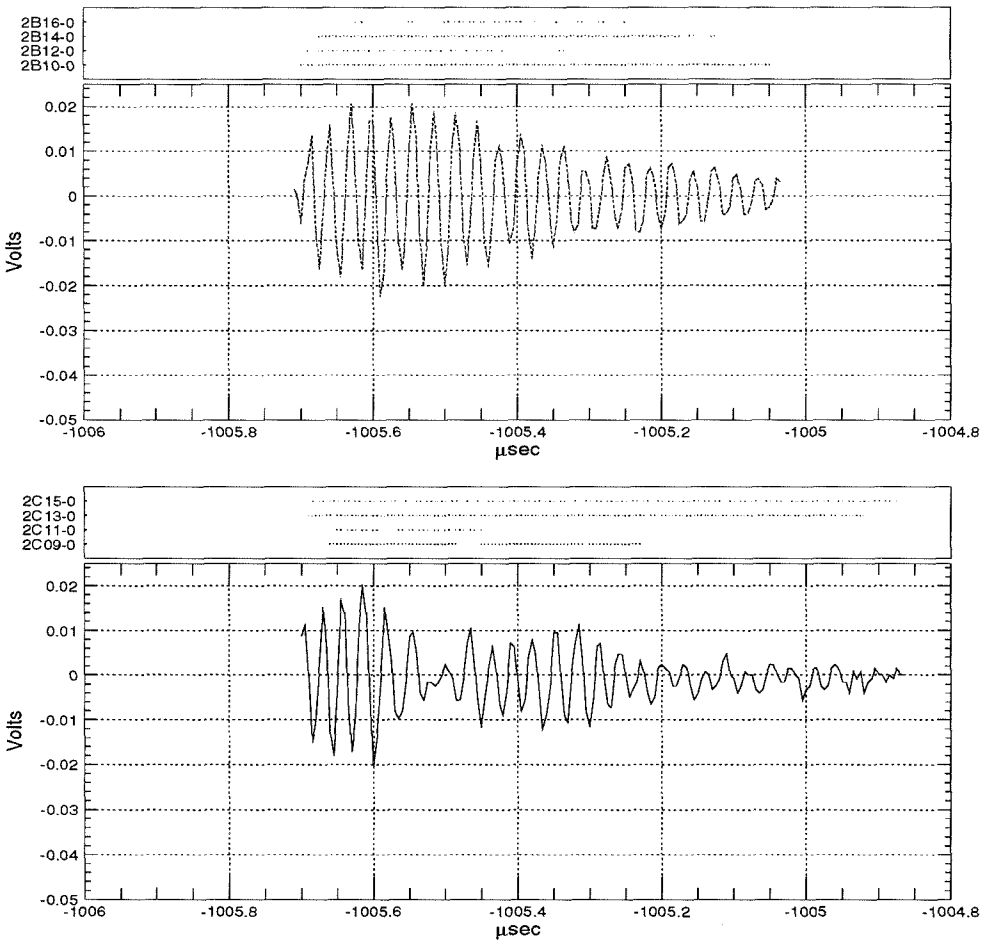


Figure 6.5: Run 13281, Event 10500. Waveforms for the center and bottom face are shown containing pulses longer than 600 ns simultaneously in both faces. The time axis is in $\mu$s before the WFD STOP.

The two waveforms originate from two separate faces (bottom and center face), and the presence of bipolar noise is simultaneous in both. In one case (Run 11137, Event 952), the electronic noise event lasted long enough to fill up the WFD data buffer and the entire history was not available. A segment of two waveforms from two faces (bottom and center) of this event is shown in Fig. 6.6. The pulse in the center face has a duration of at least 90 $\mu$s. Part of the pulse was lost due to the WFD

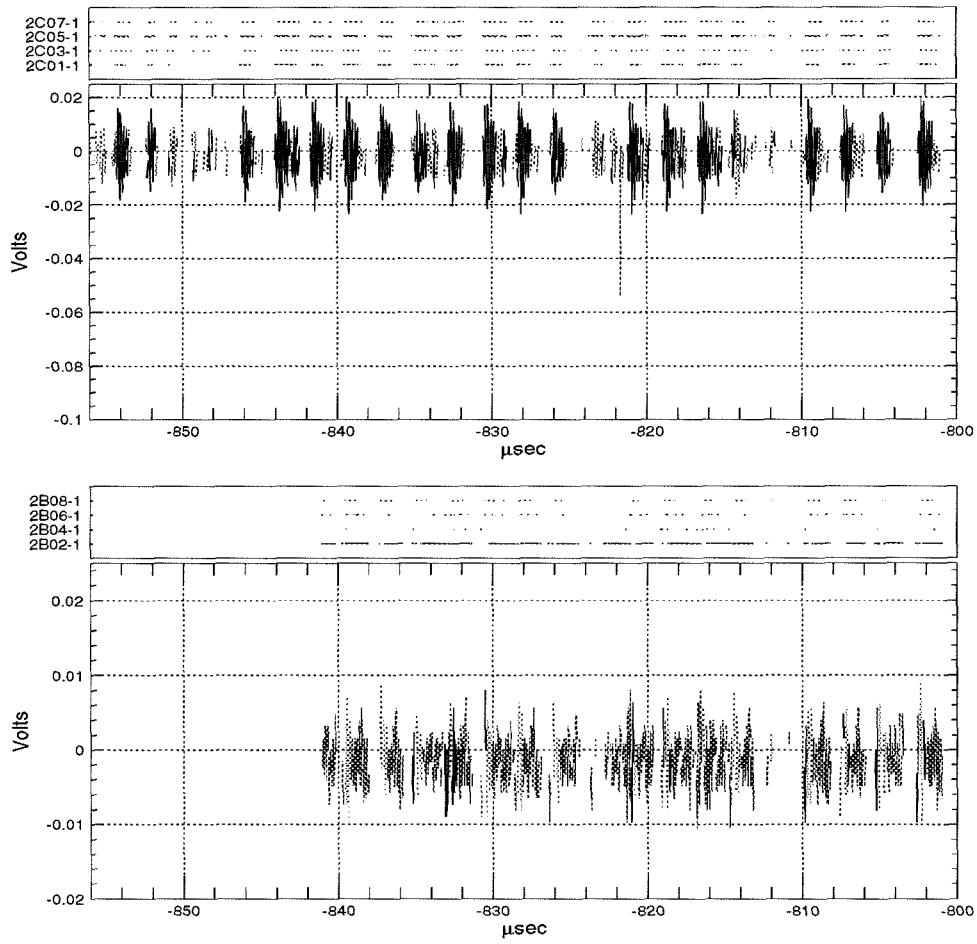


Figure 6.6: Run 11137, Event 952. Only a segment of the WFD pulses is shown. The presence of the pulse in both faces at the same time is obvious.

buffer overflow. The pulse in the bottom face had a duration of at least 70 $\mu$s and is present at the same time as the center-face pulse. Clearly, this event is easily rejected on timing considerations. A closer look at the waveforms of this event showed bipolar noise characteristics (Fig. 6.7).

Another large category that fail timing criteria are muon-induced electromagnetic showers. We discussed, in the previous section, some characteristics of these events (high multiplicity of streamer hits, fast triggers accompanying the events, high mul-

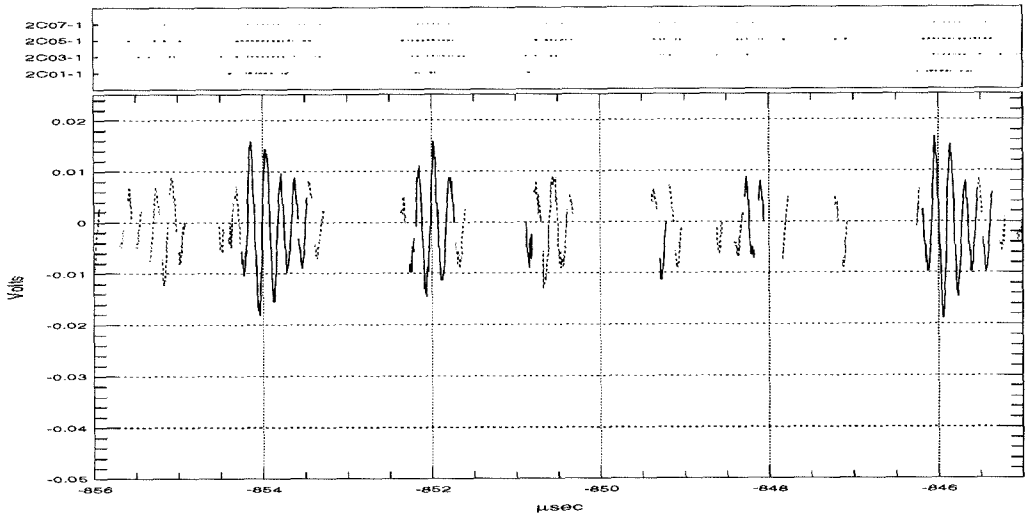


Figure 6.7: Run 11137, Event 952. A zoom in on one of the previous plots as evidence of bipolar noise waveform.

tiplicity of tanks firing the SMT, simultaneous presence of high amplitude pulses in more than one face, etc.). The "timing from the WFDs" criterion may be applied only to events that have valid WFDs. In Fig. 6.8 we show two waveforms from Run 18453, Event 3774, from the center and bottom faces. In this case, the large pulses saturated the WFD ADC and resulted in truncation. This led to an overestimate of the FWHM of the pulses and the event leaked through the WFD analysis. However, from the waveforms it is evident that the $\delta t$ between the pulses in the two faces is of the order of tens of nanoseconds; again, this is not compatible with a slow monopole and the event is rejected on timing considerations.

Events such as Run 18453, Event 3774 are accompanied by the ERP trigger. Timing from that trigger is also available and constitutes a rejection criterion, as we explain in the next section.

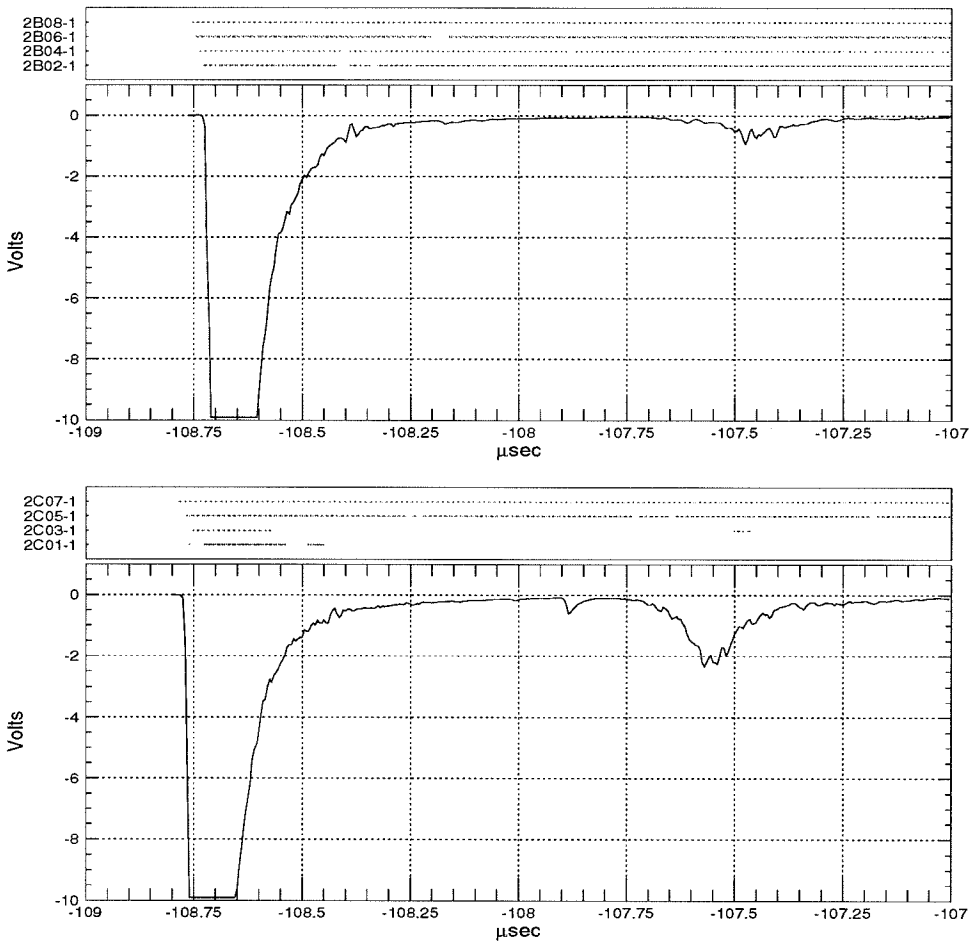


Figure 6.8: Run 18453, Event 3774. Waveforms for the center and bottom face are shown containing large amplitude pulses (simultaneously) in both faces. The pulses saturated the WFD ADC and, thus, were truncated. Time is in $\mu$s before the WFD STOP. The trailing pulse seen 1.2 $\mu$s after the main pulse is a He afterpulse.

### 6.2.3 Timing due to ERP

Recall from section 2.3.1 that the ERP (Energy Reconstruction Processor) is a scintillator trigger whose threshold is adjusted to fire on muon or larger-light-yield pulses. Its ADC, measuring the charge of the pulse, has an integration window of about 240 ns. The ERP also provides accurate timing information within 400 ns from the

first ERP trigger. If TOF is greater than 400 ns the latest boxes record only overflow values in the TDCs. If with ERP information we conclude that an event has TOF $\lesssim$ 400 ns between scintillator faces, we may safely reject the event on the basis of arguments presented in the previous section and elsewhere about the expected TOF between scintillator faces. We recall that a monopole of $\beta \simeq 4.1 \times 10^{-3}$ would cross only $\simeq$0.5 m in 400 ns. Events with more than one face firing within 400 ns should also fire the SPAM_MUON trigger, but sometimes they fail to do so, due to SPAM_MUON inefficiencies. Therefore, we reject events for which the ERP TOF between two faces is less than 400 ns.

This criterion applies only to the events which have ERP firing in all faces where the SMT fired. It rejects muon induced showers, and is helpful for events with WFD buffer overflow, i.e., where waveform timing is not available. An example of such an event is Run 11020, Event 7596. This run was characterized by SPAM_MUON inefficiency in SM6. There were 5 tanks firing the SMT, and the event passes the WFD analysis because two of the tanks had WFD overflow buffers. The ERP fired for all of the tanks that the SMT fired for, and a total of 13 tanks fired the ERP. In Table 6.1 we see a part of the ERP decoding of the event. All times of interest were

| Box | Time (ns) | SMT | Box | Time (ns) | SMT |
|---|---|---|---|---|---|
| 6B05 | -360.45 | | 6W01 | -369.52 | X |
| 6B06 | -369.55 | X | 6W02 | -371.56 | X |
| 6B07 | -372.98 | X | 6W03 | -373.69 | X |
| 6B08 | -369.07 | | 6W04 | -373.81 | |
| 6C08 | -208.04 | | 6W05 | -376.21 | |
| 6C09 | -388.07 | X | 6W06 | -367.51 | |
| 6T11 | -399.01 | | | | |

Table 6.1: Run 11020, Event 7596. Timing from ERP. The first and the fourth column show the tank names and numbers. The second and fifth show the ERP relative timing of the tanks in ns before the common STOP. In the third and the sixth column we mark (with an X) the tanks that fired the SMT.

within 400 ns of each other. The event was obviously a fast event, not compatible with a slow monopole. The high multiplicity of streamer tube hits indicated that the event was an electromagnetic shower. For purposes of illustration, a plot of the event is shown in Fig. 6.9.

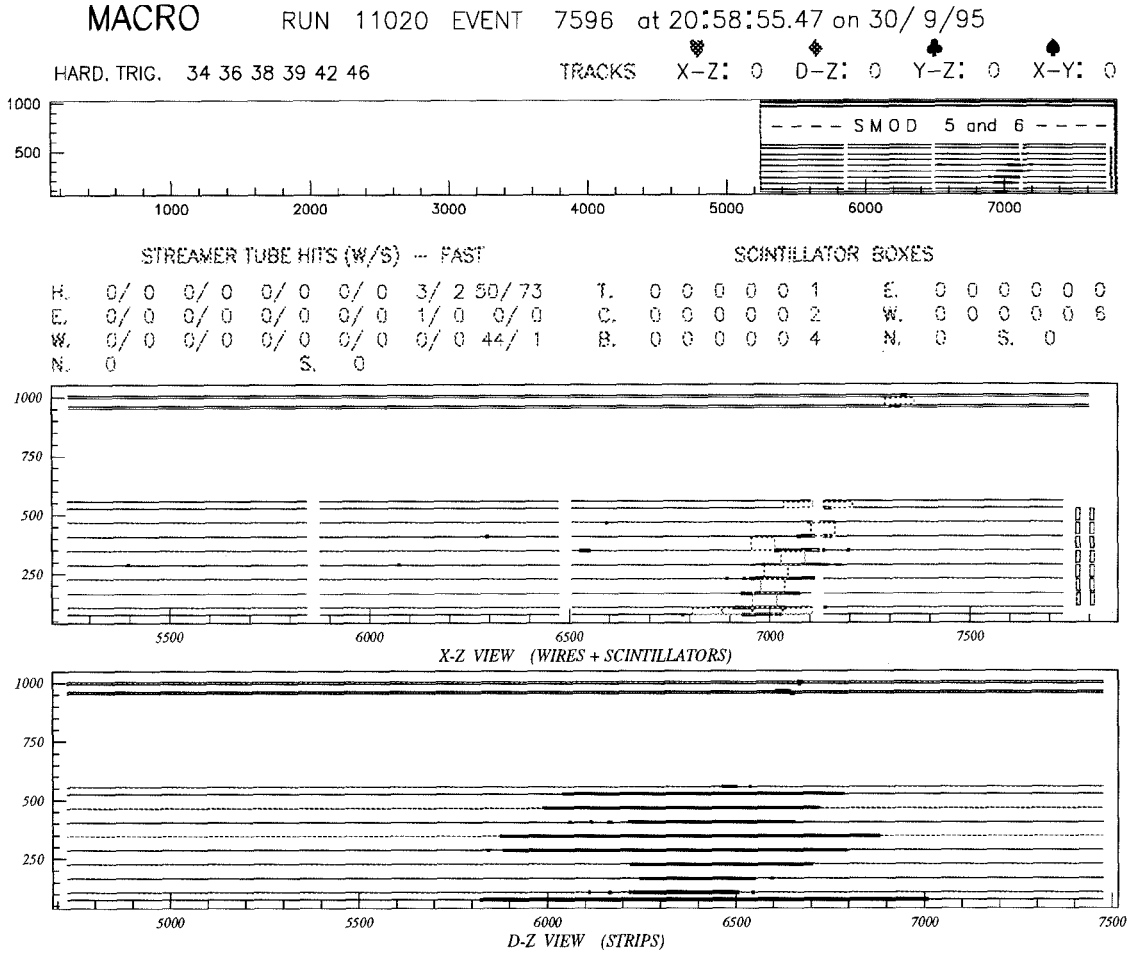


Figure 6.9: Display of Run 11020, Event 7596. Electromagnetic shower. This is a side view of SM 5 and SM 6 (looking from the west side). The horizontal scintillator counters are perpendicular to the page. The horizontal lines in the middle plot are the cross section of the horizontal streamer tube layers (the streamer tubes are vertical to the page). The fast chain is displayed, i.e., the hits are within 10 $\mu$s. The plot at the bottom is a view of the streamer strips. The scintillator counters that fire the ERP are indicated with a rectangle. In the case of vertical scintillator counters, the rectangles between streamer tube layers show the region of the tank that was hit according to the ERP. There was considerable streamer tube and scintillator activity. The electromagnetic shower mainly struck the west face.

### 6.2.4 Geometrical Considerations

Geometrical arguments were based on the fact that a slow monopole was expected to travel in a straight line. Thus, it would be impossible for the monopole to trigger a set of tanks that cannot be connected by means of a straight line. This is mostly helpful with events that have WFD buffer overflow and do not fire ERP, and accurate timing from the ERP or the WFDs was not available. Of course, it applies to some electronic noise events as well. Since in that case several other rejection criteria apply, we present as example an event for which ERP and WFD timing was unavailable. This is Run 12736, Event 3842. A plot of this event is shown in Fig. 6.10. In this event 17 tanks had an SMT: 2B05, 2B06, 2B07, 2B08, 2B10, 2B11, 2B12, 2B13, 2B14, 2C01, 2C02, 2C03, 2C11, 2C16, 2W04, 2W06 and 2W07. Of the 17 tanks involved, 16 had overflow WFD buffers, whereas one tank (2W07) had its WFD buffer missing. In particular, all of the WFD channels had ADC values below pedestal (positive voltages). We recall here that each WFD channel served four tank-ends, i.e., tank-ends 2B10-0, 2B12-0, 2B14-0, and 2B16-0 are multiplexed in one WFD channel, but a discriminator bit was set for a tank-end only if it was over threshold. In this particular case, the discriminator bit for all four tank-ends multiplexed in any channel was set for the duration of the WFD history ($\sim$125 $\mu$s), indicating that all four tank-ends were over threshold and contributing to the summed waveform. Both are indications of a hardware problem in the WFD system or a big burst of LED pulses in the lower part of the detector. Each group of four tanks was served by two WFD channels (one for each tank-end). In this event, eight WFD channels (corresponding to four groups of four tanks each) in the bottom face had buffer overflow. A real monopole would have to cross at least four tanks in the bottom face in order to induce the observed buffer overflow in all eight WFD channels. The manner in which the WFDs were multiplexed, the geometrically closest possible tanks were 2B07, 2B08, 2B10 and 2B11. It was geometrically impossible for a monopole to have a trajectory crossing these four tanks and the center face. The same was true for the center face, where once again eight WFD channels, serving 16 tanks, have buffer overflow. In the center

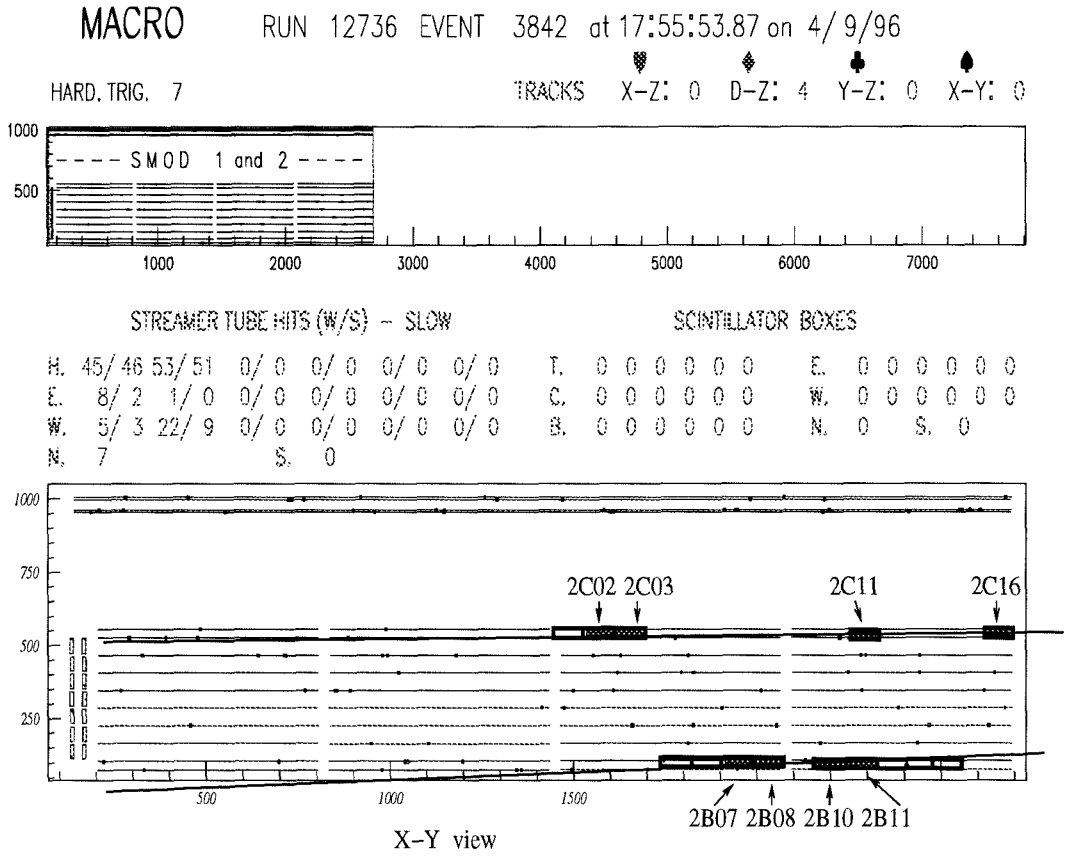


Figure 6.10: Run 12736, Event 3842. The black rectangles are the tanks that fired the SMT and had overflow WFD buffers. The filled rectangles are the geometrically closest tanks corresponding to overflow WFD buffers. The two black lines show that it is geometrically impossible for a straight line to cross all the tanks indicated by the filled rectangles in both faces.

face, the tanks geometrically closest to each other, that could induce such an effect were, tanks 2C02, 2C03, 2C11, and 2C16. A straight line crossing these tanks is not allowed to not cross any of the tanks that were hit in the bottom face. Therefore, geometrical considerations are not compatible with the passage of a single particle moving in a straight line. In all events, where we have neither ERP nor WFD timing, but rely purely on geometrical considerations, a rejection criterion based on timing from the Stop Master also applies. This is explained in the next subsection.

### 6.2.5 Timing from the Stop Master

As explained in chapter 3, the Stop Master was used to record the time of the arrival of the SMT triggers for each face. The timing from the Stop Master had a 100 ns accuracy. Moreover, the processing time of the SMT trigger had to be taken into account. This processing time was about 6 $\mu$s for the lower detector, and 20 $\mu$s for the attico. The Stop Master timing was designed to be used for time differences between faces of several $\mu$s only. Here it is used to help reject events that were not compatible with a passage of a slow particle, traveling at constant speed in a straight line.

An example of its application is Run 11887, Event 3271. This event is coincident with a data-taking period when several LED calibrations were carried out so as to finalize the calibration procedure for the SMT. There were an appreciable number of LED events during this run (as recorded by the SPU). This event involves the tanks 4B01, 4B09, 4C02, 4C14, 4T12, 4T13 and 4T14. All WFD channels corresponding to the tanks firing the SMT had filled WFD buffers. The timing in the Stop Master showed that the SMT initially fired in the bottom face, which was followed by an SMT in the center face (21 $\mu$s later) and finally by an SMT in the top face (286.5 $\mu$s later). Keeping in mind that the SMT processing time of the top face was $\simeq$14 $\mu$s longer than in the lower detector, we deduce that the pulse initiating the SMT trigger in the top face happened $\simeq$ 272 $\mu$s after that in the bottom face. The ratio

$$\frac{T_c - T_b}{T_t - T_b} = \frac{21}{272} \tag{6.1}$$

of the time differences between the triggers from the various faces is very different from the ratio of distances between the same faces (in this case $\simeq 4.5/8.9$). This is incompatible with the passage of a monopole whose velocity remains constant when crossing MACRO, and the event is rejected on that basis.

In fact, there are other criteria by which this event is rejected – like timing from the waveforms and geometrical considerations. In Fig. 6.11 and 6.12 we can see two sets of waveforms of this event. In this event the initial pulse – expected around

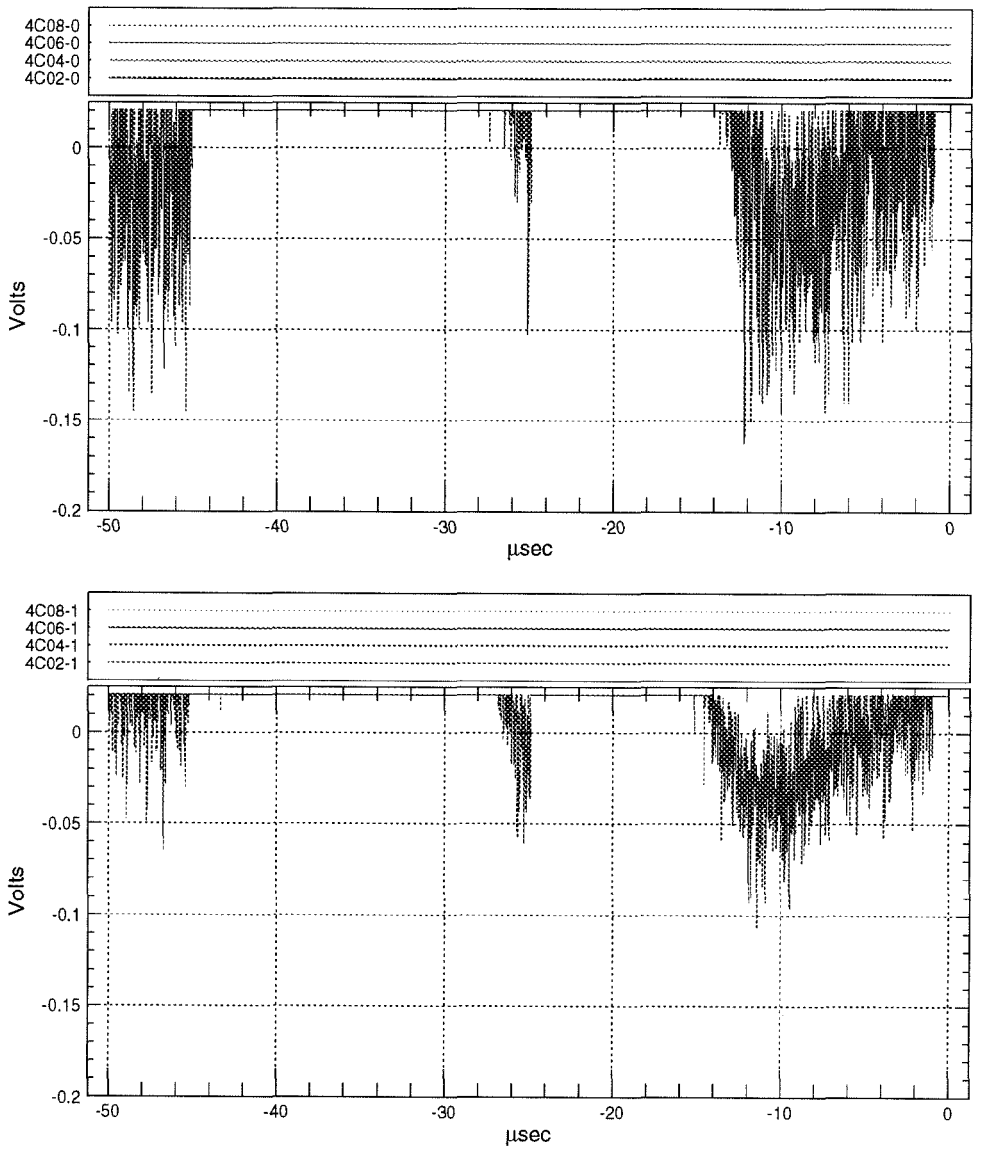


Figure 6.11: Run 11887, Event 3271. The initial pulse has been lost. The available segment of the waveform shows three pulses, something that does not agree with our expectations for a monopole. The slow rise time seen in some of the pulses is characteristic of the LED behavior.

$-1000\,\mu$s – is lost. It is noteworthy, however, that the pulses shown in the part of the WFD history that is available are not characteristic of the passage of a single particle, since there are more than a single pulse in each waveform. Moreover, pulses are present in both faces (bottom and center) at the same time, as may be seen by comparing Figs. 6.11 and 6.12. The event is probably an LED-induced event, but

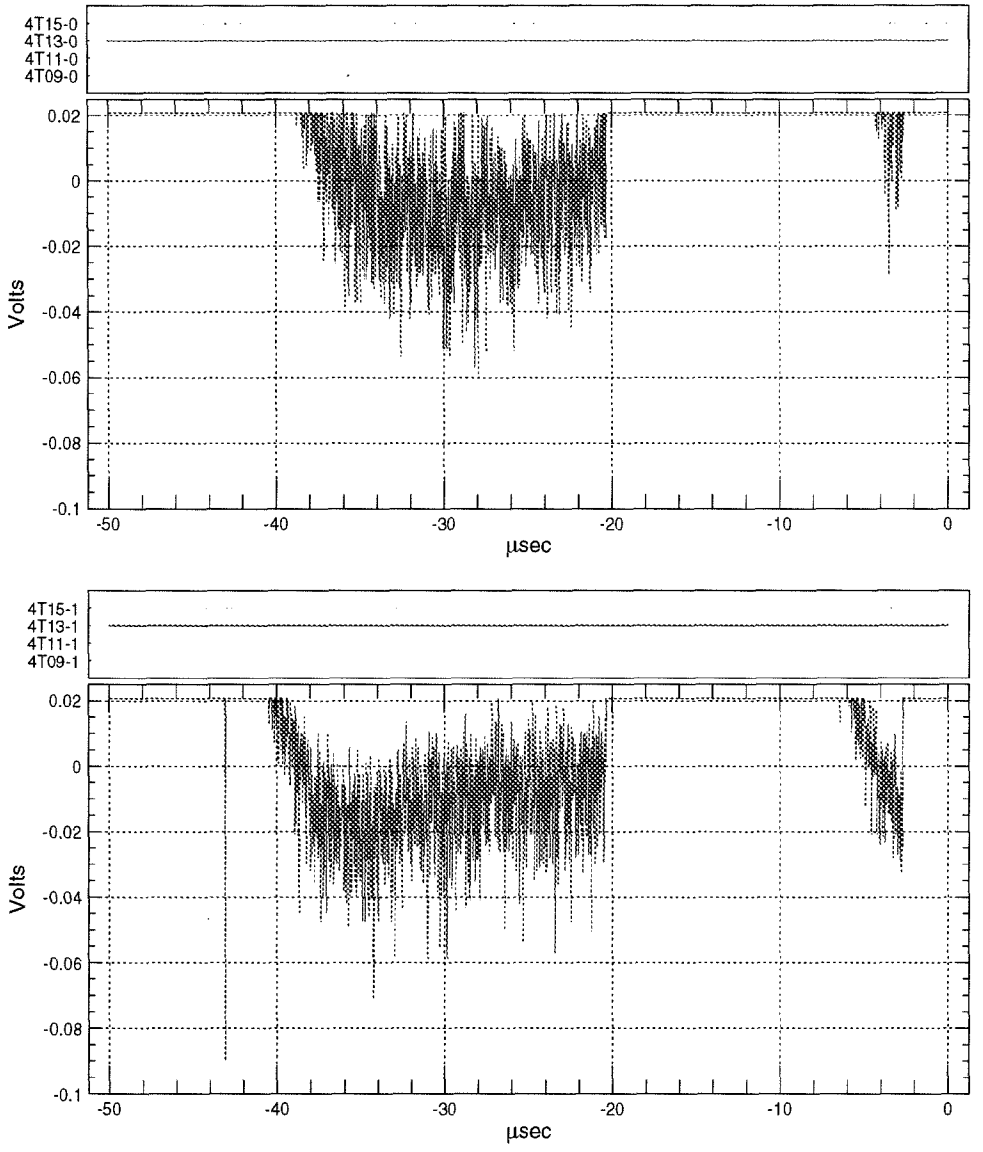


Figure 6.12: Run 11887, Event 3271.The initial pulse has been lost. The timing of the pulses shown in the available part of the waveforms overlaps with the timing of some of the pulse in the center face shown in Fig. 6.11.

there is uncertainty in this diagnosis. It is incompatible, however, with the passage of a slow monopole based on several criteria.

### 6.2.6 The LED Event

There is one clearly interesting event, Run 19441, Event 2560, for which the geometrical and timing rejection criteria do not apply, and by these considerations it was consistent with the passage of a monopole. The run was taken on a non-calibration-day and has no obvious signs of a hardware failure. SPAM_FMT fired for SM5-SM6 and SPAM_MUON fired for SM4-SM5. Two tanks were involved in the SMT: 5B09 and 5E06. The ERP also fired for these two tanks but the ERP TOF overflowed, indicating only that the TOF between the two faces was greater than 400 ns. The parts of waveforms of these two tanks that trigger the PR algorithm are shown in Figs. 6.13 and 6.14.

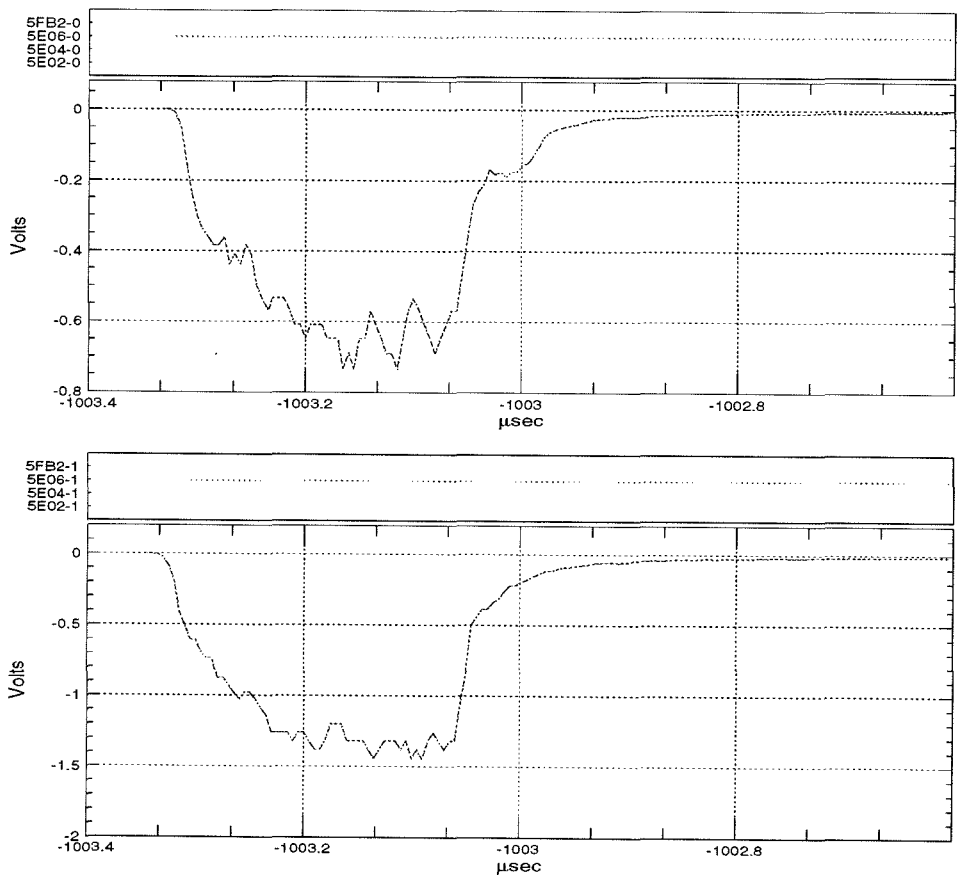


Figure 6.13: Run 19441, Event 2560. Segment of the waveforms of tank 5E06. The time axis is in units of $\mu$s before the WFD stop.

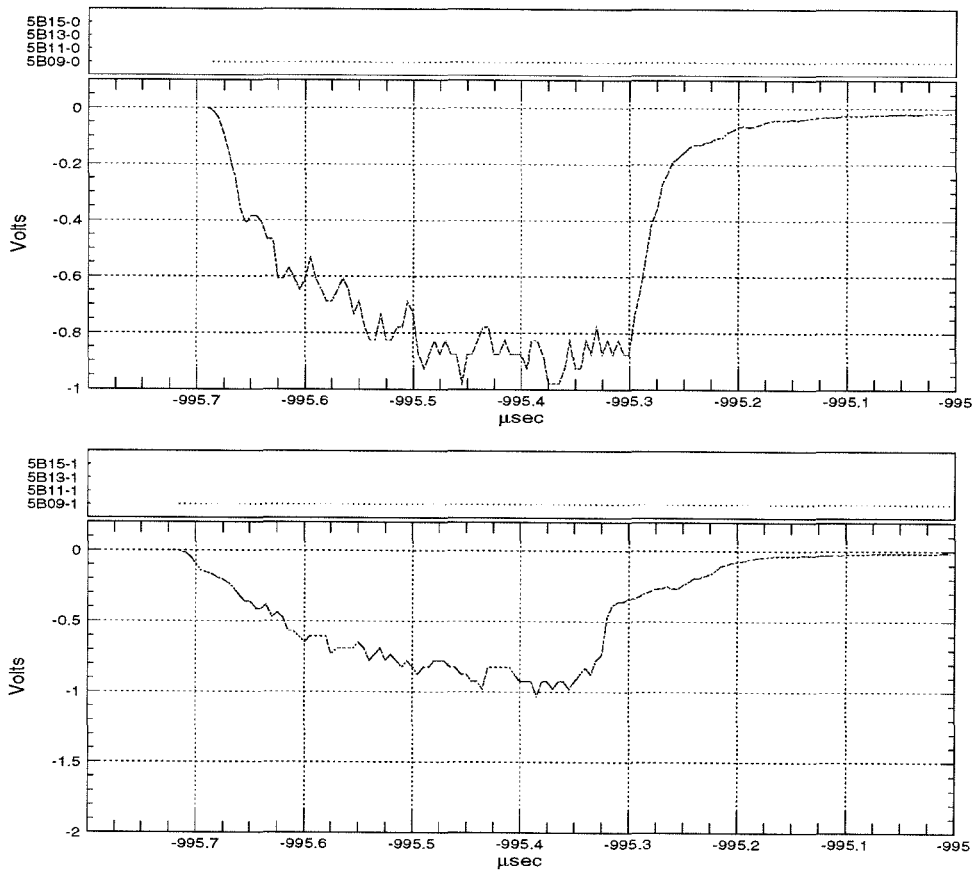


Figure 6.14: Run 19441, Event 2560. The segment of the waveforms for tank 5B09 that fires the PR algorithm. The time axis is in units of $\mu$s before the WFD stop.

The TOF estimated from the waveforms was about 7.7 $\mu$s. Streamer tube tracking was performed using both the fast and slow streamer chain (with memory depths of 10 $\mu$s and 500 $\mu$s respectively), but no streamer track crossed the two tanks. Thus, we cannot perform exact calculations of the velocity a particle with this TOF would have. We can only consider the longest and the shortest paths between the two tanks involved. This results in estimates for the $\beta$ of $1.5 \times 10^{-3} \lesssim \beta \lesssim 5.7 \times 10^{-3}$. The FWHM of the pulses in 5B09, as measured by the PR algorithm, are 350 ns and 300 ns for tank-ends 5B09-0 and 5B09-1 respectively, while for tank 5E06 the FWHMs are 240 ns and 250 ns, for tank-ends 5E06-0 and 5E06-1, respectively. From all of the above, we expect for the ratio of the pathlengths $Pl_{5E06}/Pl_{5B09} \sim 0.75$.

Then, assuming $1.5 \times 10^{-3} \lesssim \beta \lesssim 5.7 \times 10^{-3}$, we deduce 14 cm $\lesssim Pl_{5B09} \lesssim$ 56 cm and 11 cm $\lesssim Pl_{5E06} \lesssim$ 42 cm. However, the pulses have very slow rise-times, atypical of the passage of a particle. Rise-time here means the time required for the pulse to rise from 10% to 80% of its peak amplitude. Volt level pulses, resulting from the passage of particles, are expected to have very fast rise-times of order of a few nanoseconds. Alternatively, pulses with long rise times are typical of LED-induced pulses. In Fig. 6.15 we show the waveform of an LED-induced pulse of FWHM ~250 ns from a calibration run. The shape of the pulse is very similar to the shape of the pulses of this event, Run 19441, Event 2560.

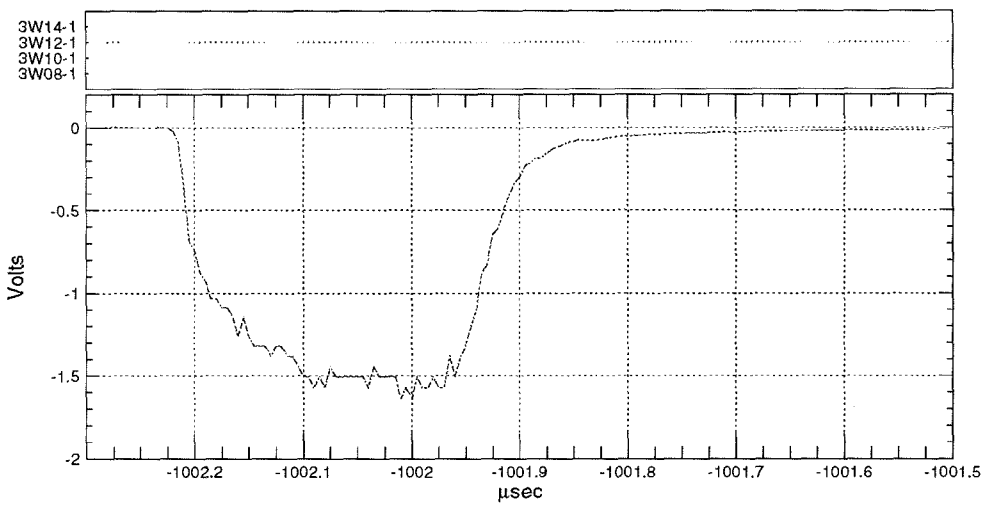


Figure 6.15: LED-induced pulse from calibration Run 91970.

We have performed a Monte Carlo, simulating monopole pulses in accordance with modeling described in section 5.2.1. We simulated pulses of 300 ns and 240 ns duration and amplitude of 800 mV to 1.2 V, similar to the ones in Run 19441, Event 2560. Two of the simulated pulses are shown in Fig. 6.16, for comparison with the pulse shapes of the pulses in event 2560 (Figs. 6.13 and 6.14). We have measured the rise-time on the simulated pulses. The result is the graph in gray plotted in Fig. 6.17. Also measured was the rise-time of LED-induced pulses in the detector. We chose pulses of 200$\leq$ FWHM $\leq$400 ns, and of amplitude between 0.6 V and 2 V.

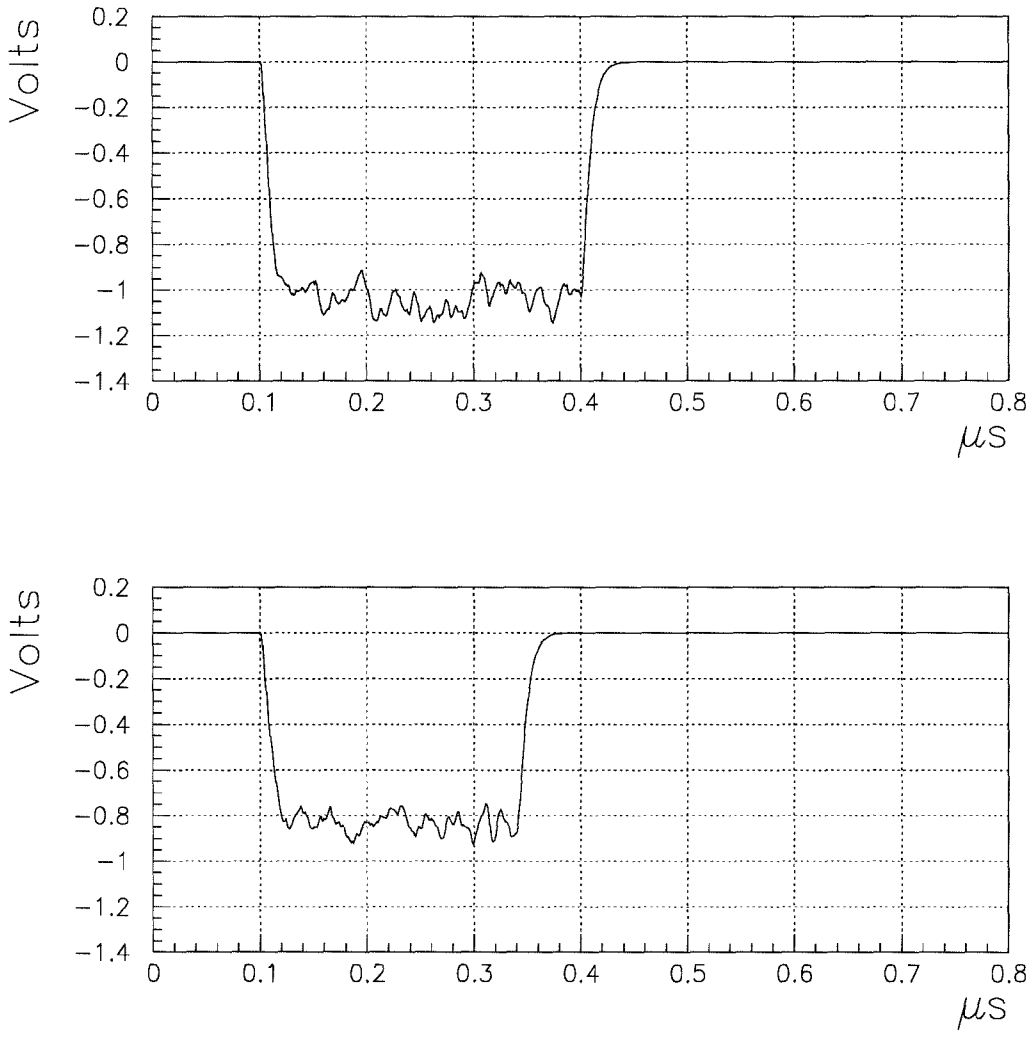


Figure 6.16: Two simulated pulses of 300 ns and 240 ns duration. The rise-time (10% to 80% of maximum) of the pulses is of the order of 10 ns.

The resultant graph is shown also in Fig. 6.17. The rise time of the four pulses in Run 19441, Event 2560 is shown in the same figure; it is obvious that Run 19441, Event 2560 does not comply with our expectations of a monopole-induced pulse. Instead, it appears to be an LED event.

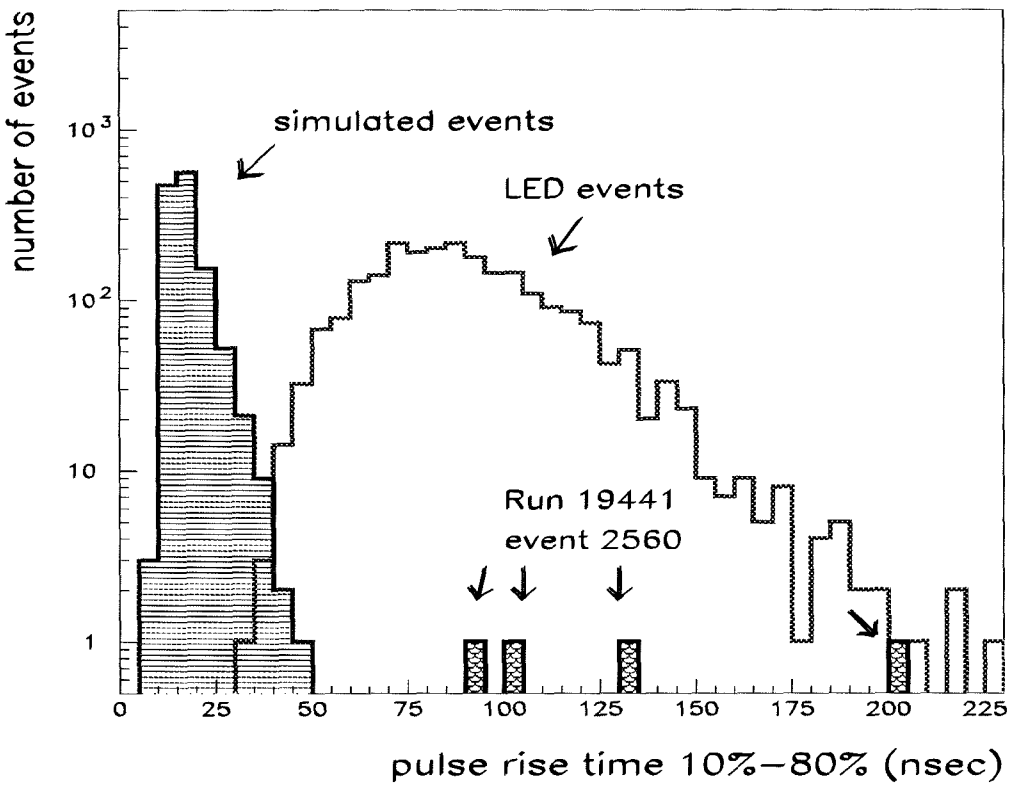


Figure 6.17: Rise time (time from 10% to 80% of maximum amplitude) for simulated monopole pulses (hatched plot), LED pulses (not hatched plot) and the four pulses of the event 2560 in run 19441 (hatched isolated points).

**Addendum**

After this analysis was performed, it was brought to the author's attention that the event described in this section (Run 19441, Event 2560) was *indeed* an LED-induced event purposely generated by two members of the scientific staff, in accordance with the American spokesman. The purpose of this psuedo-event was to test the ability of the scintillator-based analyses to detect and extract an event closely resembling a magnetic monopole, and to subsequently find valid argruments for the event's final acceptance or rejection.

In fact, further analysis of the event showed other inconsistencies with the passage of a slow monopole. In particular, the amount of light detected in the two ends of a tank is not compatible with the arrival time of the pulses in these tank-ends. This effect is evident in tank 5E06. Integration of the waveforms showed that the charge of the pulse in tank-end 1 was $\simeq 2.1$ times the charge of the pulse in tank-end 0. This means that if the pulse is due to the passage of a particle then the particle passed much closer to tank-end 1. The PMT responce H as a function of the distance x from the end of a tank is

$$H(x) = \frac{\alpha_1}{x^2} + \alpha_2 exp(-x/\alpha_3) + \alpha_4 exp(-x/\alpha_5), \tag{6.2}$$

where $\alpha_i$ are experimentaly measured fitting constants. Then, for each tank we can plot the ratio $R$ of the PMT responce in the near tank-end to the PMT responce in the far tank-end as a function of distance from the near tank-end. In the case of tank 5E06, this plot is shown in Fig. 6.18.

From this plot we see that in the case of Run 19441, Event 2560 the ratio of charge of the pulses in the two tank-ends, R=2.1, corresponds to distance $x \simeq 1.1$ m from thank-end 1 (10.1 m from tank-end 0). This is graphically illustrated in Fig. 6.19. The extra $\simeq$9 m the light would travel to reach tank-end 0 should result in a time delay of $\simeq$ 44 ns of the pulse in tank-end 0 with respect to the time of the pulse in tank-end 1. However, this did not happen in this event. Instead, the pulse in tank-end 0 reached 10% of its maximum amplitude 10 ns before the pulse in tank-end 1

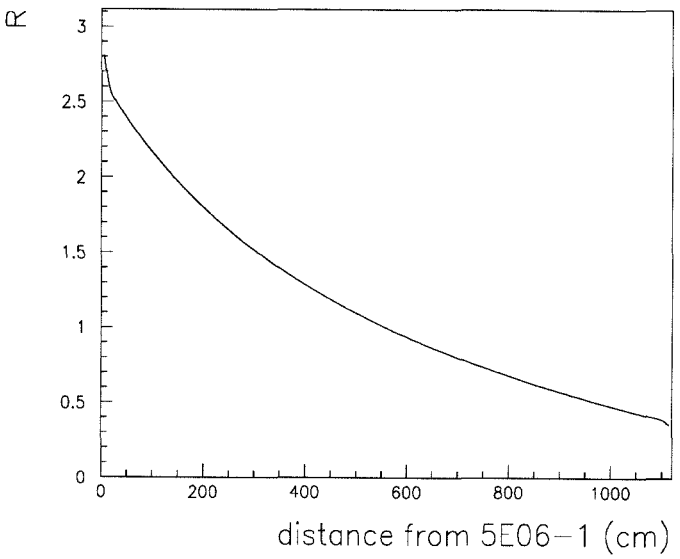


Figure 6.18: Ratio of the PMT responce in 5E06-1 to the PMT responce in 5E06-0 as a function of distance from 5E06-1.

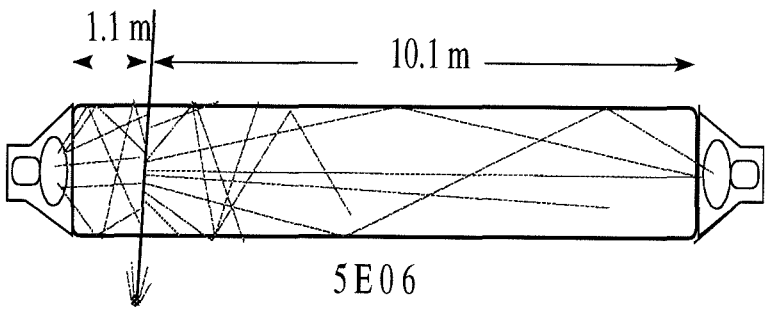


Figure 6.19: Graphic illustration of light propagation in tank 5E06 in Run 19441, Event 2560.

did, indicating that the event is not compatible to the passage of a single particle through the tank. Moreover, the timing of the two pulses recorded by ERP resulted in a position of the event $\simeq$ 4.74 m from tank-end 1, which is in conflict with the location stated above.

Concluding the section devoted to this very particular event, the author is very

happy to have confirmed with this blind test the already demonstrated (in chapters 3 and 5) capability of this search to detect magnetic monopoles of a wide range of light yields and velocities.

### 6.2.7 Analysis Conclusions

Thus we conclude that out of the 40 events that survive WFD analysis,

- 25 are electronic noise events
- 10 are muon induced-electromagnetic showers in the detector
- 4 are not diagnosed with certainty, but are probably calibration related events
- 1 is an LED-induced event

This search has not found any slow monopole candidates.

In Tables 6.2 to 6.5 we summarize the events and the rejection criteria each failed. In the tables, "N SMT" is the number of tanks that fired the SMT, "N PR" is the number of tanks that passed the PR algorithm, "StM time" stands for Stop Master timing, "Geo" stands for geometrical arguments and STR is the number of streamer tube hits in the fast chain in the relevant supermodule. The number of streamer tube hits is not a rejection criterion, as we have already pointed out, but it is displayed for informational purposes. With an "X" we mark the rejection criteria that apply for each event, with a "-" the ones that don't. Finally, in the diagnosis column, by "el. noise" we mean electronic noise event, by "e/m sh." we mean muon-induced electromagnetic showering event and by "unid/fied" we mean unidentified.

In the following chapter we will study the performance of the hardware that was used in this search. In chapter 8, we present the result of Monte Carlos based on the performance of the hardware, which calculate the exposure of the detector for this search. Having found no slow monopole candidates, a monopole upper flux limit is given in the same chapter.

| Run | Event | N SMT | N PR | WFD shape | WFD time | ERP time | StM time | Geo | STR | Diagnosis |
|---|---|---|---|---|---|---|---|---|---|---|
| 10607 | 2683 | 20 | 8 | X | X | - | - | X | 1232 | el. noise |
| 10658 | 3488 | 17 | 3 | X | X | - | - | - | 1251 | el. noise |
| 10772 | 2756 | 15 | 8 | X | X | - | - | - | 1223 | el. noise |
| 10772 | 2958 | 24 | 11 | X | X | - | - | X | 1810 | el. noise |
| 10868 | 9889 | 14 | 9 | X | X | - | - | X | 802 | el. noise |
| 11068 | 5063 | 18 | 7 | X | X | - | - | - | 1067 | el. noise |
| 11128 | 202 | 16 | 7 | X | X | - | - | - | 1246 | el. noise |
| 12159 | 4436 | 16 | 5 | X | X | - | - | - | 331 | el. noise |
| 13281 | 10500 | 13 | 5 | X | X | - | - | - | 0 | el. noise |
| 13281 | 10508 | 21 | 6 | X | X | - | - | X | 1 | el. noise |

Table 6.2: Rejection criteria for events passing the WFD analysis

| Run | Event | N SMT | N PR | WFD shape | WFD time | ERP time | StM time | Geo | STR | Diagnosis |
|---|---|---|---|---|---|---|---|---|---|---|
| 13499 | 615 | 7 | 2 | X | X | - | - | - | 1 | el. noise |
| 13558 | 10149 | 10 | 3 | X | X | - | - | - | 9 | el. noise |
| 14314 | 9363 | 7 | 2 | X | X | - | - | - | 1 | el. noise |
| 14314 | 9365 | 6 | 2 | X | X | - | - | - | 1 | el. noise |
| 15602 | 7328 | 5 | 2 | X | X | - | - | - | 1 | el. noise |
| 16854 | 6064 | 11 | 5 | X | X | - | - | - | 1 | el. noise |
| 16854 | 6208 | 11 | 7 | X | X | - | - | - | 1 | el. noise |
| 16854 | 6231 | 10 | 8 | X | X | - | - | - | 2 | el. noise |
| 16854 | 6234 | 11 | 10 | X | X | - | - | X | 2 | el. noise |
| 16854 | 6240 | 12 | 6 | X | X | - | - | - | 1 | el. noise |

Table 6.3: Rejection criteria for events passing the WFD analysis

| Run | Event | N SMT | N PR | WFD shape | WFD time | ERP time | StM time | Geo | STR | Diagnosis |
|---|---|---|---|---|---|---|---|---|---|---|
| 16854 | 6259 | 9 | 7 | X | X | - | - | X | 4 | el. noise |
| 16854 | 6260 | 10 | 4 | X | X | - | - | - | 2 | el. noise |
| 17030 | 8093 | 11 | 2 | X | X | - | - | - | 2 | el. noise |
| 17359 | 6094 | 15 | 5 | X | X | - | - | - | 0 | el. noise |
| 11137 | 952 | 13 | 5 | X | X | - | - | - | 190 | el. noise |
| 11664 | 11 | 15 | 15 | - | - | - | X | X | 0 | unid/fied |
| 11887 | 3271 | 7 | 7 | X | X | - | X | X | 0 | unid/fied |
| 12736 | 3842 | 17 | 16 | - | - | - | X | X | 1 | unid/fied |
| 12736 | 4071 | 10 | 9 | - | - | - | X | X | 2 | unid/fied |
| 19441 | 2560 | 2 | 2 | X | - | - | - | - | 3 | LED |

Table 6.4: Rejection criteria for events passing the WFD analysis

| Run | Event | N SMT | N PR | WFD shape | WFD time | ERP time | StM time | Geo | STR | Diagnosis |
|---|---|---|---|---|---|---|---|---|---|---|
| 11020 | 7596 | 5 | 2 | - | - | X | - | - | 236 | e/m sh. |
| 11020 | 9401 | 2 | 2 | - | - | X | - | - | 110 | e/m sh. |
| 11047 | 8060 | 6 | 4 | - | - | X | - | - | 177 | e/m sh. |
| 11738 | 1575 | 8 | 6 | - | - | X | - | - | 337 | e/m sh. |
| 11898 | 11064 | 15 | 7 | - | - | X | - | - | 463 | e/m sh. |
| 12726 | 5987 | 19 | 14 | - | - | X | - | - | 1658 | e/m sh. |
| 14468 | 2230 | 10 | 3 | - | X | X | - | - | 322 | e/m sh. |
| 18453 | 3774 | 13 | 5 | - | X | X | - | - | 971 | e/m sh. |
| 18875 | 8789 | 9 | 5 | - | X | X | - | - | 124 | e/m sh. |
| 19236 | 10491 | 14 | 9 | - | X | X | - | - | 665 | e/m sh. |

Table 6.5: Rejection criteria for events passing the WFD analysis

# Chapter 7

# Hardware Performance Analysis

Various hardware systems were employed in this search for slow magnetic monopoles. The proper operation of these was fundamental to the flow of this analysis and for proper calculation of the eventual acceptance (see chapter 8). To be precise, the study of the hardware performance levels involved monitoring around 1000 channels of the Slow Monopole Trigger, the Stop Master units serving these channels, and the 250 channels of the Waveform Digitizers; all of this over a period of four years and eight months of running time. During this period, automatic jobs were launched at the end of each run which computed statistics based on the full data set. We used these statistics to verify proper functioning of the hardware systems.

## 7.1 The SMT Performance

The general statistics file, compiled at the termination of each run, contained useful information about all SMT channels in the detector. This information was used to identify dead channels. Since the slow monopole trigger rate for each scintillator tank was small, we have used weekly rates, i.e., for each tank we measured the trigger rates over a livetime of 10,080 min. Trigger rates were measured in this manner for a "live week" for every tank and recorded in units of triggers per minute. An example is shown in Fig. 7.1 for a typical tank (in this case, 6B01).

The SMT was a low threshold trigger, thereby susceptible to noise, to the He content in the tubes, etc.; the SMT trigger rate varied temporally not only for each tank, but also from one tank to the next. We plot the weekly SMT rate distribution for each of the 476 tanks in the detector in Fig. 7.2. Large differences may be noted between horizontal and vertical tanks, as is also pointed out in Table 7.1. This is

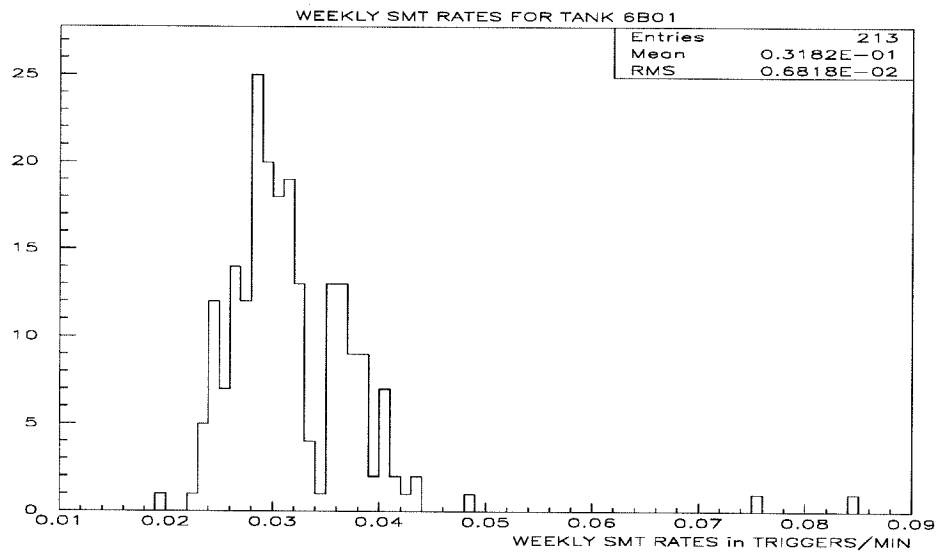


Figure 7.1: Weekly SMT rates for tank 6B01.

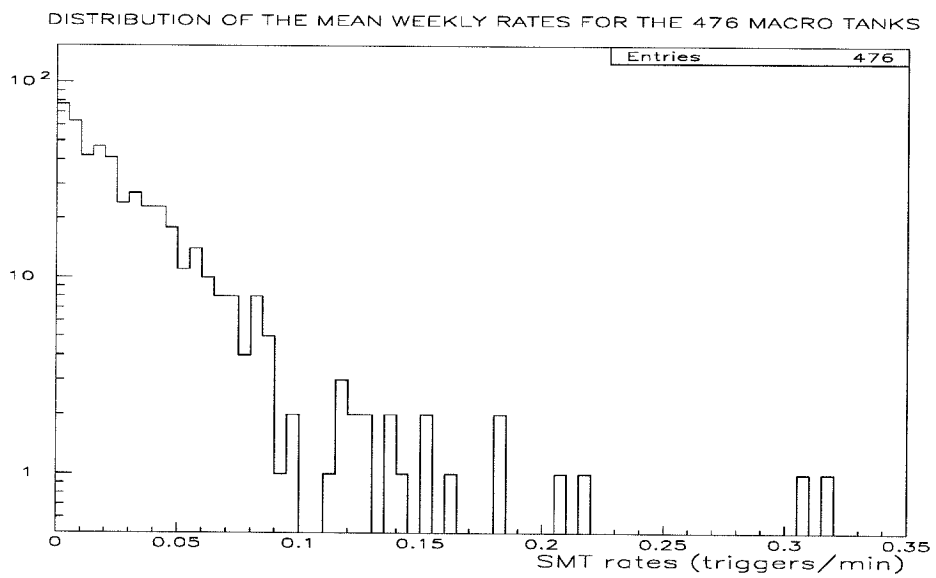


Figure 7.2: Distribution of the mean weekly SMT rates for the 476 Macro tanks.

| tanks | mean of weekly smt rates (triggers/min) |
|---|---|
| B01-B16 | 0.040 |
| C01-C16 | 0.042 |
| W01-W07, E01-E07 | 0.021 |
| W08-W14, E08-E14 | 0.005 |
| T01-T17 | 0.050 |
| N01-N07/S01-S07 | 0.011 |

Table 7.1: Average of weekly SMT rates for the different detector faces.

due to different light-collection efficiency of the two kinds of tanks and due to use of different PMT tubes (Hamamatsu) for the attico lateral tanks (W08-1W14, E08-E14). Hamamatsu tubes had lower afterpulsing rates than EMI tubes (appendix A), which resulted in lower trigger rates. Based on the weekly SMT rates, we establish the minimum time interval a tank has to remain inactive in order to be considered dead. We calculate a minimum trigger rate by excluding the lowest 3.5% outlier rates, and noting the lowest remaining non-zero rate. Based on this rate, we calculate the time interval $t_d$ for which the tank may show no trigger with probability of $3 \times 10^{-7}$. Whenever a tank showed SMT inactivity for a time interval equal to or greater to $t_d$, the tank was considered dead to the SMT. By this criterion, during the entire (approximately 4.75 years or $2.5 \times 10^6$ min of) data taking period a tank was expected to appear dead approximately once, due to an accidental lack of triggers.

In addition to the SMT monitoring, the ERP system was used to check if a tank was dead for short terms due to urgent or non-scheduled maintenance (usually due to a malfunctioning phototube). ERP rates were high enough (with a mean of 0.18 triggers $\text{min}^{-1}$ for horizontal tanks, 0.10 triggers $\text{min}^{-1}$ for vertical tanks) to allow us to evaluate the condition of a tank on a run-by-run basis. If a tank had no triggers in ERP or SMT for more than 340 min, it was considered dead for SMT purposes

for that duration. The reduction in the acceptance due to the loss of a single tank is less than 1% of the eventual acceptance, so the occasional loss of a tank did in no way severely limit the analysis.

In acceptance calculations performed on a run-by-run basis, after the exact configuration of dead channels was used, the decrease in exposure due to this cut was around 6%.

## 7.2 The WFD Stop Master Performance

The Stop Master in each supermodule was used to halt the WFDs, and this was described in some detail earlier in chapter 2. Here, we recall that it recorded the various trigger times to 100 ns accuracy. In addition, we recall that it recorded the face(s) that had had a slow monopole trigger and time-tagged these triggered faces.

The Stop Master was used, in the analysis flow, to decide whether an event was a valid two-or-more face monopole event. This was done by checking the state of two logical bits, the *intraSM* and the *crossSM coincidence* bits, which indicated whether two-or-more faces in the detector had had SMT triggers within 1 ms. In addition to the coincidence bits, the recorded times for the SMTs from the various faces of the detector were used in the analysis. For all the faces that had had an SMT within 1 ms of the first SMT trigger, the recorded arrival times ought to have had values less than the overflow value of the Stop Master counter (around 10000 counts). Thus, a valid two-face event had at least two faces with non-overflow value of the Stop Master counter. Correct functioning of the Stop Master was necessary for both the hardware-trigger based and the software based recognition of a slow monopole; for this reason its functioning has to be evaluated for the entire data taking period. Several checks were performed using data recorded in the statistics files.

### 7.2.1 The Counters

The first items to check were the Stop Master counters and these, as mentioned before, recorded times-of-arrival of faces that had had an SMT. For this, the average

overflow value of counters (for each run) was examined; the overflow value should be around the programmed $10^4$ counts (corresponding to 1 ms). The distribution of the average overflow value of the Stop Master counters is displayed in Fig. 7.3. One entry

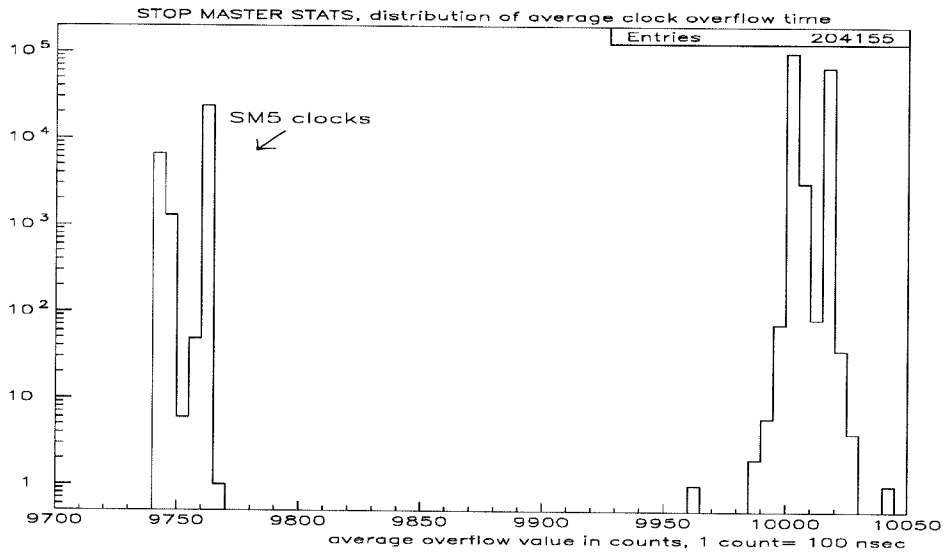


Figure 7.3: SMT counters of the Stop Master. Distribution of overflow values averaged for each run.

is made for each run and each face (each counter) with average overflow value greater than zero. Note that SM 5 counters had somewhat peculiar yet acceptable value. We exclude a face, for any run, when the value was greater than 10100 or less than 9700 counts (corresponding to 1.01 ms and 0.97 ms, respectively). The only effect of this cut was to exclude faces with zero average overflow value and was relatively benign. A zero average overflow value for the counters meant that either the Stop Master was dead, or the SMT for that supermodule had had no triggers during the run. Even the quietest supermodule, with an overall SMT trigger frequency of 16 mHz, had a probability of less than $2 \times 10^{-9}$ of having no triggers during a 20 min or longer run. Thus, faces with zero average overflow are considered dead and excluded from the data set. The total effect of this cut on exposure is around 0.6%, and mostly reflects a dead Slow Monopole Trigger for a whole supermodule. For very few instances was the malfunction attributable to the Stop Master itself.

### 7.2.2 Discussion of the Stop Master and the SMT

In addition to examining the counters, it was important to check whether the triggers arriving from the different faces of the SMT were recorded properly. For every SMT trigger on a face, a bit should have been set in the Stop Master identifying the face that had fired, along with the time-word corresponding to that face. Thus, for each event, we compared the information recorded in the SMT latches to that recorded in the Stop Master latches.

General checks, such as the presence of any SMT hits in a supermodule during runs longer than 20 min, were done initially. We reiterate that as there was negligible probability of no SMT hits, supermodules with no SMT related Stop Master bits were considered dead for the purposes of our acceptance calculation.

More specific checks for individual faces were performed on a run-by-run basis. The number of SMT triggers during a run (again, for each face of the detector) was compared with the number of times the Stop Master had recorded (by means of a non-overflow value of the counter) the arrival of an SMT from that face. Here, it was important to keep in mind the hardware differences between the two pieces of electronics: the SMT could receive triggers even when the computer BUSY signal was active. This resulted in triggers that were latched in the SMT but were not recorded elsewhere in the equipment. Their excess depended on the dead time percentage of the microVAX, which varied from run-to-run. The presence of malfunctioning photomultipliers with very high SMT rate increased this dead time percentage, as the acquisition was required to read larger event rates.

We check the *one-face* SMT triggers (i.e., SMT triggers involving a single face only in a microVAX). In these cases, if a face was active in both supermodules served by the same microVAX, we expect a deficit between SMT hits and Stop Master hits of around 0.3% (for that face). The typical time spent by acquisition in reading an event was $\simeq 0.11$ s. A face with an SMT rate of 0.03 triggers $s^{-1}$, in both SMs served by the microVAX, would have about $0.11 \times 0.03 \simeq 0.3\%$ of its triggers arriving during active acquisition of an event in the same face of the adjacent SM. These events would

be one-face SMT, but the Stop Master would not record them as they arrive while the computer BUSY signal was asserted. In Fig. 7.4, we plot the ratio of the number of times the SMT is recorded in the Stop Master to the total number of the SMT one-face events during a run. There is one entry for each face and for each run, while 90% of the entries are in the bin near 1. Note that there are instances of ratios smaller than expected.

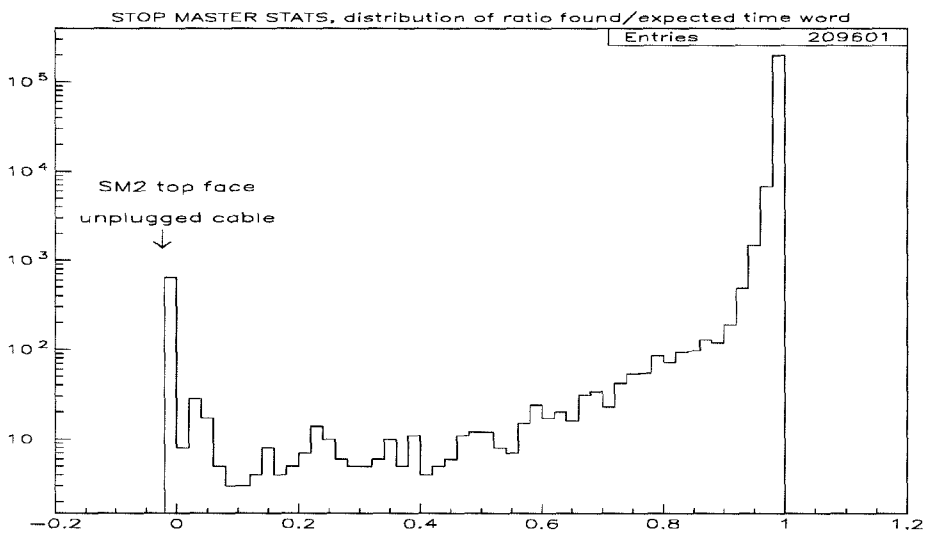


Figure 7.4: Distribution of the ratio recorded to expected Stop Master hits for one face events for all Stop Master faces and all supermodules during the data-taking period. The small values of the ratio occur mainly in the unstable, initial data-taking period.

Under closer examination, we are able to identify that the cases with ratio less than 0.4 come from the following:

- about 47% from runs during the initial, less stable data taking period, especially during the installation of the attico SMT trigger. During that period, there were problems with the SMT electronics (mainly power supply problems) and these were manifested in the Stop Master as incorrectly recorded bits and time-words.

- 46% were due to an unplugged cable in SM 2 top-face between runs 12213 and 14752.

- 6% were due to a tank with an abnormally high SMT rate in SM 2 west face between runs 12523 and 12580.

A zoom into the previous figure, plotted in Fig. 7.5, shows that the ratio is correctly nested around 0.998. From the above considerations, we exclude faces where the recorded one-face SMT hits on the Stop Master are fewer than 97% of the total number recorded on the SMT. This eliminates around 1.3% of the face-run combinations.

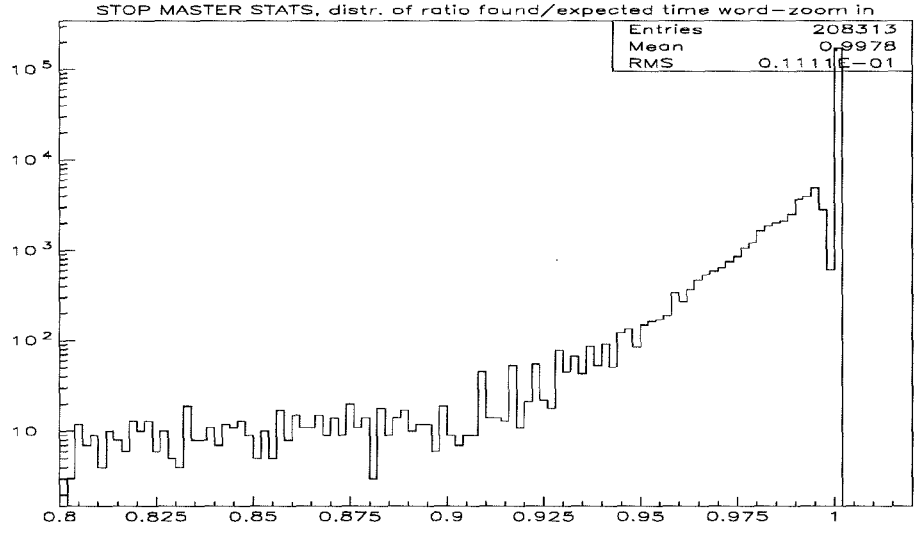


Figure 7.5: Zoom in on the distribution of the ratio recorded-to-expected Stop Master hits for one-face events.

When statistics for one-face events are inconclusive, we perform the cut using all SMT events involving that face. We expect that the ratio of the number of the times SMT hits were recorded in Stop Master to the number of total SMT hits in the run for each face to be of the order of the dead time in the microVAX (~3%); this is because when the compute BUSY signal is asserted, the Stop Master does not record any triggers. In fact, the distribution of the above ratio is peaked around 97% as shown in Fig. 7.6. Once again, small values of the ratio signal hardware errors, either with the Stop Master or with the SMT. We exclude, from the analysis, faces with the above ratio less than 0.9. That throws away an additional 1.2% of face-run

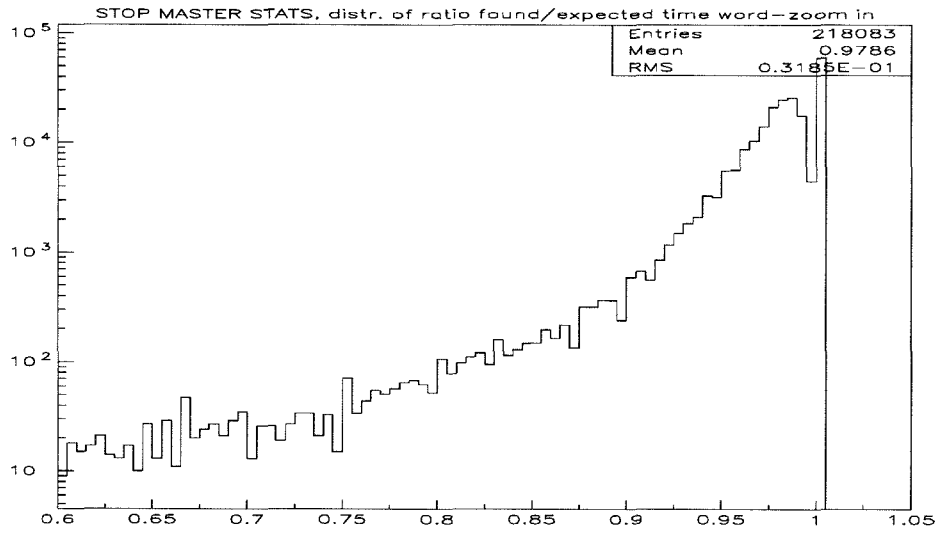


Figure 7.6: Zoom in on the distribution of the ratio recorder-to-expected Stop Master hits for all SMT events for all Stop Master faces.

combinations.

### 7.2.3 Stop Master "Fake" Hits

Another indication of Stop Master malfunction is "fake" hits. These are hits recorded by the Stop Master which are not latched in the corresponding face of the SMT. The presence of many fake hits flagged the existence of some form of hardware malfunction. The main instances were due to

- problems in the Scintillator Pattern Unit (SPU). We recall here that the SPU recorded scintillator triggers (and the Slow Monopole Streamer tube trigger), and controlled the readout of the SMT and other scintillator equipment.

- an SMT hardware problem of the unit serving the top face of SM 6, that due to a bad connection, would not properly transfer the latched data to the CAMAC back-plane.

The above situations affect the total acceptance for several runs, but there were also instances when the presence of fake hits did not present any complications for the

acceptance; for example, when miscabling would exchange the center and west faces for SM 1 in the Stop Master.

Fake triggers could appear if the Stop Master stayed alive for the SMT for 1 ms after the first trigger, while the computer BUSY might already be set in the SPU. As a consequence, the SPU might not record the presence of an SMT trigger and the SMT latches would not be read. The distribution of the ratio of the number of fake hits for a face to the number of total SMT hits for that same face is shown in Fig. 7.7. In order to get good statistics, we plot faces with more than 100 SMT hits and exclude big outliers from the plot. We eliminate cases where the presence

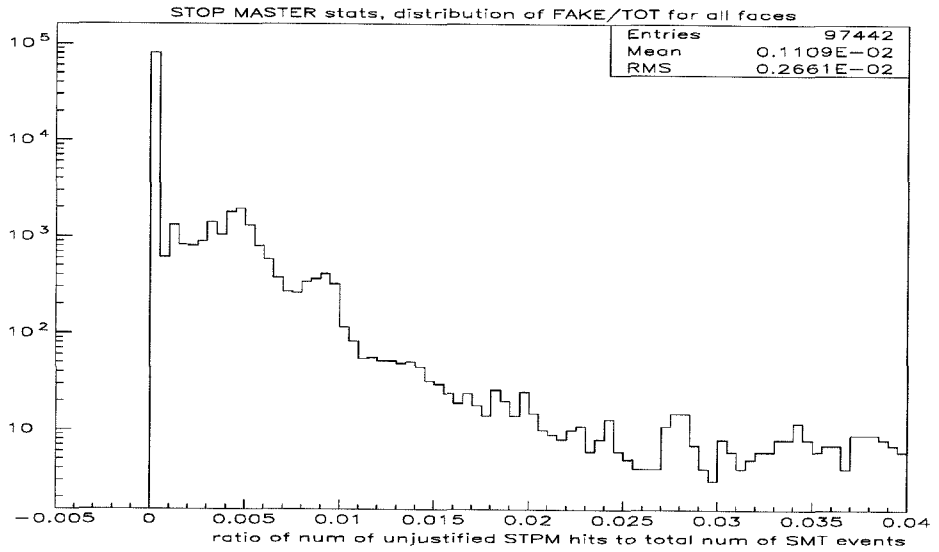


Figure 7.7: Zoom in on the distribution of the ratio of unjustified Stop Master hits to total SMT hits for faces with more than 100 hits.

of many fake hits would indicate hardware problems. More specifically, we ignore the first two fake hits for a given run in a face, and we exclude faces with a ratio of remaining fake hits to total hits greater than 0.008. This cut additionally effects approximately 1.8% of face-run pairs.

### 7.2.4 Discussion of the Stop Master and the Face Coincidence

There are two logical bits set, in each Stop Master, on the arrival of SMT triggers from two faces in the detector within a duration of 1 ms: the *intraSM* bit is set when the two faces are in the same supermodule, and the *crossSM* bit is set when the two faces are in adjacent supermodules. For the analysis flow, the presence of one of these bits is required for an event to be considered a genuine two-face monopole event with valid timing. The frequency of assertion of the intraSM and crossSM bits was typically 5 and 8 mHz, respectively; the probability of having no intraSM assertion in a 30 min run was less than $1.6 \times 10^{-4}$ and supermodules with zero occurrence of either coincidence bit (intraSM or crossSM) were considered dead for purposes of the analysis.

The function of intraSM and crossSM bits was further checked by compairing the information from the SMT with the information in the Stop Master. It was important to keep in mind the considerations made in section 7.2.2 (different treatment of computer BUSY between SMT and Stop Master), when computing the ratio of the observed to expected number of times the two bits are set. The presence of a hot tank in any face of a supermodule might create a large deficit (20-30%) in the observed-to-expected intraSM ratio. That happened because frequent firing of that tank during dead time would cause many spurious two-face SMT triggers in the SMT latches. In fact, the reason this bit was used in the analysis was to crop out all those events where hot tanks fire along with other triggers and created spurious two-face monopole triggers. In Fig. 7.8 we plot the ratio of the actual occurrence of the intraSM bit to that expected, again for all runs with duration longer than 20 minutes. We plot this ratio vs. the number of total SMT triggers of the supermodule. The clear dependence of the ratio on the number of SMT triggers allows us to conform the cut along the lines in Table 7.2.

The exclusion cut which affects an entire supermodule, was not applied when an individual face in the supermodule has already been identified as problematic in

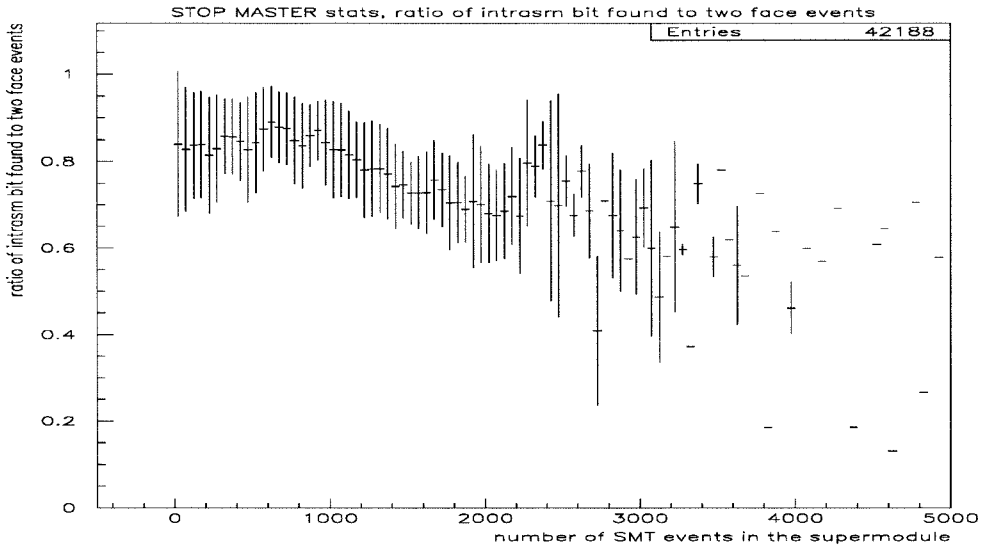


Figure 7.8: Ratio between number of times the intraSM bit is set in the Stop Master to the number of two-face SMT events (as recorded by the SMT) versus the number of SMT triggers in the supermodule. The error bar shows the RMS of the ratio.

| total SMT in the sm | cut applied below the ratio |
|---|---|
| 0-1200 | 0.7 |
| 1200-2000 | decreasing linearly from 0.7 to 0.6 |
| $> 2000$ | 0.6 |

Table 7.2: Formulation of the intraSM bit cut.

accordance with the checks described in section 7.2.2. In this case, just the identified face was excluded.

Finally, the crossSM bit was checked. Tanks firing the SMT within the dead time would also result in a deficit between the number of times the crossSM bit was set and the number of times the SMT recorded two-face triggers. In Fig. 7.9 we plot the distribution of the ratio of the number of times the crossSM bit was set to the number of two-face SMT triggers involving adjacent supermodules. Small numbers of this ratio signal hardware problems. When this ratio is less than 0.6, we judge the supermodule to have a problem with the crossSM bit, and it was cut from the

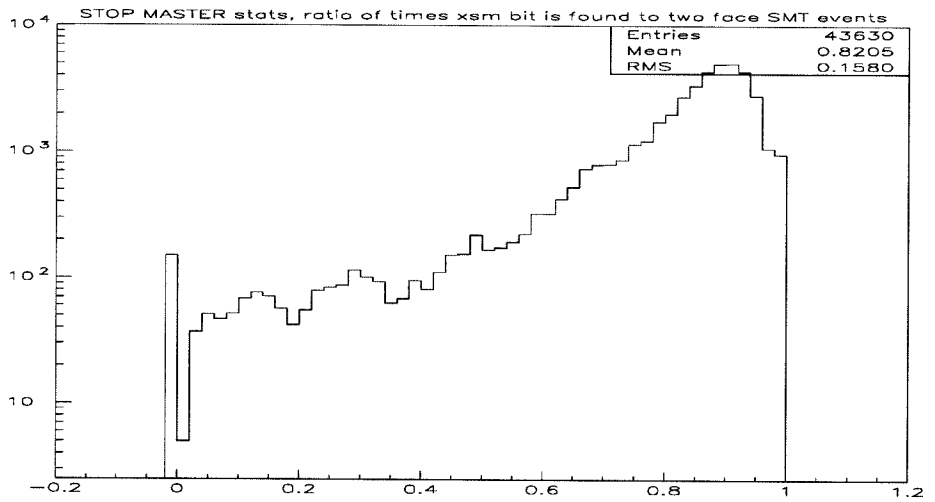


Figure 7.9: Distribution of the ratio of the number of times the crossSM bit is set in the Stop Master to the number of two-face SMT events (as recorded by the SMT).

data set. This exclusion cut, is also not applied when an individual face in one of the two adjacent SMs setting the bit had already been identified as problematic and excluded for analysis and acceptance purposes according to section 7.2.2. We have to mention here, that in legitimate two-face events, the crossSM bit was asserted in both supermodules involved in the event, so the proper functioning of either one was enough to prevent the event from being excluded.

## 7.3 The WFD Performance

WFD information was used to reject muons and radioactivity and identify monopoles from their characteristic pulse shape; therefore, a lot of effort was directed at ensuring good functioning of the waveform digitizers during the long data-taking period.

### 7.3.1 WFD Pedestal Evaluation

The conversion of the input voltage to ADC counts in the digitizers was non-linear and followed the curve shown in Fig. 7.10. The inversion, from ADC counts to volts,

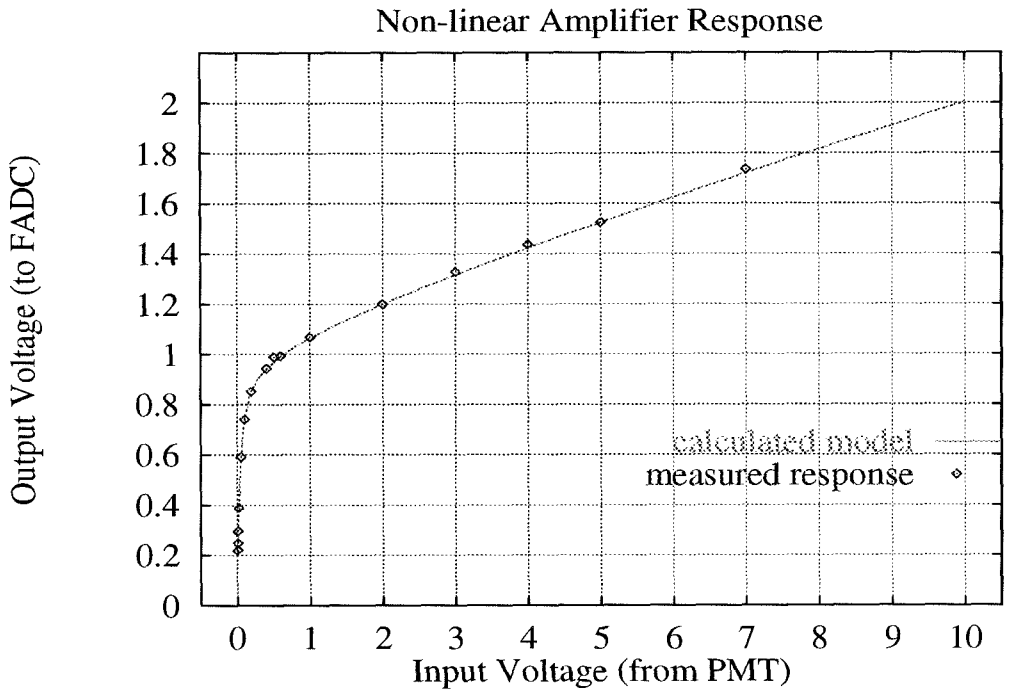


Figure 7.10: The measured response of the WFD non-linear front end compared with a mathematical model for the circuit. The data points reflect the output pulse height as the input pulse height is controlled by a pulse generator. The curve is a mathematical model of the non-linear response of the circuit.

for WFD analysis purposes was derived from this same curve. Some of the ADC counts corresponded to positive voltages. This way bipolar noise could be readily distinguished from an SPE train. In order to determine the ADC value corresponding to zero volts (called the pedestal), two digitized samples, before and after each pulse, were obtained. The pedestal value was used to convert ADC counts to volts, and was crucial for the WFD analysis. In fact, pedestal evaluation was far more critical for search of pulses of small height, and extremely important for this analysis. In Fig. 7.11 we present the distribution of pedestal means for all channels, for the entire data-taking period and in Fig. 7.12 we plot the pedestal RMS distribution.

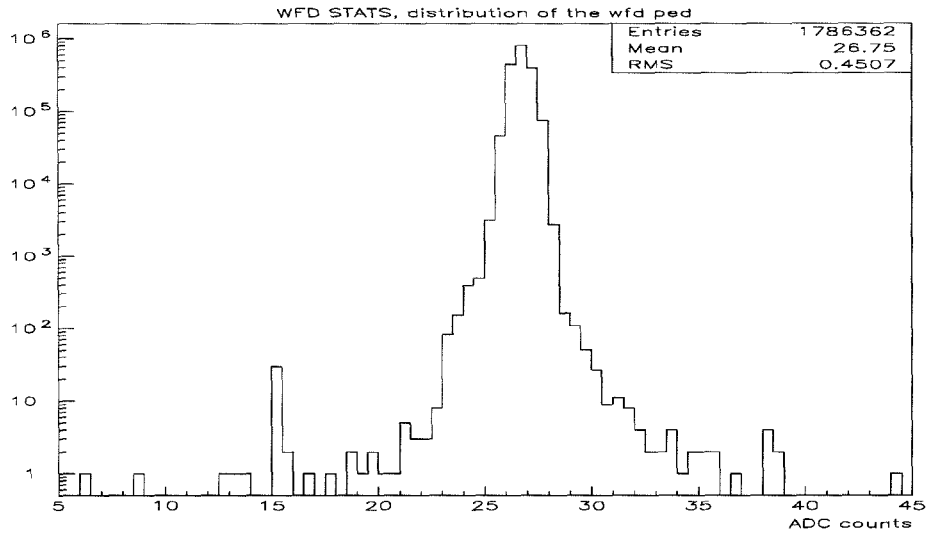


Figure 7.11: Mean pedestal value over each run for all the channels in the detector during the entire data taking period (run durations greater than 20 min). For 1758 cases when the pedestal mean was zero – the channel was dead – are not plotted in order to illustrate the area of interest better. The zero pedestal cases are mainly from the initial data taking period, and from the North and South faces which for a long time presented problems.

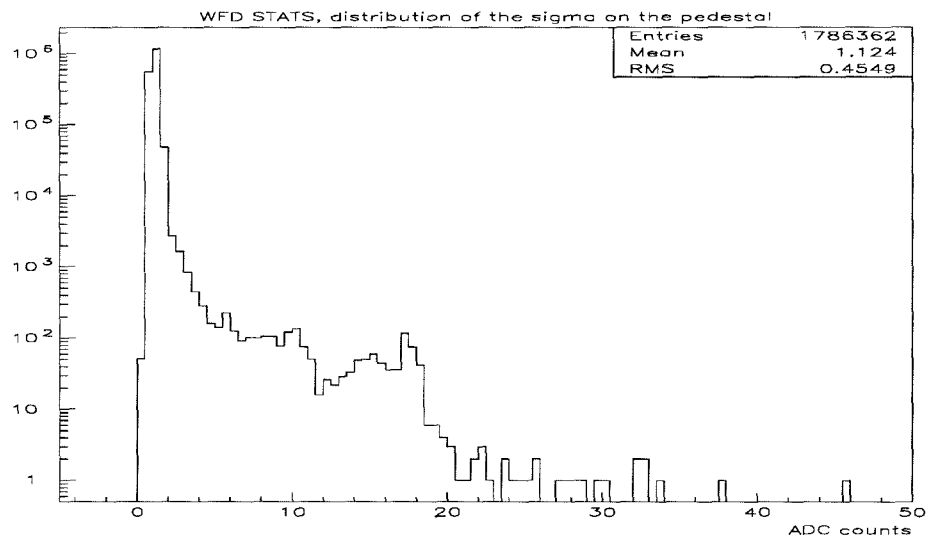


Figure 7.12: RMS on the pedestal for all the channels in the detector during the whole data taking period. Runs with duration less than 20 minutes and cases when the pedestal mean value is zero are excluded.

Small variations of the pedestal during a run did not affect the WFD analysis, as the pedestal was re-evaluated for each event. However, large variations were a sign of malfunction of the WFD channel. For the acceptance calculation, we excluded waveform channels from runs in which their mean pedestal value did not lie in the range 24 to 30 counts. Also excluded were WFD channels from runs where the RMS was greater than 2 counts. The effect of these quality cuts on the exposure is $\sim$0.6%. Fig. 7.13 shows an example waveform from channel number 14 in SM 6 with a pedestal RMS of 10.39 counts. In the waveform we see several radioactivity pulses over a 500 $\mu$s duration. Each pulse is only a few tens of nanoseconds wide. If the pedestal were not wandering due to an unknown hardware problem, the baseline of all pulses would be the same.

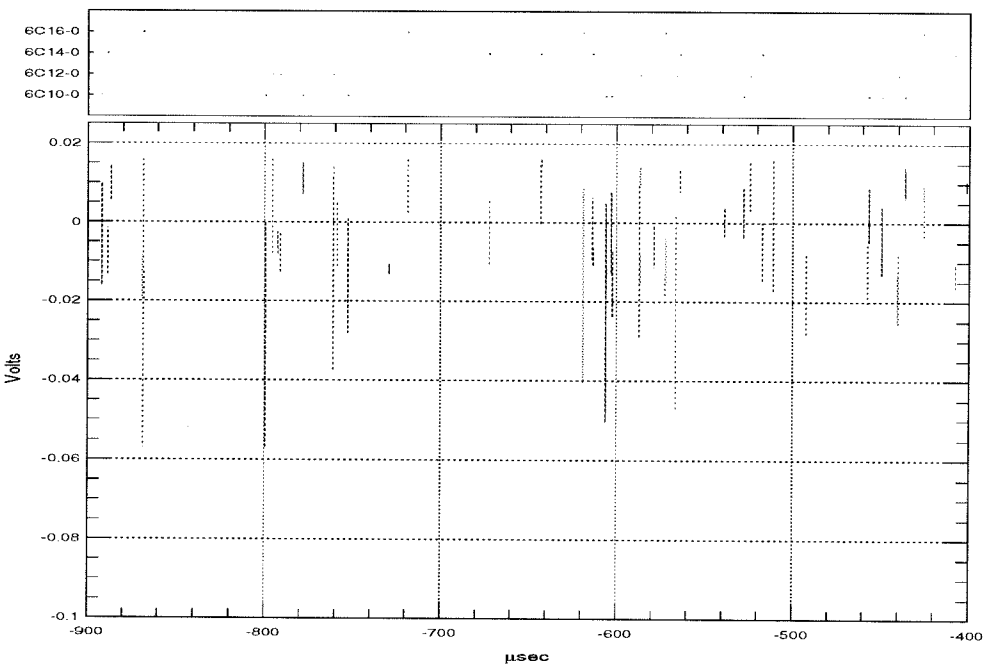


Figure 7.13: Part of an example waveform from SM 6 channel 14. The RMS on the pedestal is more than 10 counts and the instability of the baseline of the narrow radioactivity pulses present in the waveform is obvious to the eye. Had the channel operated properly, the baseline should have been the same for all pulses in the waveform.

### 7.3.2 WFD Buffer Overflow

#### WFD Buffer Overflow due to Positive Overshoot

As explained in section 3.2, without the zero-suppression, a WFD channel would not have sufficient memory to record the entire 1 ms interval between the trigger and the WFD Stop. The WFD memory capacity was initially set to 20 kB (equivalent to $\simeq$50 $\mu$s of continuously digitized waveform data). Later, it was raised to 40 kB (about 100 $\mu$s) and finally to 50 kB (about 125 $\mu$s). It was also mentioned in the same section (3.2) that from the time of initial data-taking to the time of implementation of the LAMOSSKA trigger and the WFD-fix in June 1997, channels would experience (a few times per run) legitimate large pulses such that resulting positive overshoot was above the WFD positive threshold for a time long enough to overflow the WFD buffers. As a result, the initial pulse would be overwritten and lost. An example waveform of such an event is shown in Fig. 7.14. When and if WFD channels, underwent buffer overflow for both tank-ends of any one tank, it would be impossible to identify a genuine slow monopole crossing the tank from its characteristic pulse profile.

We performed LED calibrations to better understand the limits that this problem was imposing on the detectable velocity range. We fired all tanks-ends in supermodules 1, 2, 3 and 4 with 1 $\mu$s wide pulses of various intensities. For every tank-end, the charge in the initial pulse was recorded and attempts were made to determine the maximum charge $Q_{max}$ recorded before the waveform channel would start losing the initial pulse due to the ensuing overshoot. For some tank-ends, we were unable to induce a large enough pulse due to LED limitations. At the time of these calibrations, the WFD memory capacity was set to 40 kB (or about 100 $\mu$s of continuously-digitized data). For the 477 tank-ends (out of 616 tank-ends) for which $Q_{max}$ was determinable, the quantity is plotted in Fig. 7.15. As illustrated in Fig. 7.15, for most tank-ends, $Q_{max}$ was in the range 700-800 Vns. In these WFDs, this is approximately 7 times the light yield of a MIP and corresponds to the light yield of a monopole of $\beta = 4 - 7 \times 10^{-4}$. Above this velocity we ran the risk of losing the initial pulse. We obtained even more restrictive results with pulses of 2 and 5 $\mu$s

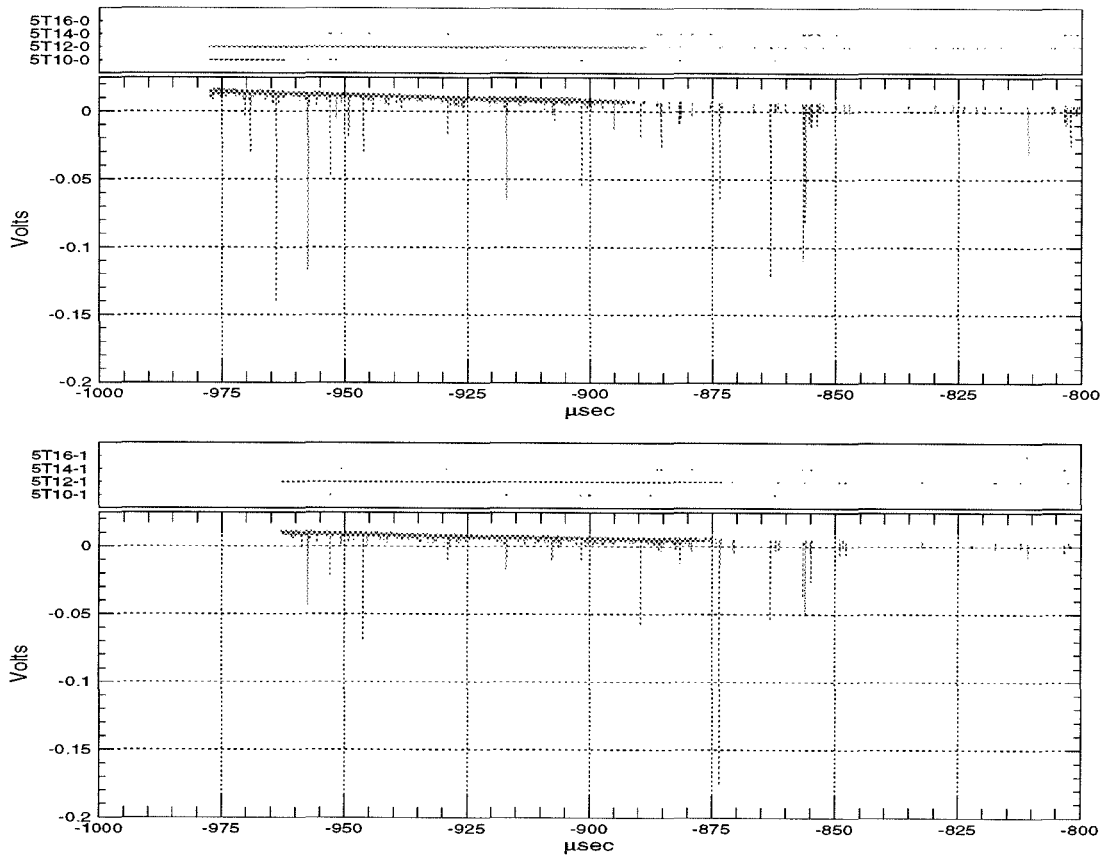


Figure 7.14: Run 12788, Event 6857. The actual pulse that triggered the SMT was near $-1000$ $\mu$s. The positive overshoot remained above threshold more than 100 $\mu$s and the WFD digitized continuously. When the memory buffer was full, older data was overwritten and the initial pulse was lost. One can see the decaying overshoot with radioactivity pulses superposed, from the beginning of the saved data until approximately $-880$ $\mu$s. After the overshoot falls below threshold, zero suppression is again effective.

width. In these cases $Q_{max}$ was even smaller (400 - 500 V ns, corresponding to even lower monopole $\beta$).

From the above, we deduce that in order to be sensitive to monopoles in the entire velocity range covered by the Slow Monopole Trigger – especially monopoles of galactic level velocities – we could not simply reject events with filled WFD buffers for the period when this problem was affecting the WFDs. For this reason and for the period before the WFD-fix was officially implemented, we considered every waveform

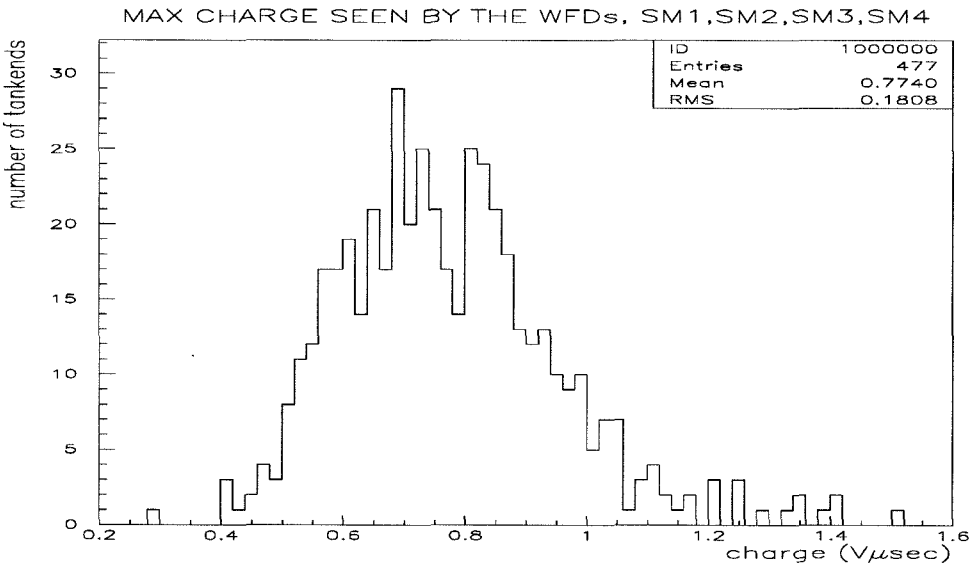


Figure 7.15: Distribution of the maximum charge seen by the WFD channels serving the tank-ends in SMs 1, 2, 3, and 4. This distribution is for 1 $\mu$s pulses and for 40 kB WFD data buffers.

with data buffer filled and with a lost primary pulse as a valid monopole event as subjected it to further analysis as described earlier.

### WFD Buffer Overflow due to Other Hardware Problems

With the exception of the few large charge events per run that could cause WFD buffers to overflow before the WFD-fix, a properly functioning channel would always record the 1 ms event history without filling the data buffer. Any channel that had too many buffer overflow events during a run was very likely experiencing hardware problems, and should be excluded from the analysis. We developed two different sets of cuts – a loose set to be applied during the less-stable initial period, and a much tighter set to be applied to data collected during the last 3 years of stable operation.

During the initial period, with on-going installation of the attico SMT, a number of problems were occasionally present. Specifically:

- The bit in the WFD control-register controlling the zero-suppression was unset.

- There were periods when the hardware stored 0 for all ADC words and digitized continuously.
- There were malfunctioning PMTs producing many SPEs.
- There were hardware problems with the VME crate. This was usually accompanied by many bus errors, affected more than one channel in a supermodule, produced a large number of waveforms with filled buffers, and had corrupted clock words.

The above hardware problems manifested themselves by creating overflowing WFD buffers more often than was expected. In Fig. 7.16 we plot a distribution of the ratio of the times a WFD buffer overflow was observed to the number of times it was read during a run. Large ratios indicate hardware problems, as positive

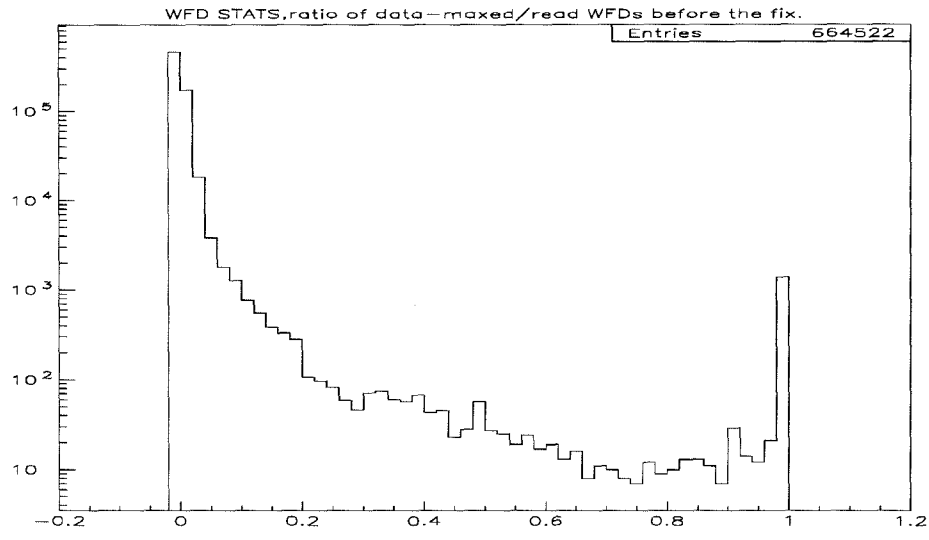


Figure 7.16: Distribution of the ratio of the number of times channels showed filled WFD buffers to the number of times they are read. For runs longer than 20 minutes only.

overshoot events occurred in less than 10% of all buffer reads.

A closer examination of WFD channels with greater than 10% overflow occurrence

found associations with WFD malfunctions listed above. Fig. 7.17 plots the distribution of the number of WFD channels with overflow for more than 10% of buffer reads. The majority occur during a few time periods when the zero-suppression bit

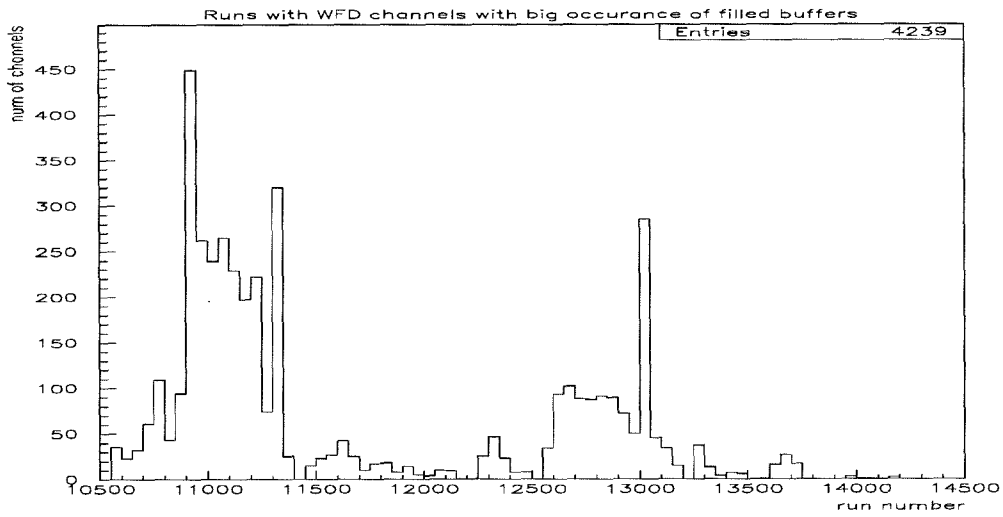


Figure 7.17: Distribution of the number of channels presenting excessive number of overflow WFD buffers before the positive overshoot problem was fixed. The peaks are due to just a few channels in SM 1 (runs 10923 to 11348) and a single channel (Channel 16) in SM 2 (runs 12500 to 13000).

was unset in SM 1 (runs 10923 to 11348), when a channel in SM 2 suffered from strong bipolar noise that was often above threshold (runs 12500 to 13000) and when all channels in SM 1 suffered from a VME crate problem (with peak around run 13000).

Therefore, for the data-taking period prior to the WFD-fix, we exclude channels that have buffer overflow for more than 10% of all waveform reads.

For data collection post WFD-fix and after the installation of LAMOSSKA, the problem caused by positive overshoot was remedied. Other hardware problems resulted in occasional events with overflow, yet the occurrence was greatly reduced when compared to the earlier periods. For this stable period, we exclude from the

acceptance calculation and from the analysis any channel that had buffer overflow for more than 2% of reads (unless it was less than or equal to twice in a single run). The excluded cases (Fig. 7.18) peak prominently during certain runs, are due to the WFD channels of SM 1, and were attributed to the loss of some power lines on the WFD crate.

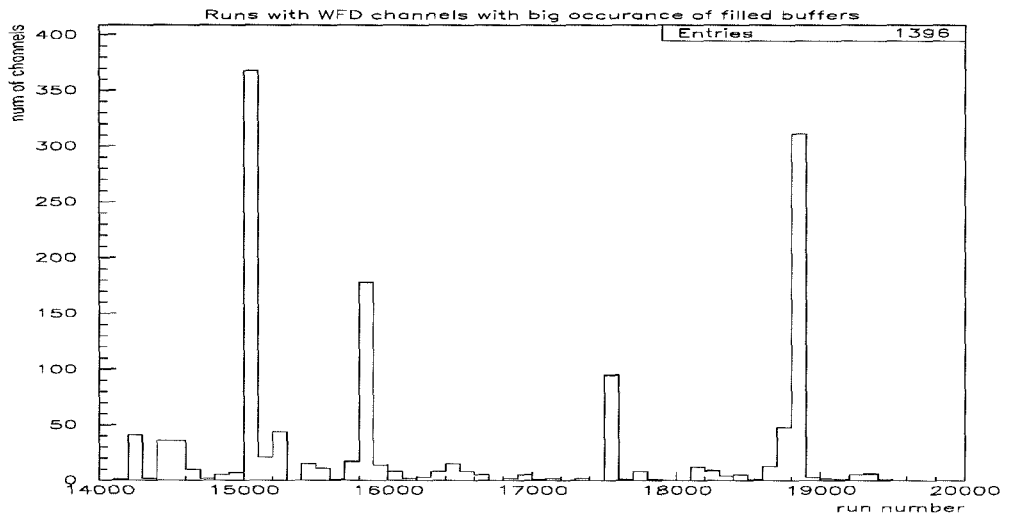


Figure 7.18: Distribution of the number of channels presenting excessive number of filled WFD buffers in the runs after the WFD-fix. SM 1 was responsible for all peaks.

For the post WFD-fix period – after excluding all channels with obvious hardware problems – events with filled buffers constituted less than 0.01% of the data and were not due to large amplitude pulses (LAMOSSKA did not fire for these events), but were due to the occasional hardware problems described above.

The decrease in the exposure for the entire data-taking period due to the above cut is around 0.2%.

### 7.3.3 Corrupted or Missing WFD Buffers

The final two types of pathological behavior of the WFDs were corrupt and completely missing data buffers.

Fig. 7.19 shows a type of buffer corruption that occurred at times. The pathology

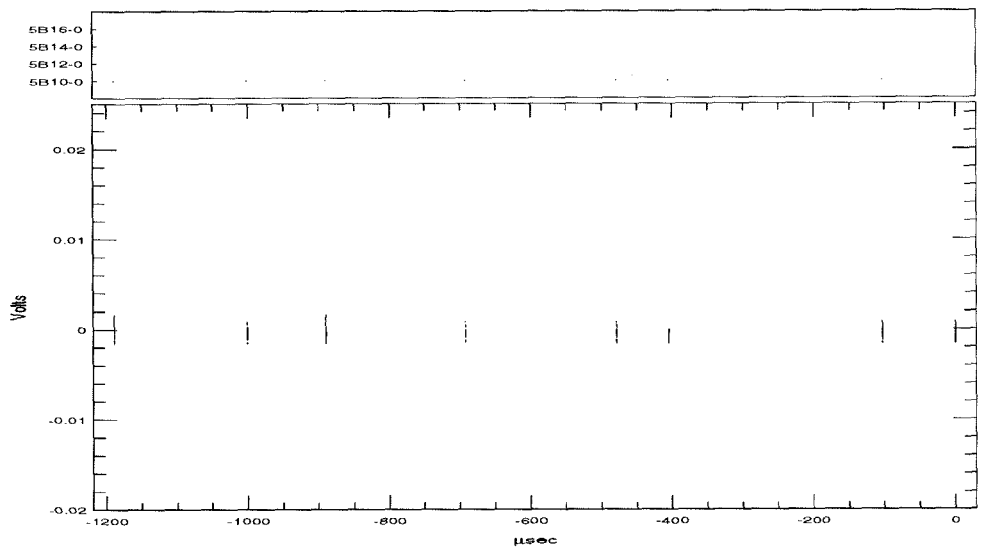


Figure 7.19: Corrupted waveform from Run 12877, Event 832. The vertical lines are not radioactivity pulses, but the result of data corruption.

seen in the figure often appears in the data around the time of the WFD-fix, when tests were performed on some WFD channels. The signature is a WFD buffer with a small number of words; channels that suffered this problem during a run often wound up with a small average number of words. Fig. 7.20 shows the distribution of the average number of words for horizontal and vertical channels of the detector during the entire data period.

We exclude channels with an average number of words per run of less than 500 for the horizontals, and less than 200 for the verticals. This cut results in a reduction of 0.1% in exposure.

Another problem was that sometimes the waveforms of one or more of the tanks

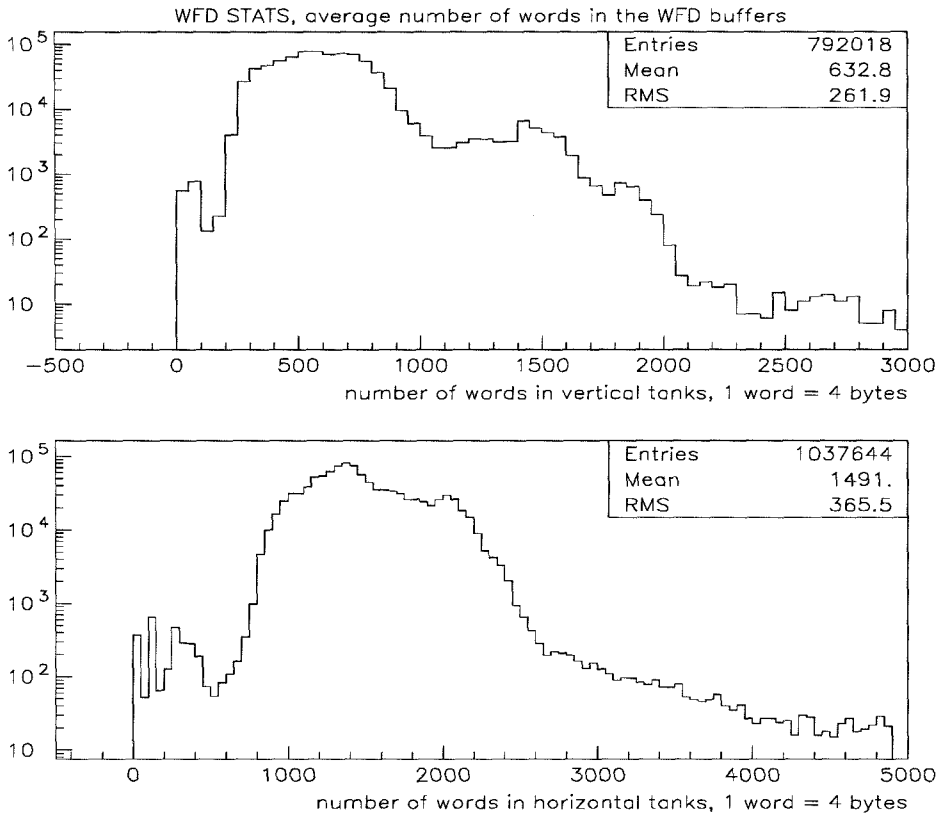


Figure 7.20: Distribution of the average number of words in the WFD buffers for channels serving vertical and horizontal tanks, respectively.

that fired the SMT were not in the data stream. About 320 events that survive all cuts before the WFD analysis have at least one tank firing the SMT with the corresponding WFD buffer absent. Almost all of these events (264) were clumped in the first data taking period, in particular around the time of installation of the attico SMT.

After that period, out of 35901 events that pass all filters before the WFD analysis only 56 have missing waveforms. From them 17 are events without SPAM_FMT trigger and each was the first event acquired by the microVAX after the start of a run.

The events with missing waveforms constitute a small percentage of the 35901 event set (0.9%). There is no indication of why this type of WFD malfunctioning should affect monopole events rather than others; with this statistical knowledge we expect that no more than 0.9% of monopole events were likely to suffer from a missed buffer. We apply this as an additional 0.9% inefficiency.

# Chapter 8

# Acceptance Calculation and Conclusions

## 8.1 Acceptance Calculation

After closely examining data collected during this experiment, we arrived at conclusions about the data quality and designed filters for the various hardware components associated with the slow monopole search with scintillators; all this was presented in chapter 7. During the nearly five years of data-taking, a detector as large as MACRO necessarily ran in various configurations. These configurations were generally stable during each data-run.

These different configurations of the detector were taken into account when calculating the acceptance for this experiment. For each run, data quality checks were performed which were explained in chapter 7. Individual SMT channels were labeled dead or alive on the basis of these quality checks. The same was true for individual WFD channels and Stop Master channels. The live time of the SMTs in various supermodules was taken as the time interval elapsed between the arrival of the first and last SMT event in that supermodule, for that run. In this way, we reconstruct the detector's exact configuration for *every* run, on which we project an isotropic flux of particles. We perform the MC calculations for all non-calibration MACRO runs with duration greater than 20 min in the data taking period July 1995-May 2000, starting with Run 10557 and ending with Run 19499. We perform the MC calculations separately for the following particle velocities:

1. $\beta = 1.0 \times 10^{-4}$
2. $\beta = 6.3 \times 10^{-4}$
3. $\beta = 1.0 \times 10^{-3}$

4. $\beta = 1.8 \times 10^{-3}$

5. $\beta = 4.1 \times 10^{-3}$

6. $\beta = 7.0 \times 10^{-3}$

7. $\beta = 1.0 \times 10^{-2}$

All detector and system based requirements were included in the analysis. More specifically, for each run and each particle velocity we generated $10^4$ events. The events were generated by choosing uniformly two points on a sphere whose diameter is equal to MACRO's longest diagonal. This way for each event a location is chosen uniformly and a direction is chosen isotropically. The number of faces and the number of boxes hit is calculated. A pathlength requirement was set, according to the sensitivity curve deduced from the SMT calibrations in chapter 3. The event was required to satisfy the pathlength requirements in at least two faces in the detector. A timing requirement was also set according to the hardware and analysis considerations. The event had to cross at least two faces in two adjacent supermodules within 1 ms. Then the exact configuration of the detector, deduced after application of the hardware quality cuts explained in chapter 7, was used. The event was required to cross at least two tanks (in different faces) for which

- the SMT channel was live,
- the WFD channel was live,
- the Stop Master module and channel were live.

The event was also required

- not to cross any two faces within 1 $\mu$s, (according to the analysis cut which rejected events with SPAM_MUON trigger),
- not to cross more than 4 faces and 6 tanks in each face (this requirement assured us that the event would not have failed the SMT multiplicity cut – step 4 – imposed in the analysis).

Only events satisfying all of the above requirements were considered accepted. We translate the ratio of accepted to generated events to detector's acceptance by multiplying it by the acceptance of the sphere. In this way, for each particle velocity from the ones mentioned above, we generate 7.5 $10^7$ events.

In Fig. 8.1 is plotted the distribution of the acceptance to monopoles with $\beta = 10^{-4}$, for the various configurations of the detector during the $\simeq$5 yr running period.

We see that the distribution is dominated by the number of supermodules in acquisition. Runs that lasted less than 20 minutes were excluded from both the analysis and the acceptance and on this plot are accumulated in the first bin. The enormous effort made to keep the detector running with all electronics in operation was well rewarded, with the highest peak in the figure corresponding to the full MACRO (all six supermodules) running.

In Fig. 8.2, we plot the exposure of the detector to magnetic monopoles for various velocities integrated over all the running time, where we have folded in the results of the calibrations (95% efficiency of the SMT channels to monopoles). We have also accounted for computer dead time (conservatively estimated to be 3%). As we see from Fig. 8.2, the exposure of the detector is practically stable in the $\beta$ range $10^{-4} \lesssim \beta \lesssim 4.1 \times 10^{-3}$, while falls rapidly for $\beta \gtrsim 4.1 \times 10^{-3}$ mainly due to pathlength requirements.

## 8.2 Conclusions

The analysis of scintillator data from MACRO, for the run period from June 1995 to May 2000, did not yield any slow magnetic monopole events. The sensitivity of the hardware to slow monopoles was extensively calibrated and discussed in chapter 3. The sensitivity of the software was also investigated in chapter 5 and shown to be better than that of the hardware. We have demonstrated that a slow GUT monopole of $10^{-4} \lesssim \beta \lesssim 4.1 \times 10^{-3}$ (with the theoretically-calculated energy losses in scintillators), passing through two or more MACRO tanks, would have been identified. As

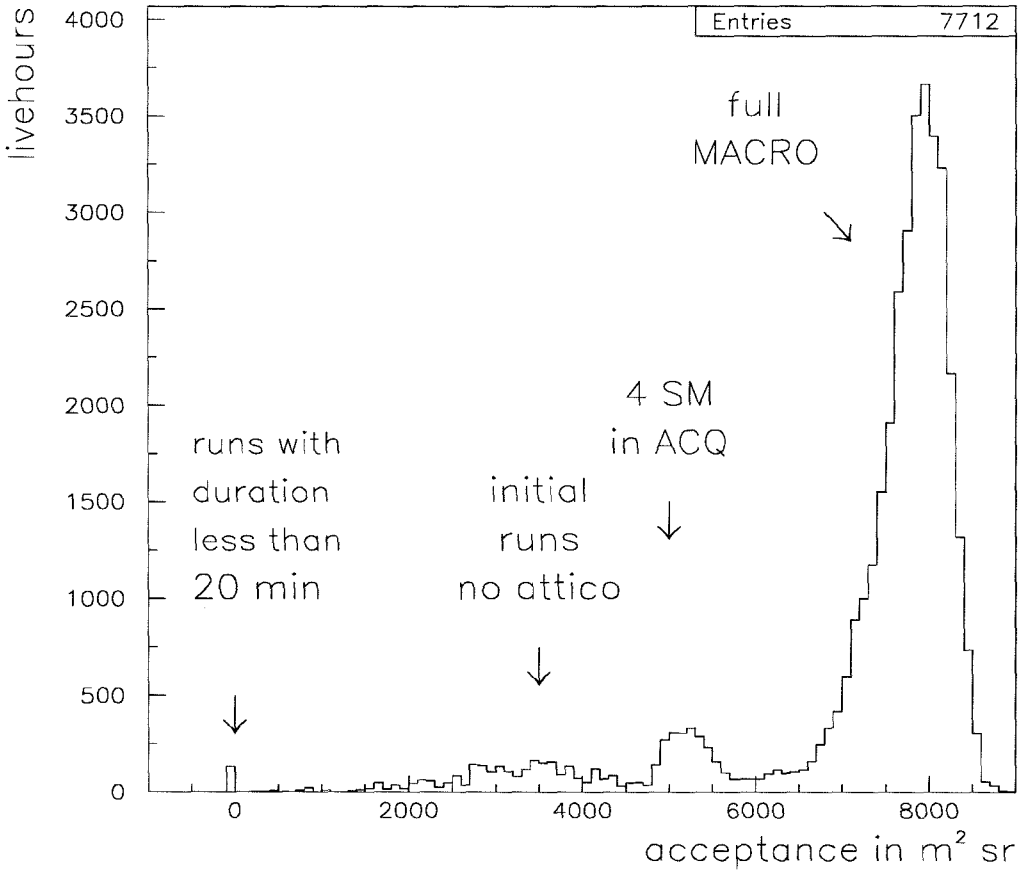


Figure 8.1: Distribution of MACRO acceptance during the 4.75 yr-long data period for monopoles of $\beta = 10^{-4}$. The detector configurations are evident.

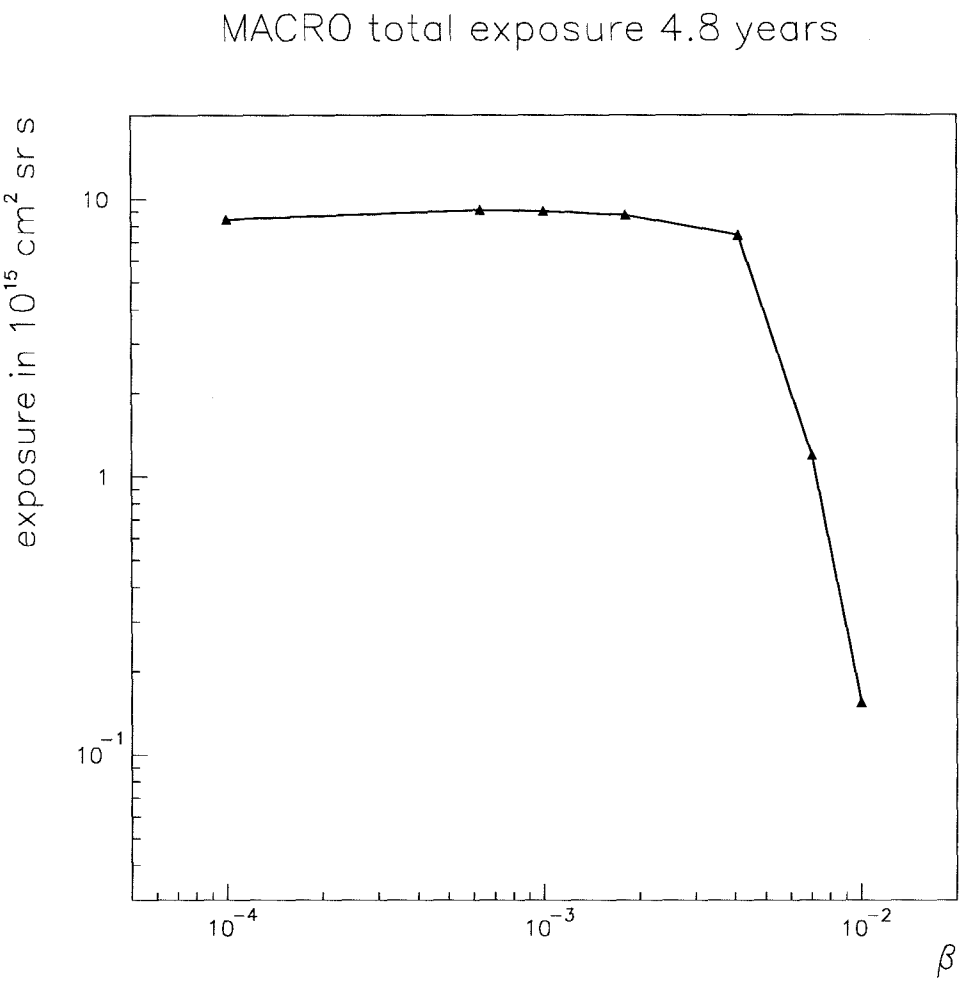


Figure 8.2: MACRO exposure, as calculated with MCs, for the 4.8 yr-long data-taking period, for monopoles of various velocities. The detector performance has been accounted for.

in all searches with null results, we have calculated the detector's exposure to an isotropic flux of particles with velocities characteristic of slow monopoles. In doing so, we have kept in mind the actual state of the detector during run time. This search sets an upper limit to an isotropic monopole flux, at the 90% confidence level, of

$$F_{max} = \frac{2.3}{E_{MACRO}}, \tag{8.1}$$

where $E_{MACRO}$ is the total MACRO exposure, which for representative monopoles of $\beta = 10^{-3}$ takes on the value

$$F_{max} = 2.5 \times 10^{-16}\, cm^{-2}\, s^{-1}\, sr^{-1}.$$

The flux limit as a function of monopole velocity set by this search is plotted in Fig. 8.3. This limit is approximately constant in the $\beta$ range $10^{-4} \lesssim \beta \lesssim 4.1 \times 10^{-3}$ and rises rapidly for $\beta \gtrsim 4.1 \times 10^{-3}$.

The above limit is based entirely on the scintillation detector and is the most stringent yet with MACRO scintillators from a single search. It is more than an order of magnitude lower than limits from previous scintillator searches in this velocity range. It does not use the streamer tubes which make it independent of the validity of the Drell effect, and it is completely independent of and complementary to monopole searches based on streamer tubes.

Setting a credible lower limit on the monopole abundance puts constraints on theoretical models describing the evolution of the very early Universe. In the theory discussion in chapter 1, we have mentioned that current experimental data is consistent with various inflationary scenarios, but there is no way yet to choose one particular scenario that best describes the evolution of the Universe and its current state. The MACRO search for magnetic monopoles now excludes models where there is no mechanism to sufficiently suppress magnetic monopole production. We are sure that it will not put any constraints on the imagination of theorists, though!

Monopole searches yield clues about the big mystery that is the Universe, favoring or disfavoring the various theoretical suggestions. For example, if the result of this search were a considerable abundance of magnetic monopoles, we would have to

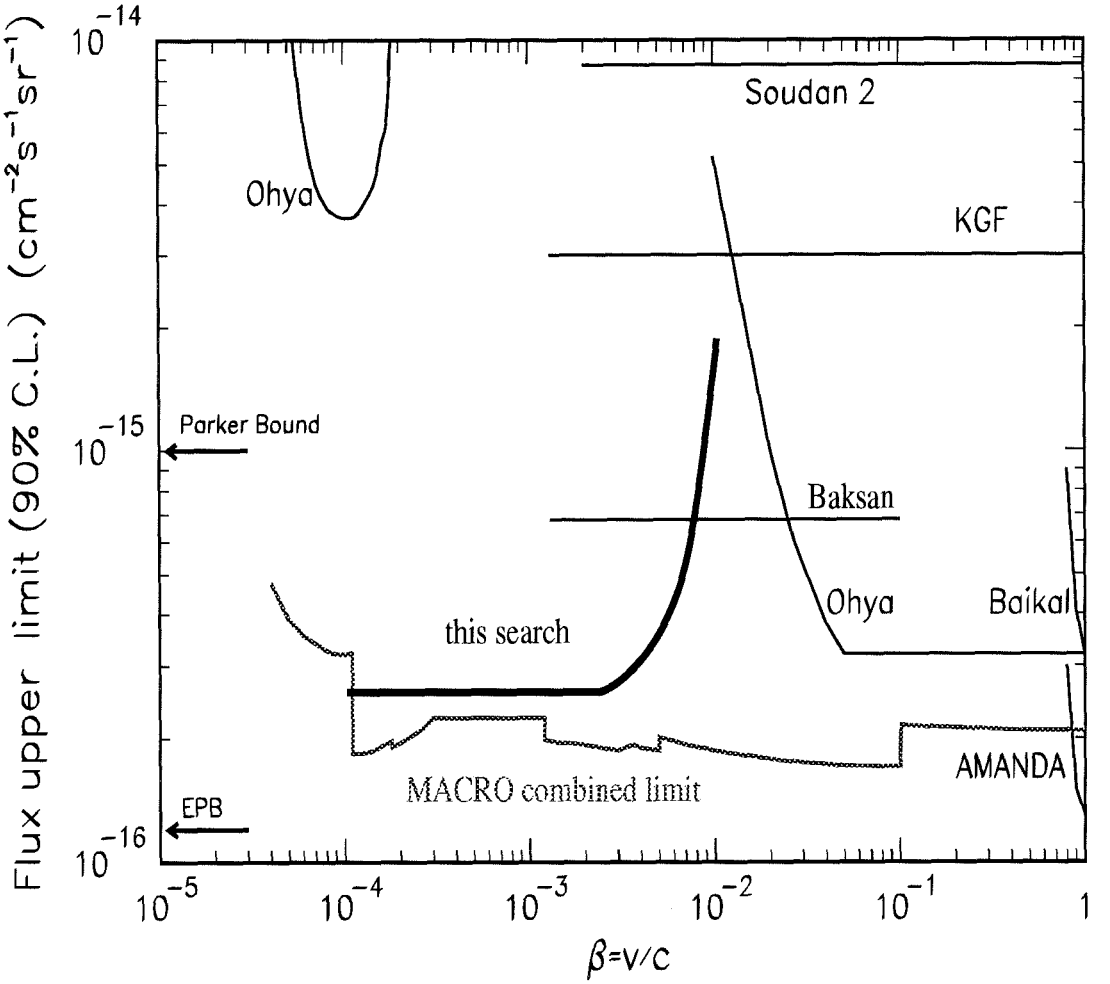


Figure 8.3: Monopole flux limit obtained with the MACRO scintillation detector ONLY from this search is plotted in bold. Limits set by other experiments are plotted as well. The MACRO combined limit plotted here (reprinted from [65]) is the limit deduced by combining all previous searches (scintillator, streamer tube and track-etch searches) done with the MACRO detector and does not include the results of this search as yet.

revisit the models of regeneration of the galactic magnetic field and suggest new ones (some have already been suggested). Instead, now, assumptions made about the regeneration of the field through dynamo action appear to be satisfactory. The same holds for assumptions made about the initial seed of the galactic magnetic field. There are many more examples of how monopole limits affect physics as a whole. Some of these we still may not know.

MACRO had been the big hope of many in the scientific community for the detection of monopoles. It would have been very exciting if we had seen one. But the magnetic monopole still hides its mysterious face from us, eludes us. That does not mean that monopoles do not exist. As Stephen Hawking once told me while at Caltech, "Magnetic monopoles might be so rare that we will never see one. Like my primordial black holes. Which is a pity, because this way I will never get the Nobel Prize."

MACRO was the first experiment characterized by redundancy and large acceptance that opened the window below the Parker bound. OK, we didn't see anything. But we did look!

The story of physics is about the human thirst for knowledge.

# Appendix A

# PMT Afterpulsing

Large pulses due to muons would tend to create significant afterpulses in the MACRO PMTs (and mainly in EMI PMTs), which could trigger the SMT hardware and affect the waveform analysis. In the software, this effect had imposed the use of a dead time for large pulses. In this appendix, we study the characteristics of the afterpulsing and its time evolution.

## A.1 PMT Afterpulsing

Typical muons events produced pulse waveforms of height 2 V and a 30-50 ns width at half maximum. The contribution of the muons to the general distribution of pulse heights becomes important around 800 mV. This is shown in figure A.1, where we plot for a typical run for tanks that did fire the SMT, a distribution of pulse heights for pulses larger than 100 mV. Artifacts due to binning in the WFD ADC are visible, as is the effect of WFD ADC saturation for pulse heights greater than 10 V (the last bin). In grey are pulses extracted from the time region $-1003.0$ $\mu$s to $-1000.5$ $\mu$s before the WFD Stop, for events that had fired SPAM_MUON and ERP in at least two faces of the detector. These are mainly muon pulses. It was observed that high amplitude pulses (like muon pulses or pulses from muon-induced electromagnetic showers) produced afterpulsing in the PMTs.

As will be demonstrated below, afterpulsing arrived in certain time windows (or zones) after the initial pulse. The main windows were:

- about 1.2 $\mu$s after the initial pulse
- about 2.4 $\mu$s after the initial pulse

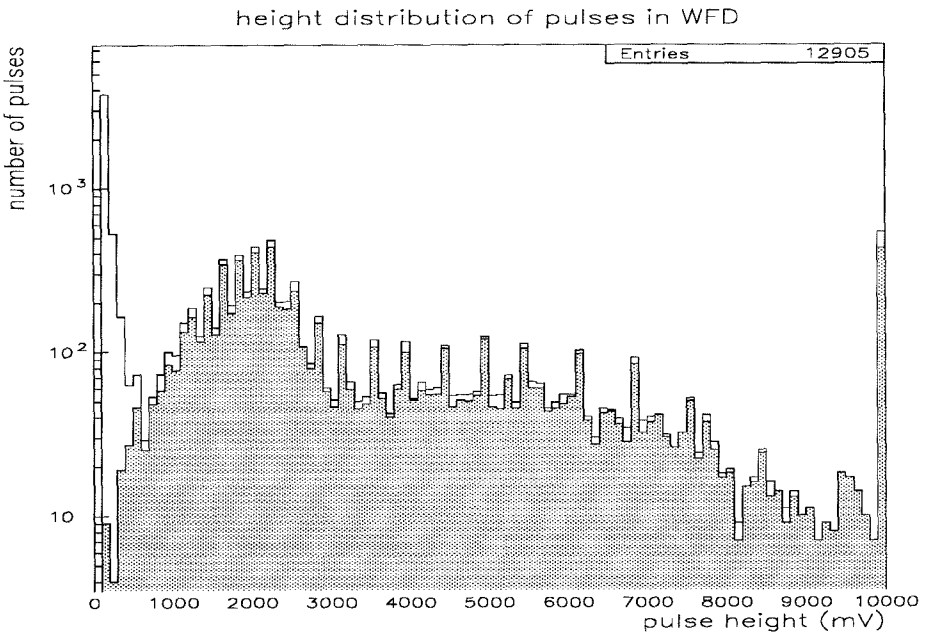


Figure A.1: The distribution of pulse heights in the waveforms for tanks that fired the SMT. The large peak at small pulse heights is due to radioactivity induced pulses. The peak at 2 V is due to muons. The grey distribution is for pulses that fired ERP and CSPAM.

- about 7.0 $\mu$s after the initial pulse

A waveform in which the afterpulsing is clearly seen is in Figs. A.2.A and A.2.B. The waveform in the figure was from tank 6T02-1. The initial pulse was larger in amplitude than the typical muon of 2 V, and was chosen so as to clearly illustrate the main characteristics of afterpulsing. The picture zooms in on the time region where the initial pulse ought to be located, i.e., $\sim$ 1000 $\mu$s before the WFD Stop, and also just after the initial pulse in order to provide evidence for the three typical time zones affected by afterpulsing. The first zone is at around 1.2 $\mu$s after the initial pulse. The light yield is quite prominent and is well concentrated around the peak. The second zone is around 2.4 $\mu$s after the initial pulse. The third time zone follows 6-7 $\mu$s after the initial pulse and the afterpulsing here resembles SPE train pulses.

In order to broadly investigate the effects of afterpulsing in a typical run, we

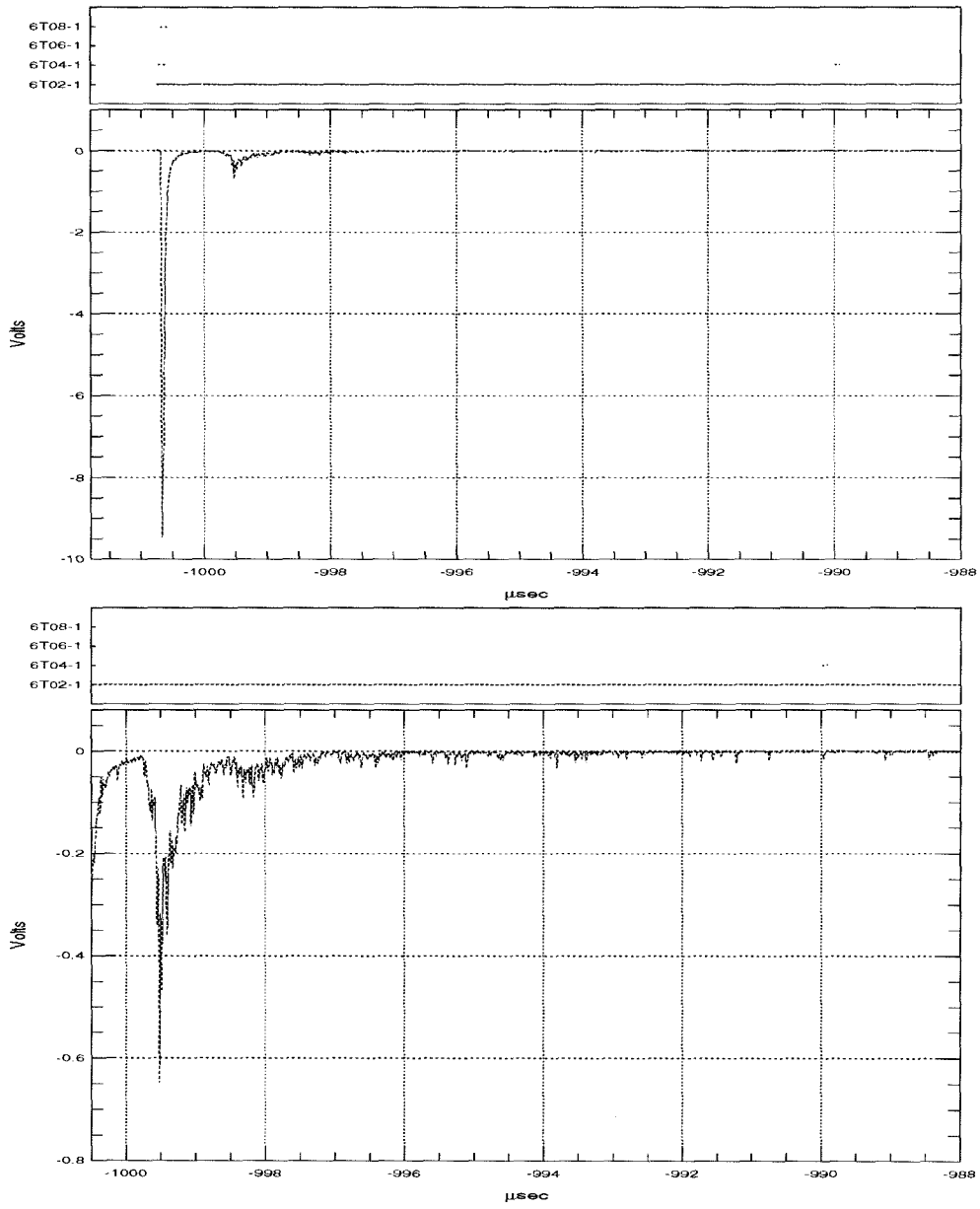


Figure A.2: A)Above: PMT pulse at about 1000.7 $\mu$s before the WFD Stop. B) Below:zoom in on the same waveform (reduced vertical scale). The pulse at $-999.5$ $\mu$s is the first afterpulse occurring 1.2 $\mu$s after the primary pulse. The afterpulse at $-998.3$ $\mu$s is also clearly distinguishable (second afterpulsing window at 2.4 $\mu$s after the initial pulse). The afterpulse in the third window around $-994$ $\mu$s, i.e., around 7 $\mu$s after the initial pulse, looks like an SPE train pulse.

examined several waveform segments that followed initial pulses larger than 800 mV. We divided the time region after the initial pulse into five windows: these are from

- 0.8 to 1.8 $\mu$s
- 1.8 to 4.5 $\mu$s
- 4.5 to 10.0 $\mu$s
- 10.0 to 25.0 $\mu$s
- 25.0 to 40.0 $\mu$s.

We found no signature of afterpulsing in time windows more than 10 $\mu$s after the initial pulse. The rest of the study will concentrate on the first three windows only; these are where we see the largest affects of afterpulsing. For each of these windows we plot the time at which the voltage peaks after the initial pulse in Figs. A.3 to A.5.

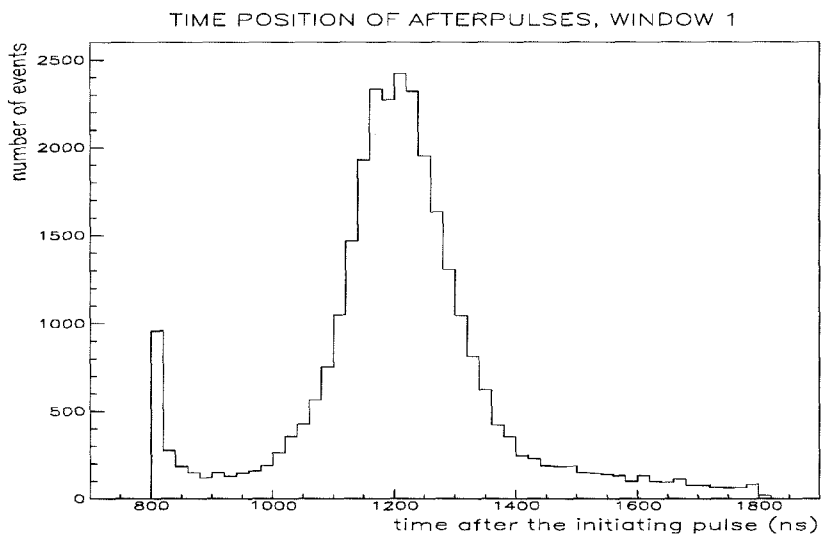


Figure A.3: Timing of the afterpulse peak in the first time window (0.8-1.8 $\mu$s) after an initial pulse of height greater than 800 mV. The peak is clearly at 1.2 $\mu$s.

In the first time window, the presence of the afterpulse was clear and it was well concentrated around 1.2 $\mu$s. In the second and third windows the presence of

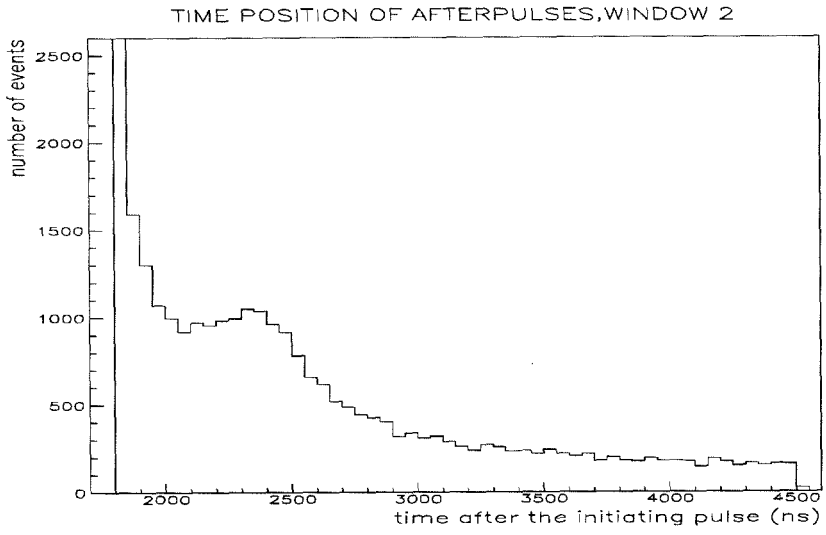


Figure A.4: Timing of the afterpulse peak in the second time window (1.8-4.5 $\mu$s) after an initial pulse of height greater than 800 mV. The peak at 2.4 $\mu$s is distinguishable over the exponential fall.

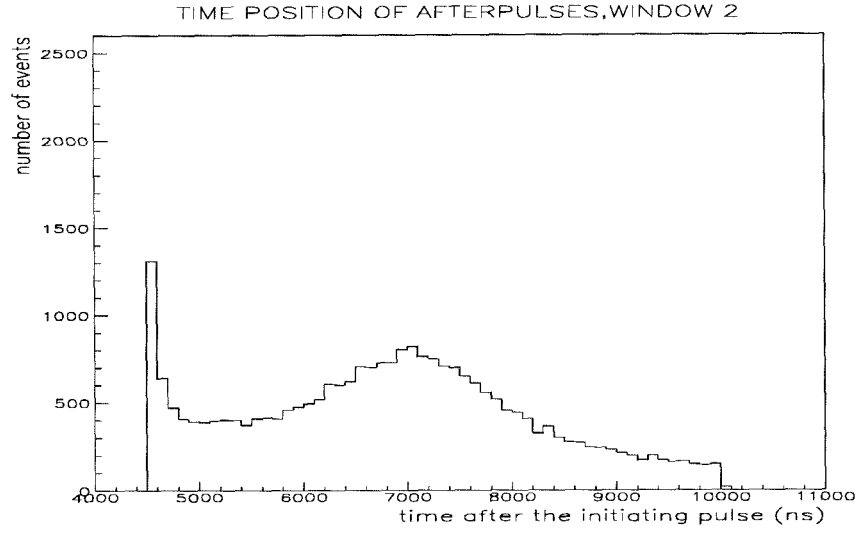


Figure A.5: Timing of the voltage peak in the third time window (4.5-10 $\mu$s) after an initial pulse of height greater than 800 mV. A peak around 7 $\mu$s is seen superposed on the exponential fall.

the afterpulsing is also noticeable. The clumping of afterpulse timing suggests the presence of He and some heavier elements in the PMT "vacuum."

## A.2 Charge Dependence of the PMT Afterpulsing

In order to study the dependence of the afterpulses on the charge of the initial pulse, we plot the mean charge of the afterpulses versus the charge of the initial pulse. To account for different duration integrating windows of 1 $\mu$s, 2.7 $\mu$s, 6.5 $\mu$s, 15 $\mu$s and 15 $\mu$s, respectively – these durations are just the widths of the above time windows – we normalize by the total integration time. We plot the mean charge of the afterpulses vs. the initial pulse in Figs. A.6 to A.8. It is clearly seen that the mean charge of the afterpulses rises with the charge of the initial pulse up to a saturation point.

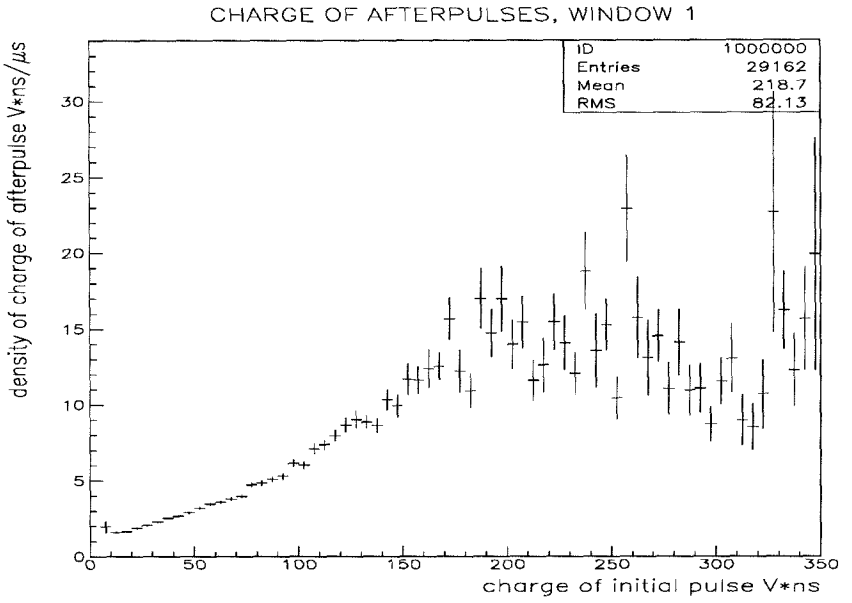


Figure A.6: Mean and RMS of the density of the charge of the afterpulses in the first time window vs. charge of the initial pulse. The dependence on the charge of the main pulse is clear.

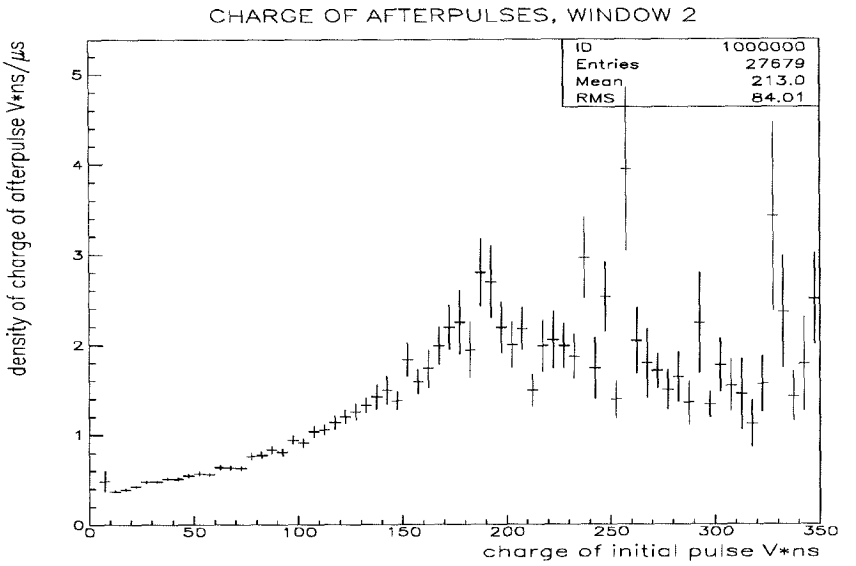


Figure A.7: Mean and RMS of the density of charge of the afterpulses in the second time window vs. charge of the initial pulse.

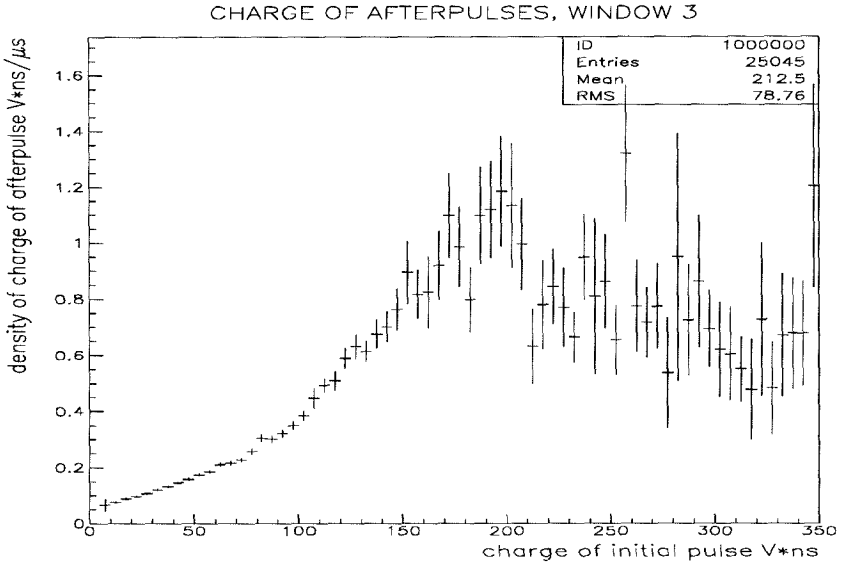


Figure A.8: Mean and RMS of the density of charge of the afterpulses in the third time window vs. charge of the initial pulse.

## A.3 Position Dependence of the Afterpulsing

The photomultiplier tubes showed a range of behavior. The effects of the afterpulsing were far more predominant in some tubes rather than others. To demonstrate this, we plot typical (averaged) ratios of the charges of the afterpulse to the main pulse for various tanks in the detector in figures A.9, A.10 and A.11. The PMTs corresponding to tank numbers 1 to 47 and 64 to 87 were of the EMI type. The Hamamatsu tubes were installed in the attico vertical tanks, and these are numbered as tanks 49 to 63 in the plot. The EMI PMTs were proven to be far more susceptible to He contamination than the Hamamatsu tubes.

Moreover, the plots show that afterpulsing was stronger for the top-face tubes (numbered as tanks 64 through 80), suggesting higher He concentrations in the area near the top of the detector.

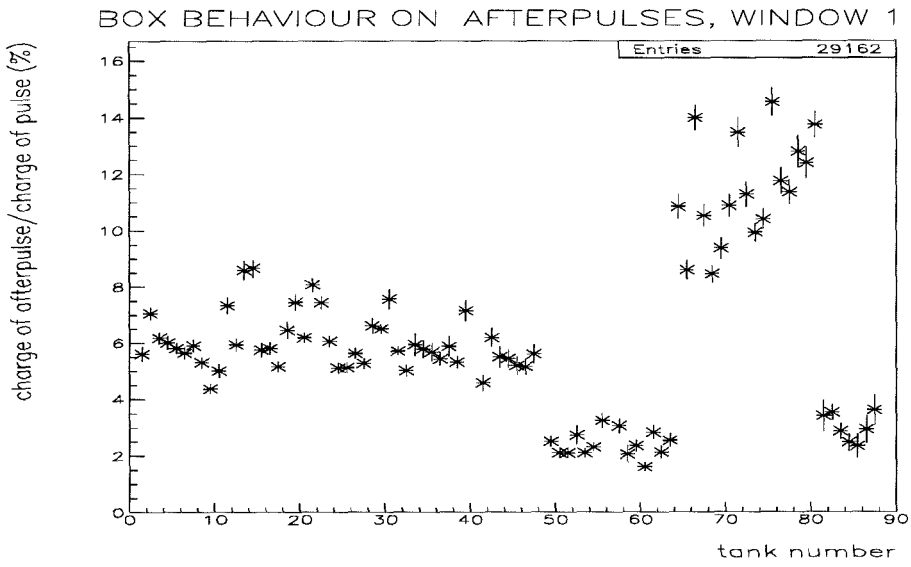


Figure A.9: Ratio of charge of afterpulses in the first time window (0.8-1.8 $\mu$s) over that of the initial pulse vs. the tank number. First time window: (0.8-1.8 $\mu$s) after the initial pulse. Tank numbering: 1-16 bottom, 17-32 center, 33-48 west-east lower, 49-63 west-east attico, 64-80 attico top, 81-87 north-south. Hamamatsu tubes are the least susceptible (in west attico and east attico faces). Tubes in the top face afterpulsed the most, suggesting higher levels of local contamination from helium.

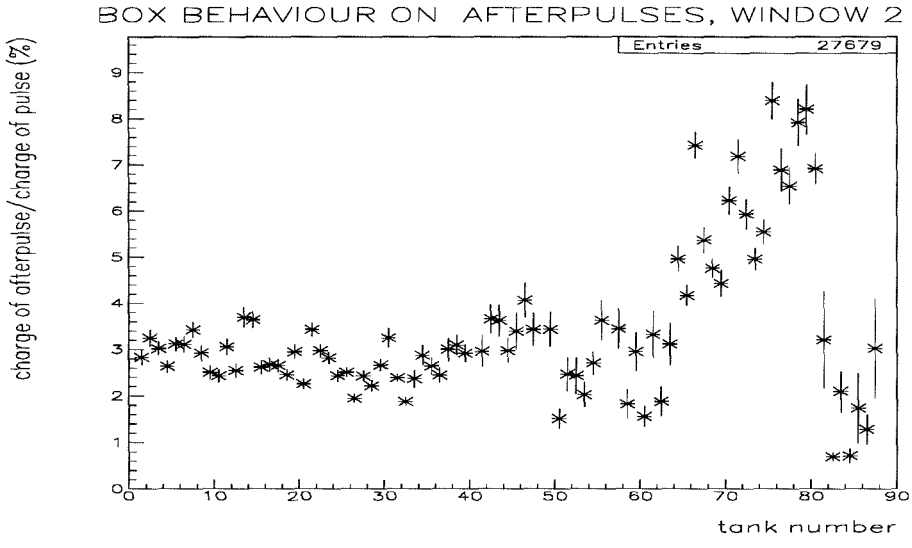


Figure A.10: Ratio of density of the charge of the afterpulses in the second time window (1.8-4.5 $\mu$s after the initial pulse) over charge of the initial pulse versus the tank number.

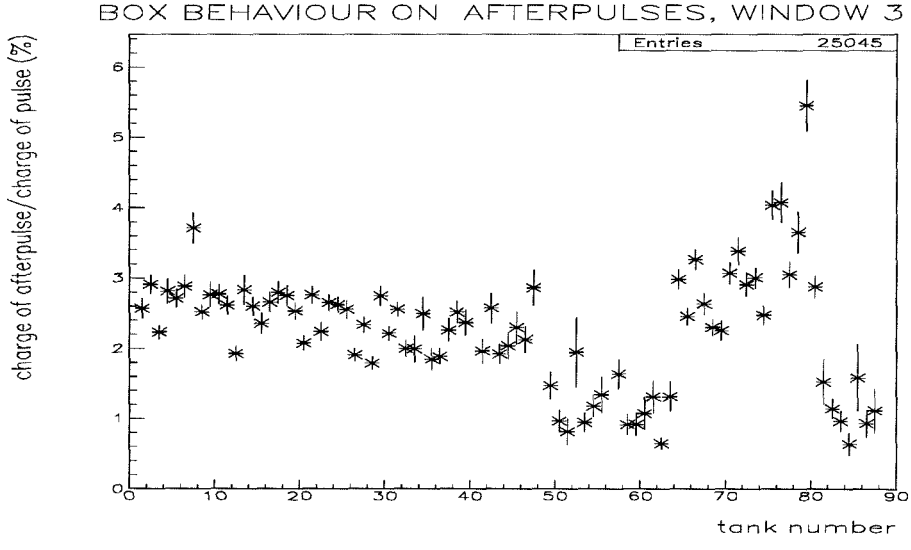


Figure A.11: Ratio of density of the charge of the afterpulses in the third time window (4.5-10 $\mu$s after the initial pulse) over the charge of the initial pulse versus the tank number.

## A.4 Time Evolution of the Afterpulsing

Helium existed in the gas mixture of the streamer tubes. Contamination of the tubes by He was deduced from the increasing rate of afterpulsing of PMT tubes mainly located in the top face. We selected and analyzed four runs (about 1 day of data) roughly six months apart, in order to examine the temporal evolution of the afterpulsing. This data sampling began in Sept. 1996 and went on until Dec. 1999. We plot (as a percentage) the mean ratio of the first afterpulse charge (first window) to the primary pulse charge versus time. Only events with initial pulses exceeding 800 mV in height were considered.

In Fig. A.12 we see time evolution of the afterpulsing for all tanks. In Fig. A.13 we see time evolution of the afterpulsing for the EMI tubes and for the Hamamatsu tubes. We note that the Hamamatsu tubes are more stable and less susceptible to afterpulsing. We recreate similar plots for different faces of the detector in figures A.14 to A.16. There was an obvious step jump in afterpulsing content between runs during April 1997 and runs during October 1997. This was due to the fixing of the capacitive coupling of the WFDs (see 3.2). Before the fix, we would underestimate the size of afterpulsing as it was superimposed under the positive overshoot. Even after taking this into account, the increase in afterpulsing was clearly much stronger for the top face.

Afterpulsing did not constitute a major problem in this monopole search, because it was easily remedied by introducing a dead time of 25 $\mu$s after large pulses. This did not result in any additional decrease in the acceptance; large pulses are mainly due to muons or muon-induced electromagnetic showers. In both cases, SPAM_MUON should have triggered. In the analysis we reject events with a SPAM_MUON trigger and this is correctly accounted for in the acceptance calculations.

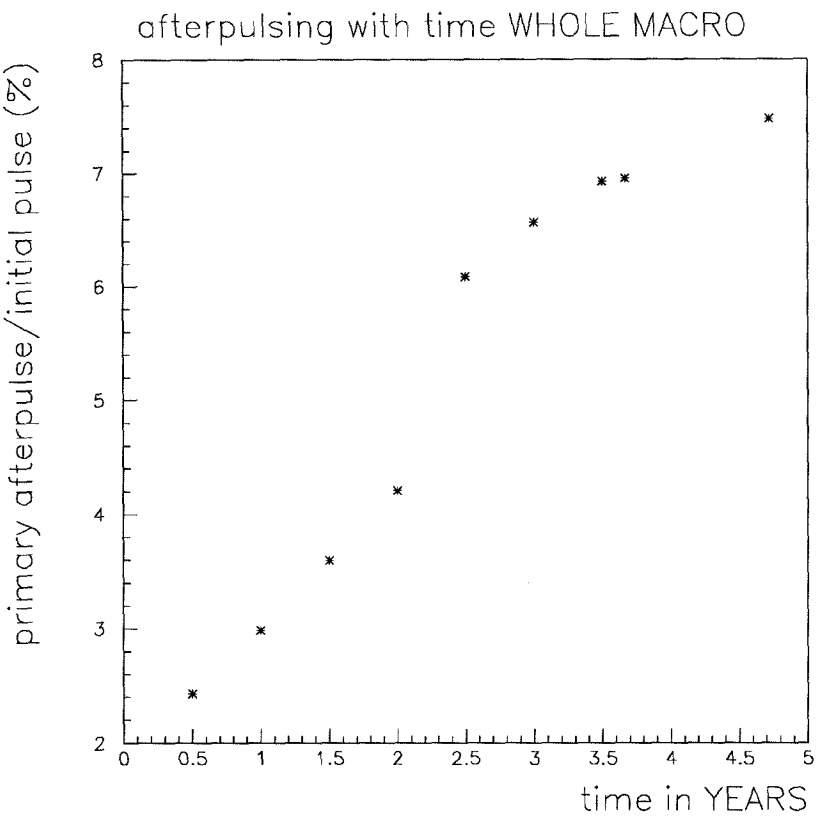


Figure A.12: Time evolution of afterpulsing for all tanks.

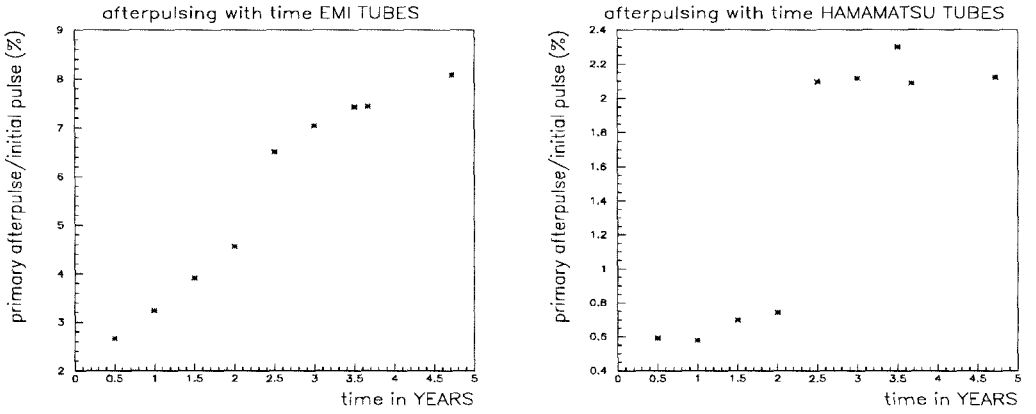


Figure A.13: Time evolution of afterpulsing for (a) EMI and (b) Hamamatsu PMTs. Note different vertical scales.

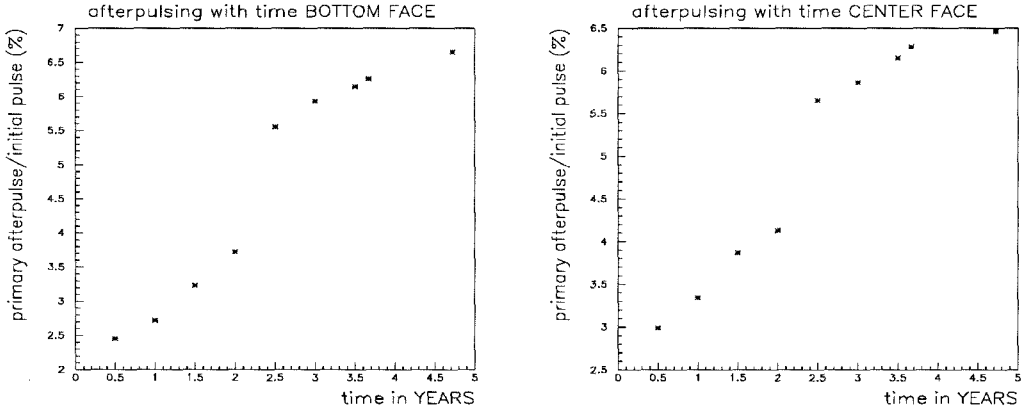


Figure A.14: a) Time evolution of afterpulsing for the BOTTOM face. b) Time evolution of afterpulsing for the CENTER face.

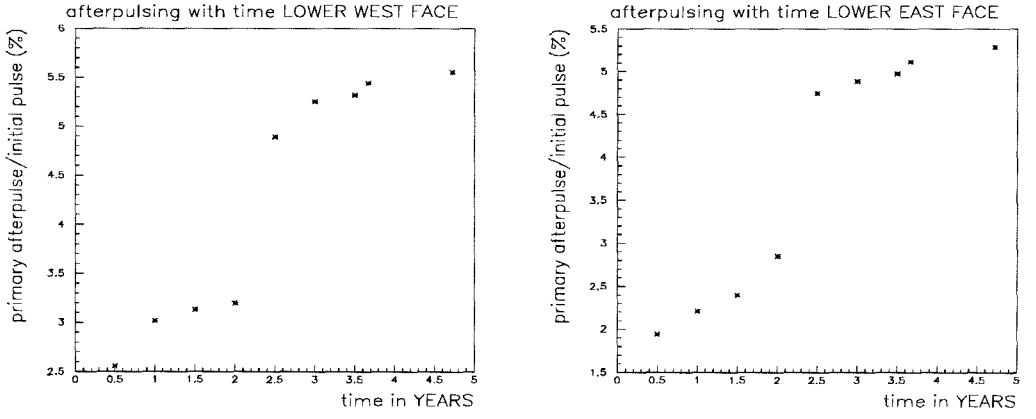


Figure A.15: a) Time evolution of afterpulsing for the LOWER WEST face. b) For the LOWER EAST face.

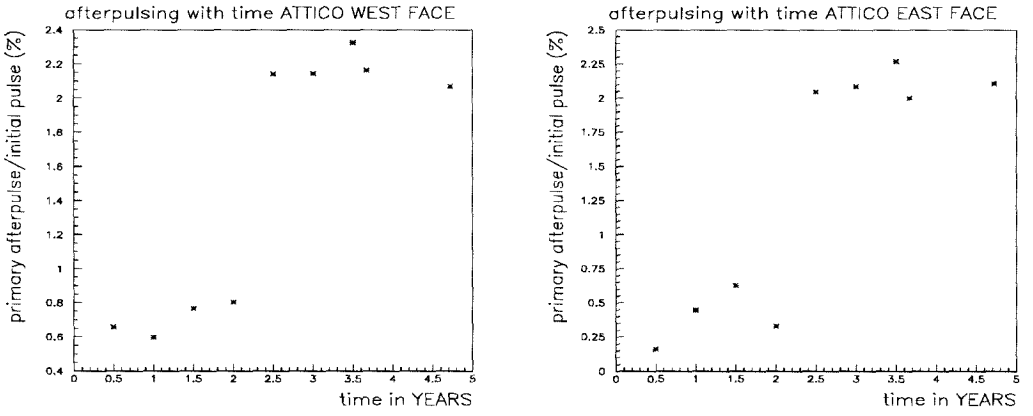


Figure A.16: a) Time evolution of afterpulsing for the ATTICO WEST face. b) For the ATTICO EAST face.

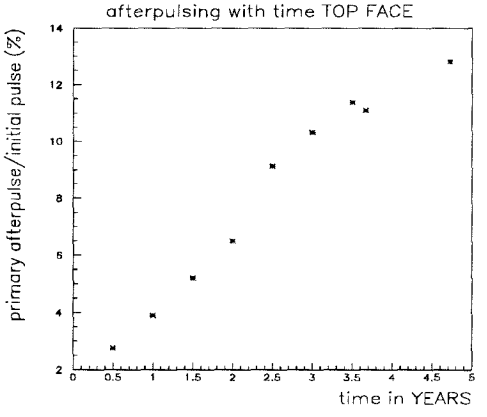


Figure A.17: Time evolution of afterpulsing for the TOP face.

# Bibliography

[1] J. D. Jackson, Classical Electrodynamics, second edition, Jon Wiley & Sons, Inc. (1975)

[2] P. A. M. Dirac, *Proc. Roy. Soc.*, A 133 (1931), 60-72

[3] J. Preskill, *Ann. Rev. Nucl. Part. Sci.*, 34 (1984), 461-530

[4] H. Georgi, S.L. Glashow, *Phys. Rev. Lett.* 32 (1974), 438-441

[5] H. Georgi, H. R. Quinn, S. Weinberg, *Phys. Rev. Lett.* 33 (1974), 451-454

[6] J. C. Pati, A. Salam, *Phys. Rev. D*, 10 (1974), 275-289

[7] C. N. Yang, *Phys. Rev. D*, 1 (1970), 2360

[8] A. M. Polyakov, *JETP Lett.*, 20 (1974), 194-195

[9] G. 't Hooft, *Nucl. Phys. B*, 79 (1974), 276-284

[10] R. N. Mohapatra, Lectures given at ICTP Summer School in Particle Physics, Trieste, Italy, 7 Jun - 9 Jul 1999. Published in Trieste 1999, Particle physics 336-394

[11] T. W. Kephart, Q. Shafi, *Phys. Lett. B*, 520 (2001), 313-316

[12] J. Preskill, *Phys. Rev .Lett*, 43 (1979), 1365

[13] L. Bracci, G. Fiorentini, *Phys. Lett. B* 124 (1983) 493, L. Bracci, G. Fiorentini, G. Mezzorani, P. Quarati, *Phys. Lett. B*143 (1984) 357

[14] T. W. B. Kibble, *J. Phys. A* 9 (1976), 1387

[15] E. W. Kolb, M. S. Turner, The Early Universe, Addison-Wesley (1990)

[16] J. Preskill, *Nuffield Workshop on the Very Early Universe*, Jun 21 - Jul 9 (1982), 119

[17] A. H. Guth, *Phys. Rev. D*, 23 (1981), 347

[18] A. H. Guth, E. Weinberg, *Nucl. Phys. B* 212 (1983), 321

[19] A. D. Linde, *Phys. Lett. B*, 108 (1982), 389

[20] A. Albrecht, P. J. Steinhardt, *Phys. Rev. Lett.*, 48 (1982), 1220

[21] A.D. Linde, *Phys. Lett. B*, 129 (1983), 177

[22] W. Collins, M. S. Turner, *Phys. Rev. D*, 29 (1984), 2158-2161

[23] L. Kofman, A. D. Linde, A. A. Starobinsky, *Phys. Rev. D*, 56 (1997), 3258

[24] L. Kofman, A. D. Linde, A. A. Starobinsky, *Phys. Rev. Lett.*, 76 (1996), 1001

[25] S. Khlebnikov, L. Kofman, A.D. Linde, I. Tkachev, *Phys. Rev. Lett.*, 81 (1998), 2012

[26] A. D. Linde, *Phys. Rep.* 333 (2000), 575-591

[27] Boomerang Collaboration (A.H. Jaffe et al.), *Phys. Rev. Lett.*, 86 (2001), 3475-3479

[28] G. Lazarides, Q. Shafi, *Phys. Lett. B*, 489 (2000), 194-202

[29] R. Jeannerot, S. Khalil, G. Lazarides hep-ph/0106035 Jun 2001

[30] A. Vilenkin, *Nucl. Phys. B*, 196 (1982), 240-258

[31] P. Langacker, S-Y Pi, Phys. Rev. Lett., 45 (1980), 1

[32] A. D. Linde, *Phys. Lett. B* 96 (1980), 293-296

[33] M. S. Turner, E. N. Parker, T. J. Bogdan, *Phys. Rev. D*, 26 (1982), 1296

[34] J. A. Harvey, M. A. Ruderman, J. Shaham, *Phys. Rev. D*, 33 (1986), 2084

[35] E. W. Kolb, M. S. Turner, *Astrophys. J.* 286 (1984), 702-710

[36] F. C. Adams, M. Fatuzzo, K. Freese, G. Tarlé, R. Watkins, M. S. Turner, *Phys. Rev. Lett.*, 70 (1993), 2511-2514

[37] M. J. Lewis, K. Freese, G. Tarlé, *Phys. Rev. D*, 62 (2000) 025002

[38] R. M. Kulsrud et al., *Astrophys. J.*, 480 (1997), 480

[39] V. A. Rubakov, *JETP Lett.*, 33 (1981) 644-646, *Pisma Zh. Eksp. Teor. Fiz.*, 33 (1981), 658-660;
V. A. Rubakov, *Nucl. Phys. B*, 203 (1982), 311-348;
V. A. Rubakov, M. S. Serebryakov, *Nucl. Phys. B*, 218 (1983), 240-268

[40] C. J. Callan, *Phys. Rev. D*, 26 (1982), 2058

[41] F. A. Bais, J. R. Ellis, D. V. Nanopoulos, K. A. Olive, *Nucl. Phys. B*, 219 (1983), 189

[42] T. F. Walsh, P. Weisz, T. T. Wu, *Nucl. Phys. B*, 232 (1984), 349

[43] A. N. Schellekens, *Phys. Rev. D*, 29 (1984), 2378

[44] A. Sen, *Nucl. Phys. B*, 250 (1985), 1

[45] K. Freese, M. S. Turner, D. N. Schramm, *Phys. Rev. Lett.*, 51 (1983), 1625-1628

[46] K. Freese, E. Krasteva, *Phys. Rev. D*, 59 (1999) 063007

[47] D. E. Groom, *Phys. Rept.*, 140 (1986), 323

[48] B. Cabrera, *Phys. Rev. Lett*, 48 (1982), 1378-1381 *Phys. Rev. D* 44 (1991), 636-660

[49] S. Bermon, C.C. Chi, C.C. Tsuei, J.R. Rozen, P. Chaudhari, M. W. McElfresh, *Phys. Rev. Lett.*, 64 (1990), 839-842

[50] M. E. Huber, B. Cabrera, M. A. Taber, R. D. Gardner, *Phys.Rev.D*, 44 (1991), 636

[51] S. P. Ahlen, *Phys. Rev. D*, 17 (1978), 229

[52] J. Lindhard, *Dan. Mat. Fys. Medd.*, 28 (1954), no. 8

[53] J. Lindhard, M. Scharff, *Phys. Rev.*, 124 (1961), 128

[54] S. P. Ahlen, K. Kinoshita, *Phys. Rev. D*, 26 (1982), 2347

[55] S. P. Ahlen, G. Tarlé, *Phys. Rev. D*, 27 (1983), 688; S. P. Ahlen, T. M. Liss, G. Tarlé, *Phys. Rev. Lett.*, 51 (1983), 940

[56] D. J. Ficenec, S. P. Ahlen, A. A. Marin, J. A. Musser, G. Tarlé, *Phys. Rev. D*, 36 (1987), 311-314; D. J. Ficenec, *Ph.D. Thesis*, UMI-90-23762-mc (1990), 115pp.

[57] J. Derkaoui, G. Giacomelli, T. Lari, G. Mandrioli, M. Ouchrif, L. Patrizii, V. Popa, *Astropart. Phys.*, 10 (1999), 339-352

[58] E. N. Alexeyev et al. ("BAKSAN"), ICRC90, Adelaide, vol. 10 (1990) 83

[59] S. D. Drell, N. M. Kroll, M. T. Mueller, S. Parke, M. H. Ruderman, *Phys. Rev. Lett.*, 50 (1983), 644; N. M. Kroll, S. Parke, V. Ganapathi, S.D. Drell, *Monopole '83:*, 295 (QCD161:N15:1983)

[60] R. Singer, D. Trautmann, *Nucl. Phys. A*, 554 (1993), 421

[61] V. Patera, *Phys. Lett. A*, 137 (1989), 259

[62] J .L. Thron et al. (Soudan-2 Collaboration), *Phys. Rev. D*, 46 (1992), 4846

[63] H. Adarkar et al. (KGF collaboration), $21^{st}$ ICRC, Adelaide, vol. 10 (1990), 95

[64] S. Orito et al., *Phys. Rev. Lett.*, 66 (1991), 1951

[65] Ambrosio et al. (the MACRO collaboration), ICRC 2001, Hamburg, Germany, Aug 07-15, 2001

[66] P. B. Price, M. H. Salamon, *Phys. Rev. Lett.*, 56 (1986), 1226

[67] P. B. Price, *Phys. Rev. Lett.*, 73 (1994), 1305

[68] BAIKAL Collaboration (L.B. Bezrukov et al.), *2nd Workshop on the Dark Side of the Universe* (1995) astro-ph/9601160 v1 1996

[69] R. Becker-Szendy et al. (IMB), *Phys. Rev. D*, 49 (1994), 2169-2173

[70] V. A. Balkanov et al. (the BAIKAL Coll.), ICRC99, Salt Lake City, UT, Aug 17-25, 1999, paper H.E. 5.3.04

[71] P. Niessen et al. (the AMANDA Coll.), ICRC99, Salt Lake City, UT, Aug 17-25, 1999, paper H.E. 5.3.05

[72] B. C. Barish, G. Giacomelli, J. T. Hong, *Phys. Rev. Lett.*, 73 (1994), 1306

[73] The MACRO Collaboration (S.P. Ahlen et al.), *Nucl.Instrum.Meth.A* 324 (1993) 337

[74] The MACRO Collaboration (M. Ambrosio et al.), technical paper, to be published

[75] G. Battistoni et al., *Nucl.Instrum.Meth.A* 235 (1985) 91

[76] J-T. Hong, *Ph.D. Thesis*, UMI-93-25360-mc (1993) 167 pp.